



# MONASH University

## **Dynamics of Associative Polymer Solutions and Polymeric Rings**

by

Aritra Santra

A thesis submitted for the degree of Doctor of Philosophy at  
Monash University in 2021

Department of Chemical Engineering  
Monash University

Clayton, Australia

July, 2021

## Copyright notice

---

©Aritra Santra (2021).

*Dedicated to my beloved parents  
for their unconditional love and support*

---

# Abstract

---

Several disparate phenomena, such as: (i) the flow behaviour of paints, coating and inks (Glass et al., 1991), (ii) the treatment of diseases in the posterior segment of the eye (Kirchhof et al., 2015), (iii) the development of food thickeners for people suffering from mastication and swallowing disorders (O’Leary et al., 2010), (iv) the designing of scaffolds with optimal characteristics for successful tissue engineering (El-Sherbiny and Yacoub, 2013), and (v) the response of hagfish when attacked by predators (Böni et al., 2016), have all got one feature in common - they are based on the unique properties of supramolecular networks formed by associative (sticky) polymer solutions. Associative polymers are macromolecules with attractive groups, and the reason for their use in such wide variety of applications is because the interactions between the sticky groups can be tuned by varying their number, strength of association and location in a polymer chain. Based on the position of stickers in polymer chains, associative polymers are classified as (a) telechelic (with stickers at the two ends of the chain) and (b) multi-sticker (with stickers along the polymer backbone). It is important to understand the static, dynamic and rheological behaviour of these special polymer solutions to design associative polymers for specific applications. In this project we develop a mesoscopic simulation algorithm to simulate associative polymer solutions with varying sets of parameters (such as concentration, chain length, number of stickers per chain, spacing between the stickers, strength of association between the stickers and solution temperature) in order to investigate the correlation of the underlying microscopic structure with the dynamics and macroscopic viscoelasticity.

It is important to characterise the equilibrium structure and properties of sticky polymer solutions in the dilute limit before attempting to understand the static and dynamic properties of a solution of sticky polymers in the semi-dilute or concentrated regimes. This has been pursued here by investigating the swelling of a sticky polymer chain as a function of the solvent quality, in other words, the thermal crossover behaviour. The universality of the swelling of the radius of gyration of a homopolymer relative to its value in the  $\theta$ -state, inde-

---

pendent of polymer-solvent chemistry, in the crossover regime between theta and athermal solvent conditions is well known. The addition of sticky monomers that have an attractive affinity for each other along the polymer backbone reduces the quality of the solvent, leading to an increase in the theta temperature of the sticky polymer solution. We examine the swelling of the radius of gyration of a sticky polymer relative to its value in the altered theta state. Using a novel potential to model the excluded volume interaction between monomers on the sticky chain, and introducing a renormalised solvent quality parameter, we carry out Brownian dynamics simulations to show that the swelling of sticky polymers is also universal, and indeed identical to that of homopolymers in the thermal crossover regime. We have also identified a  $\theta$ -surface which determines the boundary between good solvent and poor solvent conditions for sticky polymer solutions based on the sticker interaction strength. Additionally, we find that the effective monomer size under  $\theta$ -solvent condition, is identical in dilute homopolymer and sticky polymer solutions.

A salient feature of associative polymer solutions is the formation of reversible gels and networks at fairly low concentrations. The onset of gelation is governed by the polymer concentration ( $c$ ), the solution temperature ( $\hat{\tau}$ ), the number of stickers per chain ( $f$ ), the spacing between the stickers along the chain backbone ( $\ell$ ) and the strength of association between the stickers ( $\epsilon_{st}$ ) (Rubinstein and Dobrynin, 1997)(Ishida and Tanaka, 1997)(Semenov and Rubinstein, 1998)(Dobrynin, 2004). Associative polymers generally undergo two kinds of associations, one between stickers from within the same chain, called intra-chain association and the other between stickers from different chains, known as inter-chain associations. Both these associations lead to the formation of micelles and networks at fairly low concentrations. Depending on the solution temperature, associative polymer solutions undergo a phase transition and get separated into a sol phase (with finite size clusters) and a gel phase (with system spanning infinite size clusters) (Kumar and Douglas, 2001)(Baljon et al., 2007). There has been a long standing debate regarding the incipient concentration for gelation as there are several definitions proposed in the literature based on the free chain concentration, the cluster-size distribution or the scaling of viscosity, which all correspond to different signatures of gelation (Flory, 1941)(Stockmayer, 1943)(Stockmayer, 1944)(Ishida and Tanaka, 1997)(Semenov and Rubinstein, 1998). In particular, Flory (Flory,

---

1941) and Stockmayer (Stockmayer, 1943)(Stockmayer, 1944) independently proposed two different models to characterise the post-gel regime, based on differing hypotheses of cluster dynamics. Ishida and Tanaka (Ishida and Tanaka, 1997) subsequently developed a framework based on lattice theory to explore the consequences of these differing pictures. They showed that the number average chain-cluster size in the sol phase goes through a maximum at the gelation concentration in Flory’s model, while it remains constant in Stockmayer’s model, subsequent to the onset of gelation. Using an argument based on mean field theory, Rubinstein and Semenov obtain predictions in line with Flory’s model (Semenov and Rubinstein, 1998). Dobrynin (Dobrynin, 2004), on the other hand, developed a mean field theory for associative polymer solutions based on lattice geometry and blob theory and derived scaling relations to correlate the dependence of the fraction of intra-chain ( $p_1$ ) and inter-chain ( $p_2$ ) conversions of stickers on the microscopic system parameters at equilibrium and derived expressions that identify the onset of gelation. In this work we have developed a multi-particle Brownian dynamics algorithm with hydrodynamic interactions (HI) to simulate multi-sticker associative polymer solutions in dilute and semi-dilute regimes and compared our model with the predictions of the scaling theory by Dobrynin (Dobrynin, 2004).

We have identified three static signatures of gelation based on the percolation transition (Stauffer and Aharony, 1992), the maxima in the free-chain concentration (Semenov and Rubinstein, 1998) and cluster-size distribution for chains (Kumar and Douglas, 2001). However, the relationship between these static measures and the dynamics and rheological response of associative polymer solutions remains unknown. As a result of the formation of complex topologies in these polymer solutions, the relaxation behaviour is far more complicated than can be explained by a simple Maxwell model. We have performed multi-chain Brownian dynamics simulations to examine the dynamics and linear viscoelastic behaviour of multi-sticker associative polymer solutions at finite concentrations. Equilibrium and shear flow simulations are carried out to calculate linear viscoelastic properties such as zero-shear rate viscosity and dynamic moduli ( $G'$  &  $G''$ ). We have investigated the scaling with concentration of different characteristic relaxation times computed based on the decay of auto-correlation functions and the scaling of dynamic moduli, which show a cross-over in the scaling exponent near the concentration corresponding to the maxima in the free chain con-

---

centration. Additionally, we have examined the scaling of the zero-shear rate viscosity with concentration and interestingly found that the scaling exponent for the zero-shear rate viscosity also shows a cross-over near the maximum in the free chain concentration. We also explore how the time scales associated with the formation and breakage of chain clusters affect the overall relaxation behaviour over a range of concentration.

The multi-particle Brownian dynamics algorithm developed in this work to study the static and dynamic properties at equilibrium, along with the non-equilibrium rheological response across a wide range of concentrations in the dilute and semi-dilute regimes for associative polymer solutions, has enabled many of the unresolved questions about the dynamics of associative polymer solutions to be addressed satisfactorily.

Another system studied in the present thesis consists of dilute solutions of polymeric rings. Much of the dynamic and rheological response of polymer solutions are dependent on the topological structure of the polymer chains. In many cases, the ends of the polymer chains determine the static and dynamic behaviour of polymer solutions. For instance, the relaxation behaviour of dangling ends in solutions of associative polymers or the decay of end-to-end vector auto-correlation functions of polymer chains determine the dynamics and viscoelasticity of the system. Ring polymers, on the other hand, are a special class of polymers which do not have any ends. Due to such unique topology, solutions of ring polymers exhibit properties which are not commonly observed in their linear chain counterparts. In this sub-project we have studied the universal static and dynamic properties of polymeric rings in the dilute solution using Brownian dynamics simulations. The universality of the ratio of the radius of gyration to the hydrodynamic radius ( $U_{RD}$ ) as a function of solvent quality is well known for linear polymers. Here we show the universality of the ratio  $U_{RD}$  for ring polymers as a function of solvent quality. Besides, a comparative study has been done on the swelling ratio of the radius of gyration ( $\alpha_g$ ), hydrodynamic radius ( $\alpha_H$ ) and mean stretch ( $\alpha_X$ ) for linear and ring polymers. Using the swelling curve and universal ratio,  $U_{RD}$ , we have suggested a method to determine the solvent quality of polymeric rings, which is fundamentally important to model ring polymer solutions and predict the dynamics of real experimental system more accurately.

---

## Declaration

---

This thesis is an original work of my research and contains no material which has been accepted for the award of any other degree or diploma at any university or equivalent institution and that, to the best of my knowledge and belief, this thesis contains no material previously published or written by another person, except where due reference is made in the text of the thesis.

Signature:

Name: Aritra Santra

Date: 07/07/2021

---

## Journal and conference publications

---

The chapters included in this thesis contain materials from the following publications.

### Journal publications:

- (i) Aritra Santra, Kiran Kumari, Ranjith Padinahateeri, B. Dünweg and J. Ravi Prakash, *Universality of the collapse transition of sticky polymers*, **Soft Matter**, 2019, 15, 7876-7887.
- (ii) Aritra Santra, B. Dünweg and J. Ravi Prakash, *Universal scaling and characterization of gelation in associative polymer solutions*, **Journal of Rheology**, 65, 549 (2021).
- (iii) Aritra Santra, Gareth H. McKinley and J. Ravi Prakash, *Dynamic characterization of gelation in associative polymer solutions*. (In preparation).
- (iii) Aritra Santra and J. Ravi Prakash, *Universality in dilute solutions of polymeric rings at equilibrium*. (In preparation).

### Conference presentations:

- (i) Aritra Santra, B. Dünweg and J. Ravi Prakash, *Universal scaling in associative polymer solutions*, **Statistical Mechanics of Soft Matter Meeting**, 16-17 December, 2019, Adelaide, Australia.
- (ii) Aritra Santra, Gareth H. McKinley and J. Ravi Prakash, *Dynamic signatures of gelation in associative polymer solutions*, **International Congress of Rheology**, 14-17 December, 2020, Rio de Janeiro, Brazil.

---

# Acknowledgement

---

I would like to express my heartfelt gratitude to my supervisor, Prof. Ravi Prakash Jagadeeshan, without whom completing this wonderful journey of my PhD would not have been possible. His continuous moral and technical supports always kept my spirits high and made me productive. Every academic discussion with him has inspired my analytical thinking and improved my understanding of the subject. I would like to thank him for giving me the opportunity to work in his group and help me enriching my knowledge in the field of *Polymer physics* and *Polymer rheology*.

I thank Prof. Burkhard Dünweg, my co-supervisor, for all the insightful discussions related to the theory of associative polymer solutions. I specially thank Prof. Gareth H. McKinley for his interesting suggestions during our meeting on the discussion of the dynamics of associative polymer solutions. I would also like to thank Dr. Nathan Clisby and Prof. P. Sunthar, for the useful discussions on des Cloizeaux exponent and the computation of relaxation time scales. I feel fortunate enough to be a part of the Molecular Rheology Group, where I met some of the brilliant students like Kailash, Kiran, Isaac, Silpa and Nick, who is a post-doctoral fellow in our group. I enjoyed every conversation with them on various technical and non-technical topics. I should also mention my friends, Shuvashis and Sanjay for making my stay in Australia a memorable one and giving their constant support, specially, during the pandemic of COVID-19. I am grateful to all the staff at the Department of Chemical Engineering, in particular Lilyanne Price and Tracy Groves, for their help and advice on administrative matters and making my life easy in Australia.

I want to thank Monash Graduate Research (MGR) for offering me the MGS and MIPRS scholarships, without which my work would not have been possible. The research during my PhD was supported under Australian Research Council's Discovery Projects funding scheme (project number DP190101825). I take this opportunity to thank the National Computational Infrastructure (NCI Australia) and the High-Performance Computing facility team at Monash University for their assistance with the computational resources. I am specially grateful to Mr. Simon Michnowicz, Senior Application Specialist, High-Performance

---

Computing at Monash University for his continuous assistance in providing us the access to additional computational resources, whenever necessary.

# Contents

---

Certificate

Abstract i

Acknowledgement vii

List of Figures xiii

List of Tables xxvii

---

**1 Introduction 1**

1.1 Dynamics of associative polymer solutions . . . . . 1

1.2 Dynamics of ring Polymers . . . . . 5

**2 Modelling and Simulations 8**

2.1 Polymer Model . . . . . 9

2.2 Role of Hydrodynamic Interactions in Brownian Dynamics Simulations . . . 10

2.3 Governing Equations For Brownian Dynamics Simulation . . . . . 12

2.4 Bonded Interactions . . . . . 14

2.5 Non-bonded Interactions . . . . . 14

2.6 Conclusions . . . . . 18

**3 Universality of the collapse transition of sticky polymers 19**

3.1	Introduction . . . . .	19
3.2	Governing Equations and Simulation Details . . . . .	22
3.3	The $\theta$ -point for homopolymers . . . . .	24
3.3.1	The radius of gyration . . . . .	24
3.3.2	The second virial coefficient . . . . .	26
3.4	Universal swelling of homopolymers . . . . .	29
3.5	$\theta$ -point and swelling of sticky polymers . . . . .	32
3.5.1	$\theta$ -point for sticky polymer solutions . . . . .	32
3.5.2	Universal swelling of sticky polymers . . . . .	37
3.6	Discussion and conclusions . . . . .	40
<b>4</b>	<b>Universal scaling and characterisation of gelation in associative polymer solutions</b>	<b>44</b>
4.1	Introduction . . . . .	44
4.2	Model for associative polymer solutions . . . . .	48
4.3	Scaling relations for fractions of associated stickers . . . . .	50
4.4	Choice of parameters and details of simulations . . . . .	56
4.4.1	Simulation constraints . . . . .	57
4.4.2	Simulation details . . . . .	59
4.4.3	Computation of clusters . . . . .	61
4.5	Validation of scaling relations for degrees of conversion . . . . .	62
4.5.1	Dependence on spacer length and monomer concentration . . . . .	63
4.5.2	Dependence on solvent quality parameter and sticker strength . . . . .	72
4.5.3	Crossover behaviour between the scaling regimes . . . . .	77
4.5.4	Scaling of radius of gyration . . . . .	80
4.5.5	$\theta$ -solvent conditions for sticky polymer chains . . . . .	82
4.6	Hydrodynamic interactions and time to equilibration . . . . .	86
4.7	Characterisation of gelation and the gelation line . . . . .	89
4.8	Phase separation and the breakdown of scaling . . . . .	100
4.9	Summary and conclusions . . . . .	104

<b>5</b>	<b>Dynamic signatures of gelation in associative polymer solutions</b>	<b>107</b>
5.1	Introduction . . . . .	107
5.2	Governing equations . . . . .	110
5.2.1	Model for associative polymer solutions . . . . .	110
5.2.2	Dynamic properties . . . . .	110
5.3	Results and discussions . . . . .	114
5.3.1	Scaling of the chain cluster size distribution . . . . .	115
5.3.2	Stress auto-correlation function . . . . .	118
5.3.3	Zero-shear rate viscosity . . . . .	119
5.3.4	Storage ( $G'$ ) and loss ( $G''$ ) moduli . . . . .	124
5.3.5	Calculation of relaxation time . . . . .	127
5.3.6	Chain-cluster lifetime . . . . .	134
5.4	Conclusions . . . . .	134
<b>6</b>	<b>Universality in polymeric rings at equilibrium</b>	<b>138</b>
6.1	Introduction . . . . .	138
6.2	Modelling and simulations . . . . .	139
6.3	Universal ratios for static properties . . . . .	140
6.4	Universal ratios involving hydrodynamic radius . . . . .	143
6.5	Conclusions . . . . .	151
<b>7</b>	<b>Summary and future work</b>	<b>153</b>
	<b>Appendix</b>	<b>155</b>
<b>A</b>	<b>The cut-off radius for the SDK potential</b>	<b>155</b>
<b>B</b>	<b>Equivalence of sticking rules</b>	<b>162</b>
<b>C</b>	<b>Scaling relations in associative polymer solutions from lattice-based mean-field theory</b>	<b>164</b>
C.1	Intra-chain association scaling . . . . .	165
C.2	Inter-chain association scaling . . . . .	168

## **CONTENTS**

---

C.3	Free energy of associative polymers in dilute solutions . . . . .	170
D	Storage ( $G'$ ) and loss ( $G''$ ) moduli for a dilute solution of Rouse chains	171
E	Scaling of computational cost with chain size	173
F	Tabulated values of simulation results for $R_g$ , $p_1$ and $p_2$ as a function of the parameters $\{N_b, \ell, f, \epsilon_{bb}, \epsilon_{st}, c/c^*\}$	175

# List of Figures

1.1	Example of multiple crosslinks in telechelic polymers. (a) Ionic multiplets, (b) hydrophobic aggregates. Numbers show multiplicity of junctions. Reproduced from (Tanaka, 2011) . . . . .	3
1.2	Storage and loss moduli for (a) telechelic (reproduced from (Suzuki et al., 2012)), and (b) multi-sticker (reproduced from (Wagner and McKinley, 2017)) . . . . .	4
1.3	Viscosity as a function of shear rate in (a) a telechelic HEUR solution (from (Suzuki et al., 2012)) and (b) a polysaccharide (Mamaku gum) solution in which interactions are driven by hydrogen bonding (from (Jaishankar et al., 2015)) . . . . .	5
2.1	Schematic of bead-spring chain polymer model for associative polymer. $\mathbf{Q}_{\mu-1} = \mathbf{r}_{\mu} - \mathbf{r}_{\mu-1}$ represents the connector vector between bead $\mu - 1$ and $\mu$ . The green coloured beads represent the stickers. . . . .	10
2.2	Graphical representation of the SDK potential, $U_{\text{SDK}}$ , as a function of the distance between interacting molecules, $r$ , for different values of well depth $\epsilon$ . . . . .	15
3.1	Comparison of the ratio $Rg^2/(N_b - 1)$ as a function of the strength of interaction, $\epsilon_{bb}$ , for different values of chain length, $N_b$ . The solid lines represent the results obtained by Steinhauser (Steinhauser, 2005) for $N_b = 50$ and $N_b = 100$ and the broken lines are the results obtained from BD simulation. . . . .	24
3.2	The ratio $R_g^2/(N_b - 1)$ versus the well depth of the SDK potential, $\epsilon_{bb}$ , to estimate the $\theta$ -point for cutoff radius $r_c = 1.82 \sigma$ . The symbols represent simulation data and the dotted lines are drawn to guide the eye. The $\theta$ -point is estimated as the intersection of all the curves and leads to $\epsilon_{bb} = 0.45$ . . . . .	26

## LIST OF FIGURES

---

- 3.3 (a) The effective potential,  $U(r)/k_B T$ , as a function of the separation distance,  $r/R_g$ , between the centres of mass of a pair of homopolymer chains at different values of potential well depth,  $\epsilon_{bb}$ . (b) The second osmotic virial coefficient,  $B_2$ , as a function of potential well-depth,  $\epsilon_{bb}$ , for different chain lengths. The estimated value of the  $\theta$ -point,  $\epsilon_\theta$ , from the second virial coefficient is  $0.42 \pm 0.03$ . . . . . 27
- 3.4 Universal swelling behaviour of the radius of gyration,  $\alpha_g^2$ , as a function of the solvent quality,  $z$ . The red filled circles and the blue filled squares are simulation results with the SDK potential, which is compared with BD simulations obtained with the narrow Gaussian potential (Kumar and Prakash, 2003), and with experimental results for polystyrene in two solvents (Miyaki and Fujita, 1981). The solid line represents the curve fit corresponding to Eq. (3.7). . . . . 30
- 3.5 Solvent quality  $z$  versus the factor  $(1 - \epsilon_{bb}/\epsilon_\theta)\sqrt{N_b}$  for polymer chain interacting with SDK potential. The symbols are the simulation data and the straight line gives a linear fit through the data points with slope 0.1586. . . . . 31
- 3.6 The ratio  $R_g^2/(N_b - 1)$  as a function sticker strength,  $\epsilon_{st}$ , for a single sticky polymer chain with backbone monomer attraction strengths,  $\epsilon_{bb} = 0.3$  and  $0.4$ , respectively, and spacer length,  $\ell = 4, 5$  and  $6$ , as indicated in the various figure legends. In all the cases the stickers associate with functionality equal to 1. The errorbars for  $\epsilon_{st}$  at the point of intersection are estimated by an error propagation scheme discussed in Section 3.5.1. . . . . 33
- 3.7 The ratio  $R_g^2/(N_b - 1)$  at the  $\theta$ -point, denoted by  $R_{g\theta}^2/(N_b - 1)$ , for different chain lengths,  $N_b$ , spacer monomer,  $\ell$ , and backbone monomer attraction strength,  $\epsilon_{bb}$ . The dashed line corresponds to the constant value of the ratio  $R_{g\theta}^2/(N_b - 1)$ , which is estimated to be 0.603. . . . . 34
- 3.8 ((a) and (c)) The effective potential,  $U(r)/k_B T$ , as a function of the separation distance,  $r/R_g$ , between the centres of mass of a pair of sticky polymer chains at different values of sticker strength,  $\epsilon_{st}$ . ((b) and (d)) The second osmotic virial coefficient,  $B_2$ , as a function of the sticker strength,  $\epsilon_{st}$ , for different chain lengths. The estimated value of the  $\theta$ -point,  $\epsilon_{st}^\theta$ , from the second virial coefficient is  $3.231 \pm 0.012$  and  $1.215 \pm 0.065$  for  $\ell = 4, \epsilon_{bb} = 0.3$  and  $\ell = 5, \epsilon_{bb} = 0.4$ , respectively. . . . . 36

3.9	(Color online) Schematic of a $\theta$ -surface in terms of the scaled variables $(\epsilon_{st}/\epsilon_\theta - 1)$ plotted against the scaled backbone solvent quality, $(1 - \epsilon_{bb}/\epsilon_\theta)$ , and spacer length, $\ell$ . Points above the surface indicate solutions of sticky polymers in poor solvent whereas points below the surface represents solutions in a good solvent. . . . .	37
3.10	Universal swelling of the radius of gyration, $\alpha_g^2$ , as a function of the solvent quality, $z$ . The swelling of the sticky polymers with different spacer lengths, $\ell$ , and backbone monomer attraction strengths, $\epsilon_{bb}$ , is compared with the swelling of homopolymers, as indicated in the figure. The sticker functionality is equal to 1 in all cases. The solid line represents the curve fit corresponding to Eq. (3.7). . . . .	38
3.11	Sticker strength under $\theta$ -solvent conditions, $\epsilon_{st}^\theta$ , versus the spacer length, $\ell$ , for different backbone attraction strengths, $\epsilon_{bb}$ . The open symbols represent the elaborate procedure for obtaining $\epsilon_{st}^\theta$ described in Section 3.5.1, while the filled symbols are obtained by the semi-analytical procedure described in Section 3.5.2. The dashed line is drawn to guide the eye. The constant straight line indicates the limiting value of $\epsilon_{st}^\theta$ , as discussed in the context of Eq. (3.9). . . . .	40
4.1	Three scaling regimes when the chain of backbone monomers is in a good solvent. Stickers are indicated by red circles. (a) $\ell < g_T < g_c$ (Regime I), (b) $g_T < \ell < g_c$ (Regime II) and (c) $g_T < g_c < \ell$ (Regime III). . . . .	51
4.2	The dependence of ratios involving (a) intra-chain (b) inter-chain degrees of conversion, and (c) the ratio of intra-chain and inter-chain association fractions, on the monomer concentration, $c$ , with the chain backbone under Regime I ( $\ell < g_T < g_c$ ) conditions. The spacer length dependence is absorbed in the $y$ -axis. Simulations are carried out at constant solvent quality parameter $\hat{\tau}$ , and a constant sticker strength $\epsilon_{st}$ , except in (c) where two different values of $\epsilon_{st}$ have been considered. The values $\nu = 3/5$ and $\theta_2 = 1/3$ have been used (see Table 4.1). The dashed and the solid lines are drawn with slopes equal to the prediction by scaling theory, while symbols represent simulation data. . . . .	64
4.3	Variation of intra-chain ( $p_1$ ) and inter-chain ( $p_2$ ) association fractions as a function of scaled monomer concentration, $c/c^*$ , for a sticky polymer solution in Regime I.	66

4.4 The dependence of ratios involving (a) intra-chain (b) inter-chain degrees of conversion, and (c) the ratio of intra-chain and inter-chain association fractions, on the monomer concentration,  $c$ , with the chain backbone under  $\theta$ -solvent and Regime II ( $g_T < \ell < g_c$ ) conditions. The spacer length dependence is absorbed in the  $y$ -axis. Simulations are carried out at constant solvent quality parameter  $\hat{\tau}$  and sticker strength  $\epsilon_{st}$ , except in (c) where two different values of  $\epsilon_{st}$  have been considered. The values of  $\theta_2$  and  $\nu$  are 0 and 1/2, respectively for the backbone under  $\theta$ -solvent conditions, and 1/3 and 3/5, respectively, for chains with  $\epsilon_{bb} = 0$  (see Table 4.1). The dashed and the solid lines are drawn with slopes equal to the prediction by scaling theory, while symbols represent simulation data. . . . . 68

4.5 Variation of intra-chain ( $p_1$ ) and inter-chain ( $p_2$ ) association fractions as a function of scaled monomer concentration,  $c/c^*$ , for (a) a sticky polymer solution with  $N_b = 64$ ,  $\ell = 12$ ,  $f = 4$ ,  $\epsilon_{bb=0}$  and  $\epsilon_{st}$ , where the parameters correspond to Regime II and III and (b) sticky polymer solution with  $\theta$ -backbone. . . . . 69

4.6 The dependence of ratios involving (a) intra-chain (b) inter-chain degrees of conversion, and (c) the ratio of intra-chain and inter-chain association fractions, on the monomer concentration,  $c$ , with the chain backbone under Regime III conditions. The spacer length dependence is absorbed in the  $y$ -axis. Simulations are carried out at constant solvent quality parameter  $\hat{\tau} = 1$ , and constant sticker strength,  $\epsilon_{st} = 5.0$ . The values of  $\theta_2$  and  $\nu$  are 1/3 and 3/5, respectively (see Table 4.1). Insets in (a) and (b) show the range of concentration in terms of  $c/c^*$ . The dashed and the solid lines are drawn with slopes derived from the prediction and the symbols are simulation data. . . . . 71

4.7 Scaling of the ratios involving intra-chain and inter-chain degrees of conversion as a function of sticker strength,  $\epsilon_{st}$ , for systems in (a) Regime I and (b) Regime II. Symbols represent results of simulations, while the lines are drawn to guide the eye. 73

4.8	Scaling of the sum of the ratios involving intra-chain and inter-chain association fractions (see Eq. (4.12)) as a function of sticker strength, $\epsilon_{st}$ , for three systems with $N_b = 34$ , $\ell = 6$ , $f = 4$ ; $N_b = 34$ , $\ell = 4$ , $f = 6$ , and $N_b = 64$ , $\ell = 12$ , $f = 4$ , with $\epsilon_{bb} = 0$ , at $c/c^* = 1.4$ . The symbols are the simulation data and the solid line is an exponential fit to the data. Note that for Regime II depicted here, $\alpha = 1/4$ and $\beta = 2$ . . . . .	75
4.9	Master plots demonstrating validation of scaling relations for, (i) the ratio involving the intra-chain degree of conversion $p_1$ , in (a) Regimes I and II, and (c) $\theta$ -solvent conditions for backbone monomers, and, (ii) the ratio involving the inter-chain degree of conversion $p_2$ , in (b) Regimes I and II, and (d) $\theta$ -solvent conditions for backbone monomers, plotted as a function of monomer concentration, $c$ , for different spacer segment lengths $\ell$ , sticker strengths, $\epsilon_{st}$ , and solution temperatures, $\hat{\tau}$ . The exponent $\alpha = 1/4$ . The dashed and the solid lines are drawn with slopes equal to the prediction by scaling theory, while symbols represent simulation data. . . . .	76
4.10	Crossover behaviour between the different scaling regimes. (a) Change in the ratio involving the intra-chain degree of conversion $p_1$ from Regime I, where $\ell < g_T < g_c$ to Regime II, where $g_T < \ell < g_c$ , due to a change in the solvent quality parameter $\hat{\tau}$ . (b) Change in the ratio involving the inter-chain degree of conversion $p_2$ from Regime I to Regime II due to a change in $\hat{\tau}$ . (c) Change in the ratio involving the intra-chain degree of conversion $p_1$ from Regime II, where $g_T < \ell < g_c$ , to Regime III, where $g_T < g_c < \ell$ , due to a change in the concentration $c$ . (d) Change in the ratio involving the inter-chain degree of conversion $p_2$ from Regime II to Regime III, due to a change in $c$ . . . . .	78

4.11 Ratios of the radius of gyration as a function of scaled concentration,  $c/c^*$ .  $R_{g0HP}^2$  and  $R_{g0SP}^2$  are the mean-squared radius of gyration of the homopolymer (HP) and the sticky polymer (SP), respectively, in the dilute limit. The backbone monomers in both polymers are in an athermal solvent. The filled red symbols represent data for homopolymer solutions obtained from current simulations, while the yellow stars are from MPCD simulations by Huang et al. (Huang et al., 2010) The filled green squares and purple diamonds represent sticky polymer solutions. The filled blue right triangles represent a situation in which the sticky polymer chain as a whole is under  $\theta$ -solvent conditions. These different scenarios are achieved with different backbone monomer interaction strengths,  $\epsilon_{bb}$ , sticker strengths,  $\epsilon_{st}$ , and spacer lengths  $\ell$ . The dashed line is the theoretical scaling prediction (Eq. (4.13)) for unentangled semidilute homopolymer solutions. The filled blue line is drawn to guide the eye. . . . . 81

4.12 The dependence of ratios involving (a) intra-chain, and (b) inter-chain degrees of conversion, on the monomer concentration,  $c$ , with sticky polymer chains under nearly  $\theta$ -solvent conditions for sticky chains as a whole. This is achieved, for a chain with  $N_b = 34$ ,  $\ell = 6$ ,  $f = 4$ , and  $\epsilon_{bb} = 0.35$ , by setting  $\epsilon_{st} = 3.6$ , which is close to the value  $\epsilon_{st}^\theta = 3.4$  computed for these parameter values. The dashed and the solid lines are drawn with slopes that are a good fit to the symbols, which represent simulation data. . . . . 83

4.13 Variation of intra-chain ( $p_1$ ) and inter-chain ( $p_2$ ) association fractions as a function of scaled monomer concentration,  $c/c^*$ , with sticky polymer chains under nearly  $\theta$ -solvent conditions for sticky chains as a whole. . . . . 84

4.14	The transient variation of (a) the intra-chain, and (b) the inter-chain association fractions, for two different concentrations, and the time evolution of the radius of gyration at the scaled concentrations, (c) $c/c^* = 0.2$ , and (d) $c/c^* = 0.4$ . Simulations with and without hydrodynamic interactions (HI) have been displayed for both properties, with the former carried out with the hydrodynamic interaction parameter, $h^* = 0.2$ . The dashed vertical lines indicate the time required for equilibration. The choice of simulation parameters leads to a sticky polymer solution in scaling Regime II. . . . .	87
4.15	Spanning probability (SP) as a function of monomer concentration in Regime II for (a) $N_b = 24, \ell = 4, f = 4$ and (b) $N_b = 34, \ell = 4, f = 6$ , with sticker strength, $\epsilon_{st} = 5.0$ . The point of divergence of the curves at different box sizes, $L$ , is assumed to represent the concentration at the gelation threshold, and is indicated as occurring at $c_{g1}/c^* \approx 0.3$ . . . . .	91
4.16	Chain cluster-size distribution as a function of monomer concentration in Regime II for (a) $N_b = 24, \ell = 4, f = 4$ , and (b) $N_b = 34, \ell = 4, f = 6$ , with sticker strength, $\epsilon_{st} = 5.0$ . The onset of bimodality, which is assumed to represent a signature of gelation, occurs at $c_{g2}/c^* \approx 1.0$ , for each of the three chain lengths. . . . .	92
4.17	Free chain concentration as a function of monomer concentration in Regime II for different chain lengths with spacer length, $\ell = 4$ , sticker strength, $\epsilon_{st} = 5.0$ and $\epsilon_{bb} = 0$ . The maxima in the free-chain concentration is observed at $c_{g3}/c^* \approx 0.5$ . . . . .	93
4.18	Variation of inter-chain conversion, $p_2$ , and the ratio $1/[(1 - p_1)f - 1]$ with scaled concentration, $c/c^*$ , for systems with chain lengths (a) $N_b = 34$ , (b) $N_b = 39$ , (c) $N_b = 44$ and (d) $N_b = 64$ . For all the chain lengths, the values of spacer length, $\ell = 4$ , sticker strength, $\epsilon_{st} = 5$ , and backbone monomer interaction strength, $\epsilon_{bb} = 0$ , are held constant. The values of $c/c^*$ at the point of intersection of the two curves for various chain lengths are (a) 0.98, (b) 0.95, (c) 0.93 and (d) 0.89. . . . .	95
4.19	Snapshots of the simulation box for a system with parameters $\{N_b = 34, \ell = 4, f = 6, \epsilon_{bb} = 0, \epsilon_{st} = 5\}$ at (a) $c/c^* = 0.2$ , (b) $c/c^* = 0.5$ and (c) $c/c^* = 1.0$ . The red beads indicate inter-chain associations, while the green beads represent intra-chain associations. . . . .	96

4.20 Scaling of inter-chain degree of conversion,  $p_2^{g_i}$ , at the gel-point in Regime II, predicted by the three different signatures of gelation, with (a)  $(1 - p_1)f - 1$ , and (b) the number of spacer monomers  $\ell$ , for systems with constant number of stickers  $f$ , and different chain lengths  $N_b$ . The sticker strength and backbone solvent quality are kept constant at  $\epsilon_{st} = 5.0$  and  $\epsilon_{bb} = 0$ , respectively. Each symbol shape represents a system with a particular chain length  $N_b$  and the dashed lines are the Flory-Stockmayer theory predictions at each of the gelation signatures. . . . . 97

4.21 Scaling with the number of stickers per chain,  $f$ , and the spacer length,  $\ell$ , in Regime II, of the quantities  $(1 - p_{g_i})^2$  [(a) and (b), respectively], and  $[(1 - p_1^{g_i})f - 1]$  [(c) and (d), respectively], that occur in Eq. (4.14), for the different signatures of gelation. . . . . 99

4.22 Gelation concentration,  $c_{g_i}$ , as a function of the number of stickers in a chain (see Eq. (4.15)), for the three different signatures of gelation in Regime II. The sticker strength and backbone solvent quality are kept constant at  $\epsilon_{st} = 5.0$  and  $\epsilon_{bb} = 0$ , respectively. Each symbol shape represents a system with a particular chain length  $N_b$ , spacer length  $\ell$  and number of stickers per chain  $f$  and the dashed lines are the scaling predictions for each of the gelation signatures. . . . . 101

4.23 (a) Rescaled inter-chain degree of association as a function of monomer concentration, with backbone monomers under  $\theta$ -solvent conditions. For  $N_b = 24$ ,  $\theta$ -solvent conditions for the backbone are obtained by simulating ghost chains, while for  $N_b = 34$ ,  $\theta$ -solvent conditions for the backbone are obtained by using the SDK potential with  $\epsilon_{bb} = \epsilon_\theta = 0.45$ . Inset is a plot of the ratio versus  $c/c^*$ , for the case  $N_b = 24$ . The solid lines are drawn with slopes equal to the prediction by scaling theory, while symbols represent simulation data. (b) and (c) Snapshots from the simulations for the system with  $N_b = 24$  in sub-figure (a), at concentrations  $c/c^* = 0.3$ , and  $c/c^* = 1.0$ , respectively. The purple coloured beads belong to chains that are all a part of a single cluster, while the colour grey is used to represent beads in chains that do not belong to this cluster. . . . . 103

4.24 (a) Rescaled inter-chain degree of association as a function of monomer concentration, with backbone monomers under good solvent conditions corresponding to scaling regime II. The solid line is drawn with slope equal to the prediction by scaling theory, while symbols represent simulation data. (b) Snapshot from the simulations for systems with  $N_b = 34$ ,  $\ell = 4$ ,  $\epsilon_{bb} = 0$ , and  $\epsilon_{st} = 5.0$ , at concentration  $c/c^* = 1.6$ . Beads coloured purple are from chains that are all a part of the same system spanning cluster, while the grey coloured beads belong to chains that are not part of this cluster. . . . . 104

5.1 Chain cluster size distribution in semi-log scale for systems of associative polymers with spacer length  $\ell = 4$ ,  $\epsilon_{bb} = 0$  and  $\epsilon_{st} = 5.0$  at (a)  $c/c^* = 0.3$ ,  $N_b = 44$ , (b)  $c/c^* = 0.5$ ,  $N_b = 44$  and (c)  $c/c^* = 0.6$ ,  $N_b = 34$ . The solid red symbols are simulation data and the exponential decay of the cluster size distribution is shown by the dashed black lines. . . . . 116

5.2 Chain cluster size distribution in log-log scale for systems of associative polymers with spacer length  $\ell = 4$ ,  $\epsilon_{bb} = 0$  and  $\epsilon_{st} = 5.0$  at different values of  $c/c^* = \{0.3, 0.5, 0.8, 0.9\}$  and different chain lengths,  $N_b$ . The power-law behaviour of the cluster size distribution is shown by the solid black lines in (c) and (d). . . . . 117

5.3 Non-dimensionalized stress auto-correlation function,  $C^*(t)$ , for systems of associative polymers with  $N_b = 24$ ,  $\ell = 4$ ,  $f$ ,  $\epsilon_{bb} = 0$  and  $\epsilon_{st} = 5.0$  at different values of scaled monomer concentration,  $c/c^*$ , in the dilute and semi-dilute regimes. The solid black lines are fit to the simulation data using a sum of exponentials. The inset shows the entire range of  $c/c^*$  covered in the study. . . . . 119

5.4 Polymeric component of the non-dimensionalized shear viscosity,  $\eta_p^* = \frac{\eta_p}{n_p k_B T \lambda_H}$ , as a function of non-dimensional shear rate ( $\dot{\gamma} \lambda_H$ ) for different values of monomer concentration,  $c/c^*$ . The open symbols are the values of  $\eta_p^*$  calculated from shear flow simulations and filled symbols are the values of zero-shear rate viscosity,  $\eta_p^{0*}$ , evaluated from Eq. (5.10). . . . . 120

## LIST OF FIGURES

---

- 5.5 Scaling of the ratio of zero-shear rate viscosity at finite concentration,  $\eta_p^{0*}$ , to its value in the dilute limit,  $\eta_{p0}^{0*}$ , with the scaled concentration,  $c/c^*$ , for solutions of associative polymers with  $N_b = 24$ ,  $\ell = 4$ ,  $f = 4$ ,  $\epsilon_{bb} = 0$  and  $\epsilon_{st} = 5.0$ . The symbols from simulations and the dashed lines with slope 0.6 is obtained from least square fit. . . . . 121
- 5.6 Scaling of the zero-shear rate viscosity with the relative distance from the gelation concentration ( $c_g$ ) in the post gel regime. Here the gelation concentration is at  $c_g/c^* = 0.5$ . The symbols are the simulation data and the dashed line is drawn with the slope predicted by the mean-field theory. . . . . 122
- 5.7 Non-dimensional storage ( $G'^*$ ) and loss ( $G''^*$ ) moduli of associative polymer solutions as a function of dimensionless frequency,  $\omega \lambda_H$ , for different values of  $c/c^*$  with chain length  $N_b = 24$ , spacer length  $\ell = 4$ , number stickers per chain  $f = 4$ , backbone monomer interaction strength  $\epsilon_{bb} = 0$  and sticker strength  $\epsilon_{st} = 5.0$ . The filled and open circles in the plots are  $G'$  and  $G''$ , respectively. The inverse of the frequency corresponding to the point of intersection of  $G'$  and  $G''$  curves represents the characteristic relaxation time  $\tau_{1/\omega} = 1/(\omega_1 \lambda_H)$ .  $G_0$  indicates the elastic modulus. The slopes of  $G'^*$  and  $G''^*$  in the terminal flow regime are 2 and 1, respectively, as indicated in the figures. . . . . 123
- 5.8 Variation of the loss tangent,  $\tan \delta$ , with the dimensionless frequency,  $\omega \lambda_H$ , at different values of  $c/c^*$  for associative polymer solutions with  $N_b = 24$ ,  $\ell = 4$ ,  $f = 4$ ,  $\epsilon_{bb} = 0$  and  $\epsilon_{st} = 5.0$ . . . . . 124
- 5.9 Effect of chain lengths on storage ( $G'$ ) and loss ( $G''$ ) moduli of ligand-decorated ultra-high molecular weight copolymers. This figure is reproduced from the article published by Brassine et al., *Journal of Rheology*, 61(6), 1123–1134 (2017). . . . . 125
- 5.10 Scaling of the ratio of characteristic relaxation time,  $\tau_{1/\omega}$ , to its value in the dilute limit,  $\tau_{1/\omega}^0$ , with the scaled concentration,  $c/c^*$ , for solutions of associative polymers with  $N_b = 24$ ,  $\ell = 4$ ,  $f = 4$ ,  $\epsilon_{bb} = 0$  and  $\epsilon_{st} = 5.0$ . The symbols from simulations and the dashed lines with slope 0.6 is the best fit to the data. . . . . 126

- 5.11 (a) Scaled elastic modulus,  $G_0/k_B T$ , versus concentration,  $c/c^*$ , for the solutions of associative polymers with  $N_b = 24$ ,  $\ell = 4$ ,  $f = 4$ ,  $\epsilon_{bb} = 0$ ,  $\epsilon_{st} = 5.0$ . (b) Elastic modulus,  $G_0/k_B T$ , as a function of the relative distance from the gelation concentration  $\Delta = (c - c_g)/c_g$ , near the gel-point in the post gel regime, where the gelation concentration is considered to be  $c_g/c^* = 0.5$ . Symbols are the simulation data and the solid and broken lines indicate the corresponding scaling exponents. 128
- 5.12 End-to-end unit vector auto-correlation function at different monomer concentrations,  $c/c^*$ , for (a) associative polymer solutions with  $N_b = 24$ ,  $\ell = 4$ ,  $f = 4$ ,  $\epsilon_{bb} = 0$  and  $\epsilon_{st} = 5.0$  and (b) homopolymer solutions in athermal solvent ( $\epsilon_{bb} = 0$ ) with chain length  $N_b = 24$ . Symbols represents the simulation data and dashed lines are the exponential fit at different concentrations. . . . . 129
- 5.13 Ratio of the relaxation time,  $\tau$ , at finite concentration to its value in the dilute limit,  $\tau_0$ , as a function of scaled concentration,  $c/c^*$ , for solutions of homopolymers (HP) and associative (or sticky) polymers (SP). The associative polymers considered here are with  $N_b = 24$ ,  $\ell = 4$ ,  $f = 4$ ,  $\epsilon_{bb} = 0$  and  $\epsilon_{st} = 5.0$ . The homopolymer solutions, simulated using Brownian dynamics, are in athermal solvent with chain length  $N_b = 24$ . The yellow diamonds are data from the work by Huang et al. (Huang et al., 2010). The solid and dashed lines indicate the scaling exponents for homopolymer and associative polymer solutions, respectively. . . . . 130
- 5.14 Dimensionless mean bond lifetime,  $t_{\text{bond}}^*$  as a function of concentration,  $c/c^*$ , for associative polymer solutions with  $N_b = 24$ ,  $\ell = 4$ ,  $f = 4$ ,  $\epsilon_{bb} = 0$  and  $\epsilon_{st} = 5.0$ . The symbols are from simulations and the dashed line is best fit to the data. . . . 132
- 5.15 The ratio  $\tau_i/(\tau_i^0 t_{\text{bond}}^0)$  as function of the fraction of inter-chain associated stickers,  $f p_2$ , at different values of monomer concentration in the pre and post-gel regimes. Here,  $\tau_i$ 's are the large scale relaxation time estimated from various methods (index  $i$  represents the different methods) as indicated in the figure and  $\tau_i^0$ 's are the corresponding values of relaxation time in the dilute limit. Each symbol corresponds to a specific method of estimating  $\tau$  and the dashed line is prediction of the mean-field theory. . . . . 133

## LIST OF FIGURES

---

5.16	Chain cluster lifetime, $t_c^{\text{life}}$ , as a function of cluster size, $m$ , at different values of concentration, $c/c^*$ , for associative polymer solutions with $N_b = 24$ , $\ell = 4$ , $f = 4$ , $\epsilon_{bb} = 0$ and $\epsilon_{st} = 5.0$ . . . . .	135
6.1	(a) Mean square radius of gyration, $R_g^2$ , as function of chain length, $N_b$ , for ring and linear polymers. (b) The variation of the ratio of $R_g^2$ for ring and linear chains with chain length. . . . .	141
6.2	(a) The ratio $\langle X \rangle / 2R_g$ as a function of $1/\sqrt{N_b}$ for linear and ring chains in the limit of $\theta$ -solvent quality. (b) The ratio of the mean stretch of a ring and linear chain, $X_R/X_L$ , as a function of $1/\sqrt{N_b}$ at the $\theta$ -solvent condition. The extrapolated values in the limit of $N_b \rightarrow \infty$ is shown in the figure. The symbols are simulation data and the broken lines are linear fits to the data. . . . .	142
6.3	Ratio $\langle X \rangle / 2R_g$ for rings as a function of $N_b$ at a fixed value of $z^*$ . The extrapolated value in the limit of $z \rightarrow \infty$ is indicated in the figure. . . . .	143
6.4	(a) The ratio $\langle X \rangle / 2R_g$ as a function of $z$ for linear and ring chains in the long chain limit. The solid and the dashed lines represents the value of $\langle X \rangle / 2R_g$ in limit of $z \rightarrow \infty$ for linear and ring polymers, respectively. (b) The ratio of the mean stretch of a ring and linear chain, $X_R/X_L$ , as a function of $z$ in the long chain limit. . . .	144
6.5	Scaling of diffusivity, $D$ , with chain length, $N_b$ , at $z = 0$ ( $\theta$ solvent), $h^* = 0.2$ and $z = 5$ (good solvent), $h^* = 0.24$ for rings. Here $D$ is computed by the two methods discussed in the text. The dashed and solid lines indicate the scaling exponent for the two solvent qualities. . . . .	146
6.6	The ratio $U_{\text{RD}}$ as a function of $1/\sqrt{N_b}$ for rings in the limit of $\theta$ -solvent quality, $z = 0$ . The extrapolated value in the limit of $N_b \rightarrow \infty$ is shown in the figure. The symbols are simulation data and the broken lines are linear fit to the data. . . . .	147
6.7	The ratio $U_{\text{RD}}$ as a function of $z$ for rings and linear chains in the long chain limit. The dashed lines represents the value of the ratio in the limit of $z \rightarrow \infty$ for ring polymers. . . . .	149

## LIST OF FIGURES

---

6.8	The ratio $\langle X \rangle / R_H$ as a function of $z$ for (a) rings and (b) linear chains in the long chain limit. The solid line (bounded by dashed lines) represents the value of the ratio in limit of $z \rightarrow \infty$ for ring polymers. . . . .	149
6.9	Swelling ratio $\alpha_g$ , $\alpha_H$ and $\alpha_X$ plotted as a function of solvent quality, $z$ , for linear (LP) and ring (RP) polymers. . . . .	151
6.10	Ratio of gyration radius and hydrodynamic radius for ring to linear chain plotted as a function of solvent quality, $z$ . . . . .	152
A.1	(Color online) Comparison between the SDK potential ( $U_{\text{SDK}}$ ) and the conventional LJ ( $U_{\text{LJ}}$ ) and WCA ( $U_{\text{WCA}}$ ) potentials as a function of the radial distance, $r$ , for well depths $\epsilon = \epsilon_{\text{LJ}} = 2.0$ , $\sigma = 1$ , and $r_c = 1.5$ (see text for corresponding values of $\alpha$ and $\beta$ ). . . . .	156
A.2	(Color online) The ratio $R_g^2 / (N_b - 1)$ as a function of the well depth of the SDK potential, $\epsilon_{bb}$ , used to estimate the $\theta$ -point for the cutoff radius $r_c = 1.5\sigma$ . The symbols represent simulation data and the dotted lines are drawn to guide the eye. The $\theta$ -point is estimated as the intersection of all the curves and leads to $\epsilon_{bb} = 0.72$ . . . . .	157
A.3	(Color online) (a) The mean-squared radius of gyration as a function of the number of beads in a chain. The blue-coloured symbols are for different values of well-depth, $\epsilon_{bb}$ , in the absence of hydrodynamic interactions. $\bullet$ $\epsilon_{bb} = 0$ , $\blacktriangle$ $\epsilon_{bb} = 0.2$ , $*$ $\epsilon_{bb} = 0.4$ , $\blacktriangleright$ $\epsilon_{bb} = 0.6$ , $\blacktriangleleft$ $\epsilon_{bb} = 0.72$ , $+$ $\epsilon_{bb} = 0.8$ , $\blacklozenge$ $\epsilon_{bb} = 0.92$ and $\blacksquare$ $\epsilon_{bb} = 1$ . The same symbols are used with a red colour for simulations with hydrodynamic interactions. The straight lines are of slope $2\nu$ at different values of $\epsilon_{bb}$ . (b) Effective exponent $2\nu$ versus the well-depth, $\epsilon_{bb}$ , for cutoff radius $r_c = 1.5\sigma$ . . . . .	158
A.4	(Color online) The second virial coefficient $B_2$ of the SDK potential, compared with the corresponding value for the LJ potential, as a function of the cutoff radius, $r_c$ , for well-depths $\epsilon_{bb} = \epsilon_{\text{LJ}} = 1.0$ , and $\sigma = 1$ . . . . .	160

- A.5 (Color online) (a) The mean-squared radius gyration versus number of beads in a chain. The blue-coloured symbols are for different values of well-depth,  $\epsilon_{bb}$ , in the absence of hydrodynamic interactions.  $\bullet$   $\epsilon_{bb} = 0$ ,  $\blacktriangle$   $\epsilon_{bb} = 0.2$ ,  $*$   $\epsilon_{bb} = 0.4$ ,  $\blacktriangleright$   $\epsilon_{bb} = 0.45$ ,  $\blacktriangleleft$   $\epsilon_{bb} = 0.55$ ,  $+$   $\epsilon_{bb} = 0.6$ ,  $\blacklozenge$   $\epsilon_{bb} = 0.7$  and  $\blacksquare$   $\epsilon_{bb} = 0.8$ ,  $\blacklozenge$   $\epsilon_{bb} = 1$ ,  $\triangle$   $\epsilon_{bb} = 2$  and  $\square$   $\epsilon_{bb} = 3$ . The same symbols are used with a red colour for simulations with hydrodynamic interactions. The straight lines are of slope  $2\nu$  at different values of  $\epsilon_{bb}$ . (b) Exponent  $2\nu$  versus the well-depth,  $\epsilon_{bb}$ , at cutoff radius  $r_c = 1.82\sigma$ . 161
- B.1 Comparison of the equilibrium values of (a) radius of gyration,  $R_g^2$ , (b) intra-chain association fraction,  $p_1$ , and (c) inter-chain association fraction,  $p_2$ , predicted by the two different sticking rules, scheme 1 and scheme 2. Simulations are carried out with chain length  $N_b = 34$ , spacer length  $\ell = 4$ , sticker strength  $\epsilon_{st} = 5$ , and concentration  $c/c^* = 0.2$ , for the backbone monomers under athermal solvent conditions, i.e.,  $\epsilon_{bb} = 0$ . The symbols are from simulations and the solid lines are equilibrium averaged values of the static properties. . . . . 163
- D.1 Non-dimensionalized dynamic moduli ( $G'^*$  &  $G''^*$ ) as a function of dimensionless frequency,  $\omega \lambda_H$ , for a dilute solution of Rouse chains with chain length,  $N_b = 24$ . The filled (for  $G'$ ) and open (for  $G''$ ) symbols are from BD simulations at equilibrium and under oscillatory shear flow (OSF), where  $\gamma_0$  is the amplitude of oscillation. The solid and broken lines are analytical solutions for  $G'$  and  $G''$ , respectively, for Rouse chains in a dilute solution. . . . . 172

# List of Tables

3.1	Comparison between the $\theta$ -points estimated from the scaling of radius of gyration and second virial coefficient for solutions of sticky polymers with different spacer lengths, $\ell$ , and backbone monomer interaction strengths, $\epsilon_{bb}$ . . . . .	35
3.2	Estimated values of the function $g(\ell, \epsilon_{bb})$ for different values of spacer length, $\ell$ , and backbone monomer interaction strength, $\epsilon_{bb}$ . . . . .	39
4.1	Relations for the intra-chain and inter-chain association fractions, predicted by Dobrynin (Dobrynin, 2004). Table (a) corresponds to the three scaling regimes that arise when the backbone monomers are under good solvent conditions. The expressions are in terms of the spacer length $\ell$ , the number of monomers in a thermal blob $g_T$ , the number of monomers in a correlation blob $g_c$ , and the function $g_{ss}$ , which depends on the <i>effective</i> sticker strength. Note that $p = p_1 + p_2$ is the total fraction of associated stickers. Table (b) gives the corresponding relations for the case when the backbone monomers are under $\theta$ -solvent conditions, along with the simplified forms of the relations for good solvents when $g_T$ and $g_c$ are expanded in terms of the backbone solvent quality parameter $\hat{\tau}$ , the monomer concentration $c$ , and the specific choices $\nu = 3/5$ and $\theta_2 = 1/3$ are made. . . . .	54

## LIST OF TABLES

---

4.2	Parameter sets used to simulate the different scaling regimes of associative polymer solutions that arise when the backbone monomers are under $\theta$ and good solvent conditions, and when the sticky chain as a whole is under $\theta$ solvent conditions. Note that $g_T$ must be less than $N_b$ in Regime I in order for the chain to be under good solvent conditions. It must also satisfy the constraint $g_T < \ell < N_b$ in Regimes II and III. On the other hand it is possible for $g_c > N_b$ in Regimes I and II, but must satisfy $g_c < \ell < N_b$ in Regime III. . . . .	61
4.3	Values of the functions $A(\epsilon_{bb}, \ell)$ and $B(\epsilon_{bb}, \ell)$ in Eq. (4.12), for different spacer lengths, $\ell$ , and backbone monomer interaction strengths, $\epsilon_{bb}$ , determined from fitting data from simulations carried out in scaling regimes I and II. . . . .	74
4.4	Values of the functions $A_1(\epsilon_{bb}, \ell)$ and $A_2(\epsilon_{bb}, \ell)$ , and $B_1(\epsilon_{bb}, \ell)$ and $B_2(\epsilon_{bb}, \ell)$ , for different spacer lengths, $\ell$ , determined from fitting data from simulations carried out for backbone monomers under $\theta$ -solvent conditions. The two approaches correspond to using the SDK potential with $\epsilon_{bb} = \epsilon_\theta = 0.45$ , and ghost chains with no excluded volume interactions. . . . .	74
6.1	Coefficients and constants for the expression of the swelling ratio given in Eq. (6.8).	148
6.2	Coefficients and constants for the expression of the swelling ratio given in Eq. (6.8) for Linear chains and rings. . . . .	150
E.1	Estimates of CPU wall time required on the supercomputer <i>Gadi</i> to simulate a single data point on systems with different chain lengths and concentrations in Regimes II and III. . . . .	174
F.1	List of values for the radius of gyration ( $R_g$ ), and the intra-chain ( $p_1$ ) and inter-chain ( $p_2$ ) degrees of conversion as a function of concentration for different sets of parameters used in this work. . . . .	176

# Chapter 1

## Introduction

### 1.1 Dynamics of associative polymer solutions

In recent times, associative polymers have introduced a new domain in developing advanced materials, and many scientists and engineers have ventured into the quest to unravel and understand the static and dynamic properties of these special kinds of polymers. Associative polymers have sticky groups that can form reversible physical bonds which leads to formation of reversible gels and networks. These polymers are broadly classified into two classes, namely, telechelic polymers and multi-sticker polymers. Telechelic polymers have attractive end groups, whereas, multi-sticker polymers have sticky groups along the polymer backbone. Understanding the static and dynamic behaviour of associative polymers is of major interest to tune their properties for various applications such as rheology modifiers, adhesives, biomedical implants, adsorbents and many more. For instance, they are widely used as rheology modifiers in the coating, paint, water-treatment and enhanced oil-recovery industries, since their influence on solution viscosity can be adjusted molecularly by varying the chemistry and geometry of the associations, and macroscopically by changing the temperature or concentration (Glass et al., 1991)(Tripathi et al., 2006). At sufficiently high concentrations, when the suspending medium is water, associative polymers form hydrogels whose transient viscoelastic networks have found numerous applications as tissue engineering scaffolds (El-Sherbiny and Yacoub, 2013), food thickeners (O’Leary et al., 2010), drug delivery carriers, soft electronics, and sensors (Rossow and Seiffert, 2015)(Voorhaar and Hoogen-

boom, 2016)(Tsitsilianis, 2010). Many of these uses involve the application of flow fields that influence and control the formation and duration of associations, and the evolution of the transient network structures. A fundamental understanding of the nonequilibrium dynamics of physically associative polymers is consequently essential for the rational design of these systems. Successful formulation of associative polymer systems for these various applications has largely rested on using polymer chemistry to engineer innovative polymers, followed by extensive experimental investigation to select the most suitable candidates. It is not possible currently to specify a priori the particular macromolecular architecture, the precise number, strength and location of the attractive groups, the appropriate solution temperature and concentration, and the particular flow conditions which would achieve optimal product performance. Several computational studies have been carried out aimed at making progress in this direction, i.e., towards improving the understanding of the non-equilibrium response of network structures, and deciphering the connection between molecular topology and macroscopic behaviour, using a variety of different techniques based on coarse-grained bead-spring chain models for polymers (van den Brule and Hoogerbrugge, 1995)(Hernández Cifre et al., 2003)(Hernández Cifre et al., 2007)(Sprakel et al., 2009)(Myung et al., 2015)(Castillo-Tejas et al., 2016). In this work, we propose a novel alternative approach based on a multi-particle Brownian dynamics simulation methodology that accounts for hydrodynamic interactions, and which can potentially capture both static and dynamic properties at equilibrium, along with the nonequilibrium rheological response of associative polymer solutions, across a range of concentrations that span the dilute and unentangled semidilute regimes.

In solution, association between the sticky groups can take place due to hydrophobic interaction, hydrogen bonds, reversible covalent bonds, ionic interaction or metal-ligand coordination. These interactions lead to formation of cross-links and networks as shown in the Fig. 1.1. The structures formed in the solution depend on the position of sticky groups, number of stickers per chain, strength of association between the stickers, concentration of the solution and also on the solution temperature (Rubinstein and Dobrynin, 1997)(Chassenieux et al., 2011). Rubinstein and Dobrynin (Rubinstein and Dobrynin, 1997) have discussed some important properties and phenomena related to solutions of associative polymers. They note that sol-gel phase transition is an important characteristic of associative polymer solutions

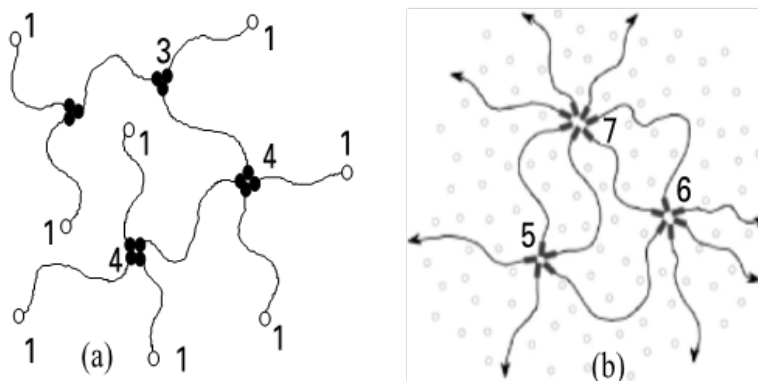


Figure 1.1: Example of multiple crosslinks in telechelic polymers. (a) Ionic multiplets, (b) hydrophobic aggregates. Numbers show multiplicity of junctions. Reproduced from (Tanaka, 2011)

and the concentration and temperature of the solution are the guiding factors for such a phase transition. The concentration at the onset of gelation in different types of solvent is still a debated issue. In the seminal work on the scaling theory of associative polymer solutions, Rubinstein and Semenov (Semenov and Rubinstein, 1998) (Rubinstein and Semenov, 2001) have proposed analytical predictions for gelation transition and inter-relationship among various parameters such as, chain length, number of stickers per chain, solution concentration and strength of association. Dobrynin further developed the scaling theory to establish relationships between microscopic interactions between stickers and monomers with system parameters and chain topology (Dobrynin, 2004). In order to validate the proposed simulation methodology, we report here the results of a detailed comparison of its predictions of equilibrium static properties with the analytical predictions of the scaling theories of Semenov and Rubinstein (Semenov and Rubinstein, 1998) and Dobrynin (Dobrynin, 2004). As will be seen, these results set the stage for a subsequent study of the equilibrium and nonequilibrium dynamics of associative polymer solutions within a systematic and coherent framework.

The viscoelastic and rheological behaviour of associative polymers emerges from the dynamical swapping between various chain conformations in response to the deformation imposed on the gels and network. As a result, the relationship between structure and the rheological response of associative polymers is a complex one. The differences in response between telechelic and multi-sticker polymers highlight the striking influence that molecular

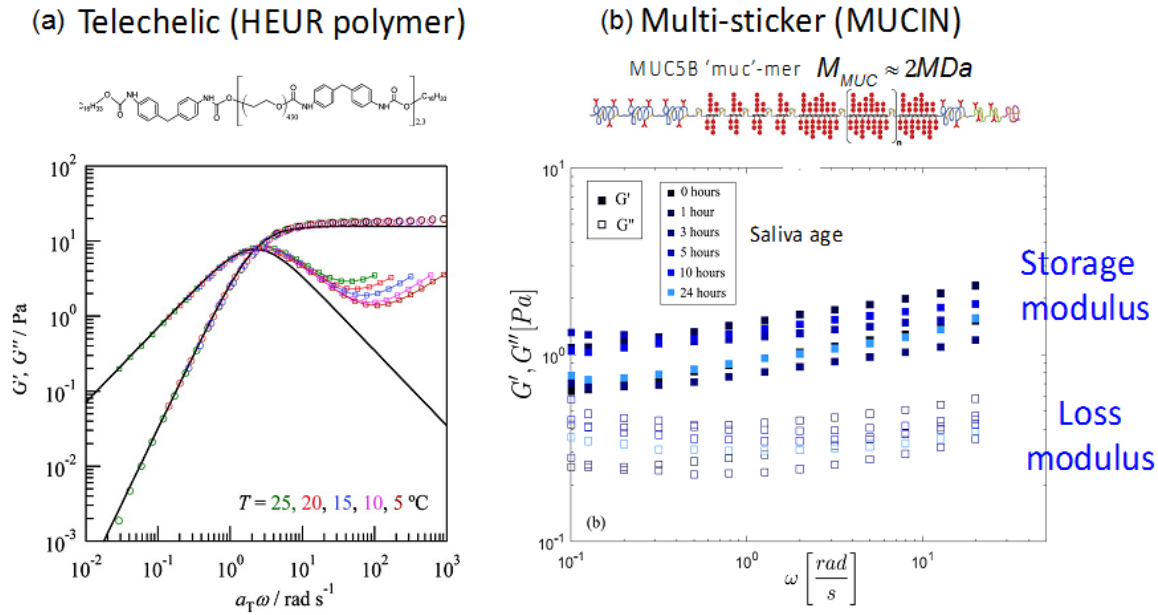
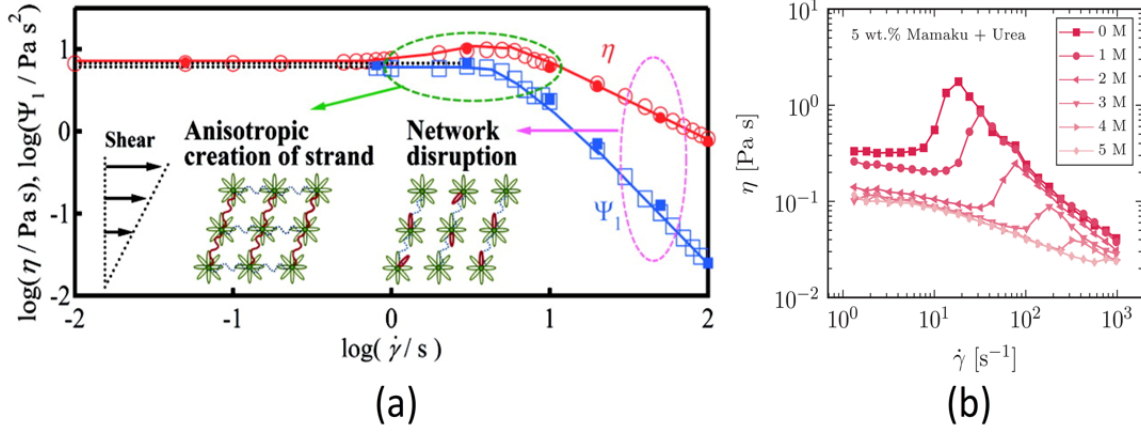


Figure 1.2: Storage and loss moduli for (a) telechelic (reproduced from (Suzuki et al., 2012)), and (b) multi-sticker (reproduced from (Wagner and McKinley, 2017))

topology and dynamics have on macroscopic observables (Suzuki et al., 2012)(Wagner and McKinley, 2017). The loss and storage moduli of telechelic associative polymer systems are typically well described by a Maxwell model with a *single* relaxation time as shown in Fig. 1.2 (a) for HEUR (hydrophobic ethoxylated urethane) solution (Suzuki et al., 2012). On the other hand, multi-sticker systems exhibit broad power law relaxation spectra with no readily discernible characteristic time scale, as displayed in Fig. 1.2 (b) for saliva (Wagner and McKinley, 2017). Origin of the differences in behaviour between these two systems is currently not well understood. The scale-free fractal microstructure of the transient network for multi-sticker systems is believed to lead to scale-free power law relaxation behaviour. However, this has not been systematically investigated to date.

Experiments have shown that telechelic solutions exhibit characteristic shear thickening behaviour at intermediate shear rates (Suzuki et al., 2012), as shown in Fig. 1.3 (a), while it is not necessarily present in multi-sticker solutions. Fig. 1.3 (b) demonstrates the elimination of shear thickening with the addition of urea to a multi-sticker polysaccharide solution (Mamaku gum), due to the disruption of hydrogen bonds that are responsible for the development of the transient network (Jaishankar et al., 2015). The existence of shear thickening at



tbh]

Figure 1.3: Viscosity as a function of shear rate in (a) a telechelic HEUR solution (from (Suzuki et al., 2012)) and (b) a polysaccharide (Mamaku gum) solution in which interactions are driven by hydrogen bonding (from (Jaishankar et al., 2015))

intermediate shear rates is attributed to the delicate interplay of the finite extensibility of chains segments, and enhanced numbers of stress-bearing polymer strands resulting from the flow (Tripathi et al., 2006). Recent experimental observations (Suzuki et al., 2012), however, suggest that the network structure remains close to the equilibrium state and demands an alternative explanation for the presence of shear thickening. There is no general agreement regarding the origin of shear thickening in telechelic polymer solutions, nor is its absence in multi-sticker solutions clearly understood. Moreover, there is no currently existing comprehensive understanding of the interplay between the microscopic topology and macroscopic viscoelasticity of associative polymer solution. In the present work we attempt to address some of these phenomena in order to bridge the gap in knowledge of the relationships between the viscoelasticity and microstructure in the case of multi-sticker associative polymer solutions.

## 1.2 Dynamics of ring Polymers

Polymer solutions have become an ubiquitous part in the development of a wide variety of consumer goods, medical products and technological applications such as paints and coating, drug delivery systems, food processing and so on. A major role in the development of many of these applications is played by the topological structure of the polymer chains.

Ring polymers are a special class of polymer which is devoid of free ends. These polymers represent the same class of molecules as the circular DNA found in chromosomes of bacteria, mitochondria, chloroplasts. Due to the absence of any free ends, polymeric rings show some unique static and dynamic behaviours. For instance, unlike linear DNA, replication in circular or ring DNA is much easier. However, there are significant challenges related to knotting and entanglement in circular DNA. Ring polymers also have a phenomenal effect on modifying the rheological behaviour of a polymer solution. Whereas much of our understanding regarding the dynamics of linear polymers is well established, the properties of ring polymers are not yet fully understood. One such phenomenon is the transition from tank-treading to tumbling motion of polymeric rings in shear flow (Chen et al., 2013)(Wang et al., 2019). Recent studies have attempted to visualise and explain this problem based on single molecule experiments (Tu et al., 2020) and numerical simulations (Chen et al., 2013)(Wang et al., 2019). However, the effect of the strength of shear flow and molecular orientation during the flow on such transition is not properly understood. Moreover, it should be admitted that even before understanding these non-equilibrium phenomena in the solution of ring polymers, it is essential to understand the equilibrium static and dynamic properties for these polymers. In case of linear homopolymers, ratios involving radius of gyration, hydrodynamic radius or mean stretch are found to show universal behaviour as a function of solvent quality in the limit of infinite chain length (Sunthar and Prakash, 2006)(Zhu et al., 2016). However, for polymeric rings the universality of these properties as a function of solvent quality and in presence of hydrodynamic interactions are not yet well-established.

In this project we have developed a Brownian dynamics simulation algorithm to simulate polymeric rings in the dilute limit which has the potential to investigate and explain the microscopic phenomena associated with the unique behaviours discussed above. At present we have carried out equilibrium simulations to establish the universality of different static and dynamics properties of dilute solutions of ring polymers. This work is fundamentally important for the development of a model for ring polymer solutions that is capable of predicting experimental observations of ring polymer dynamics, at equilibrium and in flow.

The thesis is organised as follows. In Chapter 2 we introduce the modelling and simulation

methodology for associative polymer solutions. The swelling behaviour of sticky polymers in dilute solutions is investigated in Chapter 3. Chapter 4 discusses the universal static properties of associative polymer solutions in the dilute and semi-dilute regimes. Different static signatures of gelation in associative polymer solutions are also studied in this chapter. The dynamic signatures of gelation in associative polymer solutions are characterized in Chapter 5. The universality of the equilibrium static and dynamic properties of dilute ring polymer solutions is examined in Chapter 6. Finally, the key conclusions are summarised in Chapter 7.

# Chapter 2

## Modelling and Simulations

In this chapter we discuss the details of the associative polymer model and basic governing equations of the Brownian dynamics (BD) simulation. Although several previous computational studies of associative polymer solutions have been based on Brownian dynamics as the simulation technique, they differ from each other in a number of different aspects. For instance, while in some studies entire micelles are coarse-grained to single particles (Sprakel et al., 2009)(Park and Ianniruberto, 2017), others represent individual polymer chains as bead-spring dumbbells (van den Brule and Hoogerbrugge, 1995)(Hernández Cifre et al., 2003)(Cass et al., 2008). Whereas in some recent investigations of the shear flow of associative polymer solutions, bead inertia has been taken into account in the context of Langevin dynamics of bead-spring chains (Omar and Wang, 2017)(Furuya and Koga, 2018), in earlier enquiries, associative polymers in shear flow have been modelled as non-interacting dumbbells (Hernández Cifre et al., 2003), or non-interacting bead-spring chains (Hernández Cifre et al., 2007), with beads switching between associated and dissociated states. None of these previous investigations, however, have taken hydrodynamic interactions into account.

The recent numerical investigations of associative polymer solutions by the Jülich group using multiparticle collision dynamics (MPCD) (Myung et al., 2014)(Myung et al., 2015), and by Castillo-Tejas et al. (Castillo-Tejas et al., 2016) using nonequilibrium molecular dynamics (NEMD), automatically account for hydrodynamic interactions through the exchange of momentum between the beads on polymer chains and solvent molecules, since the latter are simulated explicitly. By implementing an attractive interaction potential between selected

beads on the chain to model the association between sticker monomers, these pioneering studies have essentially extended the framework for studying semidilute polymer solutions to one that is capable of describing associative polymer solutions. In this work we introduce an alternative approach for describing associative polymer solutions that accounts for hydrodynamic interactions and is based on Brownian dynamics simulations. As in recent extensions of MPCD and NEMD, the proposed methodology is an extension of an algorithm developed previously to study semidilute polymer solutions, but in contrast to these methods, treats the solvent implicitly (Jain et al., 2012).

In Brownian dynamics simulations of associative polymer solutions, the forces acting on the monomers in a chain are broadly classified into two groups. (i) *Non-bonded* interactions between sticker-sticker, sticker-monomer or monomer-monomer, arising due to the short-range excluded volume or associative interactions and long-range hydrodynamic interactions. (ii) *Bonded* interactions due to the inter-linkages of the monomers in a polymer chain. In the following sections the modelling of each of these interactions are discussed in the context of BD simulations.

## 2.1 Polymer Model

In a BD simulation, polymer chains are modelled as a sequence of beads connected by springs, commonly known as a bead-spring chain model (Bird et al., 1987a). Each polymer chain is coarse-grained into a sequence of  $N_b$  beads connected by  $N_b - 1$  massless springs (as shown schematically in Fig. 2.1) that represent the entropic force between the adjacent beads. For associative polymers sticky groups are distributed along the chain backbone, as represented by the green beads in Fig. 2.1. In the limit of finite concentration an ensemble of such bead-spring chains is considered to be immersed in a Newtonian solvent. The simulation is set by introducing a cubic box of edge length  $L$  with periodic boundary conditions (PBC) in all directions to simulate an infinite system (Frenkel and Smit, 1996). Within the simulation box a total of  $N_c$  chains each having  $N_b$  beads are generated to produce a bulk monomer concentration of  $c = N/V$ , where,  $N = N_b \times N_c$  and  $V = L^3$  is the volume of the simulation box.

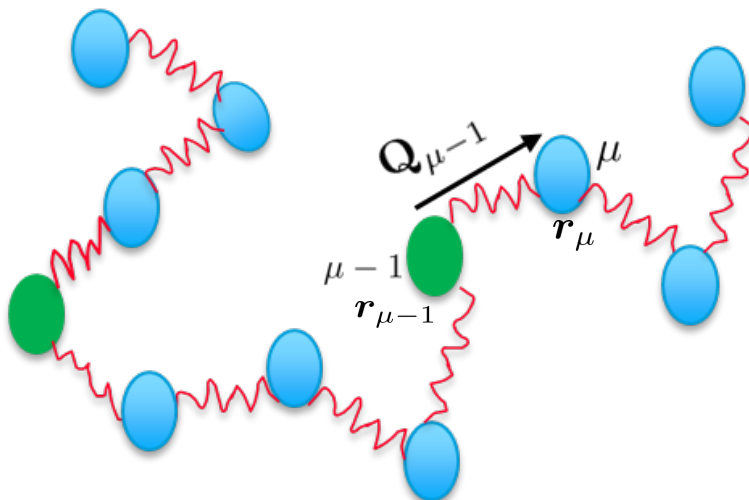


Figure 2.1: Schematic of bead-spring chain polymer model for associative polymer.  $\mathbf{Q}_{\mu-1} = \mathbf{r}_{\mu} - \mathbf{r}_{\mu-1}$  represents the connector vector between bead  $\mu - 1$  and  $\mu$ . The green coloured beads represent the stickers.

## 2.2 Role of Hydrodynamic Interactions in Brownian Dynamics Simulations

We provide here a brief discussion of the role of hydrodynamic interactions in BD simulations. Hydrodynamic interactions have been successfully incorporated over the past several decades in computational studies of polymer solution dynamics in the *dilute* concentration regime, both by methods that treat the solvent explicitly, such as non-equilibrium molecular dynamics (NEMD) (Aust et al., 1999)(Peters and Muthukumar, 1999)(Kairn et al., 2004)(Kröger, 2004)(Todd and Daivis, 2007), and by Brownian dynamics (BD) simulations (Ermak and McCammon, 1978)(Fixman, 1981)(Zylka, 1991)(Jendreyack et al., 2000)(Prabhakar and Prakash, 2002)(Larson, 2005)(Prakash, 2019). In BD, solvent degrees of freedom are eliminated completely and their effect is taken into account through long-range dynamic correlations in the stochastic displacements of the beads. These studies have established beyond doubt that the inclusion of hydrodynamic interactions is essential for investigating dynamic properties not only in the equilibrium and linear viscoelastic regimes, but also the far from equilibrium non-linear rheological material functions (Larson, 2005)(Shaqfeh, 2005)(Prakash, 2019). Accounting for hydrodynamic interactions in the *semidilute* regime of concentration, on the

other hand, is challenging since both intra and inter-molecular interactions need to be taken into consideration, particularly in the case of the latter since hydrodynamic interactions are long-ranged in space. Significant advances have been made over the last decade in our capacity to simulate semidilute polymer solutions due to the development of a variety of mesoscopic simulation techniques based on coarse-grained bead-spring chain models for polymer molecules (Ahlrichs and Dünweg, 1999)(Stoltz et al., 2006)(Kapral, 2008)(Dünweg and Ladd, 2009)(Gompper et al., 2009)(Jain et al., 2012)(Saadat and Khomami, 2015)(Jain et al., 2015). These algorithms are able to describe long polymers that overlap with each other while maintaining a low segment density, and are also able to capture the interaction of segments with each other through solvent-mediated hydrodynamic interactions. While some of the simulation techniques, such as the hybrid lattice Boltzmann-molecular dynamics (LBMD) approach (Ahlrichs and Dünweg, 1999)(Dünweg and Ladd, 2009) and the hybrid multiparticle collision dynamics-molecular dynamics (MPCD) method (Kapral, 2008)(Gompper et al., 2009) are explicit solvent methods, the Brownian dynamics simulation technique, as mentioned above, treats the solvent implicitly (Stoltz et al., 2006)(Jain et al., 2012)(Saadat and Khomami, 2015)(Jain et al., 2015).

As is well known, hydrodynamic interactions (HI) begin to get screened at the overlap concentration  $c^*$ , and get completely screened only in a polymer melt (Rubinstein and Colby, 2003)(A.Jain et al., 2012). The effects of HI are confined at sufficiently long times (Ahlrichs et al., 2001) to length scales below the size of a correlation blob, which shrinks with increasing concentration. In the unentangled semidilute regime, hydrodynamic interactions essentially determine the rich and complex dynamics of polymer solutions over a wide range of concentration (Rubinstein and Colby, 2003)(A.Jain et al., 2012)(Prakash, 2019). It can therefore be anticipated that hydrodynamic interactions will also significantly influence dynamic properties, like the on-and-off time scales for stickers, single-chain and network relaxation time, of associative polymer solutions studied in the present work. In the following section we briefly explain the governing equations for the BD simulations and the expressions used to model hydrodynamic interactions, the excluded volume interaction and spring forces. The algorithm implemented for the simulations of associative polymer solutions is an extension of the code developed by Jain et al. (Jain et al., 2012)(Jain, 2013) to simulate semi-dilute

solutions of homopolymers.

## 2.3 Governing Equations For Brownian Dynamics Simulation

The governing equation in BD simulations is a stochastic differential equation describing the evolution of the position vector  $\mathbf{r}_\mu(t)$  of a bead  $\mu$  with time  $t$ . The Euler integration algorithm for the non-dimensional Itô stochastic differential equation governing the position vector  $\mathbf{r}_\mu(t)$  is given in it's most general form as (Stoltz et al., 2006),

$$\mathbf{r}_\mu(t + \Delta t) = \mathbf{r}_\mu(t) + (\boldsymbol{\kappa} \cdot \mathbf{r}_\nu(t)) \Delta t + \frac{\Delta t}{4} \sum_{\nu=1}^N \mathbf{D}_{\mu\nu} \cdot (\mathbf{F}_\nu^s + \mathbf{F}_\nu^{\text{SDK}}) + \frac{1}{\sqrt{2}} \sum_{\nu=1}^N \mathbf{B}_{\mu\nu} \cdot \Delta \mathbf{W}_\nu \quad (2.1)$$

Here the length and time scales are non-dimensionalised with  $l_H = \sqrt{k_B T / H}$  and  $\lambda_H = \zeta / 4H$ , respectively, where  $T$  is the absolute temperature,  $k_B$  is the Boltzmann constant,  $H$  is the spring constant, and  $\zeta = 6\pi\eta_s a$  is the Stokes friction coefficient of a spherical bead of radius  $a$  where  $\eta_s$  is the solvent viscosity. The quantity  $\boldsymbol{\kappa} = (\nabla \mathbf{v})^T$  is a  $3 \times 3$  tensor, with  $\mathbf{v}$  corresponding to the unperturbed solvent velocity field. In absence of any external flow field this term is considered to be zero.  $\Delta \mathbf{W}_\nu$  is a non-dimensional Wiener process with mean zero and variance  $\Delta t$ . The components of  $\Delta \mathbf{W}_\nu$  are obtained from a real-valued Gaussian distribution with zero mean and variance  $\Delta t$ .  $\mathbf{B}_{\mu\nu}$  is a non-dimensional tensor whose evaluation requires the decomposition of the diffusion tensor  $\mathbf{D}_{\mu\nu}$ , defined as  $\mathbf{D}_{\mu\nu} = \delta_{\mu\nu} \boldsymbol{\delta} + \boldsymbol{\Omega}_{\mu\nu}$ , where  $\delta_{\mu\nu}$  is the Kronecker delta,  $\boldsymbol{\delta}$  is the unit tensor, and  $\boldsymbol{\Omega}_{\mu\nu}$  is the hydrodynamic interaction tensor. Defining the matrices  $\mathcal{D}$  and  $\mathcal{B}$  as block matrices consisting of  $N \times N$  blocks each having dimensions of  $3 \times 3$ , with the  $(\mu, \nu)$ -th block of  $\mathcal{D}$  containing the components of the diffusion tensor  $\mathbf{D}_{\mu\nu}$ , and the corresponding block of  $\mathcal{B}$  being equal to  $\mathbf{B}_{\mu\nu}$ , the decomposition rule for obtaining  $\mathcal{B}$  can be expressed as  $\mathcal{B} \cdot \mathcal{B}^T = \mathcal{D}$ . In the present study, the regularized Rotne-Prager-Yamakawa (RPY) tensor is used to compute hydrodynamic interactions (HI),

$$\mathbf{\Omega}_{\mu\nu} = \mathbf{\Omega}(\mathbf{r}_\mu - \mathbf{r}_\nu) \quad (2.2)$$

where

$$\mathbf{\Omega}(\mathbf{r}) = \Omega_1 \boldsymbol{\delta} + \Omega_2 \frac{\mathbf{r}\mathbf{r}}{r^2} \quad (2.3)$$

with

$$\Omega_1 = \begin{cases} \frac{3\sqrt{\pi} h^*}{4} \frac{h^*}{r} \left( 1 + \frac{2\pi h^{*2}}{3 r^2} \right) & \text{for } r \geq 2\sqrt{\pi} h^* \\ 1 - \frac{9}{32} \frac{r}{h^* \sqrt{\pi}} & \text{for } r \leq 2\sqrt{\pi} h^* \end{cases}$$

and

$$\Omega_2 = \begin{cases} \frac{3\sqrt{\pi} h^*}{4} \frac{h^*}{r} \left( 1 - \frac{2\pi h^{*2}}{3 r^2} \right) & \text{for } r \geq 2\sqrt{\pi} h^* \\ \frac{3}{32} \frac{r}{h^* \sqrt{\pi}} & \text{for } r \leq 2\sqrt{\pi} h^* \end{cases}$$

The hydrodynamic interaction parameter  $h^*$  is the dimensionless bead radius in the bead-spring model, defined as  $h^* = a/(\sqrt{\pi k_B T/H})$ . The decomposition of the diffusion tensor has been achieved with the help of Fixman's polynomial approximation based on the Chebyshev technique which has been widely used earlier for both single chain (Fixman, 1986)(Prabhakar and Prakash, 2004)(Prabhakar et al., 2004) and multi-chain BD simulations (Jain et al., 2012)(Stoltz et al., 2006)(Saadat and Khomami, 2015). The challenge of simulating semidilute solutions arises from the sum  $\sum_\nu \mathbf{D}_{\mu\nu} \cdot (\mathbf{F}_\nu^s + \mathbf{F}_\nu^{\text{SDK}})$  in Eq. (2.1), which is conditionally convergent. Here it is evaluated using an optimized Ewald summation technique developed previously by Jain et al. Jain et al. (2012). At equilibrium, in absence of any external flow field the static properties are found to be independent of hydrodynamic interactions. Under such a condition HI is switched off in the BD simulations by setting  $\mathbf{\Omega}_{\mu\nu} = 0$ .

$\mathbf{F}_\nu$  represents all the non-hydrodynamic forces acting on bead  $\nu$  due to all other beads. For an associative polymer solution this can be represented as  $\mathbf{F}_\nu = \mathbf{F}_\nu^s + \mathbf{F}_\nu^{\text{asso}} + \mathbf{F}_\nu^{\text{exv}}$ . Here  $\mathbf{F}_\nu^s$  is the force due to bonded interaction between adjacent beads,  $\mathbf{F}_\nu^{\text{asso}}$  is the sticker-sticker associative interaction force,  $\mathbf{F}_\nu^{\text{exv}}$  is the force due to sticker-monomer or monomer-monomer excluded volume interaction. In the following section details of the models used for the bonded and non-bonded interactions are discussed in the context of associative polymer

solutions.

## 2.4 Bonded Interactions

In the context of the bead-spring polymer chain model, the bonded interaction represents the force exerted by the connecting springs between adjacent beads. In the present study we have used a finitely extensible non-linear elastic (FENE) potential to model the entropic spring force (Warner, 1972). FENE force law consists of a spring constant that increases with increase in extension, which limits the maximum stretchability of the polymer chains. Such a model is useful to explain important rheological observations, such as the shear thinning of polymer solutions (Ryder and Yeomans, 2006). The spring force acting on bead  $\nu$  is represented as  $\mathbf{F}_\nu^s = \mathbf{F}^c(\mathbf{Q}_\nu) - \mathbf{F}^c(\mathbf{Q}_{\nu-1})$ , where  $\mathbf{F}^c(\mathbf{Q}_{\nu-1})$  is the force acting on the spring connecting bead  $\nu-1$  and  $\nu$  along the direction of the connector vector, as shown in Fig. 2.1, where  $\mathbf{Q}_{\nu-1} = \mathbf{r}_\nu - \mathbf{r}_{\nu-1}$ . The FENE spring potential is given as,

$$U_{\text{FENE}} = -\frac{1}{2}Q_0^2 \ln \left( 1 - \frac{r^2}{Q_0^2} \right) \quad (2.4)$$

where  $Q_0$  is the dimensionless maximum stretchable length of a single spring, and  $k_B T$  is used to non-dimensionalise energy. Note that the notation  $Q_0^2$  used here is the same as the more commonly used FENE  $b$ -parameter (Bird et al., 1987a)(Prabhakar and Prakash, 2004). The spring force on a bead resulting from  $U_{\text{FENE}}$  is denoted by  $\mathbf{F}_\nu^s$ .

## 2.5 Non-bonded Interactions

The attractive and repulsive components of the monomer-monomer, sticker-monomer or sticker-sticker interactions are modelled using a modified Lennard Jones potential (SDK potential) proposed by Soddemann, Dünweg and Kremer (Soddemann et al., 2001), which

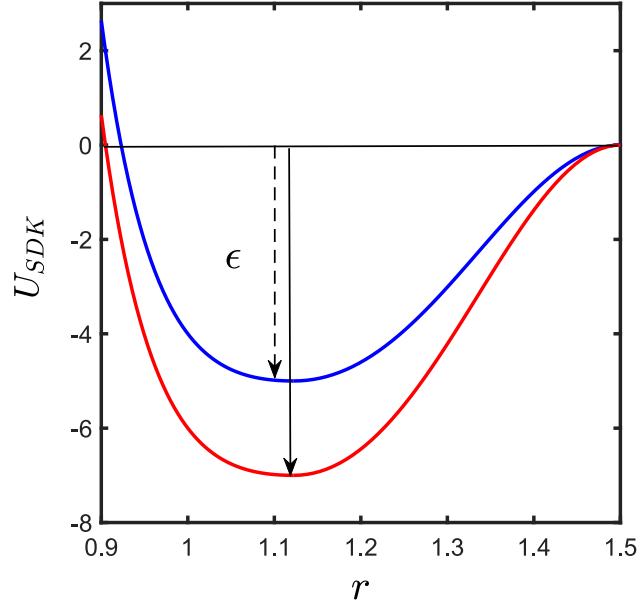


Figure 2.2: Graphical representation of the SDK potential,  $U_{\text{SDK}}$ , as a function of the distance between interacting molecules,  $r$ , for different values of well depth  $\epsilon$ .

is graphically represented in Fig. 2.2. The potential in its dimensionless form is given by,

$$U_{\text{SDK}} = \begin{cases} 4 \left[ \left( \frac{\sigma}{r} \right)^{12} - \left( \frac{\sigma}{r} \right)^6 + \frac{1}{4} \right] - \epsilon; & r \leq 2^{1/6} \sigma \\ \frac{1}{2} \epsilon \left[ \cos \left( \alpha \left( \frac{r}{\sigma} \right)^2 + \beta \right) - 1 \right]; & 2^{1/6} \sigma \leq r \leq r_c \\ 0; & r \geq r_c \end{cases} \quad (2.5)$$

where  $r_c$  is the cutoff radius,  $\epsilon$  is the potential well depth and  $\alpha$  and  $\beta$  are constants. The variable  $r$  and parameters  $\sigma$  and  $r_c$  are non-dimensionalised with respect to the length scale  $l_H$  and the potential well depth  $\epsilon$  is non-dimensionalised in terms of  $k_B T$ . Here  $\sigma$  is the non-dimensional distance at which conventional Lennard-Jones potential goes to zero. The value of the non-dimensional distance,  $\sigma$ , is taken to be 1 in the present study. The repulsive part of the potential for  $0 < r \leq 2^{1/6} \sigma$  is modelled by a truncated Lennard-Jones (LJ) potential similar to the Weeks-Chandler-Anderson (WCA) potential (Weeks et al., 1971) shifted by an amount of  $-\epsilon$  ( $\epsilon$  is a positive real number). The attractive tail is modelled

by a cosine function whose derivative at  $r = 2^{1/6}\sigma$  and cut-off  $r = 1.5\sigma$  is zero. Unlike the LJ potential, which has a long attractive tail, the short ranged attractive tail of the SDK potential smoothly approaches zero at a finite distance  $r_c$ , which leads to an increase in the simulation efficiency (Soddemann et al., 2001). In the Monte Carlo and molecular dynamics simulations previously carried out by Soddemann et al. (Soddemann et al., 2001) and Steinhauser (Steinhauser, 2005), the value of the cutoff radius,  $r_c$ , was taken to be  $1.5\sigma$  based on the interaction between the nearest neighbours. The constants  $\alpha$  and  $\beta$  are determined by applying the two boundary conditions, namely,  $U_{\text{SDK}} = 0$  at  $r = r_c$ , and  $U_{\text{SDK}} = -\epsilon$  at  $r = 2^{1/6}\sigma$ . Based on these two boundary conditions,  $\alpha$  and  $\beta$  are calculated by solving the following set of equations,

$$\begin{aligned} 2^{1/3}\alpha + \beta &= \pi \\ \left(\frac{r_c}{\sigma}\right)^2 \alpha + \beta &= 2\pi \end{aligned} \tag{2.6}$$

Considering the value of the cut-off radius  $r_c = 1.5\sigma$ , Eq. (2.6) can be solved to determine  $\alpha = 3.1730728678$  and  $\beta = -0.85622864544$ . This gives a smooth and continuous function going from the repulsive to the attractive domain. It is worth noting that the strength of attraction can be varied by changing the well depth  $\epsilon$  without altering the repulsive part of the potential. It provides a very good handle to control the strength of attraction between the stickers without varying the hardcore repulsion. However, in the context of Brownian dynamics simulations we have found that it is required to change the value of the cutoff radius  $r_c$  to  $1.82\sigma$  in order to reproduce the asymptotic scaling at different solvent quality for the polymer solutions. A detailed discussion on the rationale to choose the particular value of  $r_c$  is provided in Appendix A.

In associative polymer solutions, the potential well-depth for the backbone monomer-monomer interaction is defined by  $\epsilon_{bb}$ , whereas, that for the sticker-sticker interaction is defined by  $\epsilon_{st}$ . In the present study a sticker is modelled to associate with only one other sticker, which is defined as the functionality ( $\varphi$ ) of the stickers being equal to 1. For each pair of monomers  $\mu$  and  $\nu$ , we introduce a Boolean variable  $q_{\mu\nu} \in \{0, 1\}$ .  $q_{\mu\nu}$  is zero whenever at least one of the two monomers is a backbone monomer, while for a pair of sticker monomers,

$q_{\mu\nu}$  is zero if no bond exists between the two stickers, and  $q_{\mu\nu} = 1$  for a bonded pair of sticker monomers. The attractive strength,  $\epsilon$  of the SDK potential for a pair of monomers  $\mu$  and  $\nu$  is then given by

$$\epsilon = (1 - q_{\mu\nu}) \epsilon_{bb} + q_{\mu\nu} \epsilon_{st} \quad (2.7)$$

where, as mentioned earlier, backbone monomer-monomer interactions are denoted by  $\epsilon_{bb}$ , and the sticker monomer-monomer interactions are denoted by  $\epsilon_{st}$ . Typically,  $\epsilon_{st} \geq \epsilon_{bb}$ . At each time step, the simulation algorithm updates the variables  $q_{\mu\nu}$  for stickers according to the following simple rules:

1. Whenever two stickers  $\mu$  and  $\nu$  come within the cutoff radius of the SDK potential,  $r_c$ , the value of  $q_{\mu\nu}$  is changed from zero to one, provided that both stickers are not bonded to other stickers.
2. If three stickers are within the interaction range  $r_c$ , the decision regarding which pairs of beads stick together is made according to a scheme that depends on the bead number label of each of the stickers. Thus if stickers  $\zeta$ ,  $\delta$  and  $\rho$ , with  $\zeta < \delta < \rho$  are within interaction range  $r_c$ , then  $\zeta$  and  $\delta$  form a pair with  $q_{\zeta\delta} = 1$ , and the sticker  $\rho$  remains unbound with  $q_{\zeta\rho} = q_{\delta\rho} = 0$ . When more than three stickers are within the interaction range, the same scheme is implemented by treating each bead pair in turn and considering their respective bead number labels. While the choice of which pairs to stick based on bead number labels may seem arbitrary, it turns out that the scheme is effectively equivalent to picking the sticking pairs at random when three or more stickers are within the interaction range. Since the probability of three and higher body interactions amongst stickers is very low, and since we have considered a large ensemble of chains distributed randomly in a simulation box (implying random labelling of the stickers), the two schemes effectively produce the same results. This is explicitly demonstrated in Appendix B by comparing the predictions of different equilibrium static properties when the two different sticking rules are implemented.
3. As soon as the distance between two stickers  $\mu$  and  $\nu$  becomes greater than  $r_c$ ,  $q_{\mu\nu}$  is reset to zero, and new bondings may occur.

A knowledge of the monomer coordinates and the values of  $q_{\mu\nu}$  is clearly sufficient to calculate the interaction energy of the system uniquely. For the sake of simplicity, we have implemented a rule where bond formation or breakage is determined purely by whether sticker pairs are within or outside the cut-off radius. Typically, bond formation or breakage is determined by implementing a Monte-Carlo scheme based on a Boltzmann weight (Hoy and Fredrickson, 2009)(Sing and Alexander-Katz, 2011). In a sense, the current rule can also be considered as a special case of a method based on a Boltzmann weight, where the activation energy barrier for binding is zero, such that the probability of bond formation is unity whenever a sticker pair is within the cut-off radius, while the activation energy for unbinding is infinite, implying that bonds break only when the relative distance between previously stuck pairs is larger than the cut-off radius.

## 2.6 Conclusions

The stochastic differential equation, Eq. 2.1, described in this chapter will be integrated for different cases considered in the subsequent chapters. (i) The equilibrium static properties are evaluated in Chapter 4 by setting  $\kappa = 0$  and  $\mathbf{\Omega}_{\mu\nu} = 0$  in Eq. 2.1. (ii) In Chapter 5, the equilibrium dynamics are studied with  $\kappa = 0$  and  $\mathbf{\Omega}_{\mu\nu} \neq 0$ , where,  $h^* = 0.2$ . (iii) Simple and oscillatory shear flow simulations are carried out in Chapter 5 with  $\kappa \neq 0$  and  $h^* = 0.2$ . The same governing equations are used for simulations in the single chain dilute limit in Chapter 3 and Chapter 6, but here HI is treated for a single chain rather than using an Ewald sum.

# Chapter 3

## Universality of the collapse transition of sticky polymers

### 3.1 Introduction

Sticky polymer solutions consist of chains with sticky groups that can form reversible physical bonds, which in turn lead to the formation of reversible gels and networks. Due to the relative affinity of sticky groups for each other, sticky polymer chains are more collapsed or less swollen at a given temperature compared to the corresponding homopolymer made up of only the backbone or non-sticky monomers of the same molecular weight. For example, at the  $\theta$  temperature for the homopolymer, simple linear polymer chains in a dilute solution follow random walk (RW) statistics, whereas, the introduction of sticky groups leads to a decrease in the size of the chain due to relatively poorer solvent quality. Indeed the whole phase diagram for homopolymers (Grosberg and Khokhlov, 1994)(Rubinstein and Colby, 2003) is expected to be modified due to the presence of stickers (Semenov and Rubinstein, 1998)(Rubinstein and Semenov, 1998)(Dobrynin, 2004). In many applications like mist control or drag reduction of aviation fuel, it is necessary to have long, swollen, physically associated polymer chains in a single-phase solution (David et al., 2009b)(David et al., 2009a). For such applications, it is important to estimate the renormalised solvent quality of a sticky polymer solution in order to have some knowledge of chain conformations and the relative location of the system in the phase-space of temperature and concentration.

The universality of the swelling of the radius of gyration of a homopolymer relative to its value in the theta state in the crossover regime between theta and athermal solvent conditions is well established (Kumar and Prakash, 2003)(Miyaki and Fujita, 1981), and known to independent of polymer-solvent chemistry. The addition of sticky monomers that have an attractive affinity for each other along the polymer backbone reduces the quality of the solvent, leading to an increase in the theta temperature of the sticky polymer solution. In this chapter we address the question of how to compute the solvent quality of dilute sticky polymer solutions and examine the swelling of the radius of gyration of a sticky polymer relative to its value in the altered theta state. We carry out Brownian dynamics simulations to show that the swelling of sticky polymers is also universal, and indeed identical to that of homopolymers in the thermal crossover regime. Additionally, we find that the effective monomer size under theta solvent conditions, is identical in dilute homopolymer and sticky polymer solutions. As will be discussed subsequently, we consider the possibility that a first-order collapse might also exist in a certain parameter region for the particular model studied here, making the current observation a non-trivial one.

For homopolymers, it is well-known that in the limit of large molecular weight, static properties of polymer chains in dilute solution, such as the radius of gyration  $R_g$ , follow universal power laws in both  $\theta$  and athermal solvents. Furthermore, experiments and theoretical studies indicate that in the region between  $\theta$  and athermal solvents universal behaviour in terms of crossover scaling is still observed. For such systems the mean size of the polymer is a function of both the temperature ( $T$ ) and the molecular weight ( $M$ ) which combine to form a single variable, the solvent quality,  $z = k(1 - T_\theta/T)\sqrt{M}$ , where  $T_\theta$  indicates the temperature corresponding to a  $\theta$ -solvent and  $k$  is a chemistry-dependent constant. A plot of the swelling ratio,  $\alpha_g$ , which is the ratio of  $R_g$  in a good solvent to that in a  $\theta$ -solvent, against the solvent quality  $z$ , for  $T > T_\theta$ , collapses data on a universal master curve for a wide variety of polymer-solvent systems with an appropriate choice of the constant  $k$  (Hayward and Graessley, 1999)(Miyaki and Fujita, 1981)(Vidakovic and Rondelez, 1985)(Bercea et al., 1999). Within the framework of Brownian dynamics (BD) simulations, this collapse has been demonstrated by Kumar and Prakash (Kumar and Prakash, 2003).

To the best of our knowledge, there are no studies exploring the universal swelling be-

haviour of dilute solutions of sticky polymers. Here we have used a novel potential, proposed by Soddemann et al. (Soddemann et al., 2001) (which we denote as the SDK potential) to investigate the effect of stickers on the solvent quality and the swelling behaviour of sticky polymers in dilute solutions, using the methodology of Kumar and Prakash (Kumar and Prakash, 2003). The sticky macromolecules are modelled as multi-sticker chains with  $f$  equispaced stickers positioned along the backbone of each chain (except at the chain ends where there are no stickers) separated by  $\ell$  spacer (or backbone) monomers. A sticker is assumed to associate with only one other sticker (i.e. with functionality  $\varphi = 1$ ). Such systems can be easily designed in experiments (David et al., 2009b)(David et al., 2009a)(Guo et al., 2005). The key idea is to investigate various systems characterised by different parameters, and to check if the typical characteristics of a second-order  $\theta$  collapse are observed. Since this indeed appears to be valid in our model, we are able to verify the universality of the swelling of sticky polymer solutions.

The advantage of using the SDK potential is that it can be used to represent both the backbone monomer-monomer interactions, and the sticker monomer-monomer interactions, with a simple choice of the attractive well-depth of the potential. In the former case this is denoted by  $\epsilon_{bb}$ , while in the latter it is denoted by  $\epsilon_{st}$ . We find that the effective solvent quality of a sticky polymer solution can be represented in terms of these variables, along with the clear identification of the  $\theta$ -temperature. As a consequence, the swelling of sticky polymer chains can be examined as a function of the various parameters that control their static properties.

This chapter consists of the following sections. Section 3.2 discusses the principal governing equations and the details of the various interactions. The estimation of the well depth of the SDK potential that determines the  $\theta$ -point for homopolymer solutions is described in Section 3.3. The description of the universal swelling of homopolymers, which forms the framework within which the universal behaviour of sticky polymer solutions is discussed, is taken up in Section 3.4. The determination of the  $\theta$ -temperature of sticky polymer solutions, in terms of the appropriate value of the well depth of the SDK potential, is considered in Sec 3.5.1, while the universal swelling of sticky polymers is examined in Sec 3.5.2. The main conclusions of this chapter are summarised in Section 3.6. The optimisation of the cut-off

radius of the SDK potential and the considerations that lead to the choice of a particular value, are discussed in Appendix A.

## 3.2 Governing Equations and Simulation Details

In the present study we have simulated a single polymer chain, modelled as a sequence of coarse-grained bead-spring chain with  $N_b$  beads connected by  $N_b - 1$  entropic springs. The evolution of the bead position vector,  $\mathbf{r}_\mu$ , is governed by the following Itô stochastic differential equation, as discussed in Section 2.3,

$$\mathbf{r}_\mu(t + \Delta t) = \mathbf{r}_\mu(t) + \frac{\Delta t}{4} \sum_{\nu=1}^N \mathbf{D}_{\mu\nu} \cdot (\mathbf{F}_\nu^s + \mathbf{F}_\nu^{\text{SDK}}) + \frac{1}{\sqrt{2}} \sum_{\nu=1}^N \mathbf{B}_{\mu\nu} \cdot \Delta \mathbf{W}_\nu \quad (3.1)$$

The only difference between Eq. (3.1) and Eq. (2.1), described in Chapter 2, is in the treatment of hydrodynamic interactions (HI). In the present case HI is treated considering a single chain without any periodic images, which does not require the implementation of an Ewald summation, as discussed in Chapter 2. In this work we have adopted an implicit predictor-corrector algorithm, similar to that suggested by Öttinger (Öttinger, 1996) and implemented in their study by Prabhakar et al. (Prabhakar and Prakash, 2004), to solve the Itô stochastic differential equation.

A finitely extensible nonlinear elastic (FENE) spring potential, defined in Eq. 2.4, is used to represent the interaction between adjacent beads. All the simulations reported in this work use a value of  $Q_0^2 = 50.0$ .

Note that a large value of  $Q_0$ , as used here, implies a very soft potential that admits the possibility of self-crossing of the chain. This would pose a severe problem if we were interested in the *dynamics of dense entangled systems*. However, all our investigations in this thesis aim at the study of statics and dynamics of polymer solutions in the dilute and semi-dilute unentangled regimes. It is well known that in these regimes topological constraints do not play a role. Rather on the contrary, self-crossings are expected to speed up the exploration of phase space, and are hence advantageous for our purposes.

The excluded volume and associative interactions between pairs of beads are modelled by

the SDK potential Soddemann et al. (2001), as described in Chapter 2, with a cutoff radius,  $r_c = 1.82 \sigma$ .

From the sticking rules defined in Section 2.5, it becomes clear that the update rules give rise to a well defined configuration space of the system in the sense of statistical mechanics, such that the partition function exists. As long as there are only pairs of stickers  $\mu$  and  $\nu$  within interaction range, it is clear that the corresponding  $q_{\mu\nu}$  has to be one, while in a situation, where, for example, three stickers are all within interaction range of each other, there are three possibilities to form the bond, corresponding to the three sides of the triangle formed by the three stickers. Since all three cases are dynamically accessible, each of them must appear in the partition function. In this context, it should be emphasised that our simulation setup aims at modelling *reversible* sticker bonds.

Note also that other update rules, and/or other values of  $\varphi$ , may well be conceivable, which would then give rise to a different configuration space, and a correspondingly altered statistical mechanics of the system.

In the current scenario, the presence of the additional degrees of freedom,  $q_{\mu\nu}$ , poses a question about the existence of a second-order  $\theta$  transition. There are various examples in statistical mechanics where the coupling to an additional degree of freedom turns a second-order phase transition into a first-order transition. Some of these examples, which are relevant to the present work, are discussed in Section 3.6.

The simulations are carried out for different chain lengths,  $N_b$ , ranging from 25 to 90 beads per chain, with an equilibration run of about 8 Rouse relaxation times (estimated analytically as given in Bird et al. (Bird et al., 1987a)) and a production run of 6 to 8 Rouse relaxation times with a non-dimensional time step size  $\Delta t = 0.001$ . Data from each independent trajectory in the simulations are collected at an interval of 1000 to 5000 non-dimensional time steps over the entire production run and time averages are calculated over each of the trajectories. Average equilibrium properties and error of mean estimates are evaluated over an ensemble of such independent time averages consisting of 1000 to 2000 independent trajectories. In the case of sticky polymers, an additional pre-equilibration run of 2 to 3 Rouse times is carried out with a chain without stickers.

### 3.3 The $\theta$ -point for homopolymers

#### 3.3.1 The radius of gyration

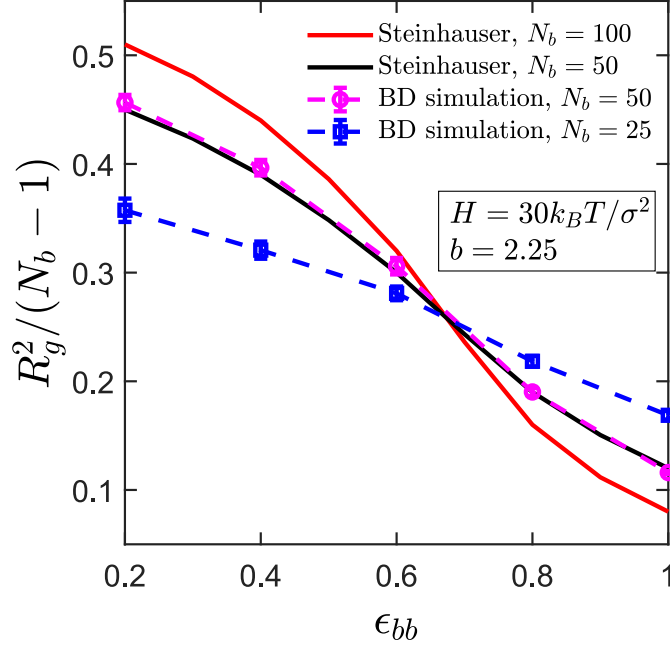


Figure 3.1: Comparison of the ratio  $R_g^2/(N_b - 1)$  as a function of the strength of interaction,  $\epsilon_{bb}$ , for different values of chain length,  $N_b$ . The solid lines represent the results obtained by Steinhauser (Steinhauser, 2005) for  $N_b = 50$  and  $N_b = 100$  and the broken lines are the results obtained from BD simulation.

For a linear polymer chain, the mean-squared radius of gyration ( $R_g^2$ ) follows the universal scaling law  $R_g^2 \sim (N_b - 1)^{2\nu}$ , where,

$$R_g^2 := \langle R_g^2 \rangle = \frac{1}{2N_b^2} \sum_{p=1}^{N_b} \sum_{q=1}^{N_b} \langle r_{pq}^2 \rangle \quad (3.2)$$

with angular brackets representing ensemble averages, and  $r_{pq} = |\mathbf{r}_q - \mathbf{r}_p|$  being the inter-bead distance. The value of the Flory exponent,  $\nu$ , depends on the solvent quality. At the  $\theta$ -temperature, linear polymer chains follow RW statistics, with  $\nu = 1/2$ , leading to the ratio  $R_g^2/(N_b - 1)$  to be independent of the chain length,  $N_b$ . Whereas, in the case of good and poor solvents,  $\nu$  takes the values  $3/5$  and  $1/3$ , respectively (Rubinstein and Colby, 2003).

For polymer chains with the SDK potential representing the excluded volume force, the temperature dependence can be captured with the potential well-depth,  $\epsilon_{bb}$ . The value,  $\epsilon_{bb} = 0$  (which is equivalent to a WCA potential), represents the athermal limit, where the chain is fully swollen. With increasing values of  $\epsilon_{bb}$ , a unique value is reached, at which the repulsive and attractive interactions between pairs of beads are precisely balanced, leading to  $\theta$ -like conditions. The value of  $\epsilon_{bb}$  at the  $\theta$ -point can be estimated by plotting the ratio  $R_g^2/(N_b - 1)$  versus  $\epsilon_{bb}$  for different chain lengths,  $N_b$ , and finding the point of intersection at which curves for different values of  $N_b$  intersect, as shown in Fig. 3.1 (Steinhauser, 2005)(Huissmann et al., 2009). In Fig. 3.1 we have reproduced the results obtained by Steinhauser for a single homopolymer chain (Steinhauser, 2005), where, FENE spring is used with a spring constant  $H = 30k_B T/\sigma^2$  and finite extensibility parameter  $b = 2.25$ . The simulations are carried out with a value of the cutoff radius for SDK potential,  $r_c = 1.5\sigma$ . The value of  $\sigma$  is chosen to be unity to make our length scale comparable with the length scale used by Steinhauser. BD simulations of a single polymer chain are carried out with 25 and 50 beads per chain for  $\epsilon_{bb}$  values ranging from 0.2 to 1.0.

Fig. 3.1 shows a very good agreement of the BD simulations with the published result (Steinhauser, 2005). The value  $\epsilon_{bb} \sim 0.66$ , where all the curves intersect, is identified as the theta point. On the other hand as  $\epsilon_{bb} \rightarrow 0$ , we obtain the athermal limit, where  $R_g^2 \sim (N_b - 1)^{1.2}$ . Beyond  $\epsilon_{bb}$  equal to 0.7 the chain is in totally collapsed regime and follows the poor solvent scaling  $R_g^2 \sim (N_b - 1)^{2/3}$  (Steinhauser, 2005). In this context, it can be perceived that an advantage of the SDK potential over the conventional LJ potential is that the complete range of solvent qualities, from poor to athermal, can be explored by varying the single parameter,  $\epsilon_{bb}$ . It has been found that although the universal scaling laws hold in  $\theta$ , good and poor solvent for a bead-spring chain interacting with the SDK potential and FENE spring force law with constant  $H = 30k_B T/\sigma^2$  and  $b = 2.25$  (*stiff spring*), it fails to reproduce the scaling with a relatively *non-stiff spring*, such as with parameters  $H = k_B T/\sigma^2$  and  $b = 50.0$ . This issue has been resolved by judiciously choosing the cutoff radius,  $r_c$ , which is discussed further in Appendix A.

Following this procedure, the  $\theta$ -point for a homopolymer chain with beads connected by FENE springs having a maximum stretchable length of  $Q_0^2 = 50.0$ , and  $r_c = 1.82\sigma$  as the

cut-off radius of the SDK potential, is found to occur at  $\epsilon_{bb} = \epsilon_\theta = 0.45$ , as displayed in Fig. 3.2

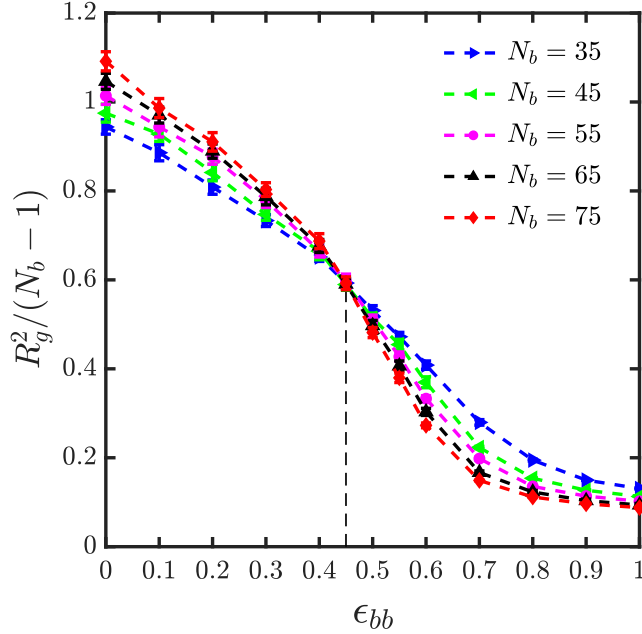


Figure 3.2: The ratio  $R_g^2/(N_b - 1)$  versus the well depth of the SDK potential,  $\epsilon_{bb}$ , to estimate the  $\theta$ -point for cutoff radius  $r_c = 1.82\sigma$ . The symbols represent simulation data and the dotted lines are drawn to guide the eye. The  $\theta$ -point is estimated as the intersection of all the curves and leads to  $\epsilon_{bb} = 0.45$ .

### 3.3.2 The second virial coefficient

In addition to the determination of the  $\theta$ -point from the scaling of radius of gyration, there is an alternative method based on the second osmotic virial coefficient ( $B_2$ ), which involves the determination of the potential of mean force,  $U(r)$ , between a pair of polymer chains with their centres of mass separated by a distance  $r$  (Dautenhahn and Hall, 1994)(Withers et al., 2003)(Narros et al., 2013). Following the procedure discussed by Dautenhahn et al. (Dautenhahn and Hall, 1994),  $U(r)$  is calculated as follows. Two independent chain configurations are chosen from two sets of equilibrated single chain conformations (each having 2000 conformations) and are randomly oriented with respect to each other, with their centres of mass separated by a distance  $r$ . For a set of values of  $r$  ranging from 0

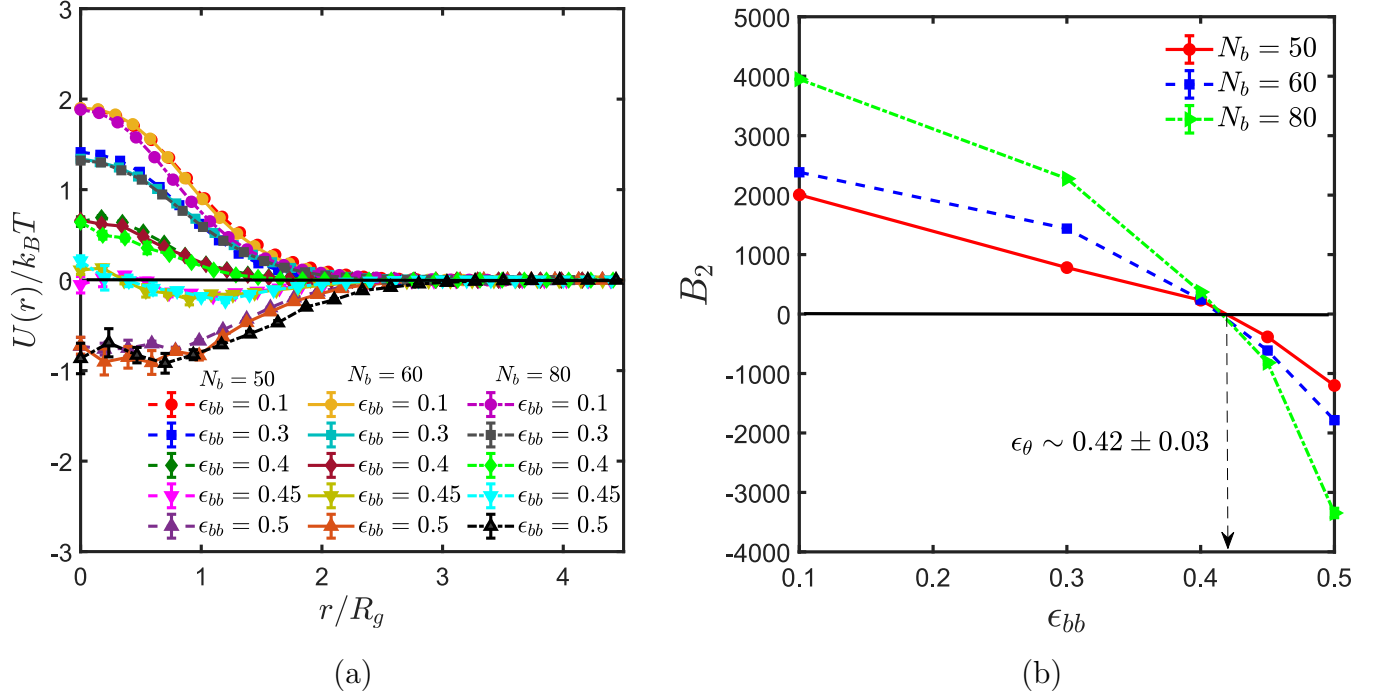


Figure 3.3: (a) The effective potential,  $U(r)/k_B T$ , as a function of the separation distance,  $r/R_g$ , between the centres of mass of a pair of homopolymer chains at different values of potential well depth,  $\epsilon_{bb}$ . (b) The second osmotic virial coefficient,  $B_2$ , as a function of potential well-depth,  $\epsilon_{bb}$ , for different chain lengths. The estimated value of the  $\theta$ -point,  $\epsilon_\theta$ , from the second virial coefficient is  $0.42 \pm 0.03$ .

to 5 times the radius of gyration, all such possible two chain configurations (about  $4 \times 10^6$  configuration pairs) are considered. For each configuration pair  $i$ , the interaction energy,  $\phi_i(r)$ , between the two chains is evaluated by computing the pair-wise potential for all pairs of beads, one taken from each chain such that

$$\phi_i(r) = \sum_{p=1}^{N_b} \sum_{q=1}^{N_b} U_{\text{SDK}_i}(r_{pq}). \quad (3.3)$$

Here  $\phi_i(r)$  is computed using the SDK potential to account for the pair-wise interaction of the beads and the indices  $p$  and  $q$  corresponds to chain 1 and 2, respectively. Finally the effective potential is evaluated from  $\phi_i(r)$  from the expression

$$\exp(-U(r)/(k_B T)) = \langle \exp(-\phi_i(r)/(k_B T)) \rangle \quad (3.4)$$

where the term on the right hand side of Eq. (3.4) is an ensemble average over all configuration pairs. The second virial coefficient is then easily calculated by evaluating the integral Rubinstein and Colby (2003)

$$B_2 = \int_0^\infty 2\pi r^2 (1 - \exp[-U(r)/k_B T]) dr. \quad (3.5)$$

Positive values of  $B_2$  indicate that the polymer solution lies in the good solvent regime, while negative values indicate that it is under poor solvent conditions. At the  $\theta$ -point,  $B_2 = 0$ .

Figure 3.3 (a) shows the effective potential,  $U(r)/k_B T$ , as a function of the distance,  $r/R_g$ , between the centres of mass. For short chains, the potential of mean force depends on chain length, but for sufficiently long chains it saturates within error bars (Krakoviack et al., 2003)(Withers et al., 2003)(Narros et al., 2013). These are typically fairly small but non-negligible for deep well depths, small distances, and long chains. At small distances sampling is difficult, since for most random pairs the Boltzmann factor is very small due to chain overlap and the strong repulsion of the SDK potential. Therefore, the average is strongly dominated by those few configurations where this is not the case, and this gives rise to an effectively very small sample size (Krakoviack et al., 2003)(Dautenhahn and Hall, 1994)(Narros et al., 2013). This problem is aggravated for increasing chain lengths and well depths.

Figure 3.3 (b) is a plot of  $B_2$  as a function of the potential well depth,  $\epsilon_{bb}$ .  $B_2$  vanishes at  $\epsilon_{bb} = 0.42 \pm 0.03$ , independently of chain length. This estimate of the  $\theta$ -point is in good agreement, within error bars, with the value calculated previously from the scaling of  $R_g^2$  ( $\epsilon_\theta \approx 0.45$ ). Since both methods lead to approximately the same estimate, the value  $\epsilon_\theta = 0.45$  has been used for all further calculations. The estimation of  $\theta$ -point is necessary to establish the universal swelling behaviour of homopolymers, the discussion of which is taken up in the following section.

### 3.4 Universal swelling of homopolymers

The swelling of homopolymers interacting with an SDK potential as the source of the excluded volume force is investigated in this section. The results are compared with the swelling of experimental polymer-solvent systems and earlier predictions of BD simulations, where the excluded volume interactions are modelled by a narrow Gaussian potential given by (Öttinger, 1996)(Prakash and Öttinger, 1999)

$$E(\mathbf{r}_{\mu\nu}) = \left(\frac{z^*}{d^{*3}}\right) k_B T \exp\left\{-\frac{1}{2} \frac{\mathbf{r}_{\mu\nu}^2}{d^{*2}}\right\} \quad (3.6)$$

Here,  $\mathbf{r}_{\mu\nu} = (\mathbf{r}_\mu - \mathbf{r}_\nu)$ ,  $d^*$  is a non-dimensional parameter that measures the range of interactions, and  $z^*$  is the non-dimensional strength of excluded volume interactions. In the context of the narrow Gaussian potential, the solvent quality is defined by  $z = z^* \sqrt{N_b}$ , which takes into account the dependence on both temperature and chain length. Kumar and Prakash performed BD simulations with the narrow Gaussian potential to obtain the universal swelling ratio as a function of solvent quality  $z$  (Kumar and Prakash, 2003). Essentially, they obtained  $\alpha_g^2$  at a particular value of  $z$  by carrying out simulations for different chain lengths  $N_b$ , where the parameter  $z^*$  was evaluated using the expression  $z^* = z/\sqrt{N_b}$ , for each choice of  $N_b$ . The data accumulated for various values of  $N_b$  was then extrapolated to the limit of  $N_b \rightarrow \infty$  to obtain the asymptotic  $\alpha_g^2$  value, at the chosen value of  $z$ . The results are plotted in Fig. 3.4 and fitted with an expression suggested earlier by renormalisation group calculations (Schäfer, 1999)(Freed, 1987)(des Cloizeaux and Jannink, 1990)

$$\alpha_g^2 = (1 + az + bz^2 + cz^3)^m \quad (3.7)$$

with fit parameters  $a = 9.528$ ,  $b = 19.48 \pm 1.28$ ,  $c = 14.92 \pm 0.93$  and  $m = 0.133913 \pm 0.0006$  (Yamakawa, 1971)(Schäfer, 1999)(Kumar and Prakash, 2003). The fitted curve is the universal thermal crossover swelling curve predicted by BD, and acts as a reference for collapsing swelling data for a range of polymer-solvent systems as discussed below.

Kumar and Prakash (Kumar and Prakash, 2003) showed that experimental data acquired previously (Miyaki and Fujita, 1981) for  $\alpha_g^2$  versus  $z$ , in a variety of different polymer-solvent

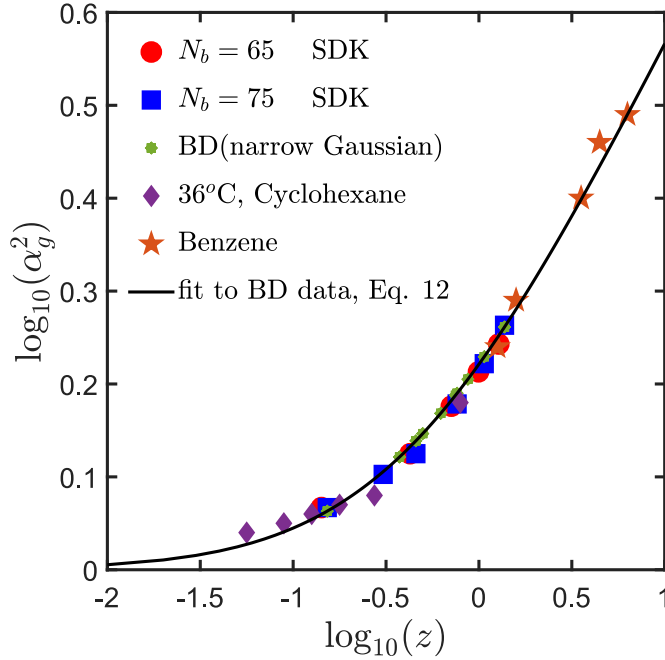


Figure 3.4: Universal swelling behaviour of the radius of gyration,  $\alpha_g^2$ , as a function of the solvent quality,  $z$ . The red filled circles and the blue filled squares are simulation results with the SDK potential, which is compared with BD simulations obtained with the narrow Gaussian potential (Kumar and Prakash, 2003), and with experimental results for polystyrene in two solvents (Miyaki and Fujita, 1981). The solid line represents the curve fit corresponding to Eq. (3.7).

systems, could also be described by the same universal curve. This is done by defining the experimental solvent quality by  $z = k_{\text{expt}} \hat{\tau} \sqrt{M}$ , where  $\hat{\tau} = 1 - (T_\theta/T)$  and adjusting  $k_{\text{expt}}$ , which is a chemistry dependent constant, in order to achieve data collapse (Kumar and Prakash, 2003). Swelling data (Miyaki and Fujita, 1981) for polystyrene in cyclohexane at 36°C, and in benzene at 25°C and 30°C, obtained in this manner are shown in Fig. 3.4. We have adopted a similar approach to check whether polymer chains with the SDK potential follow the same universal swelling behaviour. The solvent quality is defined here in terms of the potential well depth as

$$z = k_{\text{SDK}} \left( 1 - \frac{\epsilon_{bb}}{\epsilon_\theta} \right) \sqrt{N_b} \quad (3.8)$$

where  $k_{\text{SDK}}$  is a constant dependent on the interaction potential and  $\hat{\tau}_{\text{SDK}} = (1 - \epsilon_{bb}/\epsilon_\theta)$  is equivalent to the temperature dependent term,  $\hat{\tau}$ , defined earlier. Note that the factor

$(1 - \epsilon_{bb}/\epsilon_\theta)$  is defined in such a way that in the limit of a  $\theta$ -solvent its value is zero, while in the good solvent limit ( $\epsilon_{bb} = 0$ ),  $\hat{\tau}_{\text{SDK}} = 1$ . The value of  $k_{\text{SDK}}$  is obtained by the following procedure. Simulations are carried out for different values of chain length  $N_b$  and well depths  $\epsilon_{bb}$ , and the mean-squared radius of gyration  $R_g^2$  is calculated in each case. The swelling,  $\alpha_g^2$ , relative to the size of the chain under  $\theta$ -solvent conditions,  $R_{g\theta}^2$  (obtained from a simulation with  $\epsilon_{bb} = \epsilon_\theta = 0.45$ ), is calculated in each case, and the corresponding values of  $z$  are determined from the universal swelling curve given by Eq. (3.7). Finally, values of  $z$  obtained in this manner are plotted as a function of  $(1 - \epsilon_{bb}/\epsilon_\theta)\sqrt{N_b}$ , and the resultant curve is fitted with a straight line as shown in Fig. 3.5. From the slope one finds  $k_{\text{SDK}} = 0.1586$ .

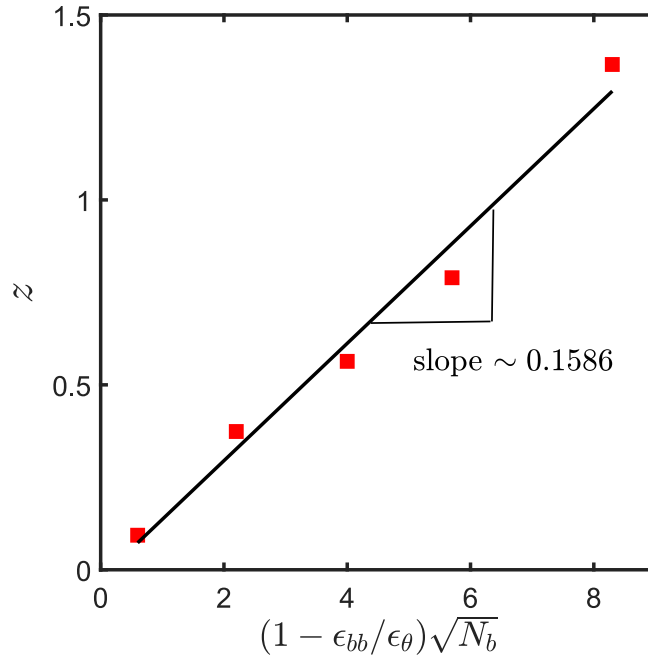


Figure 3.5: Solvent quality  $z$  versus the factor  $(1 - \epsilon_{bb}/\epsilon_\theta)\sqrt{N_b}$  for polymer chain interacting with SDK potential. The symbols are the simulation data and the straight line gives a linear fit through the data points with slope 0.1586.

The swelling of polymer chains with  $N_b = 65$  and  $N_b = 75$ , obtained with the SDK potential for a set of values of  $z$  obtained in this manner, is compared in Fig. 3.4 with earlier results from BD simulations and experimental measurements of the swelling of polystyrene in cyclohexane and benzene. It is clear that the SDK potential reproduces the universal swelling behaviour in the thermal crossover regime obtained previously with the narrow

Gaussian potential. It is worth noting here, however, that in the case of the SDK potential, we have not extrapolated finite chain data to the long chain limit, as was done for the narrow Gaussian potential. We found that this was unnecessary since the results for  $N_b = 65$  and  $N_b = 75$  already lie on the universal curve.

## 3.5 $\theta$ -point and swelling of sticky polymers

As mentioned earlier, the inclusion of sticky groups decreases the effective solvent quality. The purpose of this section is to present results which establish, within the studied parameter range, that the collapse of the sticky polymer chain is a standard second order  $\theta$  transition. We show this by demonstrating that all the methods that have been applied to homopolymers, both for the localisation of the  $\theta$  transition (as discussed in the Section 3.3), and for the study of the universal scaling for the swelling (as discussed in the previous section) is transferable.

### 3.5.1 $\theta$ -point for sticky polymer solutions

#### Scaling of the radius of gyration

For the sticky chain, we keep  $\epsilon_{bb}$  and  $\ell$  fixed, and study  $R_g^2$  as a function of  $\epsilon_{st}$ , which we use as the control parameter that drives the transition. Following the procedure described in Section 3.3.1 for homopolymers, intersection plots for  $R_g^2/(N_b - 1)$  versus  $\epsilon_{st}$  are presented in Fig. 3.6, which allows us to find the  $\theta$ -point for various choices of  $\epsilon_{bb}$  and  $\ell$ ,  $\epsilon_{st}^\theta = \epsilon_{st}^\theta(\epsilon_{bb}, \ell)$ . The error in  $\epsilon_{st}^\theta$  is estimated by linear interpolation between the data points adjacent to the intersection, combined with standard error propagation. We will show shortly that for our model,  $\epsilon_{st}^\theta$  can be determined by an alternative simpler, and perhaps more accurate, procedure.

It is interesting to note that the ratio  $R_{g\theta}^2/(N_b - 1)$  at the  $\theta$ -point, denoted by  $R_{g\theta}^2/(N_b - 1)$ , assumes a constant value, as shown in Fig. 3.7, for monomers interacting via the SDK potential, irrespective of the spacer length and backbone solvent quality. It is also evident that the value of the ratio  $R_{g\theta}^2/(N_b - 1)$  is the same for both homopolymers and sticky

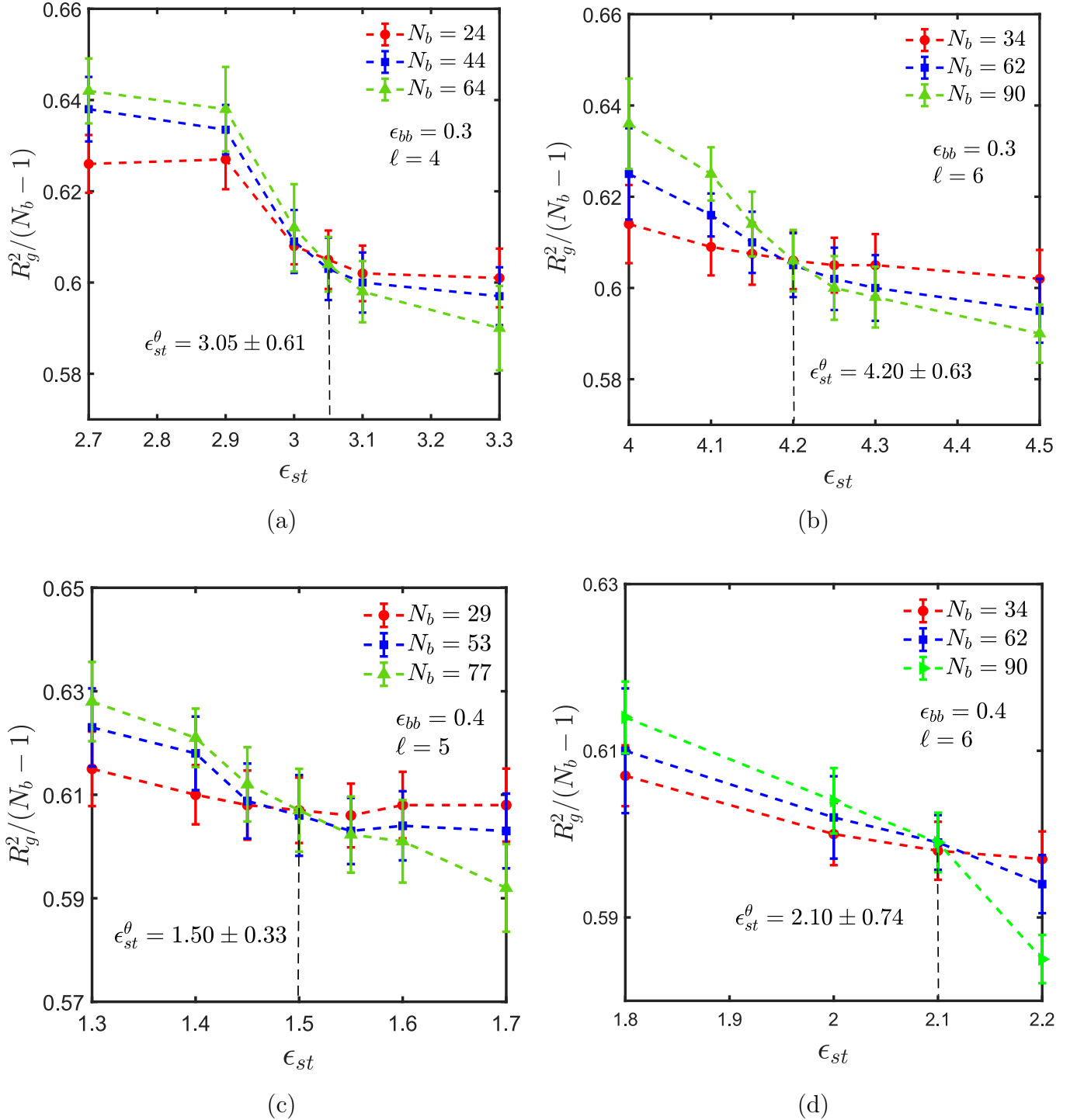


Figure 3.6: The ratio  $R_g^2/(N_b - 1)$  as a function sticker strength,  $\epsilon_{st}$ , for a single sticky polymer chain with backbone monomer attraction strengths,  $\epsilon_{bb} = 0.3$  and  $0.4$ , respectively, and spacer length,  $\ell = 4, 5$  and  $6$ , as indicated in the various figure legends. In all the cases the stickers associate with functionality equal to 1. The errorbars for  $\epsilon_{st}$  at the point of intersection are estimated by an error propagation scheme discussed in Section 3.5.1.

polymers, suggesting that the Kuhn step length is the same in both cases, and is independent of the presence of sticky groups. This implies that one does not need to do simulations for each and every system in order to estimate the  $\theta$ -point and calculate the corresponding  $R_{g\theta}^2$ . This, of course, simplifies matters substantially. It is worth emphasising, however, that this is most probably a special feature of our model, and probably will no longer be true for chemically more realistic models.

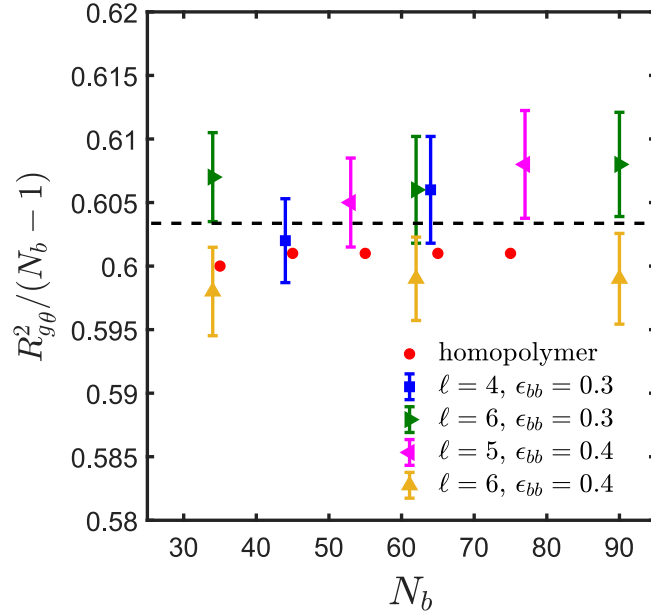


Figure 3.7: The ratio  $R_{g\theta}^2 / (N_b - 1)$  at the  $\theta$ -point, denoted by  $R_{g\theta}^2 / (N_b - 1)$ , for different chain lengths,  $N_b$ , spacer monomer,  $\ell$ , and backbone monomer attraction strength,  $\epsilon_{bb}$ . The dashed line corresponds to the constant value of the ratio  $R_{g\theta}^2 / (N_b - 1)$ , which is estimated to be 0.603.

### Calculation of the second virial coefficient

For sticky polymers, the estimation of the  $\theta$ -point from the second virial coefficient was carried out as was done for homopolymers (see Section 3.3.2), with a set of about  $5 \times 10^7 - 10^8$  configurations of chain pairs. Since the Boolean variables  $q_{\mu\nu}$  (see Section 3.2) were not stored in the course of the simulations, it was necessary in situations where there were three stickers within interaction distance of each other, to define  $q_{\mu\nu}$  by some rule. Following the sticking rule defined in Section 3.2, we picked the two stickers according to the order of monomer

$\ell$	$\epsilon_{bb}$	$\epsilon_{st}^\theta$ (from $R_g^2$ scaling)	$\epsilon_{st}^\theta$ (from $B_2$ )
4	0.3	$3.05 \pm 0.61$	$3.231 \pm 0.012$
5	0.4	$1.50 \pm 0.33$	$1.215 \pm 0.065$
6	0.3	$4.20 \pm 0.63$	—
6	0.4	$2.10 \pm 0.74$	—

Table 3.1: Comparison between the  $\theta$ -points estimated from the scaling of radius of gyration and second virial coefficient for solutions of sticky polymers with different spacer lengths,  $\ell$ , and backbone monomer interaction strengths,  $\epsilon_{bb}$ .

labels to be bonded. For the rare case of four or more stickers, we proceeded in an analogous fashion.

Figures 3.8 show the effective interaction potentials and second virial coefficients for systems with spacer lengths  $\ell = 4, 5$ , and  $\epsilon_{bb} = 0.3, 0.4$ . One sees that even though the method is hampered by similar problems as in the homopolymer case, it is nevertheless possible to locate the  $\theta$ -point with reasonable accuracy, which is actually significantly better than that obtained from the scaling of  $R_g^2$ . The results are summarised in Table 3.1. With increase in spacer length ( $\ell = 6$ ) and sticker strength, the sampling gets poorer and less efficient, as explained in Section 3.3.2, such that it was not possible to determine the  $\theta$ -point by the virial coefficient method satisfactorily.

### The $\theta$ -surface for sticky polymers

Since the location of the  $\theta$ -point,  $\epsilon_{st}^\theta$ , depends on both  $\ell$  and  $\epsilon_{bb}$ , the full phase diagram of the system is three-dimensional, with a two-dimensional surface of  $\theta$ -points separating the good and poor solvent regions. Figure 3.9 is a schematic representation of such a surface, where we confine attention to the physically interesting case  $\epsilon_{st} > \epsilon_{bb}$ . This implies that under  $\theta$  conditions for the chain as a whole, the backbone is in a relatively good solvent ( $\epsilon_{bb} < \epsilon_\theta$ ), meaning that the conformations are the result of a competition between backbone-backbone repulsion and sticker-sticker attraction.

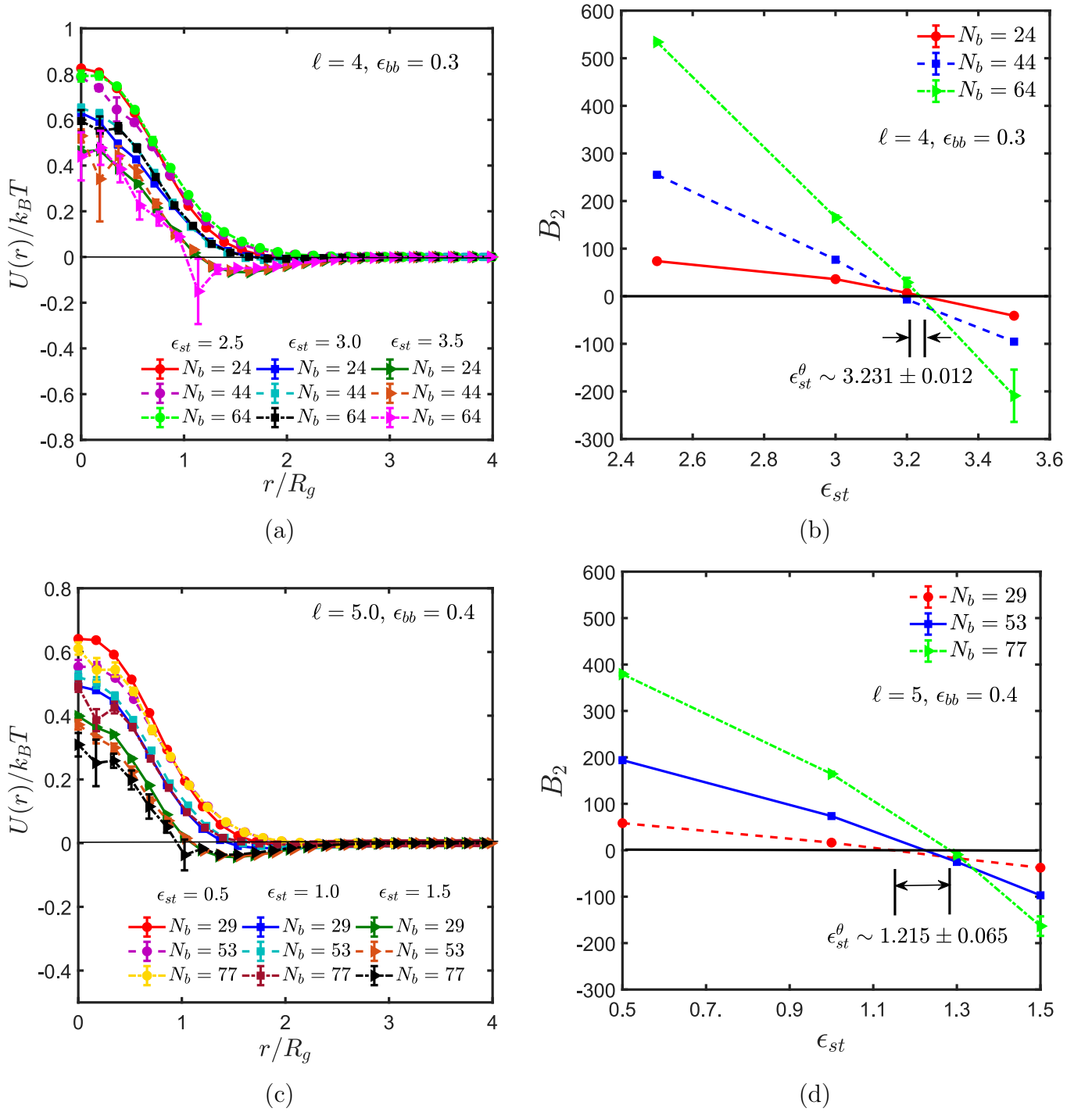


Figure 3.8: ((a) and (c)) The effective potential,  $U(r)/k_B T$ , as a function of the separation distance,  $r/R_g$ , between the centres of mass of a pair of sticky polymer chains at different values of stiker strength,  $\epsilon_{st}$ . ((b) and (d)) The second osmotic virial coefficient,  $B_2$ , as a function of the stiker strength,  $\epsilon_{st}$ , for different chain lengths. The estimated value of the  $\theta$ -point,  $\epsilon_{st}^\theta$ , from the second virial coefficient is  $3.231 \pm 0.012$  and  $1.215 \pm 0.065$  for  $\ell = 4$ ,  $\epsilon_{bb} = 0.3$  and  $\ell = 5$ ,  $\epsilon_{bb} = 0.4$ , respectively.

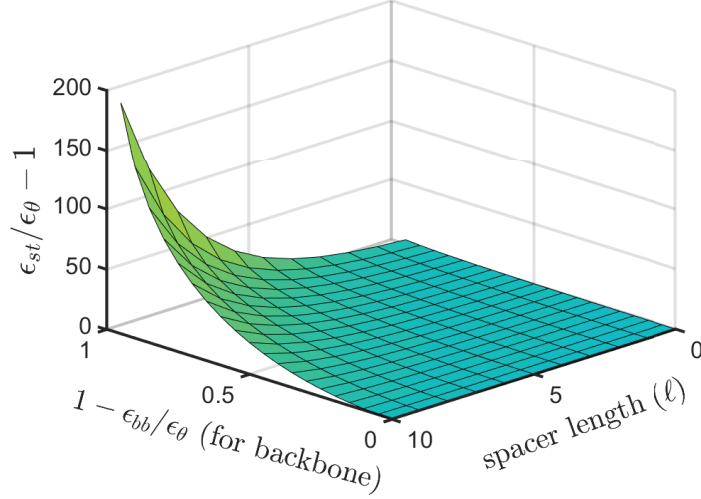


Figure 3.9: (Color online) Schematic of a  $\theta$ -surface in terms of the scaled variables  $(\epsilon_{st}/\epsilon_\theta - 1)$  plotted against the scaled backbone solvent quality,  $(1 - \epsilon_{bb}/\epsilon_\theta)$ , and spacer length,  $\ell$ . Points above the surface indicate solutions of sticky polymers in poor solvent whereas points below the surface represents solutions in a good solvent.

### 3.5.2 Universal swelling of sticky polymers

In order to study the universal swelling for the sticky chain, a suitable definition of the solvent quality parameter  $z$  is required. Based on our choice of  $\epsilon_{st}$  as the independent control parameter that drives the transition, it is logical to generalise Eq. (4.4) as

$$z = g(\ell, \epsilon_{bb}) \left( 1 - \frac{\epsilon_{st}}{\epsilon_{st}^\theta(\ell, \epsilon_{bb})} \right) \sqrt{N_b} \quad (3.9)$$

where  $g(\ell, \epsilon_{bb})$  is a material dependent function of spacer length ( $\ell$ ) and backbone monomer interaction strength ( $\epsilon_{bb}$ ). In the limit of  $\epsilon_{st} = \epsilon_{bb}$ , the effective solvent quality becomes the same as that of the corresponding homopolymer, and the sticky chain becomes indistinguishable from it (see Eq.(2.7)). By definition, for  $\epsilon_{st} = \epsilon_{st}^\theta$  the overall solvent quality  $z = 0$ .

For obtaining the swelling curve for sticky polymers, one can exploit the simplification that comes from the constancy of the ratio  $R_{g\theta}^2/(N_b - 1)$ , independent of all other parameters, which renders the need for extra simulations to calculate  $R_{g\theta}^2$  superfluous. Simulations are carried out for different values of  $\ell$ ,  $\epsilon_{bb}$ ,  $\epsilon_{st}$ , and  $N_b$ , and the swelling ratio,  $\alpha_g^2$ , is then calculated for each set of these parameters. For values of  $\ell$  and  $\epsilon_{bb}$  for which  $\epsilon_{st}^\theta$  is known,

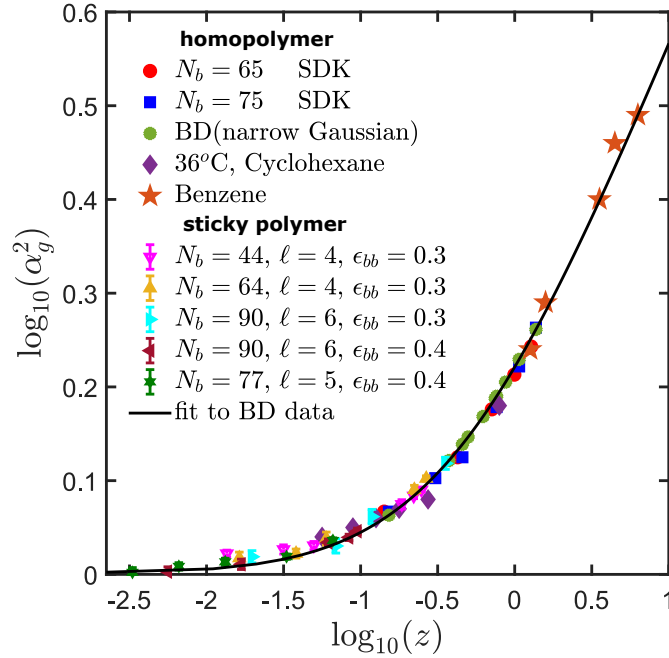


Figure 3.10: Universal swelling of the radius of gyration,  $\alpha_g^2$ , as a function of the solvent quality,  $z$ . The swelling of the sticky polymers with different spacer lengths,  $\ell$ , and backbone monomer attraction strengths,  $\epsilon_{bb}$ , is compared with the swelling of homopolymers, as indicated in the figure. The sticker functionality is equal to 1 in all cases. The solid line represents the curve fit corresponding to Eq. (3.7).

$g(\ell, \epsilon_{bb})$  can be estimated using the same technique as was used to find  $k_{\text{SDK}}$  in the case of homopolymers, discussed in Section 3.4. The results are tabulated in Table 3.2. Plotting  $\alpha_g^2$  versus  $z$ , as displayed in Fig. 3.10, shows that the swelling of sticky polymers relative to its  $\theta$  state follows the same universal curve already presented in Fig. 3.4 for homopolymer systems.

The existence of the universality of the swelling of sticky polymers, which has been established above, can be used to determine the  $\theta$ -point  $\epsilon_{st}^\theta(\ell, \epsilon_{bb})$ , along with  $g(\ell, \epsilon_{bb})$ , for any pair of values of  $\ell$  and  $\epsilon_{bb}$ , without the complicated analysis of subsection 3.5.1. One only needs data for two different  $\epsilon_{st}$  values, while  $N_b$ ,  $\ell$ , and  $\epsilon_{bb}$  are being kept fixed. The swelling curve allows us to transform the  $\alpha_g^2$  values to corresponding solvent qualities  $z$ . Therefore, inserting all known parameters into Eq. (3.9) gives rise to two equations with two unknowns which, after solution, provide the desired values  $g(\ell, \epsilon_{bb})$  and  $\epsilon_{st}^\theta(\ell, \epsilon_{bb})$ . A sample calculation to demonstrate the above method is as follows. The parameters chosen

$\ell$	$\epsilon_{bb}$	$g(\ell, \epsilon_{bb})$
4	0.3	$0.0415 \pm 0.0021$
6	0.3	$0.0437 \pm 0.0024$
5	0.4	$0.0113 \pm 0.0011$
6	0.4	$0.0124 \pm 0.0011$

Table 3.2: Estimated values of the function  $g(\ell, \epsilon_{bb})$  for different values of spacer length,  $\ell$ , and backbone monomer interaction strength,  $\epsilon_{bb}$ .

are  $N_b = 64$ ,  $\ell = 4$ ,  $\epsilon_{bb} = 0.3$  and the two sticker strengths are  $\epsilon_{st} = 1.0$  and  $2.5$ . Considering  $R_{g\theta}^2/(N_b - 1) = 0.603$ , the values of  $\alpha_g^2$  obtained from the simulations for the given set of parameters are equal to  $1.245$  and  $1.105$  for  $\epsilon_{st} = 1.0$  and  $\epsilon_{st} = 2.5$ , respectively. The corresponding values of  $z$  are estimated from Eq. (3.7) to be  $0.2635$  and  $0.096$  for  $\epsilon_{st} = 1.0$  and  $\epsilon_{st} = 2.5$ , respectively. Substituting the values of  $z$  in Eq. (3.9) and simultaneously solving the two linear equations for the unknowns, gives  $\epsilon_{st}^\theta(\ell, \epsilon_{bb}) = 3.36$  and  $g(\ell, \epsilon_{bb}) = 0.047$ , which is, within error bars, consistent with the previously estimated values of  $\epsilon_{st}(\ell, \epsilon_{bb}) = 3.05 \pm 0.61$  and  $g(\ell, \epsilon_{bb}) = 0.0415 \pm 0.0021$  (see Fig. 3.6 (a) and Table 3.2).

A comparison of the values of  $\epsilon_{st}^\theta$  obtained from the semi-analytical estimation procedure discussed above with that from full-blown simulations as carried out in the context of Fig. 3.6, for different spacer monomers  $\ell$  and backbone solvent qualities  $\epsilon_{bb}$ , is shown in Fig. 3.11. The plot shows a satisfactory agreement between the two methods and implies that the calculation of  $\epsilon_{st}^\theta$  using Eq. (3.9) provides a reasonable estimate of the  $\theta$ -point for the sticky polymer systems. Fig. 3.11 also suggests, as expected intuitively, that the sticker strength at the  $\theta$ -point,  $\epsilon_{st}^\theta$ , increases monotonically with spacer length,  $\ell$ , for a given value of  $\epsilon_{bb}$ . With an increase in spacer monomers, the sticker density along the polymer backbone decreases, and it requires a much higher attractive strength for the stickers to make the chain follow RW statistics. In all our simulations, the value of the sticker strength  $\epsilon_{st}$  is taken to be greater than  $\epsilon_\theta$ , while  $\epsilon_{bb} < \epsilon_\theta$ . The corresponding increase in solvent quality for the backbone is thus compensated by an increased attraction between the stickers. At  $\epsilon_{bb} = \epsilon_\theta$ , the backbone is in a  $\theta$ -solvent condition, and under such circumstances the sticker strength at the  $\theta$ -point,

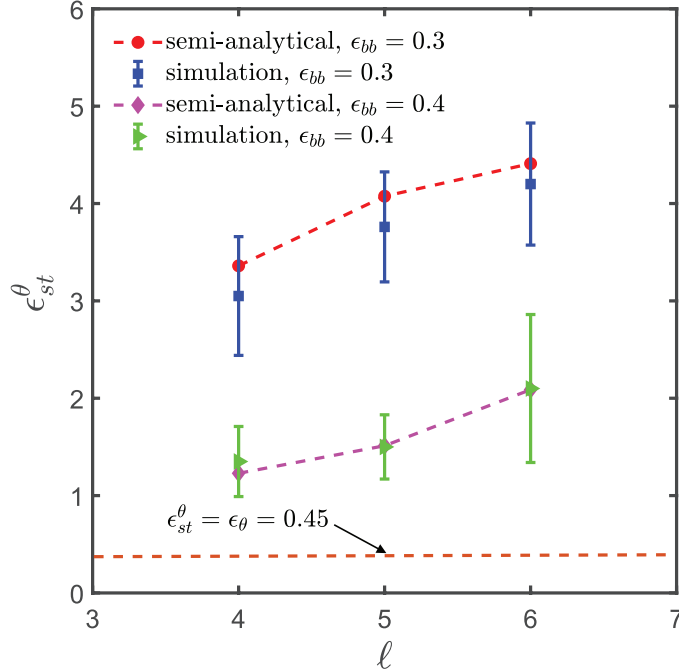


Figure 3.11: Sticker strength under  $\theta$ -solvent conditions,  $\epsilon_{st}^\theta$ , versus the spacer length,  $\ell$ , for different backbone attraction strengths,  $\epsilon_{bb}$ . The open symbols represent the elaborate procedure for obtaining  $\epsilon_{st}^\theta$  described in Section 3.5.1, while the filled symbols are obtained by the semi-analytical procedure described in Section 3.5.2. The dashed line is drawn to guide the eye. The constant straight line indicates the limiting value of  $\epsilon_{st}^\theta$ , as discussed in the context of Eq. (3.9).

$\epsilon_{st}^\theta$ , is equal to  $\epsilon_\theta$ , which is the limiting value of  $\epsilon_{st}^\theta$ , indicated by the constant straight line in Fig. 3.11 and discussed previously in the context of Eq. (3.9).

### 3.6 Discussion and conclusions

Using the Soddemann-Dünweg-Kremer potential to model excluded volume interactions, and defining a renormalised solvent quality for sticky polymer solutions, the swelling of the radius of gyration has been shown to be identical to the universal swelling of homopolymers in the thermal crossover regime. Additionally, the Kuhn segment length under  $\theta$  conditions, for our model, is found to be the same for chains with and without stickers. This allows, in combination with the known universal swelling curve, a fairly easy determination of the two-dimensional  $\theta$ -surface embedded in the three-dimensional  $(\ell, \epsilon_{bb}, \epsilon_{st})$  phase diagram.

The collapse transition observed here is a standard second-order transition and as a

consequence, all scaling laws and universal properties are faithfully reproduced. In the parameter range that we have studied, a strong first-order transition can be ruled out. In hindsight this is perhaps not too surprising, since the only theoretical possibility for the existence of first-order behaviour arises from a strong coupling of the conformational degrees of freedom to the Boolean degrees of freedom that describe functionality. As seen from Eq. (2.7), the strength of the coupling is directly proportional to  $\epsilon_{st} - \epsilon_{bb}$ . In the parameter range where we did the simulations, this difference was never very large. For this reason, the possibility of a first-order transition in the opposite limit  $\epsilon_{st} - \epsilon_{bb} \gg 1$  cannot be ruled out within the framework of the current investigation.

One might then consider a situation where the backbone is under very good solvent conditions,  $\epsilon_{bb} = 0$ , while  $\epsilon_{st}$  is so large that nevertheless a collapse would occur. Note that in such a situation the transition would be *entropy*-driven rather than *energy*-driven. This is so because the condition  $\varphi = 1$  for the bonds would lead to a complete saturation, with no residual attraction being left. The reason for a collapsed conformation would then be merely entropic because such a state allows for many more possibilities to form bonds than a swollen chain, which would only allow association of stickers that are near each other on the chain. Note, however, that such a situation would essentially be impossible to simulate with standard Brownian dynamics, simply because the breaking of a once-formed bond would be extremely rare. It might be possible to investigate such a situation with advanced Monte Carlo algorithms like parallel tempering (Earl and Deem, 2005), but this is beyond the scope of the present investigation.

There are a number of previous studies, in the context of models for both synthetic and biological polymer solutions, where a first-order rather than a second-order transition has been observed. For instance, in the model proposed by Jeppesen and Kremer (Jeppesen and Kremer, 1996) for the phase-behaviour of polyethylenoxide in water, each monomer has a Boolean degree of freedom that enters the interaction energy. Depending on the strength of the coupling parameter, they find a second or first-order transition, with the first order transition being entropy driven for reasons similar to those discussed above. More recently, Scolari et al. (Scolari and Lagomarsino, 2015) have developed a model for the folding of chromosomes due to self-attraction, and the formation of loops due to bridging proteins. Their

model is similar to that used here for sticky polymers, with the bridging interactions (which are distributed uniformly along the backbone of the polymer) playing the role of stickers. However, their model differs from the one used here in certain key aspects. Firstly, the interaction energy in their system can be completely determined from the position coordinates of the beads, and secondly their functionality is not restricted to one. As a result, there are no additional Boolean degrees of freedom, and complex micellar structures are formed with multiple stickers forming clusters. Within the framework of such a model, for certain parameter values, they observe a first order collapse transition which is driven by competition between the energy gained from forming a core of bridging monomers versus the entropy lost by looping backbone monomers. Another relevant recent work where a first-order transition has been observed is by Michieletto et al. (Michieletto et al., 2016), who have examined the 3D dynamics of chromatin folding coupled to 1D dynamics of epigenetic spreading, with a semiflexible bead-spring chain as a model for chromatin fiber. In this model, each bead can have two possible colours, with the colour denoting the epigenetic state and like colours attracting each other. The addition of the colour variable to position coordinates, leads to additional Boolean degrees of freedom, with the interaction energy not being calculable by chain conformation alone. Beads are recoloured periodically with a standard Metropolis acceptance criteria based on the energy difference between beads that are spatially proximate. Unlike in the present model, where the number of stickers is fixed, the number of strongly attracting like-coloured monomers is not constant but calculated dynamically based on proximity and energy of neighbouring monomers. It is observed that a critical value of attraction between like colours exists that separates the chain conformations into a swollen state, with the colours distributed homogeneously along the chain, and a collapsed globular state, with one colour dominant. It is argued that the first-order transition arises because of the coupling between 3D folding dynamics of the polymer and the 1D epigenetic spreading. Interestingly, in contrast to the present model, a second-order transition is never observed for the parameter values that have been examined.

Though the universal swelling of the radius of gyration in dilute sticky polymer solutions in the thermal crossover regime has been demonstrated here with the help of the Soddemann-Dünweg-Kremer potential, which has many desirable properties, we expect this behaviour

to be independent of the specific choice of the excluded volume potential. We hope that this intriguing behaviour predicted by simulations will be tested and validated against careful experiments in the future.

# Chapter 4

## Universal scaling and characterisation of gelation in associative polymer solutions

### 4.1 Introduction

An essential feature of physically associative polymer solutions is the prevalence of *intra-chain* and *inter-chain* associations between the attractive groups on the chains, which lead to the formation of gels and network structures. While gelation in associative polymer solutions at a moderate concentration is a well known phenomenon, there has always been a long standing debate to identify gelation transition in these systems because of the different competing definitions of the transition, corresponding to different signatures of gelation. Scaling relations have been proposed for associative polymer solutions based on mean field theory and lattice theory to characterise gelation by correlating the intra-chain ( $p_1$ ) and inter-chain ( $p_2$ ) association fraction of the stickers with various parameters that define the system, such as the number of attractive groups (stickers) on a chain ( $f$ ), the number of monomers between two stickers (or the spacer length  $\ell$ ), the strength of association between the stickers ( $\epsilon_{st}$ ), the monomer concentration ( $c$ ), and the solution temperature ( $T$ ). Apart from a preliminary Monte Carlo study Kumar and Panagiotopoulos (1999), these

predictions have, to our knowledge, so far not been thoroughly tested through simulations. In this work we have developed a multi-particle Brownian dynamics simulation algorithm with a Soddemann-Duenweg-Kremer potential that accounts for pairwise excluded volume interactions between both backbone monomers and associating groups (stickers) on a chain, to describe the static behaviour of associative polymer solutions, across a range of concentrations into the semidilute unentangled regime. The formulation adopted in the present work enables a careful examination of the predictions of the mean field theory for the scaling dependence of  $p_1$  and  $p_2$  on system parameters. In the mean-field theory, proposed by Dobrynin (Dobrynin, 2004), different regimes of scaling behaviour are identified depending on the monomer concentration, the density of stickers on a chain, and whether the solvent quality for the backbone monomers corresponds to  $\theta$  or good solvent conditions. In the present study, simulation results validate the predictions of the mean-field theory across a wide range of parameter values in all the scaling regimes. The value of the des Cloizeaux exponent,  $\theta_2 = 1/3$ , proposed by Dobrynin for sticky polymer solutions, is shown to lead to a collapse of simulation data for all the scaling relations considered here.

With increasing monomer concentration, associative polymer solutions undergo a transition from the sol to the gel phase with the appearance of an incipient system spanning network. Dobrynin has pointed out that within the framework of a mean-field lattice based theory for associative polymer solutions, it is not possible to identify the location of the sol-gel transition, since chains are not distinguished as belonging to the sol or the gel phase (Dobrynin, 2004). As a result, in order to describe the phase behaviour of associative polymer solutions within mean-field theory, Dobrynin (Dobrynin, 2004) assumes a modified form of the Flory-Stockmayer expression (Flory, 1953)(Stockmayer, 1944)

$$p_2 = \frac{1}{(1 - p_1)f - 1} \quad (4.1)$$

which relates the degree of inter-chain conversion  $p_2$  at the gelation threshold, to the number of stickers on a chain available for inter-chain association,  $(1 - p_1)f$ . In the original Flory-Stockmayer theory it is assumed that the fraction of intra-chain associations  $p_1$  is zero (which is expected to hold at high concentrations), leading to following well known simple relation

at the location of the sol-gel transition

$$p_2 = \frac{1}{f-1} \quad (4.2)$$

It should be noted that the Flory-Stockmayer theory assumes that the gel network is a treelike structure and prohibits the formation of loops (Rubinstein and Colby, 2003). Semenov and Rubinstein (Semenov and Rubinstein, 1998), on the other hand, show that Eq. (4.2) can be formally derived if one assumes that the sol-gel transition coincides with the monomer concentration at which the concentration of free chains in the system (i.e. those with no inter-chain associations) undergoes a maximum. In real polymer networks, one expects that the formation of loops is a common occurrence. In the formalism adopted in the present work, the formation of cyclic structures is not prohibited, and as a result, we are able to examine both the validity of Eq. (4.1), and the assumption of Semenov and Rubinstein (Semenov and Rubinstein, 1998) regarding the coincidence of the sol-gel transition with the free chain concentration maximum.

Interestingly, from an equilibrium statics point of view (as opposed to a rheological characterisation (Winter and Chambon, 1986)(Li and Aoki, 1997)(Li et al., 1997)), there does not appear to be a commonly agreed definition of the concentration at which the sol-gel transition occurs. Descriptions of gelation based on percolation models define the sol-gel transition as the concentration at which the first system spanning network appears (Rubinstein and Colby, 2003). Alternatively, the sol-gel transition is also identified as the concentration at which the probability distribution of chain cluster sizes becomes bimodal (Kumar and Panagiotopoulos, 1999). In this interpretation, it is expected that in the sol phase the probability of finding a cluster with  $m$  chains decreases monotonically with increasing  $m$ , while the appearance of a second peak in the probability distribution, at a non-zero value of  $m$ , signals the onset of gelation. It is not clear if the three definitions of the sol-gel transition, namely, the appearance of the system spanning network, the appearance of bi-modality in the chain cluster size probability distribution, or the occurrence of a maximum in the free-chain concentration, are all located at the same monomer concentration, and if the degree of inter-chain conversion  $p_2$  is related to the number of stickers on a chain available for inter-

chain association by Eq. (4.1), in all the three definitions. These questions are examined in the present work, and we show that while the three different definitions are located at different monomer concentrations, the dependence of  $p_2$  on  $p_1$  and  $f$  is given by Eq. (4.1) in all three cases, for sufficiently long chains.

The outline of this chapter is as follows. In Section 4.2, model for the associative polymer solutions implemented in the multi-particle Brownian dynamics algorithm is described. In Section 4.3, a brief summary of the predictions of scaling theories (Semenov and Rubinstein, 1998)(Dobrynin, 2004) for the degrees of intra-chain and inter-chain conversions as a function of system parameters, is given. These predictions provide a basis for identifying the quantities that need to be evaluated by simulations, and a framework for the interpretation of simulation results. Essentially, the theories identify three different regimes of scaling behaviour depending on the solvent quality of the backbone monomers, the monomer concentration and the density of stickers along the backbone. Section 4.4 discusses the choice of various simulation parameter values that enables the exploration of these different scaling regimes. Simulation predictions for the dependence of the degrees of conversion on spacer length and concentration, at constant temperature and sticker strength, are discussed in subsection 4.5.1, while subsection 4.5.2 first examines the influence of temperature and sticker strength, before combining the dependencies on all system parameters together in master plots. The cross-over in the scaling behaviour from one regime to the other is discussed in subsection 4.5.3. A comparison of the scaling of radius of gyration with concentration between homopolymer and sticky polymer solutions is carried out in subsection 4.5.4 and the behaviour of a sticky polymer solution in which the chains as a whole are under  $\theta$ -solvent conditions, is considered in subsection 4.5.5. In Section 4.6 we briefly discuss the role played by hydrodynamic interactions on the time scales for equilibration of different static properties. Section 4.7 considers the sol-gel transition and the various definitions that are used to find its location, and the validity of the modified Flory-Stockmayer expression at the gelation threshold (Eq. (4.1)) is examined. An interesting correlation observed between the breakdown of scaling predictions and the occurrence of phase separation is highlighted in Section 4.8. Finally, the key results of this chapter are summarised in the concluding section.

## 4.2 Model for associative polymer solutions

The sticky polymers have been modelled here as a linear sequence of  $N_b$  coarse-grained beads connected by  $N_b - 1$  entropic springs (Bird et al., 1987a), as described in Chapter 2. Each polymer is a multi-sticker chain with  $f$  equispaced stickers positioned along the backbone (except at the chain ends where there are no stickers) separated by  $\ell$  spacer (or backbone) monomers. A sticker is assumed to associate with only one other sticker (i.e. with functionality  $\varphi = 1$ ). In general, while the proposed methodology can support any value for  $\varphi$ , the specific choice of  $\varphi = 1$  is made here in order to compare simulation predictions with the analytical predictions of Semenov and Rubinstein (Semenov and Rubinstein, 1998) and Dobrynin Dobrynin (2004), where this constraint on sticker functionality has been chosen for the sake of simplicity. Note that once  $\ell$  and  $f$  are fixed, the number of beads in a chain can be calculated from,

$$N_b = (f + 1)\ell + f \quad (4.3)$$

An associative polymer solution is modelled as an ensemble of such bead-spring chains, immersed in an incompressible Newtonian solvent. A total of  $N_c$  chains are initially enclosed in a cubic and periodic cell of edge length  $L$ , giving a total of  $N = N_b \times N_c$  beads per cell at a bulk monomer concentration of  $c = N/V$ , where  $V = L^3$  is the volume of the simulation cell.

The bonded interactions between the beads are represented by a FENE spring force with FENE  $b$ -parameter,  $b = 50.0$ . The short-ranged backbone-backbone and backbone-sticker excluded volume interactions and the sticker-sticker associative interaction are modelled by the SDK potential, described in Section 2.5. In Chapter 3, we have examined the collapse transition of dilute sticky polymer solutions and found it convenient to use the SDK potential (Soddemann et al., 2001) as an alternative to the Lennard-Jones potential, to model the pair-wise interactions between both the backbone and sticker monomers. In this section, we briefly summarise some of the key results of Chapter 3 that are relevant to the present chapter. This is necessary because the predictions of the scaling theories of Semenov and Rubinstein (Semenov and Rubinstein, 1998) and Dobrynin Dobrynin (2004), with which we plan to compare the results of simulations, depend on which of three different scaling regimes

the sticky polymer solution belongs to.

For homopolymer solutions, we have shown in Chapter 3 that when the SDK potential is used in conjunction with Brownian dynamics simulations, the expected asymptotic scaling behaviour, in all regimes of solvent quality, is obtained with  $r_c = 1.82\sigma$  (for which  $\alpha = 1.5306333121$  and  $\beta = 1.213115524$ ). Since only backbone monomer-monomer interactions exist for homopolymers, the well-depth  $\epsilon$  is equal to  $\epsilon_{bb}$  for all bead pairs. In Chapter 3, it is shown, both from the scaling of the radius of gyration with chain length and from an estimation of the second virial coefficient, that  $\theta$ -solution conditions are reproduced for  $\epsilon_{bb} := \epsilon_\theta = 0.45$ . As a consequence, the choice  $\epsilon_{bb} < 0.45$  leads to good solvents, while  $\epsilon_{bb} > 0.45$  leads to poor solvents. In particular, by defining the solvent quality  $z = k_{\text{SDK}} \hat{\tau} \sqrt{N_b}$ , where the parameter  $\hat{\tau}$  is defined in terms of the potential well-depth by,

$$\hat{\tau} = \left(1 - \frac{\epsilon_{bb}}{\epsilon_\theta}\right) \quad (4.4)$$

we show that by an appropriate choice of the constant  $k_{\text{SDK}}$ , simulation predictions of the swelling ratio  $\alpha_g$ , which is the ratio of the radius of gyration  $R_g$  in a good solvent to that in a  $\theta$ -solvent, can be collapsed on to the universal swelling curve of  $\alpha_g$  versus  $z$  that describes the thermal crossover between  $\theta$  and good solvents (Schäfer, 1999). Note that  $\hat{\tau}$  corresponds physically to  $(1 - T_\theta/T)$ , so that in accordance with its definition in the experimental literature, (Schäfer, 1999)(Hayward and Graessley, 1999)(Pan et al., 2014b)(Pan et al., 2014a) the solvent quality  $z \sim (1 - T_\theta/T)\sqrt{M}$ , where  $T_\theta$  is the  $\theta$ -temperature, and  $M$  is the molecular weight.

As mentioned earlier, the introduction of stickers on chains alters the solvent quality of a polymer solution. In particular, we have shown in Chapter 3 that the well-depth of the SDK potential,  $\epsilon_{st}^\theta$ , at which  $\theta$ -solution conditions are observed in sticky polymer solutions is different from that for homopolymer solutions ( $\epsilon_\theta$ ), and that it depends on the backbone well-depth  $\epsilon_{bb}$  and spacer length  $\ell$ . A schematic representation of this dependence is shown in Fig. 3.9, where the two-dimensional surface corresponds to values of  $\epsilon_{st}^\theta(\ell, \epsilon_{bb})$  that separate good and poor solvent regions. Since  $\epsilon_{bb} < \epsilon_\theta < \epsilon_{st}$ , chain conformations are a result of a competition between backbone-backbone repulsion and sticker-sticker attraction. As

indicated in Fig. 3.9, the value of  $\epsilon_{st}^\theta$  keeps increasing: (i) as the backbone solvent quality gets better at a given value of  $\ell$ , and (ii) with increasing spacer length, at a given value of  $\epsilon_{bb}$ .

As will become evident in subsequent sections, the behaviour of dilute sticky polymer solutions summarised here is very helpful for estimating sticky chain parameters and the well-depths of the SDK potential that lead to simulation results in the precise scaling regimes defined in the theory of Dobrynin (Dobrynin, 2004), thereby enabling a direct comparison between them.

### 4.3 Scaling relations for fractions of associated stickers

The phase behaviour of physically associative polymer solutions has been described theoretically by a number of different analytical approaches (Rubinstein and Dobrynin, 1997)(Ishida and Tanaka, 1997)(Semenov and Rubinstein, 1998)(Dobrynin, 2004)(Tanaka, 2011)(Tanaka and Matsuyama, 1989)(Erukhimovich et al., 2001)(Ozaki and Koga, 2020). The majority of these studies only treat the presence of inter-chain associations and neglect the formation of intra-chain associations, which is a reasonable approximation at sufficiently high polymer concentrations. The theory developed by Dobrynin (Dobrynin, 2004), on the other hand, explicitly accounts for the presence of intra-chain associations as well. In the present work, since the simulations can predict both intra and inter-chain degrees of conversion, we compare our results with the predictions of Dobrynin’s theory. It should be noted, however, that the scaling predictions by Semenov and Rubinstein (Semenov and Rubinstein, 1998) are identical to those of Dobrynin (Dobrynin, 2004) for the fraction of stickers bonded by inter-chain associations.

An expression for the free energy of an associative polymer solution has been derived by Dobrynin (Dobrynin, 2004) with the help of a lattice based mean-field theory, combined with blob scaling arguments to describe polymer chain conformations in semidilute solutions. By minimising the free energy with respect to both intra and inter-chain degrees of conversion, equations for the dependence of the equilibrium degrees of conversion  $p_1$  and  $p_2$  on system parameters, such as  $T$ ,  $c$ ,  $\ell$ ,  $\epsilon_{st}$ , etc., are obtained. A brief discussion on the derivation of the

scaling relations is given in Appendix C. Though Dobrynin (Dobrynin, 2004) also estimates the phase diagram of associative polymer solutions in the temperature and concentration plane, we do not attempt to map out the entire phase diagram with simulations in the present work. In section 4.7, however, we briefly consider the relationship predicted by simulations between the monomer concentration,  $c$ , and the number of stickers,  $f$ , along the gelation line that separates the sol and gel phases, and compare with the prediction of scaling theory.

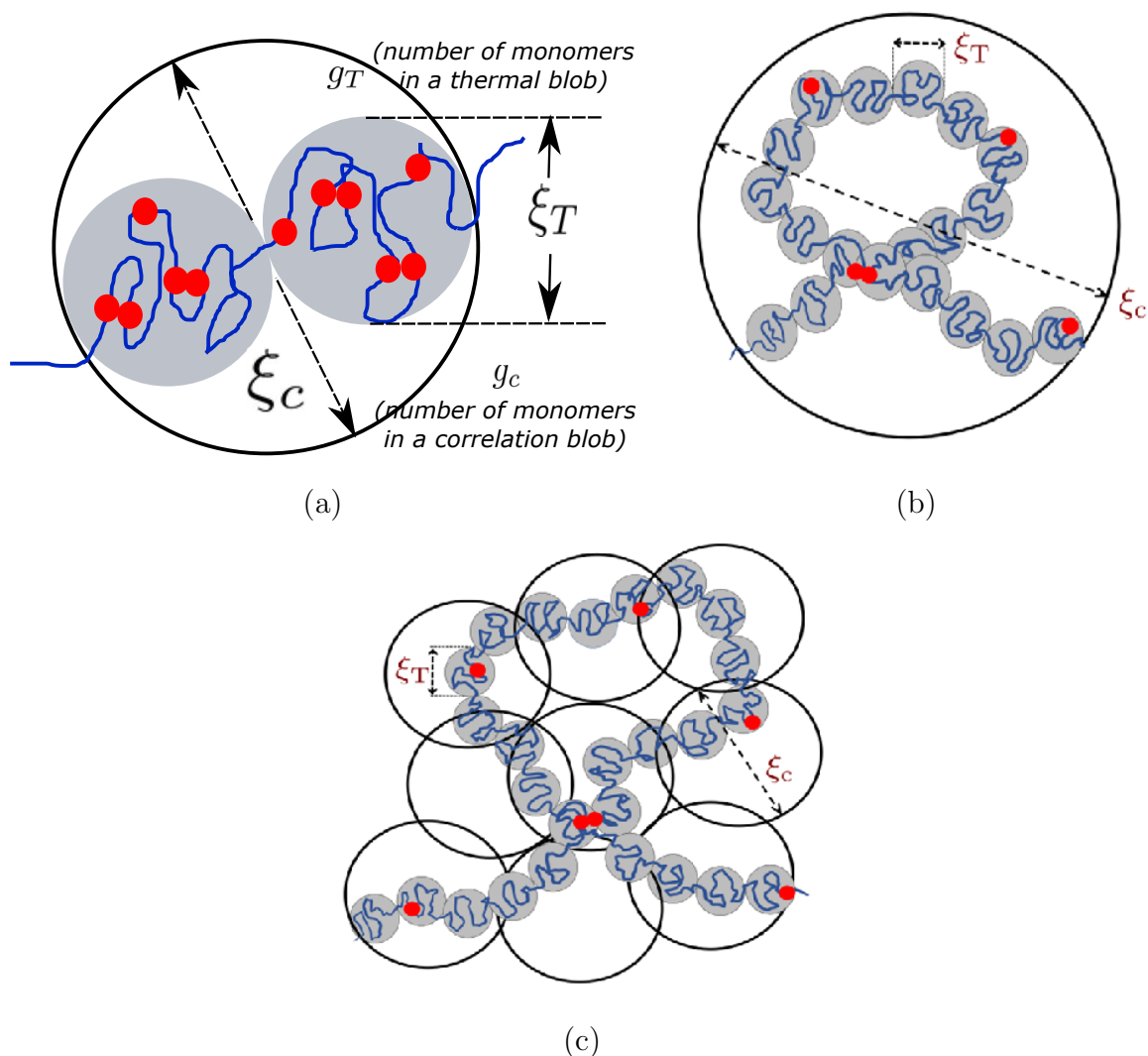


Figure 4.1: Three scaling regimes when the chain of backbone monomers is in a good solvent. Stickers are indicated by red circles. (a)  $l < g_T < g_c$  (Regime I), (b)  $g_T < l < g_c$  (Regime II) and (c)  $g_T < g_c < l$  (Regime III).

Dobrynin (Dobrynin, 2004) derives separate sets of relations for the fractions  $p_1$  and

$p_2$ , depending on the quality of the solvent with respect to the backbone monomers (i.e., whether they are in  $\theta$  or good solvents), and the number of monomers between two stickers ( $\ell$ ). In particular, when the chain of backbone monomers is under good solvent conditions, three separate regimes are identified that are best understood in terms of the schematic representation in Fig. 4.1, which is inspired by a similar figure in Ref. 24.

As is well known, semidilute polymer solutions that lie in the double crossover region of solvent quality and concentration can be described in terms of thermal and correlation blobs, which represent the dependence on solvent quality  $z$  and scaled concentration  $c/c^*$  (A.Jain et al., 2012)(Prakash, 2019). The size of a thermal blob is denoted by  $\xi_T$ , with  $g_T$  numbers of monomers in it, while the size of a correlation blob is denoted by  $\xi_c$ , with  $g_c$  numbers of monomers in it. The three regimes defined by Dobrynin (Dobrynin, 2004) depend on the relative magnitudes of  $\ell$ ,  $g_T$  and  $g_c$ , as indicated in Fig. 4.1.

A central element in Dobrynin's theory is the estimation of the probability of two stickers coming together to form a bond. Under  $\theta$ -solvent conditions this is straightforward to determine since a polymer chain obeys random walk statistics and the probability of contact between two monomers on a chain is proportional to the probability of loop formation between two ends of a Gaussian chain segment (Rubinstein and Colby, 2003)(Dobrynin, 2004). For a segment of chain with  $\ell$  monomers between stickers, this implies that the probability of sticker contact is  $p_\theta(\ell) \sim \ell^{-3/2}$ . The situation is more complicated in a good solvent, and depends on which of the three regimes in Fig. 4.1 is relevant. In Regime I (Fig. 4.1 (a)), since there are many stickers in a thermal blob, and a chain segment within a thermal blob obeys random walk statistics, the sticker association probability is governed by the same physics as for a chain under  $\theta$ -solvent conditions. On the other hand, in Regime II (Fig. 4.1 (b)), the calculation of the probability that two stickers come into contact involves two steps. First two thermal blobs must come into contact, followed by two stickers within these thermal blobs coming together to form a bond. Since thermal blobs follow self-avoiding walk statistics, their probability of contact is equivalent to the probability that two internal monomers of a chain in a good solvent come into contact. This problem was first solved using renormalisation group methods by des Cloizeaux (des Cloizeaux, 1980), who derived the following expression for the probability of contact between two internal monomers on a self-avoiding

walk chain,

$$p_{\text{good}} \sim \left[ \frac{\delta}{r(n)} \right]^{3+\theta_2} \quad (4.5)$$

where  $\delta$  is the spatial distance between the two monomers,  $r(n)$  is the root mean squared end-to-end distance between the two monomers, which are considered to be separated by  $n$  monomers along the chain backbone, and  $\theta_2$  is a geometrical exponent, the so-called des Cloizeaux exponent (Redner, 1980)(Witten and Prentis, 1982)(Duplantier, 1989)(Hsu et al., 2004). The numerical value of  $\theta_2$  will be discussed shortly below. Once the thermal blobs are in contact, the probability that two stickers within them come into contact is estimated using the same expression as for two monomers on a segment of a chain under  $\theta$ -solvent conditions. Using similar arguments, Dobrynin (Dobrynin, 2004) also derives the probability of two stickers coming into contact when the good solvent conditions for the chain backbone correspond to those represented by Regime III.

With this background, the relevant relations for the degrees of intra and inter-chain conversion derived by Dobrynin (2004) are displayed in Table 4.1. Note that  $p = p_1 + p_2$  is the total fraction of associated stickers. Table 4.1 (a) displays the most general form of the relations when the backbone monomers are under good solvent conditions, for the three different scaling regimes that have been identified in Fig. 4.1. The relations are in terms of  $\ell$ ,  $g_T$ ,  $g_c$ , and  $g_{ss}$ . The function  $g_{ss}$  is assumed to depend exponentially on an *effective* associating energy  $\tilde{\epsilon}_a$ , which is a combination of the interaction energy between stickers,  $\epsilon_{st}$ , and the Flory-Huggins interaction energy between monomer and solvent molecules on adjacent lattice sites,  $\epsilon_{ps}$ . In the context of scaling theory, where the solvent is treated explicitly, the magnitude of  $g_{ss}$  can be chosen independently from  $\ell$ . When the spacer segment length  $\ell$  is changed while keeping  $\epsilon_{st}$  fixed, it is possible to control the influence of  $g_{ss}$  on chain statistics independently by appropriately tuning  $\epsilon_{ps}$ . The situation is more subtle in the model adopted in the present work, since the solvent is treated implicitly rather than explicitly. It is not possible to keep  $\epsilon_{st}$  and  $\epsilon_{bb}$  fixed, and vary only  $\ell$  without also simultaneously influencing chain statistics, since as exemplified by the schematic representation in Fig. 1, the effective interaction energy between stickers, which determines the conformations of polymer chains in a sticky polymer solution, is a complex function of  $\epsilon_{st}$ ,  $\epsilon_{bb}$ , and  $\ell$ . As a

(a)	$\frac{p_1(1-p_1/2)}{(1-p)^2}$	$\frac{p_2}{(1-p)^2}$	$\frac{p_1(1-p_1/2)}{p_2}$
Regime I	$g_{ss} \ell^{-3/2}$	$g_{ss} \ell^{-1} g_T^{-1/2} (g_T/g_c)^{\nu(3+\theta_2)-1}$	$g_T^{1/2} \ell^{-1/2} (g_c/g_T)^{\nu(3+\theta_2)-1}$
Regime II	$g_{ss} \ell^{-3/2} (g_T/\ell)^{\nu(3+\theta_2)-\frac{3}{2}}$	$g_{ss} \ell^{-1} g_T^{-1/2} (g_T/g_c)^{\nu(3+\theta_2)-1}$	$(g_c/\ell)^{\nu(3+\theta_2)-1}$
Regime III	$g_{ss} \ell^{-3/2} (g_T/g_c)^{\nu(3+\theta_2)-\frac{3}{2}}$	$g_{ss} \ell^{-1} g_T^{-1/2} (g_T/g_c)^{\nu(3+\theta_2)-1}$	$(g_c/\ell)^{1/2}$

$$\nu = \frac{3}{5}; \quad \theta_2 = \frac{1}{3}; \quad g_T = \hat{\tau}^{-2}; \quad g_c = \hat{\tau}^{-\frac{6\nu-3}{3\nu-1}} c^{-\frac{1}{3\nu-1}} = \hat{\tau}^{-\frac{3}{4}} c^{-\frac{5}{4}}$$

(b)	$\frac{p_1(1-p_1/2)}{(1-p)^2}$	$\frac{p_2}{(1-p)^2}$	$\frac{p_1(1-p_1/2)}{p_2}$
$\theta$ -solvent	$g_{ss} \ell^{-3/2}$	$g_{ss} \ell^{-1} c$	$\ell^{-1/2} c^{-1}$
Regime I	$g_{ss} \ell^{-3/2}$	$g_{ss} \hat{\tau}^{-1/4} \ell^{-1} c^{5/4}$	$\hat{\tau}^{1/4} \ell^{-1/2} c^{-5/4}$
Regime II	$g_{ss} \hat{\tau}^{-1} \ell^{-2}$	$g_{ss} \hat{\tau}^{-1/4} \ell^{-1} c^{5/4}$	$\hat{\tau}^{3/4} \ell^{-1} c^{-5/4}$
Regime III	$g_{ss} \hat{\tau}^{-5/8} \ell^{-3/2} c^{5/8}$	$g_{ss} \hat{\tau}^{-1/4} \ell^{-1} c^{5/4}$	$\hat{\tau}^{-3/8} \ell^{-1/2} c^{-5/8}$

Table 4.1: Relations for the intra-chain and inter-chain association fractions, predicted by Dobrynin (Dobrynin, 2004). Table (a) corresponds to the three scaling regimes that arise when the backbone monomers are under good solvent conditions. The expressions are in terms of the spacer length  $\ell$ , the number of monomers in a thermal blob  $g_T$ , the number of monomers in a correlation blob  $g_c$ , and the function  $g_{ss}$ , which depends on the *effective* sticker strength. Note that  $p = p_1 + p_2$  is the total fraction of associated stickers. Table (b) gives the corresponding relations for the case when the backbone monomers are under  $\theta$ -solvent conditions, along with the simplified forms of the relations for good solvents when  $g_T$  and  $g_c$  are expanded in terms of the backbone solvent quality parameter  $\hat{\tau}$ , the monomer concentration  $c$ , and the specific choices  $\nu = 3/5$  and  $\theta_2 = 1/3$  are made.

consequence, the function  $g_{ss}$  depends on all three of these variables, and in general cannot be varied independently of spacer length  $\ell$ . The nature of this dependence is discussed in more detail in section V B. Table 4.1 (b) gives the simplified form of the equations for good solvent conditions that are used in the current work, along with the corresponding relations for the case when the backbone monomers are under  $\theta$ -solvent conditions. Before discussing the derivation of these simplified relations, however, it is worth making a few remarks about the des Cloizeaux exponent  $\theta_2$ .

The value  $\theta_2 = 0.71$  was derived by des Cloizeaux (des Cloizeaux, 1980) approximately using renormalised field theory. Subsequently, it was shown by Witten (Witten and Prentis, 1982) and Duplantier (Duplantier, 1989) that  $\theta_2$  could be related analytically to critical

exponents that characterise star polymers. The critical exponents for star polymers with up to 80 arms have been obtained extremely accurately by Hsu et al. (Hsu et al., 2004), using Monte Carlo simulations with the PERM algorithm. Based on the expression connecting  $\theta_2$  to the critical exponents of stars derived by Duplantier (Duplantier, 1989), and using the values computed for these exponents by Hsu et al. (Hsu et al., 2004), one can determine that  $\theta_2 = 0.8142(17)$ . This is probably the most refined value of the des Cloizeaux exponent that has been estimated to date. In addition to reporting the value for the exponent  $\theta_2$  derived by des Cloizeaux (des Cloizeaux, 1980), Dobrynin (Dobrynin, 2004) also estimates a value for  $\theta_2$  using an alternative argument. Essentially, by equating the probability of binary contact between monomers within a correlation blob (in the context of the mean field theory) to the contact probability given by Eq. (4.5), Dobrynin (Dobrynin, 2004) obtains  $\theta_2 = 1/3$ , which is considerably different from the value of the des Cloizeaux exponent derived from combining analytical arguments with Monte Carlo simulations. However, the latter value has been obtained for a self-avoiding walk chain in the dilute limit. The value of  $\theta_2$  in the context of associative polymer solutions at finite concentrations, where both Flory screening and attractive interactions between stickers is present, is currently unknown. We will show subsequently that using  $\theta_2 = 1/3$  leads to excellent collapse of simulation data under a wide range of conditions.

The simplified form of Dobrynin's relations can be obtained by expanding  $g_T$  and  $g_c$  in terms of the backbone solvent quality parameter  $\hat{\tau}$ , and the monomer concentration  $c$ . Within the blob scaling ansatz, for a semidilute solution in the double crossover region, the number of thermal blobs  $\mathcal{N}_T$ , and the number of correlation blobs  $\mathcal{N}_c$  on a chain, are determined solely by the solvent quality  $z$ , and the scaled concentration  $c/c^*$ , respectively (A.Jain et al., 2012)

$$\begin{aligned}\mathcal{N}_T &= z^2 \\ \mathcal{N}_c &= \left(\frac{c}{c^*}\right)^{\frac{1}{3\nu-1}}\end{aligned}\tag{4.6}$$

where  $\nu$  is the Flory exponent, and the overlap concentration  $c^*$  is defined by,

$$c^* = \frac{N_b}{(4\pi/3)R_{g0}^3}\tag{4.7}$$

Here,  $R_{g0} := \sqrt{\langle R_{g0}^2 \rangle}$  is the radius of gyration of a homopolymer chain of backbone monomers in the dilute limit. It follows that,

$$\begin{aligned} g_T &= \frac{N_b}{\mathcal{N}_T} \sim \hat{\tau}^{-2} \\ g_c &= \frac{N_b}{\mathcal{N}_c} = N_b \left( \frac{c}{c^*} \right)^{-\frac{1}{3\nu-1}} \end{aligned} \quad (4.8)$$

In a good solvent, since a homopolymer is a self-avoiding walk of thermal blobs,  $R_{g0} = \xi_T (N_b/g_T)^\nu$ , where  $\xi_T = bg_T^{1/2}$ , and  $b$  is the size of a monomer. It follows that,  $c^* \sim N_b^{1-3\nu} g_T^{3\nu-3/2}$ , and from Eq. (4.8),

$$g_c = \hat{\tau}^{-\frac{6\nu-3}{3\nu-1}} c^{-\frac{1}{3\nu-1}} \quad (4.9)$$

Substituting for  $g_T$  and  $g_c$  from Eqs. (4.8) and (4.9) into the general scaling relations in Table 4.1 (a), and setting  $\nu = 3/5$  and  $\theta_2 = 1/3$ , leads to the expressions displayed in Table 4.1 (b). The choice of simulation parameters that enable the validation of these scaling predictions, and the details of the simulation algorithm are discussed in the next section.

## 4.4 Choice of parameters and details of simulations

In order to establish the validity of scaling laws, one would ideally vary independent variables such as the concentration and temperature, and parameters such as the number of stickers, spacer length and so on, over a very wide range of values so as to capture not only the asymptotic regimes, but also the crossover behaviour from one regime to another. In the present instance, this goal is constrained due to several factors. Firstly, the different scaling regimes are not obtained by varying the magnitude of a single variable. This is unlike, for instance, in the case of homopolymer solutions where one can go from the dilute to the concentrated entangled regime via the semidilute unentangled, semidilute entangled and concentrated unentangled regimes, by just varying the concentration (Rubinstein and Colby, 2003). Secondly, the need to remain in the good solvent regime of the sticky polymer

solution (i.e., below the  $\theta$ -surface shown schematically in Fig. 3.9) in order to avoid phase separation imposes constraints on the choice of parameter values. Finally, the use of the Brownian dynamics simulations methodology, which has the advantage of accurately predicting dynamic properties due to the incorporation of hydrodynamic interactions, makes the computations very intensive (even in the absence of HI). Each of these points are discussed in greater detail in section 4.4.1 below, while the particulars of the current algorithm are given in sections 4.4.2 and 4.4.3.

### 4.4.1 Simulation constraints

In Dobrynin's scaling theory (Dobrynin, 2004), the different scaling regimes depend on the relative magnitudes of the spacer length  $\ell$ , the number of monomers in a thermal blob  $g_T$ , and the number of monomers in a correlation blob  $g_c$  (as shown schematically in Fig. 4.1). As a result, in order to traverse from Regime I ( $\ell < g_T < g_c$ ) to Regime II ( $g_T < \ell < g_c$ ) it is necessary to change either  $\ell$  or the solvent quality parameter  $\hat{\tau}$  (which affects  $g_T$ ). Changing the concentration (which would change  $g_c$ ) would have no effect, provided both  $g_T$  and  $\ell$  were maintained less than  $g_c$ . On the other hand, in order to traverse from Regime II ( $g_T < \ell < g_c$ ) to Regime III ( $g_T < g_c < \ell$ ), one can either change  $\ell$  or the concentration  $c$ . Changing  $\hat{\tau}$  would have no effect provided  $g_T$  was always maintained the smallest of the three magnitudes. Note that Dobrynin's scaling theory does not consider the case where  $g_c < g_T$ , which would occur for concentrations  $c > c^{**}$ , where  $c^{**}$  represents the concentration at which  $\xi_c = \xi_T$ . These considerations imply that it is not possible to move all the way from Regime I to Regime III through the change of a single variable, such as the concentration.

Since  $\hat{\tau}$  is given by Eq. (4.4), the values of  $\hat{\tau}$  are in the range,  $0 \leq \hat{\tau} \leq 1$ , for  $0 \leq \epsilon_{bb} \leq \epsilon_\theta$  (which follows from the requirement that the backbone monomers must be in a good solvent), and consequently,  $1 \leq g_T \leq \infty$  (setting all unknown pre-factors equal to 1). Since the values of concentration are in the range  $0 \leq c/c^* \leq c^{**}/c^*$ , we have,  $N_b (c^{**}/c^*)^{-\frac{1}{3\nu-1}} \leq g_c \leq \infty$ . The lower bound is always satisfied provided  $g_T < g_c$ . While conceptually, both  $g_c$  and  $g_T$  can be greater than  $N_b$ , the spacer length  $\ell$ , which is an input parameter in the simulations, must satisfy,  $1 \leq \ell \leq N_b$ . Since there must be at least one or more thermal blobs in a chain for good solvent conditions,  $g_T$  must be less than  $N_b$  in Regime I. For this reason, and

in order to satisfy the constraint with regard to  $\ell$ ,  $g_T$  must be less than  $N_b$  in Regimes II and III, while  $g_c$  cannot be greater than  $N_b$  in Regime III.

With this background, we can now consider the constraints that exist in each of the regimes with respect to the choice of parameters. Consider Regime I, where  $\ell < g_T < g_c$ . Since a reasonable length of spacer segment must be chosen to enter the scaling regime, the value of  $\ell$  cannot be too small. The value of  $g_T$  increases rapidly from 1 as  $\epsilon_{bb}$  increases from 0 to  $\epsilon_\theta$  (since  $g_T = [1 - (\epsilon_{bb}/\epsilon_\theta)]^{-2}$ ). While it is consequently not difficult to achieve  $g_T > \ell$ , its value cannot be too large, since the need to maintain  $N_b \geq g_T$  would lead to excessive computational cost from simulating long chains (as discussed in greater detail below). The requirement that the scaled concentration  $c/c^*$  must be such that  $g_c > g_T$ , connects the range of variation of  $c/c^*$  to the choice of  $\epsilon_{bb}$ . As can be seen from Eq. (4.8), a large value of  $c/c^*$  implies choosing a large value of  $N_b$  in order to satisfy the constraint on  $g_c$ . Clearly, for a given chain length  $N_b$ , there is a limit to how closely  $\epsilon_{bb}$  can approach  $\epsilon_\theta$  (since  $g_T \leq N_b$ ), and also an upper bound on the choice of  $c/c^*$  (since  $g_c > g_T$ ).

The value of  $\epsilon_{bb}$  also affects the choice of sticker strength  $\epsilon_{st}$ . It is clear from Fig. 3.9 that for a given value of  $\ell$ , the value of  $\epsilon_{st}^\theta$  decreases with increasing  $\epsilon_{bb}$ . As will be seen later, in order to avoid phase separation with increasing concentration, it is necessary for  $\epsilon_\theta < \epsilon_{st} < \epsilon_{st}^\theta$ , which corresponds to good solvent conditions for the sticky polymer solution as a whole. At the same time, it is necessary to sufficiently separate the values of  $\epsilon_{bb}$  and  $\epsilon_{st}$  in order to achieve a reasonable frequency and duration of association between stickers, and to distinguish between sticky and homopolymer solutions.

Of the three scaling regimes, it is relatively easiest to simulate Regime II ( $g_T < \ell < g_c$ ), since  $g_T$  can be chosen to have a small value by choosing  $\epsilon_{bb}$  close to zero. This also leads to a fairly wide range of permissible values for  $c/c^*$ . Nevertheless, for large values of  $\ell$ , maintaining  $g_c > \ell$  would require larger and larger values of  $N_b$  for increasing values of  $c/c^*$  (as can be seen from Eq. (4.8)), leading to excessive computational cost.

The smallest value of the scaled concentration permissible in Regime III is  $c/c^* = 1$ . This is because, for this value (from Eq. (4.8))  $g_c = N_b$ , and Regime III requires that  $g_c < \ell (\leq N_b)$ . As discussed above, it is straightforward to achieve a small value of  $g_T$  by choosing  $\epsilon_{bb}$  close to zero. However, both the requirements that  $c/c^* \geq 1$  and  $\ell > g_c$ , lead

to significant computational costs since they imply an increase in the number of monomers in a simulation cell, associated with an increase in the number of chains in a box, and large values of  $N_b$ , respectively.

It is clear from the discussion above that for given values of  $\epsilon_{st}$  and  $N_b$ , simulations in any one of the three different scaling regimes can be carried out by appropriately choosing the values of  $\ell$ ,  $\epsilon_{bb}$  and  $c/c^*$ . The range of values of these parameters that can be explored is, however, very dependent on the chain length  $N_b$ . Provided that large enough values of  $N_b$  are used, it would in principle be possible to thoroughly examine both the asymptotic scaling behaviour in all the different regimes, and the crossover between them. The computational intensity of the current Brownian dynamics algorithm, however, places quite stringent restrictions on the range of values that can be explored. The majority of the results reported here have been carried out on Australia's peak research supercomputer based at the National Computational Infrastructure. Details of the machine, and the computational cost estimates for simulating chains of various lengths  $N_b$ , spacer lengths  $\ell$ , and concentrations  $c/c^*$  have been given in Appendix E. It suffices here to say that while  $N_b = 34$ ,  $\ell = 6$ ,  $c/c^* = 2.0$  requires roughly 3 hours of CPU time,  $N_b = 79$ ,  $\ell = 15$ ,  $c/c^* = 6.5$  requires around 3 days and 9 hours of CPU time for obtaining data at these individual concentrations, from a typical simulation. This computational intensity has implied that we have only been able to explore a limited range of parameter values. Nevertheless, as will be seen from the results presented below, the simulations are adequate to reach clear conclusions regarding the validity of the scaling predictions in the different regimes, and to tease out some aspects of the crossover behaviour. It is hoped that future improvements in the BD algorithm will enable a more complete examination of the predictions of the scaling theory.

Table 4.2 summarises all the values of parameters (with  $g_T$  and  $g_c$  rounded to the nearest integer) used in the current simulations in order to explore the different scaling regimes.

#### 4.4.2 Simulation details

The protocol described below is followed with regard to the selection of parameter values listed in Table 4.2. For any choice of values of  $N_b$  and  $\epsilon_{bb}$ , single chain simulations are carried out to determine  $R_{g0}$  and the end-to-end vector  $R_{e0}$ . Note that the finite extensibility

parameter is set to  $Q_0 = \sqrt{50}$  in all the simulations reported here. The size of the simulation box is then fixed at  $L = 2R_{e0}$  to ensure that chains do not overlap with themselves in the periodic cell. Once  $L$  is determined, the monomer concentration  $c$  (and consequently  $g_c$ ) can be adjusted by choosing the number of chains  $N_c$  in a simulation cell, since  $c = (N_c \times N_b)/L^3$ . The scaled concentration  $c/c^*$  (with  $c^*$  defined in Eq. (4.7)) can also then be estimated. Finally, the choice of the number of stickers  $f$  per chain determines the number of spacer monomers  $\ell$  between stickers. In this manner, the relative magnitudes of  $\ell$ ,  $g_T$  and  $g_c$  can be varied to probe each of the three scaling regimes that arise when the backbone monomers are under good solvent conditions. In the case when the backbone monomers are under  $\theta$ -solvent conditions, two different procedures are followed here. In the first, we set  $\epsilon_{bb} = \epsilon_\theta = 0.45$  in the SDK potential to reproduce  $\theta$  conditions for the backbone, and in the second, we neglect excluded volume (EV) interactions altogether, i.e., we simulate ghost chains that can cross themselves and each other.

Once the parameter choices are made, a typical simulation consists of a pre-equilibration run of about 3 to 4 Rouse relaxation times for a system of chains with only backbone monomers and no stickers, followed by the introduction of stickers and an equilibration run of about 5 to 8 Rouse relaxation times. Finally, sampling is carried out over a production run of about 5 Rouse relaxation times. Time averages, from each independent trajectory, are calculated during the production run, from a set of data collected at intervals of 1000 to 5000 non-dimensional time steps between sampling points. Ensemble averages and error of mean estimates of different equilibrium properties are then computed over a collection of such independent time averages, evaluated from 64 to 128 independent trajectories. All simulations without HI have been carried out with a non-dimensional time-step  $\Delta t = 0.001$ . In the absence of hydrodynamic interactions, the CPU time for the BD algorithm used here to determine all the static properties, scales linearly with system size  $N$ , for a fixed simulation box size  $L$ . It should be noted, however, that when the box size is increased, for instance to accommodate chains with a larger number of beads  $N_b$ , there is a large change in the pre-factor for the calculation of CPU time, due to various changes in bookkeeping, such as neighbour lists and so on.

	$(N_b, \ell, f)$	$\epsilon_{bb}$	$\epsilon_{st}$	$g_T$	$c/c^*$	$g_c$
$\theta$	(24, 4, 4)	No EV	5.0	–	0.1 – 1.6	–
	(34, 4, 6)	No EV	5.0	–	0.1 – 0.5	–
	(34, 6, 4)	No EV	2.5	–	0.1 – 0.6	–
	(29, 4, 5)	0.45	5.0	–	0.2 – 0.8	–
	(34, 4, 6)	0.45	5.0	–	0.2 – 1.2	–
	(34, 6, 4)	0.45	2.5	–	0.1 – 0.6	–
Regime I ( $\ell < g_T < g_c$ )	(29, 4, 5)	0.3	2.5	9	0.7 – 2.0	45 – 12
	(34, 4, 6)	0.3	2.5	9	0.8 – 1.6	45 – 19
	(34, 6, 4)	0.3	2.0	9	0.8 – 1.6	45 – 19
	(34, 6, 4)	0.35	2.5	20	1.0 – 1.5	34 – 20
Regime II ( $g_T < \ell < g_c$ )	(24, 4, 4)	0.0	5.0	1		57 – 11
	(29, 5, 4)	0.0	5.0	1		69 – 13
	(34, 4, 6)	0.0	5.0	1		
	(34, 6, 4)	0.0	5.0	1	0.5 – 1.9	81 – 15
	(34, 6, 4)	0.0	4.0	1		
	(39, 4, 7)	0.0	5.0	1		93 – 17
	(44, 4, 8)	0.0	5.0	1		105 – 20
(64, 12, 4)	0.0	5.0	1		152 – 29	
Regime III ( $g_T < g_c < \ell$ )	(64, 12, 4)	0.0	5.0	1	4.0 – 6.5	11 – 6
	(79, 15, 4)					14 – 8
Sticky $\theta$ chain	(34, 6, 4)	0.35	3.6	20	0.2 – 6.0	254 – 4

Table 4.2: Parameter sets used to simulate the different scaling regimes of associative polymer solutions that arise when the backbone monomers are under  $\theta$  and good solvent conditions, and when the sticky chain as a whole is under  $\theta$  solvent conditions. Note that  $g_T$  must be less than  $N_b$  in Regime I in order for the chain to be under good solvent conditions. It must also satisfy the constraint  $g_T < \ell < N_b$  in Regimes II and III. On the other hand it is possible for  $g_c > N_b$  in Regimes I and II, but must satisfy  $g_c < \ell < N_b$  in Regime III.

### 4.4.3 Computation of clusters

The estimation of the fraction of associated intra and inter-chain stickers (required for the validation of scaling relations), and the enumeration of the number of chains in a cluster (required for the identification of the gelation transition), are both carried out here with the help of the cluster computation algorithm proposed by Sevick et al. (Sevick et al., 1988) A brief description of the application of the algorithm in the context of sticky polymer solutions is given here.

To compute the intra-chain and inter-chain associations between stickers, a connectivity matrix for sticky beads is constructed such that, for any pair of stickers  $i$  and  $j$ , the corresponding element in the connectivity matrix has a value equal to 1 for direct contact

( $r_{ij} \leq r_c$ ) and 0 otherwise. Clearly, in general, there can also be stickers which are not in direct contact but still belong to the same cluster through indirect contacts. The Sevick et al. (Sevick et al., 1988) algorithm also takes this into account and generates a reduced connectivity matrix, where each linearly independent column of the matrix represents a cluster of stickers which are either in direct or indirect contact. The total number of such independent columns gives the number of clusters in the system. In the simulations carried out here, however, there are no indirect contacts between stickers since they always associate in pairs (the functionality of stickers has been chosen to be one). All the necessary information regarding the state of intra-chain or inter-chain association, of every sticker in the system, is recovered by appropriately labelling the non-zero elements in each independent column of the reduced connectivity matrix.

A similar connectivity matrix is also constructed for entire chains to determine whether they are either directly or indirectly connected to other chains via at least one sticky bead. Note that in this case there can be indirect contacts between chains, since there is typically more than one sticker per chain. The information on the number of chains in a cluster, or the spatial span of a cluster of chains, can be obtained from the columns of the chain connectivity matrix.

## 4.5 Validation of scaling relations for degrees of conversion

It is clear from the values given in Table 4.2 for the various simulation parameters used in the results reported here, that a more extensive variation of parameters has been carried out in Regime II compared to the other regimes. As discussed above, this is essentially because of the relative ease of simulating Regime II, both due to the physics of sticky polymer solutions, and due to the constraints of the current computational algorithm. All the same, as will be clear from the results in this section, the simulations that have been carried out in Regimes I and III are still sufficient to establish the validity of the scaling relations in these regimes.

The scaling relations summarised in Table 4.1 are examined here in two steps. We first

consider the dependence of the degrees of intra and inter-chain conversion on the length of the spacer segment between stickers,  $\ell$ , and the monomer concentration  $c$  in Section 4.5.1, followed by an examination of their dependence on the solvent quality parameter,  $\hat{\tau}$ , and the function of the effective sticker strength,  $g_{ss}$  in Section 4.5.2. The crossover behaviour from Regime I to Regime II, and from Regime II to Regime III is examined in Section 4.5.3. The difference in the scaling of the radius of gyration with concentration between homopolymers and sticky polymers is discussed in Section 4.5.4. Finally, the special situation where the sticky polymer chain as a whole is under  $\theta$ -solvent conditions is examined in Section 4.5.5. The data presented in this section for the dependence of  $R_g$ ,  $p_1$  and  $p_2$  on the various parameters  $\{N_b, \ell, f, \epsilon_{bb}, \epsilon_{st}, c, c/c^*\}$ , in the form of figures, is also given in tabular form in the Appendix F, so that they are readily available for comparison with any model predictions that may be made in the future.

### 4.5.1 Dependence on spacer length and monomer concentration

The dependence of  $p_1$  and  $p_2$  on  $\ell$  and  $c$  is considered in this section, while keeping  $\hat{\tau}$  and sticker strength  $\epsilon_{st}$  constant, in each of the different scaling regimes. We first consider the case where the backbone monomers are under Regime I conditions, followed by a consideration of Regimes II and III. The case of  $\theta$ -solvent conditions for the backbone is examined simultaneously with Regime II.

#### Regime I

The validity of scaling predictions for Regime I, as given in the first row of Table 4.1 (b) with  $\ell < g_T < g_c$ , with  $\hat{\tau}$  and sticker strength  $\epsilon_{st}$  held constant, are shown in Figs. 4.2. It should be noted that in order to express the ratio involving intra-chain and inter-chain associations only as a function of concentration,  $c$ , the spacer length ( $\ell$ ) dependence has been absorbed into the  $y$ -axis. According to the prediction of scaling theory in Regime I, the ratio  $[p_1(1 - p_1/2)/(1 - p^2)] \ell^{3/2}$  is expected to be independent of monomer concentration  $c$ . On the other hand, Figure 4.2 (a) appears to suggest a weak dependence of this ratio on concentration. It should be noted that while the fraction of intra-chain associated stickers  $p_1$

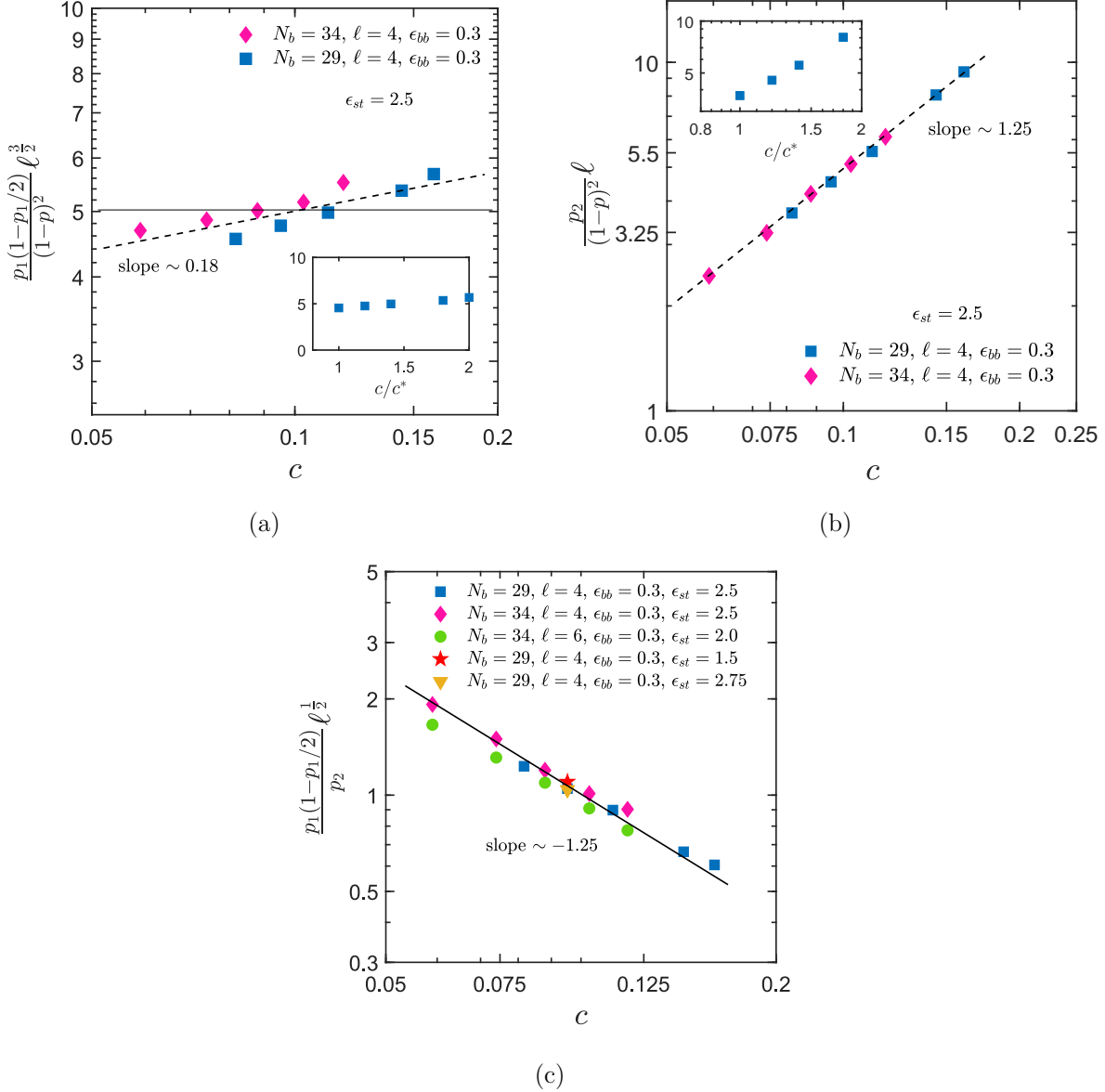


Figure 4.2: The dependence of ratios involving (a) intra-chain (b) inter-chain degrees of conversion, and (c) the ratio of intra-chain and inter-chain association fractions, on the monomer concentration,  $c$ , with the chain backbone under Regime I ( $\ell < g_T < g_c$ ) conditions. The spacer length dependence is absorbed in the  $y$ -axis. Simulations are carried out at constant solvent quality parameter  $\hat{\tau}$ , and a constant stiker strength  $\epsilon_{st}$ , except in (c) where two different values of  $\epsilon_{st}$  have been considered. The values  $\nu = 3/5$  and  $\theta_2 = 1/3$  have been used (see Table 4.1). The dashed and the solid lines are drawn with slopes equal to the prediction by scaling theory, while symbols represent simulation data.

decreases with increasing concentration, the total fraction of associated stickers  $p$  increases with increasing concentration due to the dominant role played by the increase in the fraction of inter-chain associated stickers  $p_2$  with increasing concentration. The reason for such an increase in the total fraction is because of the availability of more stickers with the increase in concentration. It should be noted that the stickers have limited functionality ( $= 1$ ), which hinders the formation of association if the stickers are already bounded. But with increase in concentration the number of free stickers available for bond formation simply increases. On the other hand, opportunity for the formation of inter-chain bonds is more than that of intra-chain associations as the number of chains per unit volume increases with increase in concentration. Whereas, the number of intra-chain bonds is always limited to the number of stickers in a chain, which is independent of concentration. This explains why the inter-chain association dominates with increase in concentration. An illustration of this phenomenon is provided in Figure 4.3 by plotting the intra-chain and inter-chain conversion fractions as a function of scaled concentration,  $c/c^*$ , for Regime I. Similar trends are also observed in Regime II and III and the  $\theta$ -condition as discussed in the subsequent sections. Such a behaviour might be responsible for the observed weak dependence, but simulations for larger chain lengths would be needed to confirm that it is not a result of finite size effects. According to scaling theory, the ratio  $[p_2/(1 - p^2)] \ell$  increases with concentration in this regime with an exponent of 1.25 (when  $\theta_2$  is chosen to be  $1/3$ ), which is validated by the simulation results displayed in Fig. 4.2 (b). Finally, as can be seen in Fig. 4.2 (c), the ratio of these conversions,  $[p_1(1 - p_1/2)/p_2] \ell^{1/2}$ , also largely follows the predicted dependence on concentration. This can be expected given the weak dependence of the ratio involving  $p_1$  on concentration, and the dominant role played by the ratio involving  $p_2$ . Apart from the overall agreement between the predictions and simulation results, there are a few other observations worth noting.

In Regime I, only the ratio involving  $p_2$  depends on the des Cloizeaux exponent  $\theta_2$ , as reflected in its dependence on the monomer concentration  $c$  (see first row in Table 4.1 (a)). It is striking to observe that the choice of value of  $\theta_2 = 1/3$ , derived by Dobrynin (Dobrynin, 2004), leads to a collapse of data for all the simulation parameters examined in Figs. 4.2 (b). This observation is more rigorously illustrated in the scaling behaviour for Regime II which

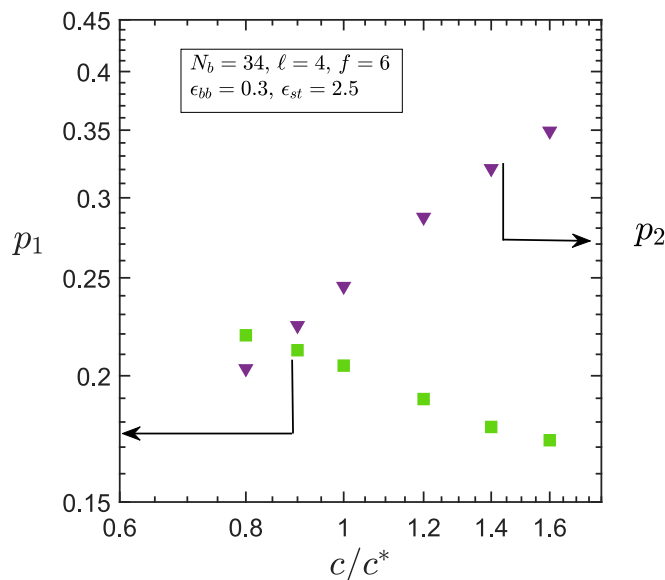


Figure 4.3: Variation of intra-chain ( $p_1$ ) and inter-chain ( $p_2$ ) association fractions as a function of scaled monomer concentration,  $c/c^*$ , for a sticky polymer solution in Regime I.

is investigated for a wider range of parameters.

Even though the spacer length  $\ell$  has been absorbed into the  $y$ -axis for consistency with the representation in other regimes as shown later, the dependence on  $\ell$  has not been examined in Figs. 4.2 since all the simulations have been carried out for a single value of  $\ell = 4$ . This is because, as discussed earlier in Section 4.3, changing  $\ell$  changes the effective sticker strength  $g_{ss}$ , even if  $\epsilon_{st}$  is held constant. Interestingly, however, according to scaling theory, the ratio of intra-chain and inter-chain association fractions,  $[p_1(1 - p_1/2)/p_2] \ell^{1/2}$ , is independent of sticker strength since both intra-chain and inter-chain association fractions have the same dependence on  $g_{ss}$ . As a result, different values of  $\ell$  and  $\epsilon_{st}$  should have no influence on the value of this ratio. This is demonstrated in Fig. 4.2 (c) for two values of  $\ell$ , and a few different values of  $\epsilon_{st}$ . A similar collapse of data for a wider range of values of  $\ell$ , and  $\epsilon_{st}$  is demonstrated for this ratio in Regime II below.

It should be noted that when there are many values of chain length  $N_b$  involved in the same plot, it is not possible to plot the dependence of the ratios involving  $p_1$  and  $p_2$  on  $c/c^*$ , since  $c^*$  depends on  $N_b$ . The dependence on  $c/c^*$  for a single value of  $N_b$  is consequently shown in the insets to Figs. 4.2 (a) and (b), to give an idea of the range of values of the scaled concentration that have been examined here. The range of values of  $c/c^*$  examined

in all the scaling regimes is also indicated in Table 4.2.

### $\theta$ -solvent and Regime II

The scaling relations corresponding to  $\theta$ -solvent and Regime II conditions for backbone monomers are given in the first and third rows of Table 4.1 (b), respectively, and the results of simulations in these regimes, with  $\hat{\tau}$  and sticker strength  $\epsilon_{st}$  constant, are shown in Figs. 4.4. In order to display both cases in the same set of plots, the dependence on spacer length  $\ell$  is absorbed into the  $y$ -axis in Figs. 4.4 (a) and (c), noting that  $\ell^{\nu(3+\theta_2)}$  reduces to the  $\theta$ -solvent case for  $\nu = 1/2$  and  $\theta_2 = 0$ , and to the Regime II case when  $\nu = 3/5$  and  $\theta_2 = 1/3$ . This substitution is not necessary for the fraction of inter-chain associations (Fig. 4.4 (b)), since the dependence on  $\ell$  is the same in both cases. Interestingly, as discussed in greater detail in Section 4.5.2 below, it turns out that  $g_{ss}$  does not depend on  $\ell$  for the special case when  $\epsilon_{bb} = 0$ , i.e., when the backbone monomers are in an athermal solvent. This independence enables an examination of the dependence of the degrees of conversion on  $\ell$  in Regimes II and III, independently of  $\epsilon_{st}$ , unlike in the  $\theta$ -solvent and Regime I regimes. We now consider the Regime II and  $\theta$ -solvent cases in turn.

The scaling with monomer concentration of the ratios involving the intra-chain and inter-chain degrees of conversion, under Regime II conditions, can be seen in Figs. 4.4 (a) and (b) to obey scaling predictions (given in the second row of Table 4.1 (b)). Similar to the observation in Regime I, the choice of value  $\theta_2 = 1/3$ , leads to data collapse across the entire range of parameter values considered in Regime II as well. It is clear from Table 4.1 (a) that  $\theta_2$  appears in the scaling exponents for both the variables  $\ell$  and  $c$  in Regime II. The impressive collapse of data seen in Figs. 4.4 consequently provides convincing evidence of the validity of Dobrynin's estimate of the  $\theta_2$  exponent in sticky polymer solutions.

Another observation from Figs. 4.4, which is common to both the intra and inter-chain association fractions in Regime II, is that the collapse of data for different values of  $\ell$  indicates that the dependence on spacer length is captured accurately by scaling theory. Note that the exponent of  $\ell$  in the ratio involving  $p_1$  is 2 (for  $\nu = 3/5$  and  $\theta_2 = 1/3$ ), and as a consequence, a variation of  $\ell$  between 4 and 12 in Figs. 4.4 (a) represents an exploration over a considerably wide range of the values of  $\ell$ . Concurrently, Fig. 4.4 (c) shows that the ratio of intra-chain

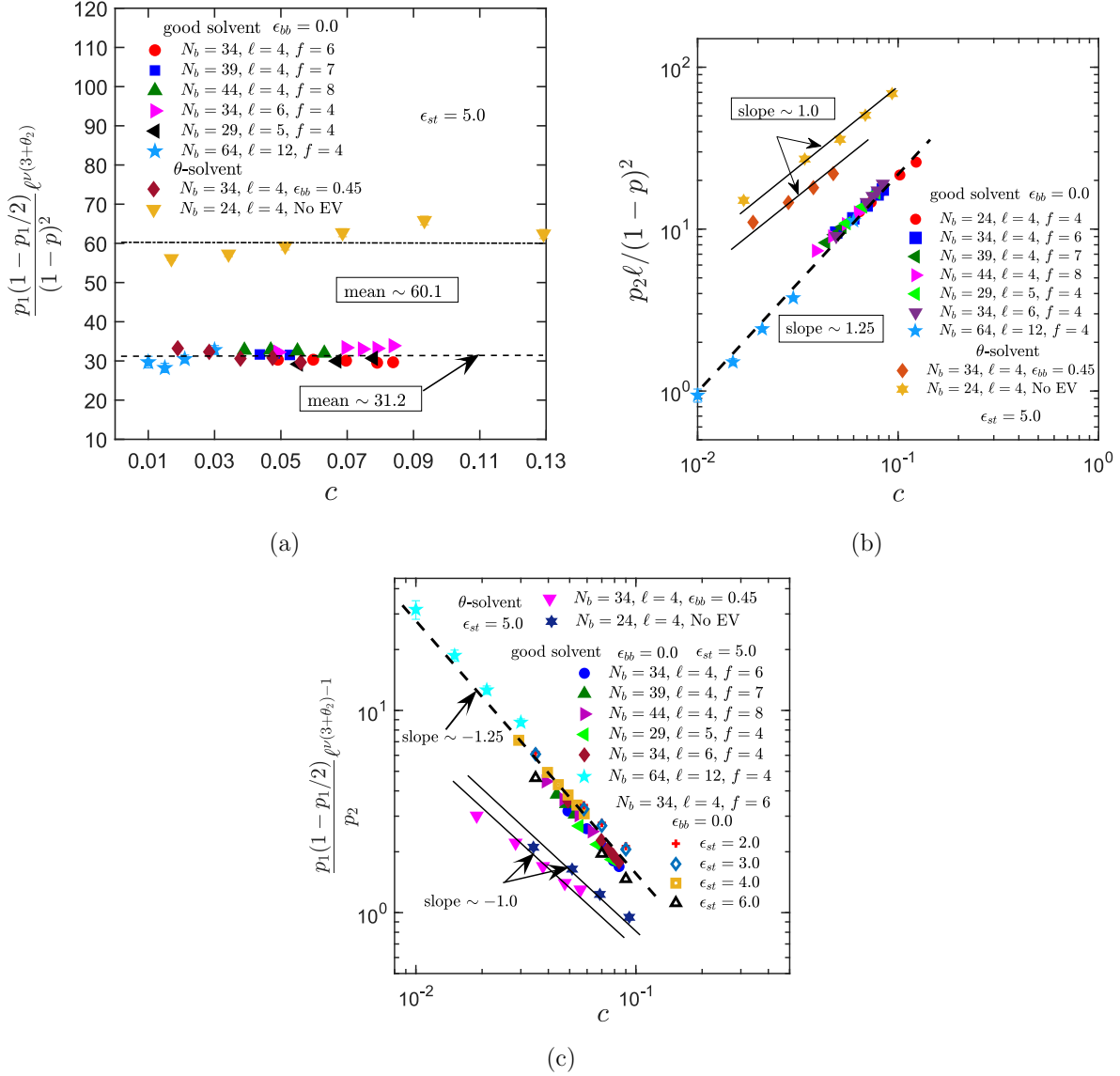


Figure 4.4: The dependence of ratios involving (a) intra-chain (b) inter-chain degrees of conversion, and (c) the ratio of intra-chain and inter-chain association fractions, on the monomer concentration,  $c$ , with the chain backbone under  $\theta$ -solvent and Regime II ( $g_T < \ell < g_c$ ) conditions. The spacer length dependence is absorbed in the  $y$ -axis. Simulations are carried out at constant solvent quality parameter  $\hat{\tau}$  and sticker strength  $\epsilon_{st}$ , except in (c) where two different values of  $\epsilon_{st}$  have been considered. The values of  $\theta_2$  and  $\nu$  are 0 and  $1/2$ , respectively for the backbone under  $\theta$ -solvent conditions, and  $1/3$  and  $3/5$ , respectively, for chains with  $\epsilon_{bb} = 0$  (see Table 4.1). The dashed and the solid lines are drawn with slopes equal to the prediction by scaling theory, while symbols represent simulation data.

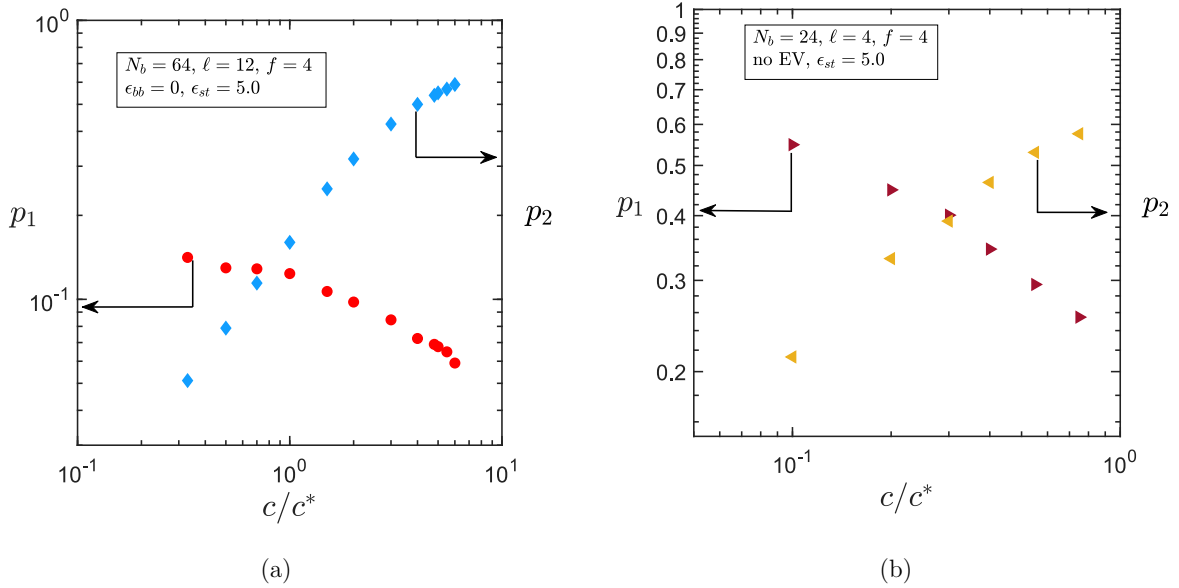


Figure 4.5: Variation of intra-chain ( $p_1$ ) and inter-chain ( $p_2$ ) association fractions as a function of scaled monomer concentration,  $c/c^*$ , for (a) a sticky polymer solution with  $N_b = 64$ ,  $\ell = 12$ ,  $f = 4$ ,  $\epsilon_{bb}=0$  and  $\epsilon_{st}$ , where the parameters correspond to Regime II and III and (b) sticky polymer solution with  $\theta$ -backbone.

and inter-chain conversions,  $[p_1(1 - p_1/2)/p_2] \ell$ , also follows the predicted scaling. Moreover this ratio is independent of the effective sticker strength, since both intra and inter-chain degrees of conversion have an identical dependence on  $g_{ss}$ . As can be seen from Fig. 4.4 (c), this prediction is supported by simulations that show data collapse for several different values of  $\epsilon_{st}$ .

Recall that the case with backbone monomers under  $\theta$ -solvent conditions has been simulated here with two different approaches. The first is to neglect excluded volume interactions altogether, and to treat, as is commonly done, the simulation of  $\theta$  conditions to be identical to simulating ideal (or ghost) chains that can cross each other. The second approach is to use a value of  $\epsilon_{bb} = \epsilon_\theta = 0.45$ , which has been shown to reproduce scaling predictions for homopolymer chains consistent with  $\theta$ -solvent conditions. As can be seen from Table 4.1 (b), scaling theory predicts that in this case as well, the ratio  $[p_1(1 - p_1/2)/(1 - p^2)] \ell^{3/2}$  is independent of monomer concentration. Fig. 4.4 (a), which displays the results of the two approaches, demonstrates the validation of this prediction. When the SDK potential with  $\epsilon_{bb} = \epsilon_\theta$  is used, the numerical value of the ratio is identical to that for the Regime II case

(with the appropriate scaling with  $\ell$  taken into account). On the other hand, the value of the ratio is higher for the case of ideal chains. As will be demonstrated in Section 4.5.2, this difference arises from a difference in the function  $g_{ss}$  in the two cases.

The exponent  $\theta_2$  is not relevant for backbone monomers under  $\theta$ -solvent conditions, and according to Table 4.1 (b), scaling theory predicts that the ratio  $[p_2/(1-p^2)] \ell$  increases linearly with concentration in this case. As can be seen from Fig. 4.4 (b), this prediction is validated by both the approaches used here to simulate a backbone chain under  $\theta$ -solvent conditions. It is clear from Fig. 4.4 (c) that the ratio of intra and inter-chain degrees of conversion,  $[p_1(1-p_1/2)/p_2] \ell^{1/2}$ , also follows the predicted dependence on monomer concentration  $c$ . A discussion of the dependence on the variables  $\ell$  and  $\epsilon_{st}$ , in this case, is postponed to Section 4.5.2. In the both the good solvent condition and  $\theta$ -solvent condition, the individual degrees of conversion for the intra-chain and inter-chain association, shown in Figs. 4.5 are found to follow a similar trend with concentration,  $c/c^*$ , as observed in Regime I. It should be noted that the range of concentration shown in Figure 4.5 (a) span both Regime II and III (with good solvent quality for the backbone). As will be seen subsequently, the values of concentrations depicted in Figs. 4.4 (a) and (b) and listed in Table 4.2 for the good solvent backbone are well into the regime where the sticky polymer solution is in the gel phase. As a consequence, all the simulation results presented here so far, clearly indicate that the scaling relations hold true in both the sol and gel phases, and as pointed out by Dobrynin (Dobrynin, 2004), do not distinguish between them.

### Regime III

The constraints associated with carrying out simulations in Regime III ( $g_T < g_c < \ell$ ) have been detailed in Section 4.4.1. We have considered two values of chain length,  $N_b = 64$  and 79, respectively, in this regime, with spacer lengths  $\ell = 12$  and 15. According to Eq. (4.8), with  $N_b = 64$ ,  $g_c < 11$ , for  $c/c^* > 4$ , while with  $N_b = 79$ ,  $g_c < 14$ , for  $c/c^* > 4$ . Thus, with the number of monomers in a thermal blob  $g_T = 1$  (since  $\epsilon_{bb} = 0$ ), any value of  $c/c^*$  in the range  $4 < c/c^* < 28$  (33) (corresponding to  $g_c \approx 1$  for  $N_b = 64$  (79)) would correspond to Regime III conditions for both these values of chain length. As indicated in the insets to Figs. 4.6 (a) and (b) and Table 4.2, a range of values of  $c/c^*$  from 4 to 6.5 has been simulated

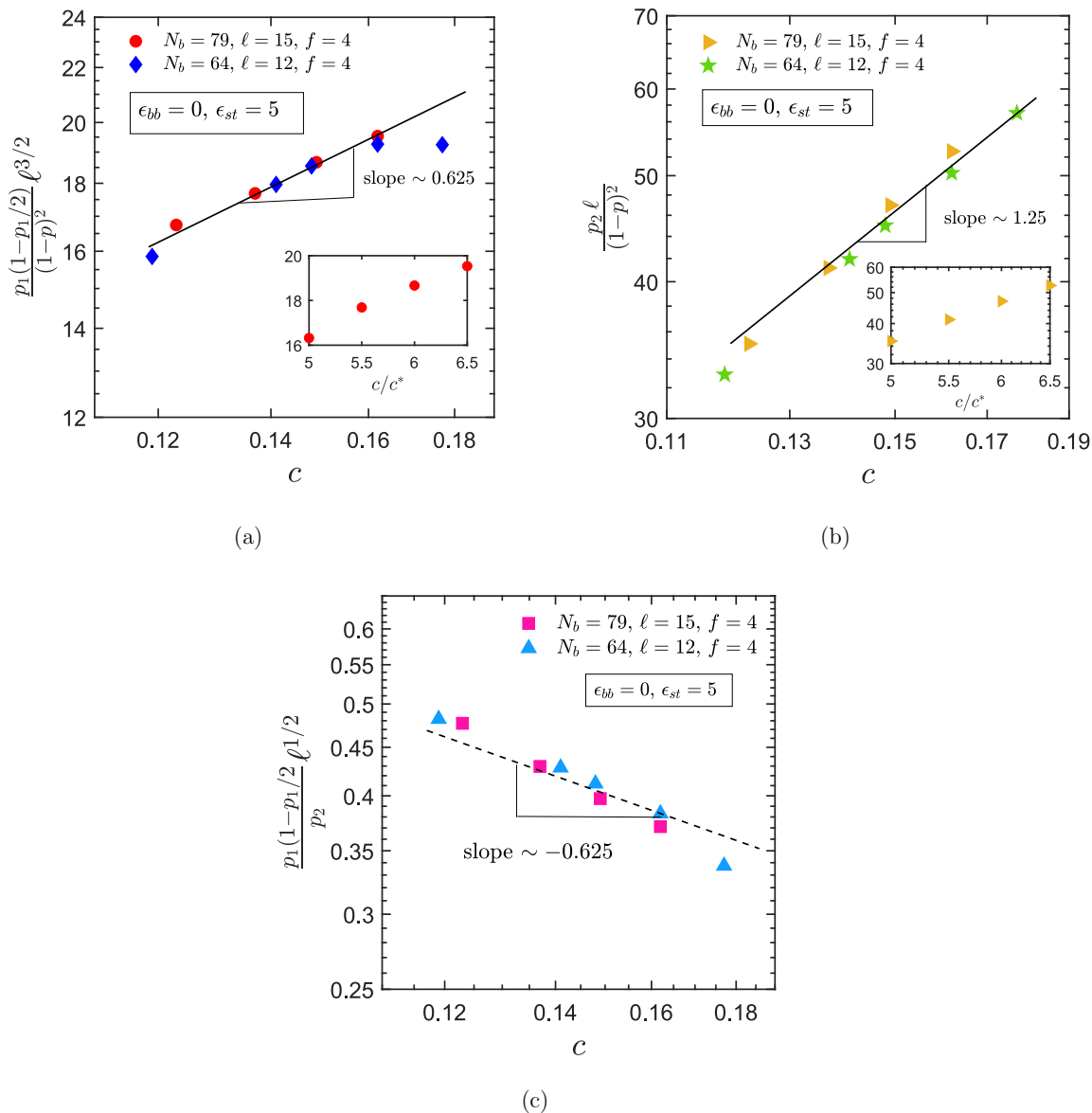


Figure 4.6: The dependence of ratios involving (a) intra-chain (b) inter-chain degrees of conversion, and (c) the ratio of intra-chain and inter-chain association fractions, on the monomer concentration,  $c$ , with the chain backbone under Regime III conditions. The spacer length dependence is absorbed in the  $y$ -axis. Simulations are carried out at constant solvent quality parameter  $\hat{\tau} = 1$ , and constant stiker strength,  $\epsilon_{st} = 5.0$ . The values of  $\theta_2$  and  $\nu$  are  $1/3$  and  $3/5$ , respectively (see Table 4.1). Insets in (a) and (b) show the range of concentration in terms of  $c/c^*$ . The dashed and the solid lines are drawn with slopes derived from the prediction and the symbols are simulation data.

here to explore Regime III, due to limitations of the computational cost for simulating larger values of  $c/c^*$ .

Similar to the simulation results observed in the previous two regimes, Figs. 4.6 show that the scaling of the intra-chain and inter-chain conversion ratios with monomer concentration in Regime III, at constant  $\hat{\tau}$  and  $\epsilon_{st}$ , are also in good agreement with the theoretical prediction (given in the third row of Table 4.1 (b), assuming  $\theta_2 = 1/3$ ). The absorption of the dependence on spacer length into the  $y$ -axis and the collapse of data seen for the two different values of  $\ell$  simulated here, is inline with the predicted dependence on  $\ell$  by scaling theory. However, it would be desirable to carry out simulations for a greater range of values of  $\ell$  for a thorough validation of the scaling prediction. The deviation from scaling theory observed in Fig. 4.6 (a) for the simulated value of the ratio involving  $p_1$  at the highest value of  $c$ , when  $N_b = 64$ , suggests that there are probably too few monomers in a correlation blob ( $g_c \approx 6$ ) for the scaling ansatz to be valid at this chain length. This is, however, not the case when  $N_b = 79$ , or for the ratio involving  $p_2$  (at both the values of chain length used here), since it can be seen from Figs. 4.6 (a) and (b), respectively, that scaling predictions for both the ratios are confirmed by simulation results.

### 4.5.2 Dependence on solvent quality parameter and sticker strength

Defining the quantities,

$$\alpha = \frac{\nu \theta_2}{3\nu - 1}, \quad \text{and} \quad \beta = \nu(3 + \theta_2),$$

the scaling relations for the ratios involving intra and inter-chain degrees of conversion given in Table 4.1 can be represented by the following common expressions in both Regimes I and II,

$$\frac{p_1(1 - p_1/2)}{(1 - p)^2} \ell^{\beta_i} \hat{\tau}^{2\beta_i - 3} \sim g_{ss}; \quad i = 1, 2$$

$$\frac{p_2}{(1 - p)^2} \ell \hat{\tau}^\alpha c^{-(1+\alpha)} \sim g_{ss}$$
(4.10)

where  $\beta_1 = \beta - (1/2)$  applies in Regime I, and  $\beta_2 = \beta$  applies in Regime II. Setting  $\nu = 3/5$  and  $\theta_2 = 1/3$ , gives  $\alpha = 1/4$  and  $\beta = 2$ , and leads to the recovery of the simplified relations displayed in Table 4.1 (b), for these two scaling regimes. The representation of

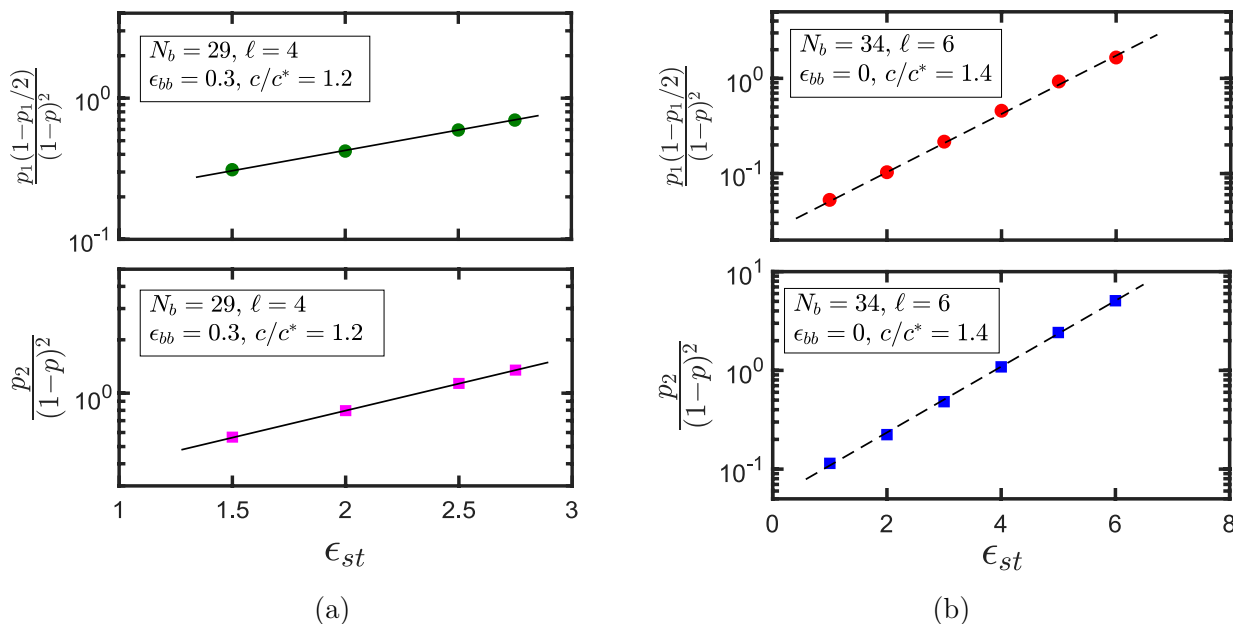


Figure 4.7: Scaling of the ratios involving intra-chain and inter-chain degrees of conversion as a function of sticker strength,  $\epsilon_{st}$ , for systems in (a) Regime I and (b) Regime II. Symbols represent results of simulations, while the lines are drawn to guide the eye.

the scaling relations in the forms given in Eqs. (4.10), focusses attention on the function of effective sticker strength,  $g_{ss}$ . According to scaling theory (Dobrynin, 2004), for fixed values of backbone solvent quality parameter  $\hat{\tau}$  (or equivalently,  $\epsilon_{bb}$ ), and spacer length  $\ell$ , the ratios involving intra and inter-chain degrees of conversion should depend exponentially on  $\epsilon_{st}$ . This expectation is clearly fulfilled in both the scaling regimes, as can be seen in Figs. 4.7, for the particular parameter values that have been examined here.

As discussed previously, in the present implicit solvent model, the function  $g_{ss}$  depends on all three variables  $\epsilon_{st}$ ,  $\epsilon_{bb}$ , and  $\ell$ , and cannot, in general, be varied independently of spacer length  $\ell$ . Here we propose the form,

$$g_{ss} = A(\epsilon_{bb}, \ell) \exp [B(\epsilon_{bb}, \ell) \epsilon_{st}] \quad (4.11)$$

which accounts for the expected dependence on all the three parameters. The functions  $A(\epsilon_{bb}, \ell)$  and  $B(\epsilon_{bb}, \ell)$  can be determined by fitting simulation data. Since both the ratios involving intra and inter-chain degrees of conversion have the same dependence on  $g_{ss}$ , they

can be combined to maximise the data available for the purpose of fitting,

$$\frac{p_1(1-p_1/2)}{(1-p)^2} \ell^{\beta_i} \hat{\tau}^{2\beta_i-3} + \frac{p_2}{(1-p)^2} \ell \hat{\tau}^\alpha c^{-(1+\alpha)} = 2 A(\epsilon_{bb}, \ell) \exp [B(\epsilon_{bb}, \ell) \epsilon_{st}] \quad (4.12)$$

Values of the functions  $A$  and  $B$  obtained in this manner, for the various choices of  $\epsilon_{bb}$  and  $\ell$  used here, are displayed in Table 4.3.

$\ell$	$\epsilon_{bb}$	$A$	$B$
6	0.0	4.65	0.76
4	0.3	6.17	0.70
6	0.35	5.07	0.72

Table 4.3: Values of the functions  $A(\epsilon_{bb}, \ell)$  and  $B(\epsilon_{bb}, \ell)$  in Eq. (4.12), for different spacer lengths,  $\ell$ , and backbone monomer interaction strengths,  $\epsilon_{bb}$ , determined from fitting data from simulations carried out in scaling regimes I and II.

$\ell$	$\epsilon_{bb}$	$A_1$	$B_1$	$A_2$	$B_2$
4	0.45	0.673	0.638	5.25	0.781
4	no EV	1.614	0.611	9.672	0.693
6	0.45	0.369	0.797	3.477	0.879
6	no EV	1.06	0.73	5.44	0.87

Table 4.4: Values of the functions  $A_1(\epsilon_{bb}, \ell)$  and  $A_2(\epsilon_{bb}, \ell)$ , and  $B_1(\epsilon_{bb}, \ell)$  and  $B_2(\epsilon_{bb}, \ell)$ , for different spacer lengths,  $\ell$ , determined from fitting data from simulations carried out for backbone monomers under  $\theta$ -solvent conditions. The two approaches correspond to using the SDK potential with  $\epsilon_{bb} = \epsilon_\theta = 0.45$ , and ghost chains with no excluded volume interactions.

Simulations carried out for the case where backbone monomers are under  $\theta$ -solvent conditions indicate that the function  $g_{ss}$  is not the same for the ratios involving intra and inter-chain degrees of conversion, and that they cannot be combined together, as was done in Eq. (4.12) for backbone monomers under good solvent conditions. The scaling relations for the two ratios in the  $\theta$ -solvent case, displayed in the last row of Table 4.1 (b), can be recovered from Eqs. (4.10) by setting  $\beta_i = 3/2$  and  $\alpha = 0$ . Using  $A_1(\epsilon_{bb}, \ell)$  and  $B_1(\epsilon_{bb}, \ell)$  to denote the functions occurring in the fit to the function  $g_{ss}$  for the ratio involving  $p_1$ , and

similarly,  $A_2(\epsilon_{bb}, \ell)$  and  $B_2(\epsilon_{bb}, \ell)$  for the ratio involving  $p_2$ , their estimated values are given in Table 4.4.

Interestingly, as mentioned earlier, for the case when  $\epsilon_{bb} = 0$  (which is the value used here to simulate the good solvent conditions corresponding to Regimes II and III), it can be seen from Fig. 4.8 that the function  $g_{ss}$  appears to be independent of spacer length  $\ell$ . This lack of dependence is responsible for the collapse of data for different values of  $\ell$  shown in Figs. 4.4 (a) and (b) for Regime II, and Figs. 4.6 (a) and (b) for Regime III, while the dependence of  $g_{ss}$  on  $\ell$  in Regime I, and for backbone monomers under  $\theta$ -solvent conditions, implies that a similar collapse cannot be considered for these cases.

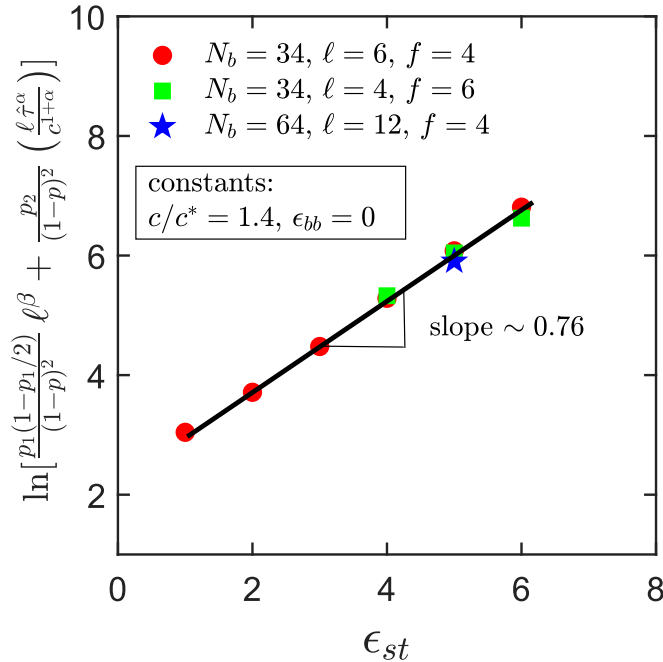


Figure 4.8: Scaling of the sum of the ratios involving intra-chain and inter-chain association fractions (see Eq. (4.12)) as a function of sticker strength,  $\epsilon_{st}$ , for three systems with  $N_b = 34$ ,  $\ell = 6$ ,  $f = 4$ ;  $N_b = 34$ ,  $\ell = 4$ ,  $f = 6$ , and  $N_b = 64$ ,  $\ell = 12$ ,  $f = 4$ , with  $\epsilon_{bb} = 0$ , at  $c/c^* = 1.4$ . The symbols are the simulation data and the solid line is an exponential fit to the data. Note that for Regime II depicted here,  $\alpha = 1/4$  and  $\beta = 2$ .

The validation of the scaling relations displayed in Table 4.1 (b) for the ratios involving  $p_1$  and  $p_2$ , in terms of all the relevant scaling variables, for (i) backbone monomers under good solvent conditions corresponding to Regimes I and II, and (ii) backbone monomers under  $\theta$ -solvent conditions, is demonstrated in the respective subfigures of Fig. 4.9. It is

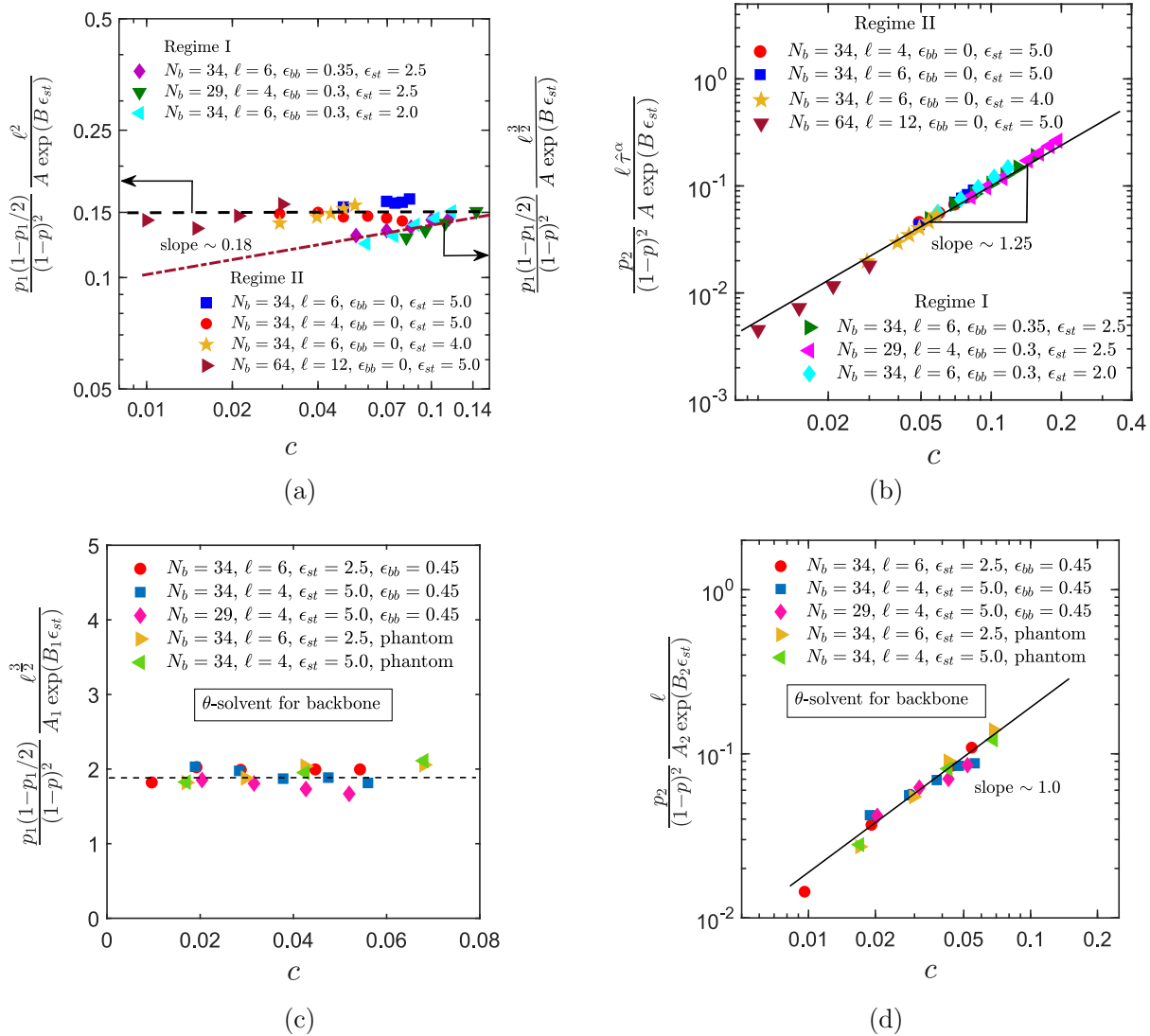


Figure 4.9: Master plots demonstrating validation of scaling relations for, (i) the ratio involving the intra-chain degree of conversion  $p_1$ , in (a) Regimes I and II, and (c)  $\theta$ -solvent conditions for backbone monomers, and, (ii) the ratio involving the inter-chain degree of conversion  $p_2$ , in (b) Regimes I and II, and (d)  $\theta$ -solvent conditions for backbone monomers, plotted as a function of monomer concentration,  $c$ , for different spacer segment lengths  $\ell$ , sticker strengths,  $\epsilon_{st}$ , and solution temperatures,  $\hat{\tau}$ . The exponent  $\alpha = 1/4$ . The dashed and the solid lines are drawn with slopes equal to the prediction by scaling theory, while symbols represent simulation data.

clear that when the dependence of the effective sticker strength on the spacer length  $\ell$  is taken into account, then all the simulation data can be collapsed onto master plots for the dependence of the ratios involving  $p_1$  and  $p_2$  on monomer concentration  $c$ . Note that the weak dependence on concentration observed for the ratio involving  $p_1$  in Regime I (contradictory to the prediction of scaling theory) appears to persist at other values of  $\epsilon_{st}$  as well. The values of the ratio in the Regimes I and II approach each other with increasing concentration. Whether the weak power law dependence on  $c$  in Regime I persists at higher concentrations and higher chain lengths needs further examination. Even though Eq. (4.10) indicates that the ratio  $p_1(1 - p_1/2)/(1 - p)^2$  depends on  $\hat{\tau}$  in Regime II, the choice  $\epsilon_{bb} = 0$  implies that  $\hat{\tau} = 1$ , and consequently it does not appear on the  $y$ -axis label in Fig. 4.9 (a). Nevertheless, it is worth noting that the pre-factor to the solvent quality parameter  $\hat{\tau}$  affects the value of the ratio displayed in Fig. 4.9 (a) for Regime II.

In the case of  $\theta$ -solvent conditions for the backbone, we have seen in Figs. 4.4 that although the scaling of the ratios involving  $p_1$  and  $p_2$  with concentration are identical for the two models used to simulate  $\theta$  conditions for the backbone, the pre-factors are different, which results in a difference in the numerical values. Nevertheless, from Fig. 4.9 (c) and Fig. 4.9 (d) we can conclude that the difference in the pre-factors arises from the factor,  $g_{ss}$ , which is found to be different for the two models for the  $\theta$ -solvent condition. By absorbing the dependence of  $g_{ss}$  in the  $y$ -axis we observe the expected data collapse, as can be seen in Figs. 4.9 (c) and (d).

### 4.5.3 Crossover behaviour between the scaling regimes

The crossover between Regimes I and II is driven by the solvent quality parameter  $\hat{\tau}$ , while that between Regimes II and III is driven by the concentration  $c$ , as discussed earlier in Section 4.4.1. Within the constraints of the relatively narrow range of parameters that have been explored here (due to the computational intensity of the Brownian dynamics simulations), a preliminary examination of the crossover behaviour between Regimes I and II is shown in Figs. 4.10 (a) and (b), and that between Regimes II and III is displayed in Figs. 4.10 (c) and (d).

The dependence of the ratio involving  $p_1$  on the concentration  $c$ , in scaling regimes I

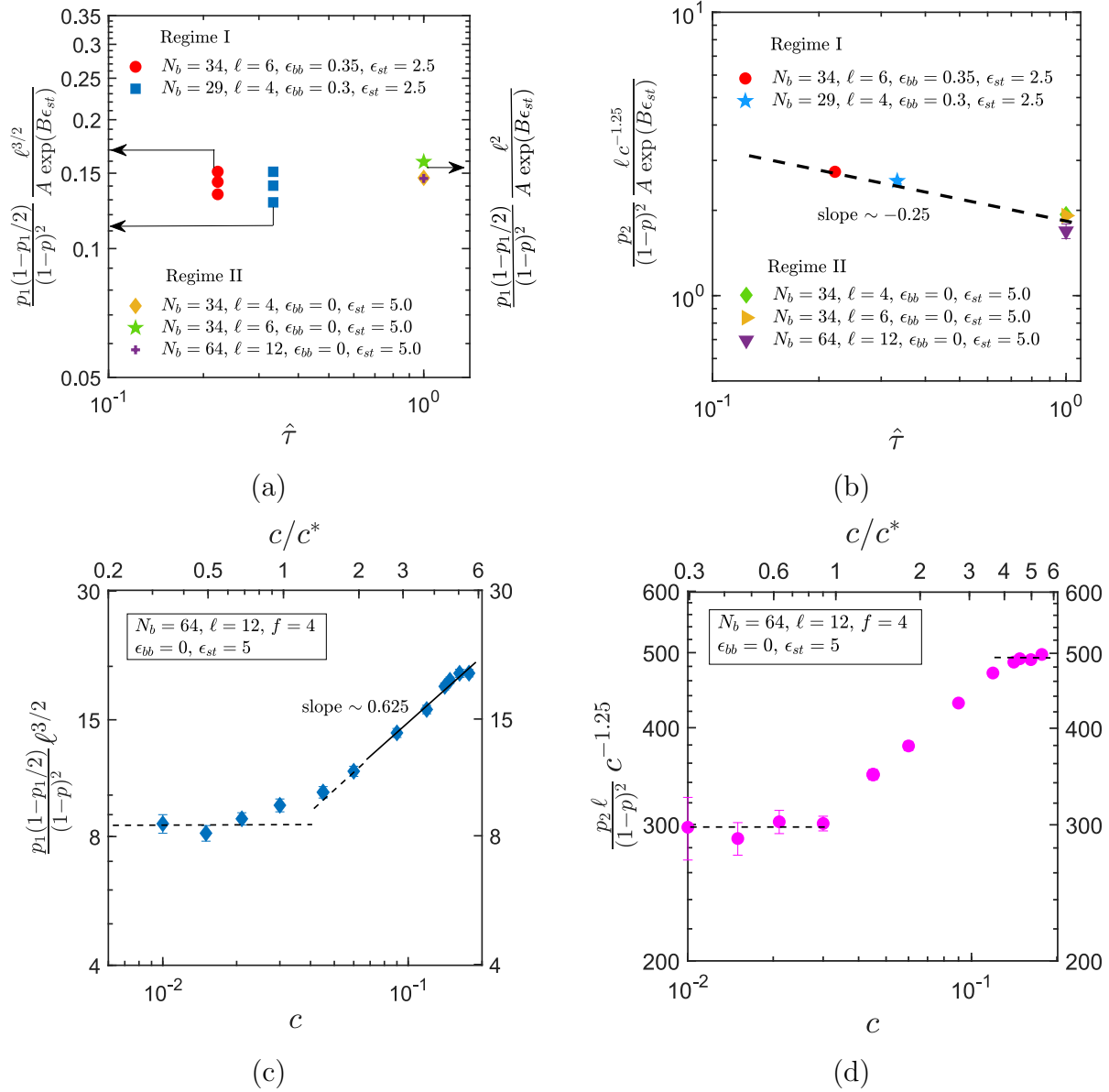


Figure 4.10: Crossover behaviour between the different scaling regimes. (a) Change in the ratio involving the intra-chain degree of conversion  $p_1$  from Regime I, where  $\ell < g_T < g_c$  to Regime II, where  $g_T < \ell < g_c$ , due to a change in the solvent quality parameter  $\hat{\tau}$ . (b) Change in the ratio involving the inter-chain degree of conversion  $p_2$  from Regime I to Regime II due to a change in  $\hat{\tau}$ . (c) Change in the ratio involving the intra-chain degree of conversion  $p_1$  from Regime II, where  $g_T < \ell < g_c$ , to Regime III, where  $g_T < g_c < \ell$ , due to a change in the concentration  $c$ . (d) Change in the ratio involving the inter-chain degree of conversion  $p_2$  from Regime II to Regime III, due to a change in  $c$ .

and II, has been plotted together in Fig. 4.9 (a), and discussed in that context. With regard to the dependence on the solvent quality parameter  $\hat{\tau}$ , it is clear from first and second rows of Table 4.1 (b), that the ratio is independent of  $\hat{\tau}$  in Regime I, and it scales with an exponent  $-1$  in Regime II. As a consequence, when plotted as a function of  $\hat{\tau}$ , we expect to see a constant value in Regime I, and then a crossover into Regime II with an asymptotic slope of  $-1$ . With the current set of simulations, however, this behaviour cannot be observed due to the paucity of values of  $\hat{\tau}$  at which the simulations have been carried out. Essentially, two values of  $\hat{\tau} = 0.22$  and  $0.33$  have been used in Regime I, and its value has been set equal to one in Regime II. The values of the ratio at these values of  $\hat{\tau}$ , with the dependence on  $\ell$  and  $g_{ss}$  absorbed into the  $y$ -axis, are displayed in Fig. 4.10 (a). While it would be possible to obtain data at other values of  $\hat{\tau}$  in Regime II, the marginal difference in the magnitude of the ratio in the two regimes would make it difficult to observe the  $-1$  exponent in this regime. Further, the weak dependence on concentration leads to the scatter of the data seen in Regime I. Clearly, simulations of much longer chains, and over a wider range of values of  $\hat{\tau}$ , would be required to adequately describe the crossover of the ratio involving  $p_1$  between Regimes I and II.

The dependence on concentration  $c$  of the ratio involving  $p_2$  is predicted to be the same in both Regimes I and II according to scaling theory (see first and second rows of Table 4.1 (b)), which has been verified by the simulation results displayed in Fig. 4.9 (b). In order to examine the dependence of the ratio on just  $\hat{\tau}$ , the concentration has been absorbed into the  $y$ -axis in Fig. 4.10 (b). To avoid the overlaying of data at different concentrations on top of each other, their average value has been reported in the figure. Similarly, the dependence on  $\ell$  and  $g_{ss}$  has also been absorbed into the  $y$ -axis, as was done previously in Fig. 4.9 (b). Scaling theory predicts that the ratio depends on  $\hat{\tau}$  with an exponent  $\alpha = -1/4$  in both Regimes I and II. This expectation is verified in Fig. 4.10 (b), where the values of the ratio at  $\hat{\tau} = 0.22$  and  $0.33$  correspond to Regime I, and the values at  $\hat{\tau} = 1$  correspond to Regime II. The crossover between the two regimes appears to be smooth, though it is desirable to confirm this with additional data points in both regimes.

The crossover between Regimes II and III has been examined for a single system with  $N_b = 64$  and  $\ell = 12$ , since amongst the many data sets used in the current simulations, it is

one that spans both regimes. Recall that according to scaling theory, the ratio involving  $p_1$  is independent of concentration in Regime II and scales as  $c^{5/8}$  in Regime III, while the ratio involving  $p_2$  scales as  $c^{5/4}$  in both Regimes II and III. These asymptotic scaling regimes and the crossover between them is displayed in Figs. 4.10 (c) and (d), where, in the latter, the dependence on concentration has been absorbed into the  $y$ -axis to highlight the crossover behaviour. As displayed in Table 4.2, in the simulations carried out here, the upper bound of the scaled concentration  $c/c^*$  in Regime II is 1.9, while the lower bound in Regime III is 4.0. With these bounds in mind, it is clear that the ratio involving  $p_1$  appears to leave Regime II around  $c/c^* = 1$ , but already exhibits Regime III scaling by  $c/c^* = 2$ . On the other hand, while the ratio involving  $p_2$  also appears to leave Regime II around  $c/c^* = 1$ , it displays the asymptotic scaling of Regime III only by  $c/c^* = 4$ . As discussed earlier in section 4.4.1, the actual lower bound to Regime III is  $c/c^* = 1$ . As a result, it is expected that for longer chain lengths, the ratio will exhibit asymptotic Regime III scaling at smaller values of  $c/c^*$ . While within scaling theory, the pre-factor for the dependence of the ratio involving  $p_2$  on concentration  $c$  is the same in both regimes, simulations seem to indicate that it may be different in the two regimes since the asymptotic constants displayed in Figs. 4.10 (d) are not the same. Establishing the true nature of the crossover, and the values of the pre-factors with greater certainty would require simulations with longer chains.

#### 4.5.4 Scaling of radius of gyration

It is interesting to observe the variation with  $c/c^*$  of the radius of gyration ratio,  $R_g^2/R_{g0HP}^2$ , displayed in Fig. 4.11, of an individual chain in a sticky polymer solution, and compare it with the behaviour of a chain in a homopolymer solution. Here,  $R_{g0HP}$  is the radius of gyration of the homopolymer chain in the dilute limit. The asymptotic scaling law for the radius of gyration ratio as a function of the scaled concentration  $c/c^*$ , in semidilute unentangled homopolymer solutions, is well known (Doi and Edwards, 1986)(Daoud et al., 1975)(Pelissetto, 2008)(Huang et al., 2010),

$$\left. \frac{R_g^2}{R_{g0}^2} \right|_{HP} = \left( \frac{c}{c^*} \right)^{(2\nu-1)/(1-3\nu)} \quad (4.13)$$

Equation (4.13) describes the shrinking of individual chains with increasing concentration due to the presence of Flory screening. It is clear from the filled red symbols, which are the results of current simulations, and the yellow stars, which are the results of MPCD simulations by Huang et al. (Huang et al., 2010), that the radius of gyration ratio for homopolymer solutions is constant at low concentrations (as expected for dilute solutions), and then decreases in a broad crossover region between  $c/c^* = 0.4$  to  $c/c^* \approx 3$ , as it changes from the dilute to the asymptotic semidilute scaling regime, where it decreases with a power law. The dashed black line in Fig. 4.11 is drawn with slope equal to the asymptotic scaling exponent  $-0.25$ . On the other hand, the filled green and purple symbols, representing sticky polymer solutions with backbone under athermal solvent ( $\epsilon_{bb} = 0$ ), reflect a very different behaviour.

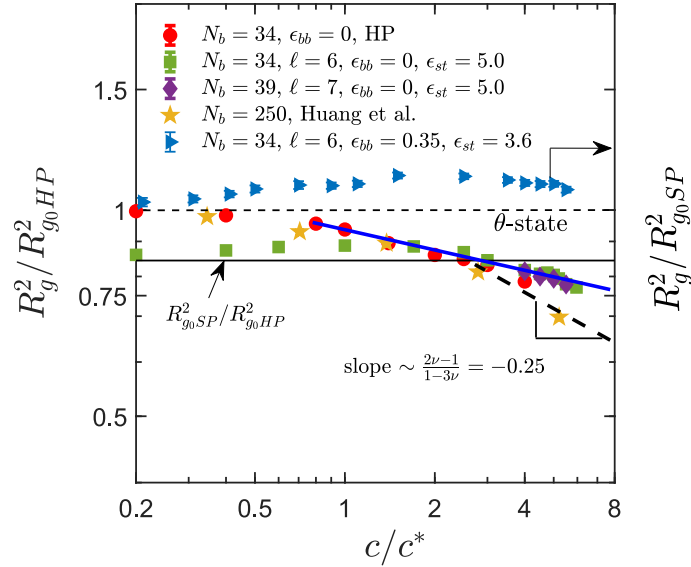


Figure 4.11: Ratios of the radius of gyration as a function of scaled concentration,  $c/c^*$ .  $R_{g0HP}^2$  and  $R_{g0SP}^2$  are the mean-squared radius of gyration of the homopolymer (HP) and the sticky polymer (SP), respectively, in the dilute limit. The backbone monomers in both polymers are in an athermal solvent. The filled red symbols represent data for homopolymer solutions obtained from current simulations, while the yellow stars are from MPCD simulations by Huang et al. (Huang et al., 2010). The filled green squares and purple diamonds represent sticky polymer solutions. The filled blue right triangles represent a situation in which the sticky polymer chain as a whole is under  $\theta$ -solvent conditions. These different scenarios are achieved with different backbone monomer interaction strengths,  $\epsilon_{bb}$ , sticker strengths,  $\epsilon_{st}$ , and spacer lengths  $\ell$ . The dashed line is the theoretical scaling prediction (Eq. (4.13)) for unentangled semidilute homopolymer solutions. The filled blue line is drawn to guide the eye.

The ratio of the radius of gyration for a chain in a sticky polymer solution to that for an

equivalent homopolymer chain in the dilute limit,  $R_{g0SP}^2/R_{g0HP}^2$ , is less than one because of the presence of stickers and the concomitant existence of intra-chain associations. Its value, determined from single chain simulations, is indicated by the filled black line in Fig. 4.11. At low concentrations, the magnitude of the ratio (filled green symbols) remains close to the dilute limit value, and appears to increase gradually with increasing concentration. The gradual increase can be ascribed to the increase in inter-chain associations with increasing concentration, that occur at the expense of intra-chain associations. It could also be a finite size effect, which could be confirmed with simulations for longer chains. The start of the crossover into the semidilute regime due to Flory screening seems to be delayed until  $c/c^* \approx 2$ , and it is clear from Fig. 4.11 that the crossover seems to persist beyond  $c/c^* = 6$ , with the asymptotic scaling regime not yet reached at this concentration, as indicated by the filled blue line. It should be noted the onset of this crossover is expected to depend on the parameters  $\epsilon_{st}$ ,  $\epsilon_{bb}$  and  $\ell$ . These dependencies have not been studied in the present work and are worthy of investigation in the future. The behaviour displayed in Fig. 4.11 indicates that polymer conformations in solutions of sticky polymers are significantly different from those of homopolymer chains in good solvent conditions, upon which the scaling theory is based. This aspect will be considered further in Section 4.5.5 below, when sticky polymer solutions in which chains as a whole are under  $\theta$ -solvent conditions ( $\epsilon_{bb} = 0.35$ ,  $\epsilon_{st} = 3.6$ ) (filled blue triangles in Fig. 4.11) are discussed.

#### 4.5.5 $\theta$ -solvent conditions for sticky polymer chains

The scaling relations listed in Table 4.1 have all been derived by considering the quality of the solvent relative to backbone monomers on the sticky polymer chain (Dobrynin, 2004), with the spacer length between stickers, solvent quality parameter and the monomer concentration determining the particular scaling regime that is relevant. In this section, we briefly consider a situation that has not been not treated so far within the framework of scaling theory, namely, one in which the sticky polymer chain as a whole is under  $\theta$ -solvent conditions. As discussed in Section 4.2,  $\theta$ -solvent conditions for a sticky polymer chain can be realised by setting  $\epsilon_{st}$  equal to the corresponding value of  $\epsilon_{st}^\theta$ , for the given values of  $\epsilon_{bb}$  and  $\ell$ .

The dependence of the ratios involving  $p_1$  and  $p_2$  on  $c$ , for a system in which the sticky

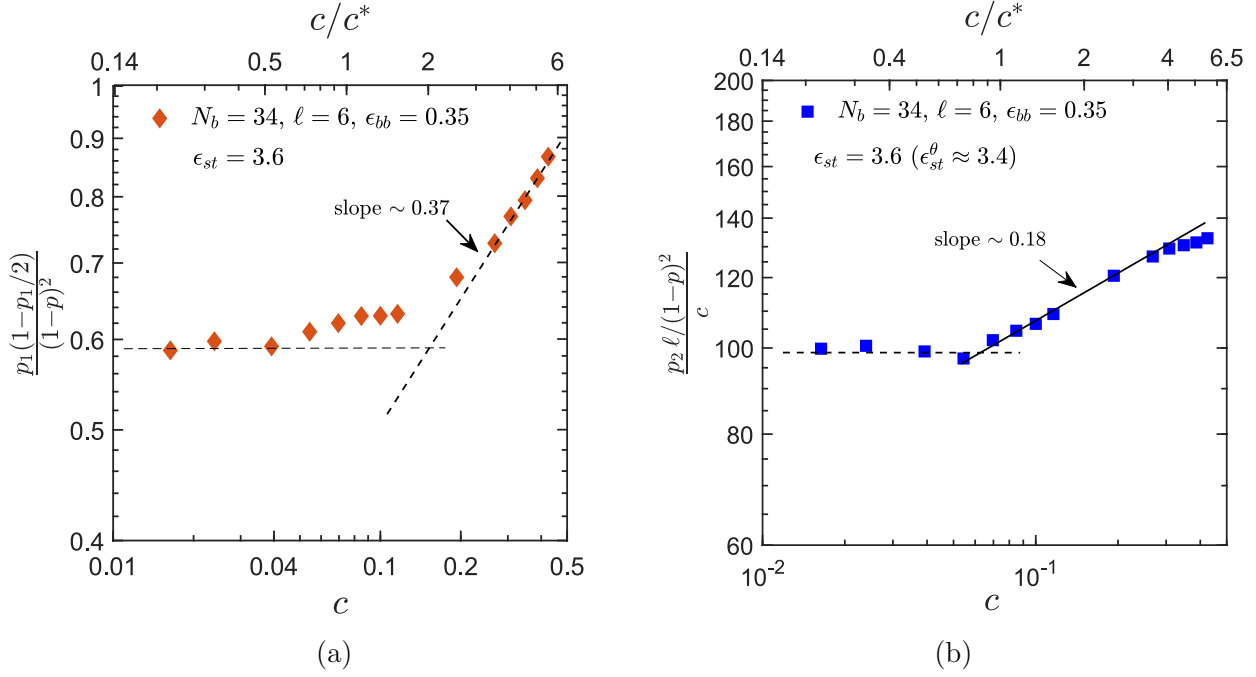


Figure 4.12: The dependence of ratios involving (a) intra-chain, and (b) inter-chain degrees of conversion, on the monomer concentration,  $c$ , with sticky polymer chains under nearly  $\theta$ -solvent conditions for sticky chains as a whole. This is achieved, for a chain with  $N_b = 34$ ,  $\ell = 6$ ,  $f = 4$ , and  $\epsilon_{bb} = 0.35$ , by setting  $\epsilon_{st} = 3.6$ , which is close to the value  $\epsilon_{st}^\theta = 3.4$  computed for these parameter values. The dashed and the solid lines are drawn with slopes that are a good fit to the symbols, which represent simulation data.

polymer chains as a whole are under  $\theta$ -solvent conditions, is displayed in Figs. 4.12 (a) and (b), respectively, for a chain with  $N_b = 34$ ,  $\ell = 6$ ,  $f = 4$ , and  $\epsilon_{bb} = 0.35$ . For these parameter values, using the method discussed previously in Chapter 3, it can be shown that  $\epsilon_{st}^\theta \approx 3.4 \pm 0.4$ . The simulation results reported in Figs. 4.12 were carried with  $\epsilon_{st} = 3.6$ , which is in the range of values required to achieve  $\theta$ -solvent conditions. It is clear from the figures that the observed dependence on monomer concentration of the intra and inter-chain association fractions is unlike that seen in any of the scaling regimes studied previously.

Before discussing the results in this section, it is worth making a few remarks about the system that has been studied here ( $N_b = 34$ ,  $\ell = 6$ ,  $f = 4$ ,  $\epsilon_{st} = 3.6$ ) in the context of the scaling theory. Firstly, in terms of just the backbone monomers, the chain is under good solvent conditions, since  $\epsilon_{bb} = 0.35 < \epsilon_\theta = 0.45$ . It is the presence of stickers that makes the conditions  $\theta$ -like for the overall chain. Since  $\epsilon_{bb}$  is held fixed at a value of 0.35, the number of monomers in a thermal blob is fixed at  $g_T = 20$ , independent of the concentrations

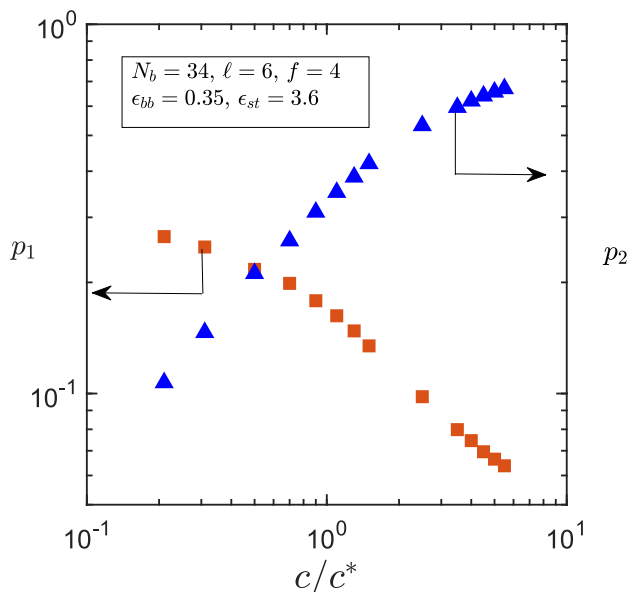


Figure 4.13: Variation of intra-chain ( $p_1$ ) and inter-chain ( $p_2$ ) association fractions as a function of scaled monomer concentration,  $c/c^*$ , with sticky polymer chains under nearly  $\theta$ -solvent conditions for sticky chains as a whole.

that have been studied. Since the overall chain under  $\theta$ -solvent conditions has not been considered in the scaling theory, a wide range of concentrations has been explored here ( $0.2 \leq c/c^* \leq 6$ ), independent of the bounds imposed by the different scaling regimes. For the chain of backbone monomers, this variation of  $c/c^*$  implies that the number of monomers in a correlation blob varies in the range  $254 \geq g_c \geq 4$ . It is straightforward to show from Eq. (4.8) that  $g_c < g_T$  for  $c/c^* > 1.5$ , and  $g_c < \ell = 6$ , for  $c/c^* > 4.0$ . Both these situations have not been examined within the framework of scaling theory, even for sticky polymer chains under good solvent conditions.

With this discussion in mind, it can be observed from Figs. 4.12 (a) and (b) that both association fractions exhibit a crossover in scaling behaviour at around  $c/c^* \approx 1$ . The ratio involving  $p_1$  is fairly independent of concentration until this crossover value, at which point the dependence grows and reaches an asymptotic slope of about 0.37. In order to more clearly examine the dependence on concentration of the ratio involving  $p_2$ , its value has been divided by  $c$  on the  $y$ -axis. Clearly, the scaling with concentration is linear at low concentrations, similar to that observed for chains whose backbone monomers are under  $\theta$ -solvent conditions. Beyond the value of  $c/c^* \approx 0.7$ , the slope assumes a value of  $\approx 1.18$ ,

which is less than the slope of 1.25 observed for chains with backbones under good solvent conditions. However, for  $c/c^* \gtrsim 4$ , the ratio deviates from this scaling presumably due to the number of monomers in a correlation blob becoming smaller than the spacer length  $\ell$  as a result of the relatively short chain length,  $N_b = 34$ , used in the current simulations.

It is instructive to study the dependence on concentration of both the degrees of conversion in conjunction with the variation with  $c/c^*$  of the radius of gyration ratio,  $R_g^2/R_{g0SP}^2$ , displayed in Fig. 4.11 (filled blue right triangles,  $y$ -axis on the right of figure). For a homopolymer solution under  $\theta$ -solvent conditions, this ratio is constant, independent of concentration, since there is no Flory screening. In the case of the sticky polymer chains under  $\theta$ -solvent conditions considered here, the radius of gyration ratio appears to be a weak function of concentration. The ratio increases gradually, followed by a slow decrease beyond the threshold value of  $c/c^* \approx 1$ , which coincides with the value at which the change in concentration dependence is observed for the ratios involving  $p_1$  and  $p_2$  in Figs. 4.12. The initial increase in size can be correlated with the reduction in the intra-chain association fraction  $p_1$  displayed in Fig. 4.13, in which it can be seen that  $p_1$  rapidly decreases beyond  $c/c^* \approx 1$ , with the inter-chain association fraction  $p_2$  then becoming the dominant mode of association.

The scaling of the radius of gyration behaviour observed here for a sticky polymer chain under overall  $\theta$ -conditions may well be due to finite size effects. In principle, one expects that for sufficiently long chains, the renormalization of the solvent quality that occurs due to setting  $\epsilon_{st} = \epsilon_{st}^\theta$  would lead to a true  $\theta$ -state, with a radius of gyration that is independent of concentration. The special case considered in this section has not been investigated further here. Nevertheless, the preliminary results clearly indicate that the scaling behaviour of the intra and inter-chain association fractions is intimately connected to the underlying conformations of the sticky polymer chains.

## 4.6 Hydrodynamic interactions and time to equilibration

As is well known, hydrodynamic interactions (HI) begin to get screened at the overlap concentration  $c^*$ , and get completely screened only in a polymer melt (Rubinstein and Colby, 2003)(A.Jain et al., 2012). However, for a wide range of concentration in the dilute and semi-dilute unentangled regimes, hydrodynamic interactions significantly influence the dynamic properties of polymer solutions (Rubinstein and Colby, 2003)(A.Jain et al., 2012)(Prakash, 2019). Considering the effects of HI on the dynamics of homopolymer solutions, it can be presumed that HI will have significant influence on the dynamics of sticky polymer solutions as well. It seems worthwhile therefore to examine the role of HI in associative polymer solutions, to determine the concentration beyond which they begin to get screened, and to establish whether there is a concentration beyond which their influence on dynamics can be safely ignored. While hydrodynamic interactions have no effect on equilibrium static properties, they do, nevertheless, play a role in determining the timescale over which equilibration is achieved. In this section, the influence of HI on the time taken by the intra and inter-chain association fractions, and the radius of gyration, to reach their respective stationary values, is examined.

The hydrodynamic interaction is modelled by the regularised Rotne-Prager-Yamakawa tensor, as described in Section 2.3 in the context of Brownian dynamics simulations. For all the simulation results reported in this section, we use a value of hydrodynamic interaction parameter  $h^* = 0.2$ .

As mentioned in Section 4.4, prior to sampling equilibrium data, a typical simulation involves two equilibration steps. In the first, a run of about 3 to 4 Rouse relaxation times is carried out for a system of chains with only backbone monomers and no stickers. In the second step, stickers are introduced and a further run of about 5 to 8 Rouse relaxation times is carried out. For the results discussed in this section, hydrodynamic interactions are switched on at the end of the first step, simultaneously with the introduction of stickers. The transient trajectories during the second equilibration step are sampled in order to study the influence of hydrodynamic interactions.

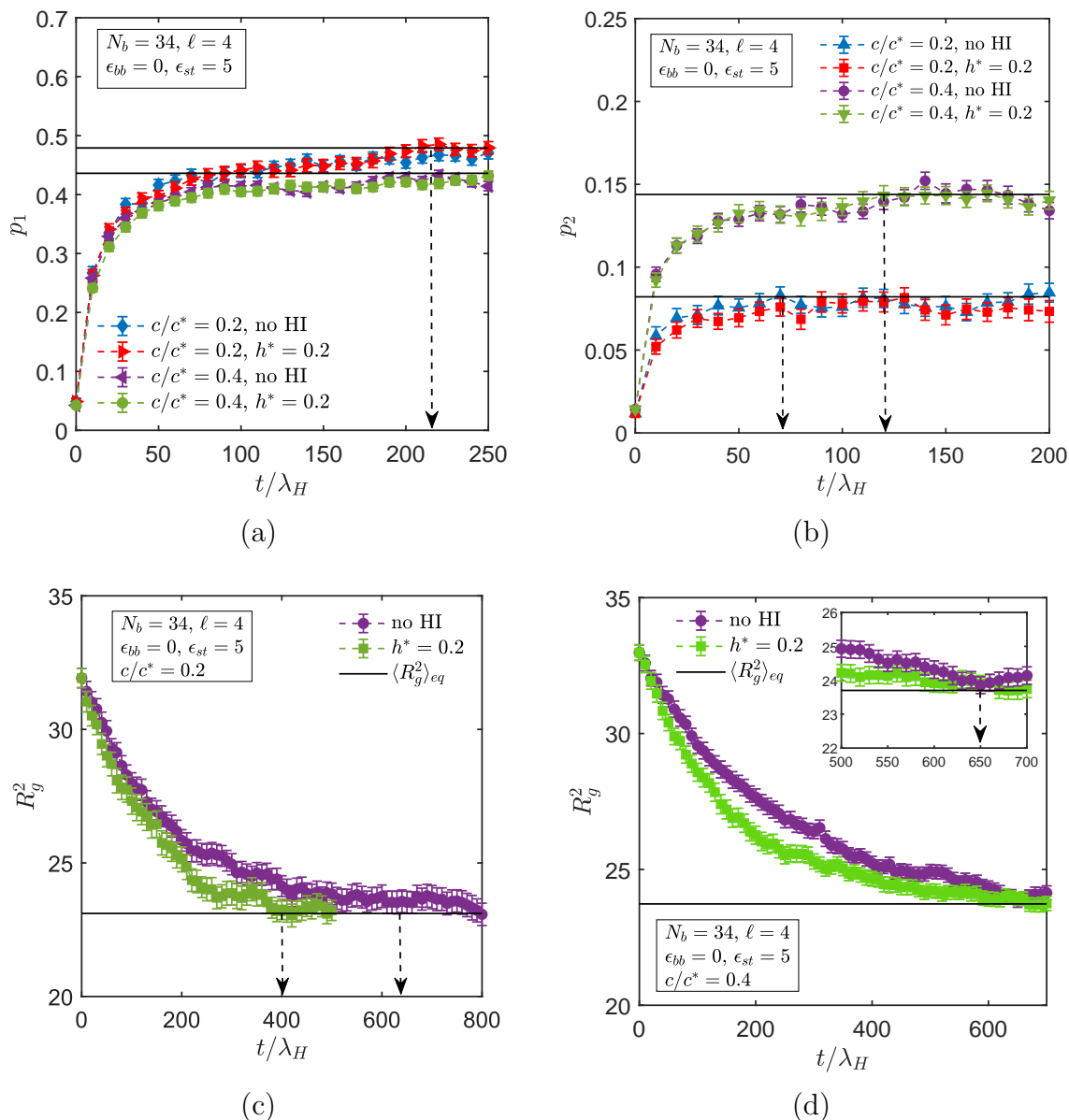


Figure 4.14: The transient variation of (a) the intra-chain, and (b) the inter-chain association fractions, for two different concentrations, and the time evolution of the radius of gyration at the scaled concentrations, (c)  $c/c^* = 0.2$ , and (d)  $c/c^* = 0.4$ . Simulations with and without hydrodynamic interactions (HI) have been displayed for both properties, with the former carried out with the hydrodynamic interaction parameter,  $h^* = 0.2$ . The dashed vertical lines indicate the time required for equilibration. The choice of simulation parameters leads to a sticky polymer solution in scaling Regime II.

The transient variation of the intra and inter-chain association fractions are shown in Figs. 4.14 (a) and (b), respectively, for two different scaled concentrations,  $c/c^* = 0.2$  and  $c/c^* = 0.4$ , and the time evolution of the radius of gyration at the same two values of concentration, are shown in Figs. 4.14 (c) and (d), respectively. The simulation parameters are such that, within the framework of scaling theory, the system lies in Regime II (see Fig. 4.1 (b)). For both the degrees of conversion and the radius of gyration, simulations with and without hydrodynamic interactions have been displayed. Since both are static properties, their equilibrium values are unaffected by hydrodynamic interactions, and as can be clearly observed in Figs. 4.14, this is indeed the case, with the results of simulations with and without hydrodynamic interactions being identical at sufficiently long times, when the systems have equilibrated.

Interestingly, it appears from Fig. 4.14 (a) and (b), that both  $p_1$  and  $p_2$  are unaffected by hydrodynamic interactions for the entire period of observation, from the moment the stickers are turned on to the time at which equilibration is achieved (denoted by the dashed vertical lines). Both the degrees of conversion are seen to increase with increasing concentration. On the other hand, while the time to equilibration for  $p_1$  is the same at  $c/c^* = 0.2$  and  $c/c^* = 0.4$ , it takes longer for  $p_2$  to equilibrate at the higher concentration. It is worth noting that for the sticker strength examined here, the time required for the equilibration of  $p_1$  and  $p_2$ , which is a reflection of the diffusive timescale for stickers to find each other in space, is significantly shorter than the time required for the equilibration of the radius of gyration, which is a property of the chain as a whole.

In contrast to their lack of influence on the degrees of conversion, hydrodynamic interactions appear to have a pronounced influence on the time needed for the radius of gyration to equilibrate at  $c/c^* = 0.2$ . As can be seen from the two trajectories in Fig. 4.14 (c) that correspond to simulations with (green squares) and without hydrodynamic interactions (purple circles), a stationary state is reached by a non-dimensional time,  $t/\lambda_H \approx 400$ , in the former case, while it requires  $t/\lambda_H \approx 650$  in the latter case. At the higher value of scaled concentration,  $c/c^* = 0.4$ , however, even though the transient trajectories are different, both simulations with and without hydrodynamic interactions appear to reach a stationary state by a non-dimensional time,  $t/\lambda_H \approx 650$  (see inset to Fig. 4.14 (d)). This suggests that the

influence of hydrodynamic interactions decreases with increasing concentration, as may be expected with the onset of screening in unentangled semidilute solutions. As observed from the results in the main paper, the value of the scaled concentration,  $c/c^* = 0.2$ , corresponds to a system in the sol phase, while according to at least one of the signatures of gelation considered in this work, which will be shortly discussed in the following section, the value  $c/c^* = 0.4$ , corresponds to a system in the gel phase. As a consequence, we may expect that dynamic properties such as relaxation times in the sol phase will be significantly affected by the presence of hydrodynamic interactions. While in this section we have discussed the effect of hydrodynamic interactions only on the equilibration time of static properties, it has a far stronger impact on the scaling of various dynamic properties and viscoelasticity of associative polymer solutions, considered in detail in Chapter 5.

## 4.7 Characterisation of gelation and the gelation line

The mean-field theoretical framework has been used by Semenov and Rubinstein (Semenov and Rubinstein, 1998) and Dobrynin (Dobrynin, 2004) to map out the phase diagram of associative polymer solutions in the temperature-concentration plane, and within the phase diagram, to identify different domains in the single phase sol and gel states. Essential to the demarcation of the different phase boundaries in these theories, is the use of the original Flory-Stockmayer expression, Eq. (4.2), that relates the fraction of inter-chain associations  $p_2$  at the sol-gel transition to the number of stickers  $f$  on a chain. Typically, Eq. (4.2), rather than the Dobrynin modified (Dobrynin, 2004) Flory-Stockmayer expression, Eq. (4.1), is used since the fraction of intra-chain associations  $p_1$  is considered to be negligibly small. While this is a reasonable assumption at sufficiently high concentrations,  $p_1$  and  $p_2$  are of comparable magnitudes for most of the concentrations examined here. Consequently, substituting Eq. (4.1) (rather than Eq. (4.2)) into the expression for  $p_2$  in the second of Eqs.(4.10), leads to the following expression for the dependence of the monomer concentration,  $c_g$ , along the

*gelation line* that separates the sol and gel states, on all the system parameters,

$$c_g \sim \left( \frac{\hat{\tau}^{\frac{\nu\theta_2}{3\nu-1}} \ell}{[(1-p_1^g)f-1](1-p_g)^2 g_{ss}} \right)^{\frac{3\nu-1}{\nu(3+\theta_2)-1}} \quad (4.14)$$

Here,  $p_1^g$  is the fraction of intra-chain associated stickers and  $p_g$  is the total fraction of associated stickers at the sol-gel transition. Clearly, both Eq. (4.1) and Eq. (4.14) are testable elements of the scaling theory, which have not been examined so far by molecular simulations. In this work, we examine the validity of Eqs. (4.1) and (4.14) in a limited way, i.e., we confine our attention to determining the dependence of  $p_2$  on  $p_1$  and  $f$ , and the variation of  $c_g$  along the gelation line, for fixed values of the solvent quality parameter  $\hat{\tau}$  and sticker strength  $\epsilon_{st}$ , in the special case where the backbone monomers are in good solvent conditions corresponding to scaling regime II. Additionally, we examine the dependence of  $p_1^g$  and  $p_g$  on  $\ell$ , and on  $f$ , in order to eliminate them from Eq. (4.14), and as a consequence, obtain the dependence of  $c_g$  on just the sticky chain properties,  $\ell$  and  $f$ .

In order to verify if the prediction of the gelation line by scaling theory is accurate, it is first necessary to locate the concentration at which the sol-gel transition occurs. As mentioned in Section 4.1, there are at least three different approaches in the literature with regards to this question, and here we examine each of them in turn.

From a geometric perspective, the inception of gelation can be defined as the monomer concentration at which a system spanning network occurs (Stauffer and Aharony, 1992)(Tanaka and Matsuyama, 1989)(Tanaka, 1998). The concentration at which such a percolation transition occurs, denoted here by  $c_{g1}$ , can be determined by calculating the probability of finding a cluster of chains that spans the simulation box, and estimating how this probability changes with changing concentration. The so-called spanning probability is computed here by identifying the chains that belong to a cluster from the chain connectivity matrix, and comparing the maximum span of the cluster with the box size,  $L$ . If the span of a cluster of chains along any direction is greater than or equal to the box size, the cluster is identified as system spanning. The spanning probability is computed over an ensemble of 64 to 128 independent trajectories, where each trajectory consists of a set of data collected at an interval of 1000 to

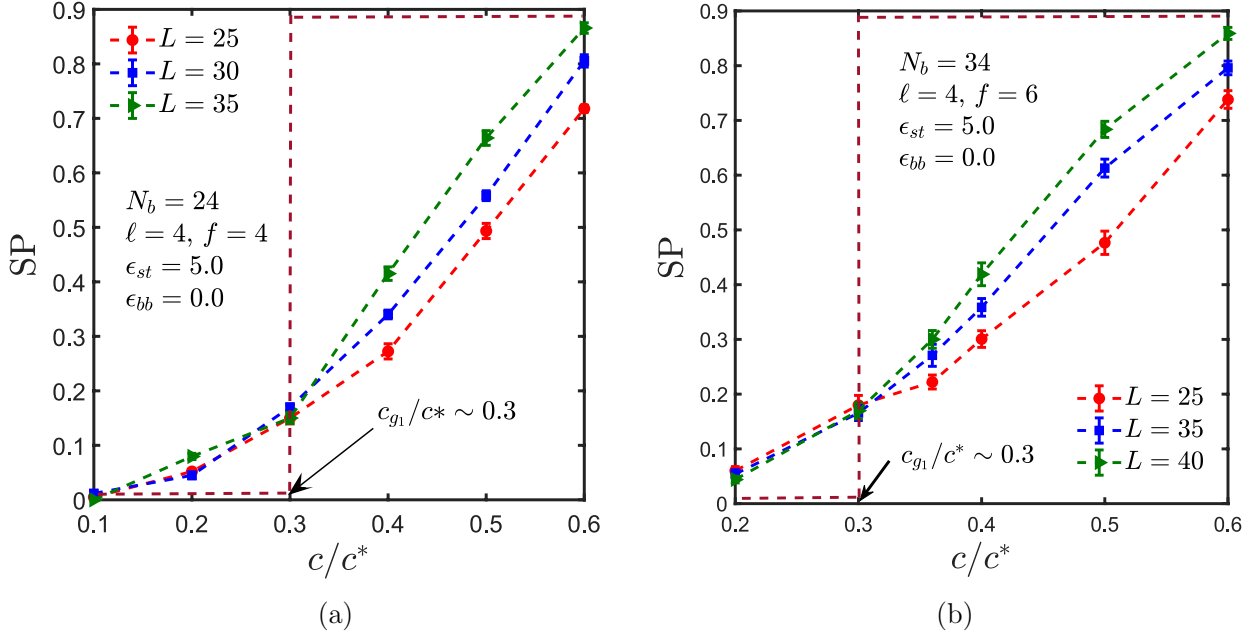


Figure 4.15: Spanning probability (SP) as a function of monomer concentration in Regime II for (a)  $N_b = 24$ ,  $\ell = 4$ ,  $f = 4$  and (b)  $N_b = 34$ ,  $\ell = 4$ ,  $f = 6$ , with sticker strength,  $\epsilon_{st} = 5.0$ . The point of divergence of the curves at different box sizes,  $L$ , is assumed to represent the concentration at the gelation threshold, and is indicated as occurring at  $c_{g1}/c^* \approx 0.3$ .

5000 non-dimensional time steps over the entire production run. For an infinitely large simulation box, the probability of finding a cluster that spans the entire box, at a low monomer concentration below the gelation threshold, is essentially zero. With increasing concentration, the spanning probability is expected to undergo a sharp transition at the monomer concentration that corresponds to the percolation transition, and instantly attain a value of one. For a finite box size, however, the variation of spanning probability with concentration is expected to be more gradual, since even at low concentrations, there is a finite probability of finding a system spanning cluster. In this case, the gelation threshold can be determined by computing the spanning probability for a number of systematically increasing box sizes. It is expected that if the studied systems are large enough, their spanning probability curves will intersect at a common point, which represents an accurate estimate of the percolation threshold (Stauffer and Aharony, 1992)(Christensen and Moloney, 2005). Here, simulations have been carried out for three different box sizes, and in each case, the spanning probability (SP) has been computed as a function of monomer concentration, as displayed in Fig. 4.15.

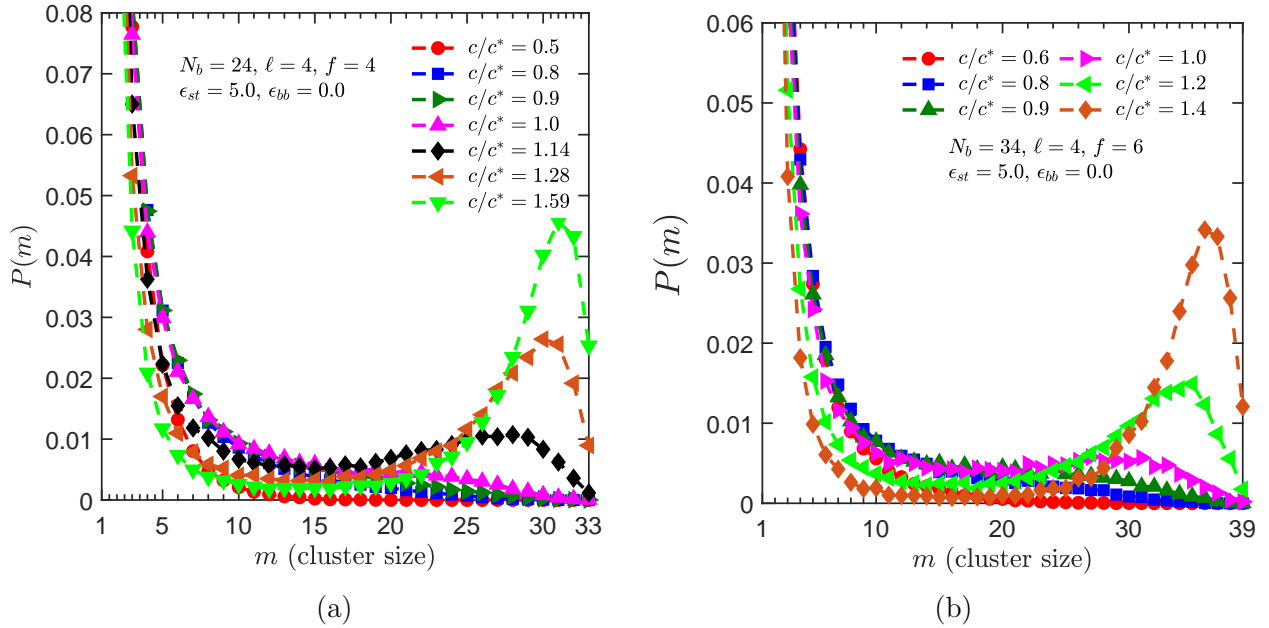


Figure 4.16: Chain cluster-size distribution as a function of monomer concentration in Regime II for (a)  $N_b = 24$ ,  $\ell = 4$ ,  $f = 4$ , and (b)  $N_b = 34$ ,  $\ell = 4$ ,  $f = 6$ , with sticker strength,  $\epsilon_{st} = 5.0$ . The onset of bimodality, which is assumed to represent a signature of gelation, occurs at  $c_{g2}/c^* \approx 1.0$ , for each of the three chain lengths.

Rather than each box size leading to a distinctive spanning probability curve, which intersect at a unique point, it is observed that at low concentrations, the curves for different box sizes overlap within error bars, probably as a result of insufficiently long chains and the box sizes not being large enough. Beyond a certain scaled concentration, however, the curves are seen to separate and diverge. The location of this change in behaviour has been identified here as the concentration at which percolation transition occurs. The value of the scaled concentration,  $c_{g1}/c^* \approx 0.3$ , is found to be independent of chain length, for systems with a fixed spacer length  $\ell$ , sticker strength  $\epsilon_{st}$ , and backbone monomer solvent quality  $\epsilon_{bb}$ , as can be seen in Fig. 4.15.

In associative polymer solutions, the existence of geometric percolation does not necessarily imply the existence of a persistent network since the bonds between stickers are weak and reversible (Kumar and Panagiotopoulos, 1999)(Kumar and Douglas, 2001). As mentioned earlier, an alternative approach Kumar and Panagiotopoulos (1999)(Kumar and Douglas, 2001) identifies the occurrence of an incipient gel in sticky polymer solutions with the onset of bimodality in the chain-cluster size distribution,  $P(m)$ , where  $m$  is the number

of chains in a cluster. Fig. 4.16 displays  $P(m)$  computed here at different monomer concentrations, for two different values of chain length  $N_b$ , at the specified values of  $\ell$ ,  $\epsilon_{st}$  and  $\epsilon_{bb}$ . The plots suggest that the distribution function decreases monotonically with increasing  $m$  at low monomer concentrations, but becomes bimodal with increasing concentration. The occurrence of a peak at a large cluster size is considered to be correlated with the existence of percolating chain-clusters. Here, the concentration at which the slope of  $P(m)$  versus  $m$  first becomes positive, at some value of  $m$ , is considered to be the location of the sol-gel transition, and is denoted by  $c_{g2}$ . For the given parameter values, the onset of bimodality is found to occur at  $c_{g2}/c^* \approx 1.0$ , which is significantly higher than  $c_{g1}/c^*$ , the location of the percolation transition. The value of the gelation concentration,  $c_{g2}/c^*$ , is found to be independent of chain length, as in the case of  $c_{g1}/c^*$ . It is apparent from Fig. 4.15 that as the monomer concentration approaches  $c_{g2}/c^*$ , the spanning probability tends to unity, suggesting that, at this concentration, there is a significant increase in the probability of finding a cluster with size sufficiently large to span the entire system.

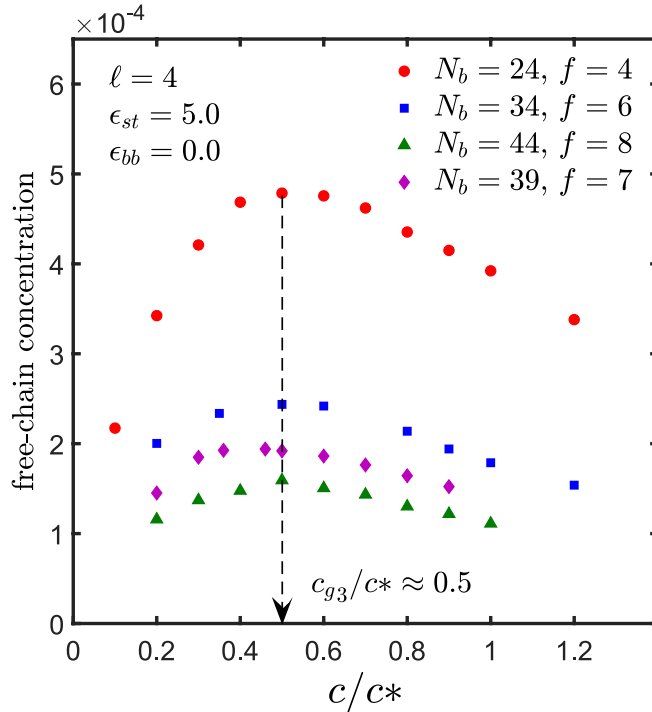


Figure 4.17: Free chain concentration as a function of monomer concentration in Regime II for different chain lengths with spacer length,  $\ell = 4$ , sticker strength,  $\epsilon_{st} = 5.0$  and  $\epsilon_{bb} = 0$ . The maxima in the free-chain concentration is observed at  $c_{g3}/c^* \approx 0.5$ .

The third and final signature of gelation considered here is the proposal by Semenov and Rubinstein (Semenov and Rubinstein, 1998) that the maxima in the free chain concentration coincides with the sol-gel transition. Recall that this assumption is the basis for their derivation of Eq. (4.2). Figure 4.17 is a plot of the free chain concentration versus monomer concentration, for various values of chain length  $N_b$ , at the specified values of  $\ell$ ,  $\epsilon_{st}$  and  $\epsilon_{bb}$ . Free chains, i.e., those with no inter-chain associations, are essentially chain clusters with only one chain in them, and can consequently be identified with the help of the same cluster computation algorithm used here for determining the other two signatures of gelation. The value of the concentration corresponding to the maximum for each symbol set in Fig. 4.17, denoted here by  $c_{g_3}$ , is established by fitting a parabola to the data close to the maxima, and finding the location at which the slope is zero. We find that  $c_{g_3}/c^* \approx 0.5$ , which lies between the two scaled concentrations,  $c_{g_1}/c^*$  and  $c_{g_2}/c^*$ , the locations of the sol-gel transition from the two approaches discussed previously. As is clear from Fig. 4.17, consistent with the observations for  $c_{g_1}/c^*$  and  $c_{g_2}/c^*$ , the scaled concentration  $c_{g_3}/c^*$ , is also independent of chain length. The fact that  $c_{g_3}/c^* > c_{g_1}/c^*$  implies that, even after a system spanning network is formed, new chains added to the system join the sol-phase for a range of concentrations, before joining the gel-phase.

According to Flory-Stockmayer theory (Flory, 1953)(Stockmayer, 1944) (appropriately modified by Dobrynin (Dobrynin, 2004)), the gel-point coincides with the value of  $c/c^*$  at which  $p_2 = 1/[(1 - p_1)f - 1]$ . The variation of inter-chain conversion,  $p_2$ , and the ratio  $1/[(1 - p_1)f - 1]$  with scaled concentration,  $c/c^*$ , is presented in Figs. 4.18 for systems with different chain lengths,  $N_b$ , at constant  $\ell$ ,  $\epsilon_{st}$  and  $\epsilon_{bb}$ . Clearly, the points of intersection between the two curves in the different subfigures of Figs. 4.18 are the Flory-Stockmayer theory estimates of  $c/c^*$  at the gel point, in all these cases. The estimate of the gel-point appears to be independent of chain length, and close to the value evaluated from the onset of bimodality in the chain-cluster size distribution, i.e.,  $c/c^* \approx 1$ .

It is intriguing that the two gelation concentrations  $c_{g_1}/c^* \approx 0.3$  and  $c_{g_3}/c^* \approx 0.5$ , corresponding to the inception of a system spanning network, and to the free-chain concentration maximum, respectively, occur below the overlap concentration, while that corresponding to the onset of bimodality  $c_{g_2}/c^* \approx 1.0$ , is more in accord with the intuitive expectation of gela-

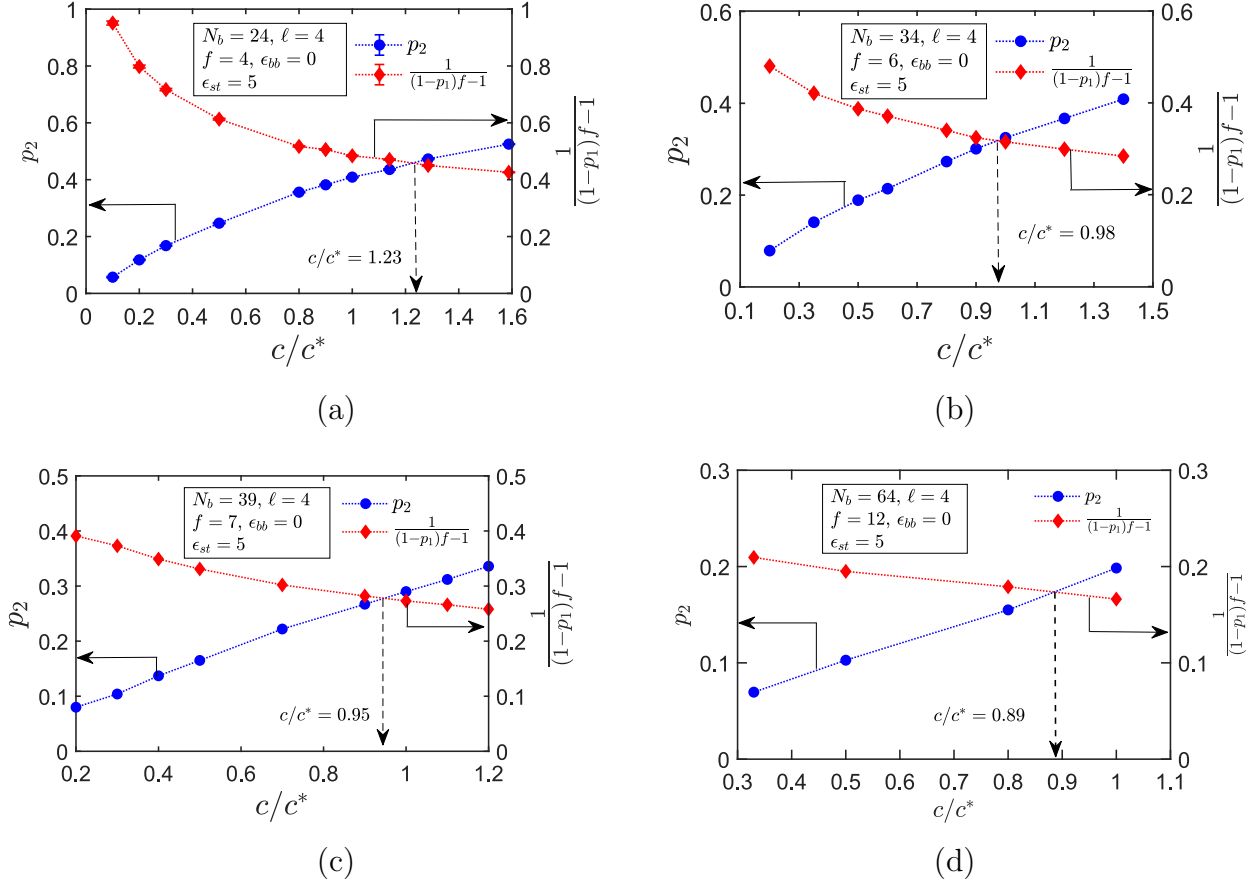


Figure 4.18: Variation of inter-chain conversion,  $p_2$ , and the ratio  $1/[(1 - p_1)f - 1]$  with scaled concentration,  $c/c^*$ , for systems with chain lengths (a)  $N_b = 34$ , (b)  $N_b = 39$ , (c)  $N_b = 44$  and (d)  $N_b = 64$ . For all the chain lengths, the values of spacer length,  $\ell = 4$ , sticker strength,  $\epsilon_{st} = 5$ , and backbone monomer interaction strength,  $\epsilon_{bb} = 0$ , are held constant. The values of  $c/c^*$  at the point of intersection of the two curves for various chain lengths are (a) 0.98, (b) 0.95, (c) 0.93 and (d) 0.89.

tion occurring at  $c_g \approx c^*$ . This is perhaps related to the fact that geometrical percolation can occur even though the solution is not solid-like, which is the common understanding of a gel. As shown previously Kumar and Douglas (2001), the volume fraction at the percolation threshold is a function of the sticker-sticker interaction strength  $\epsilon_{st}$ , and it approaches the onset of solid-like behaviour with increasing  $\epsilon_{st}$ . For relatively low values of  $\epsilon_{st}$ , while a system spanning network might occur, the frequent pairing and unpairing of stickers leads to a gel that is not rigid Kumar and Douglas (2001). Indeed, as shown by the simulation snapshots in Figs. 4.19, there is no discernible change in the distribution of chains across the simulation cell when the geometrical (and free-chain maximum concentration) is crossed. It

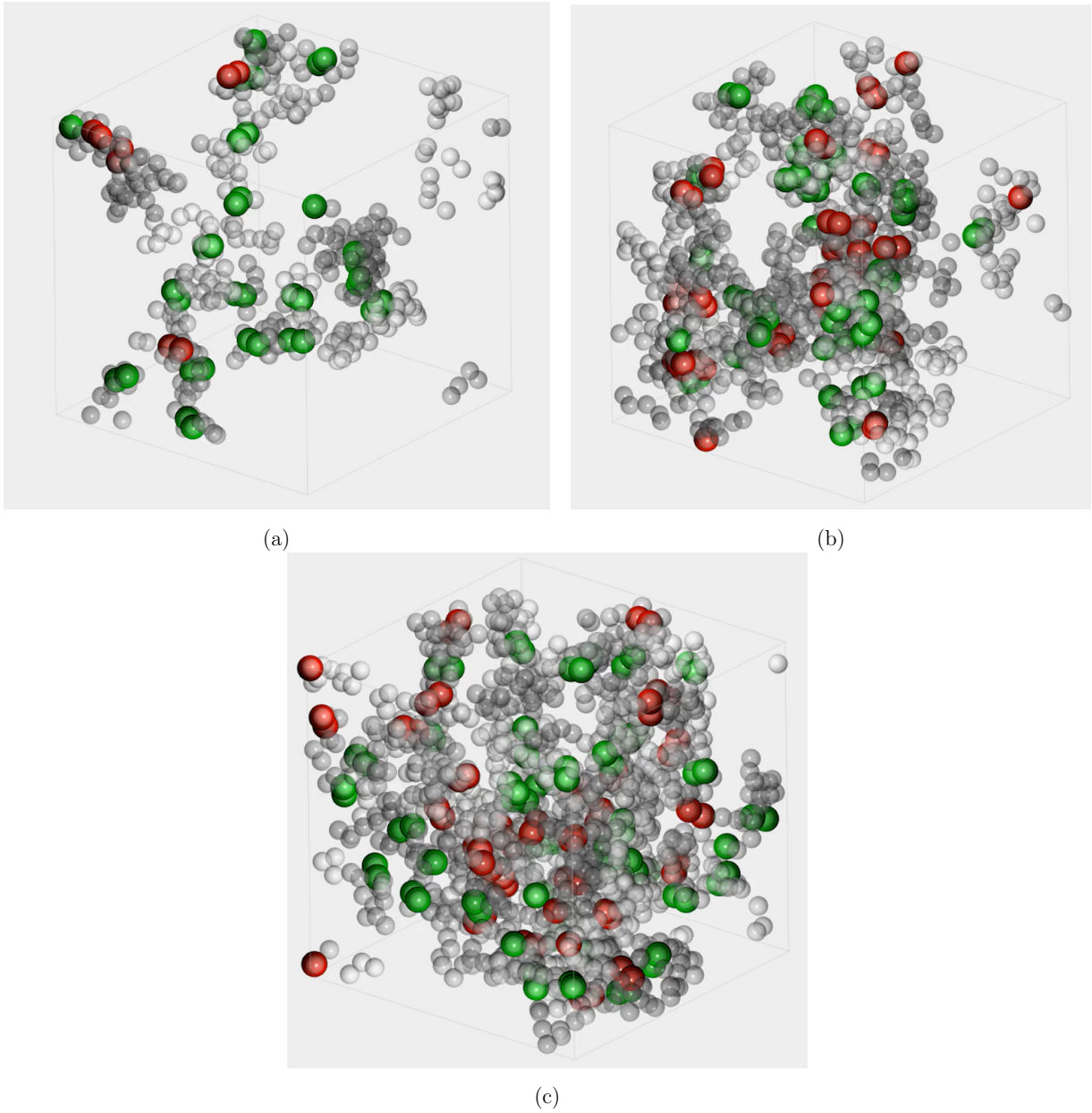


Figure 4.19: Snapshots of the simulation box for a system with parameters  $\{N_b = 34, \ell = 4, f = 6, \epsilon_{bb} = 0, \epsilon_{st} = 5\}$  at (a)  $c/c^* = 0.2$ , (b)  $c/c^* = 0.5$  and (c)  $c/c^* = 1.0$ . The red beads indicate inter-chain associations, while the green beads represent intra-chain associations.

would be interesting to study the dependence of the three gelation signatures on the sticker strength, and to examine if any of the estimates of the sol-gel transition concentration determined here coincides with that identified through rheological experiments (Winter and Chambon, 1986)(Li and Aoki, 1997)(Li et al., 1997), which would identify the transition to solid-like behaviour. Addressing this question satisfactorily would require the incorporation of hydrodynamic interactions, in order for the dynamics of sticky polymer solutions to be captured accurately.

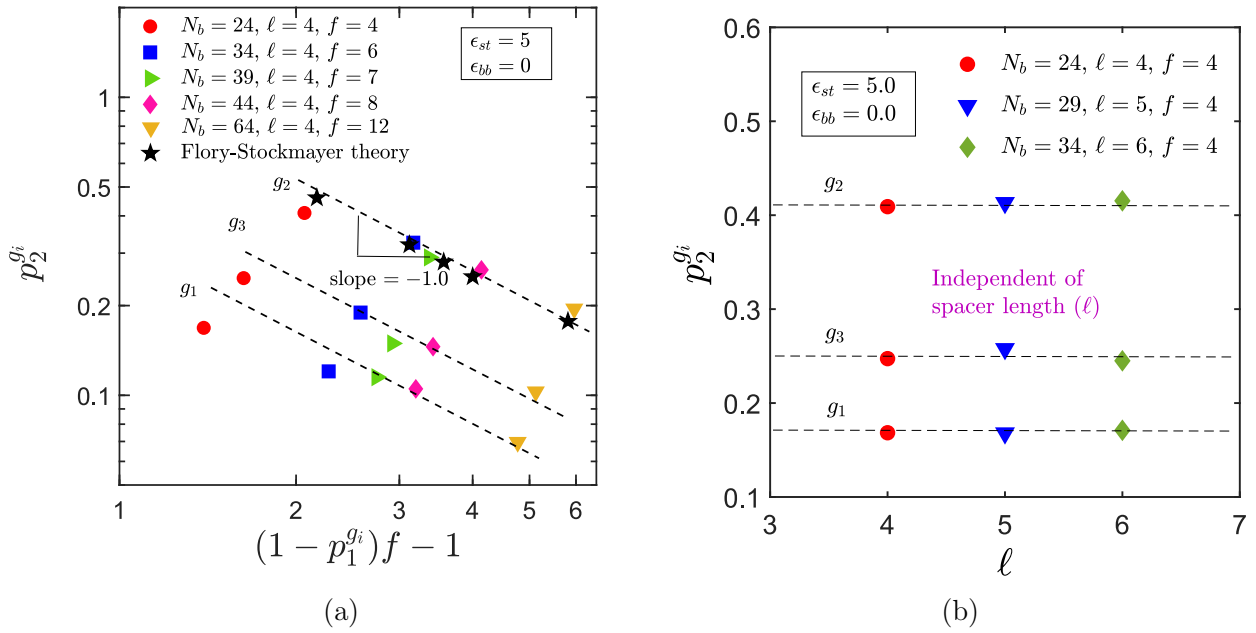


Figure 4.20: Scaling of inter-chain degree of conversion,  $p_2^{g_i}$ , at the gel-point in Regime II, predicted by the three different signatures of gelation, with (a)  $(1 - p_1)f - 1$ , and (b) the number of spacer monomers  $\ell$ , for systems with constant number of stickers  $f$ , and different chain lengths  $N_b$ . The sticker strength and backbone solvent quality are kept constant at  $\epsilon_{st} = 5.0$  and  $\epsilon_{bb} = 0$ , respectively. Each symbol shape represents a system with a particular chain length  $N_b$  and the dashed lines are the Flory-Stockmayer theory predictions at each of the gelation signatures.

Having determined the concentrations at the gel-point predicted by the different signatures of gelation, we can now verify if the dependence of  $p_2^g$  on  $p_1^g$  and  $f$  coincides with the prediction of the modified form of the Flory-Stockmayer theory (Flory, 1953)(Stockmayer, 1944)(Dobrynin, 2004). In other words, we can check if the dependence of  $p_2^{g_i}$  on  $[(1 - p_1^{g_i})f - 1]$  obeys Eq. (4.1), where  $g_i = g_1, g_2, g_3$ , represents the three signatures of gelation. It is clear from Fig. 4.20 (a) that for all the three signatures of gelation,  $p_2^g$  follows a linear scaling

with the inverse of  $((1 - p_1^{g_i})f - 1)$  for sufficiently long chains as predicted by Eq. (4.1). Compared to gelation signatures  $g_2$  and  $g_3$ , however, the approach to linear scaling for  $g_1$  occurs at larger values of  $N_b$ . As mentioned earlier, the Flory-Stockmayer theory estimate of the gel-point matches well with the gel-point determined from the onset of bimodality in the chain-cluster size distribution ( $g_2$ ).

The independence of the value of  $c/c^*$  at the gel-point from chain length  $N_b$  has been demonstrated for all the gelation signatures by keeping the spacer length  $\ell$  fixed, while varying the number of stickers  $f$  per chain. In Fig. 4.20 (b), the dependence of the fraction of inter-chain associations at the gel-point,  $p_2^{g_i}$ , on the spacer length,  $\ell$  (and consequently,  $N_b$ ), for the three signatures of gelation, is displayed for chains with a fixed number of stickers  $f$ . Clearly,  $p_2^{g_i}$  is independent of  $\ell$ . Since  $p_2^{g_i} = 1/[(1 - p_1^{g_i})f - 1]$ , and  $p_2^{g_i}$  is independent of  $\ell$ , this implies that  $p_1^{g_i}$  should also be independent of  $\ell$ , at fixed values of  $f$ . This is demonstrated shortly below.

The verification of the expression for the gelation line, Eq. (4.14), as mentioned earlier, is examined here for the restricted case of constant  $\hat{\tau}$  and  $\epsilon_{st}$ . Further, we wish to eliminate the quantities  $(1 - p_1^g)f - 1$  and  $(1 - p_g)^2$  from Eq. (4.14) so as to determine the dependence of  $c_g$  on just the sticky chain properties,  $\ell$  and  $f$ . In order to do so, the dependence of  $(1 - p_1^{g_i})f - 1$  and  $(1 - p_{g_i})^2$  on  $\ell$  and  $f$  is displayed in Figs. 4.21. It is clear from Fig. 4.21 (a) that at a fixed value of  $\ell$ ,  $(1 - p_{g_i})^2$  is independent of  $f$  for all the three different signatures of gelation, while Fig. 4.21 (b) implies that for a fixed value of  $f$ ,  $(1 - p_{g_i})^2$  scales linearly with  $\ell$  in all three cases. Fig. 4.21 (c) suggests that when  $\ell$  is constant,  $[(1 - p_1^{g_i})f - 1]$  scales linearly with  $f$ , for sufficiently long chains. Finally, as anticipated above, Fig. 4.21 (d) indicates that when  $f$  is constant,  $p_1^{g_i}$  tends to a constant value, independent of  $\ell$ , when  $N_b$  becomes large. As observed earlier, the approach to asymptotic behaviour is slower in the case of  $g_1$ , compared to that of  $g_2$  and  $g_3$ .

Substituting the dependences on  $\ell$  and  $f$  for the quantities  $[(1 - p_1^g)f - 1]$  and  $(1 - p_g^2)$ , summarised in Figs. 4.21, into Eq. (4.14), leads to the following expression for the monomer

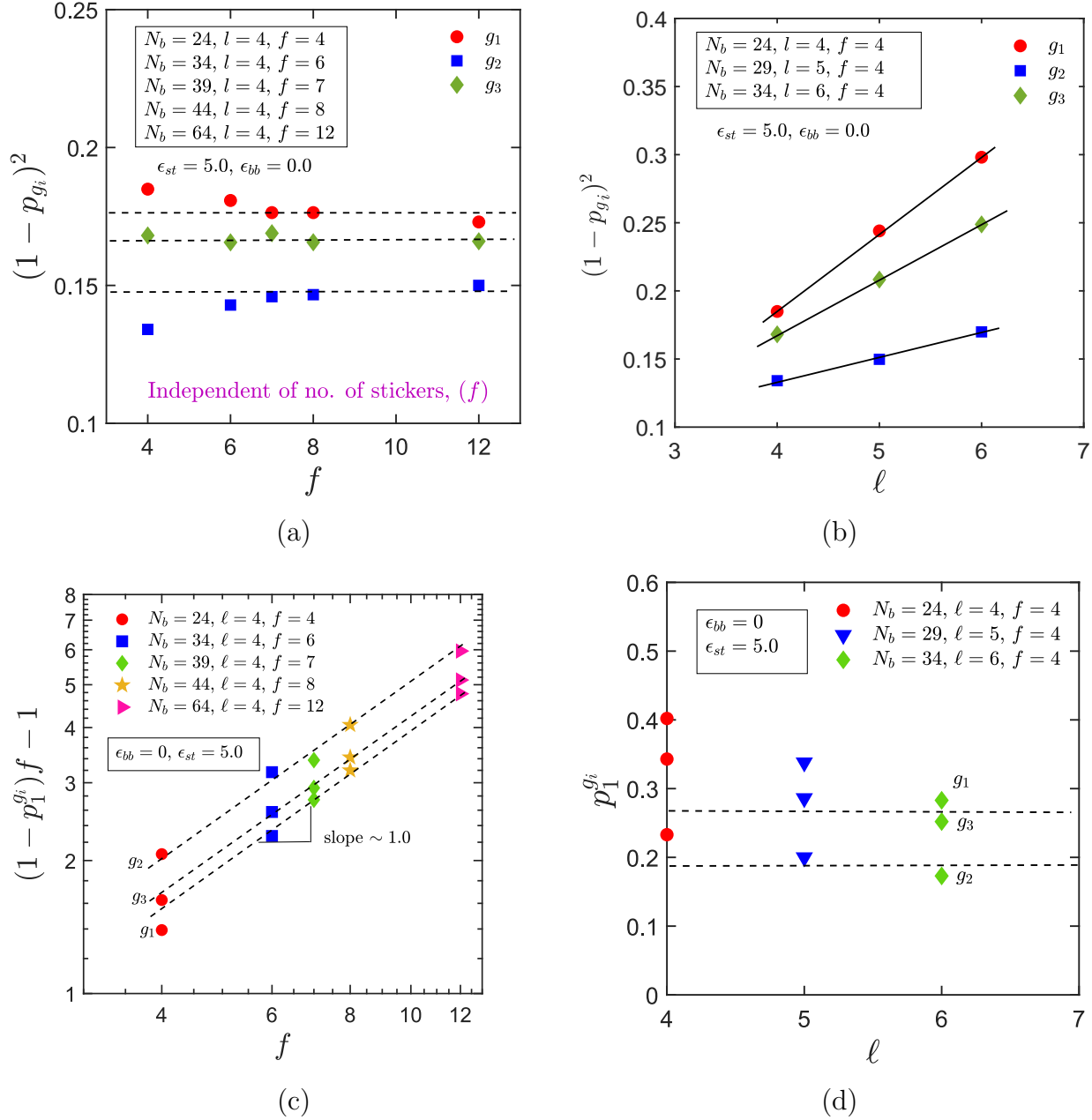


Figure 4.21: Scaling with the number of stickers per chain,  $f$ , and the spacer length,  $\ell$ , in Regime II, of the quantities  $(1 - p_{g_i})^2$  [(a) and (b), respectively], and  $[(1 - p_1^{g_i})f - 1]$  [(c) and (d), respectively], that occur in Eq. (4.14), for the different signatures of gelation.

concentration along the gelation line,

$$c_{g_i} \sim \left[ \frac{\hat{\tau}^{\frac{\nu\theta_2}{3\nu-1}}}{f g_{ss}} \right]^{\frac{3\nu-1}{\nu(3+\theta_2)-1}} \sim f^{-\frac{4}{5}} \quad (4.15)$$

where the assumptions of constant  $\hat{\tau}$  and  $\epsilon_{st}$ , and the values,  $\nu = 3/5$  and  $\theta_2 = 1/3$ , have been used to derive the second expression, which indicates that  $c_{g_i}$  depends only on  $f$  and not on  $\ell$ . It is clear from the results displayed in Fig. 4.22, that simulations validate the revised expression for the gelation line, Eq. (4.15), for all the three different signatures of gelation. The overlapping of data corresponding to different values of  $\ell$ , for systems with  $f = 4$ , also demonstrates the independence of  $c_{g_i}$  from the number of spacer monomers between stickers. It is undoubtedly desirable to verify experimentally both the general and restricted forms of the dependence of  $c_{g_i}$  on system parameters given in Eq. (4.15), as it would simultaneously permit an evaluation of the correctness of the scaling of  $p_2$  predicted by Eq. (4.1), the dependences revealed in Figs. 4.21, and the correct value of the des Cloizeaux exponent  $\theta_2$ .

## 4.8 Phase separation and the breakdown of scaling

A solution of sufficiently long polymers under poor solvent conditions will phase separate with increasing monomer concentration. This applies both to homopolymer solutions (Rubinstein and Colby, 2003), and to sticky polymer solutions (Dobrynin, 2004). In the case of sticky polymer solutions, we have calculated in Chapter 3 the second osmotic virial coefficient  $B_2$  by determining the potential of mean force,  $U(r)$ , between a pair of polymer chains with their centres of mass separated by a distance  $r$  (Dautenhahn and Hall, 1994)(Withers et al., 2003). We have shown that for a chain of length  $N_b$ , with given values of the backbone solvent quality  $\epsilon_{bb}$ , and spacer length  $\ell$ , this procedure can be used to determine the value of sticker strength  $\epsilon_{st}^\theta$  at which the sticky polymer chain as a whole behaves as a chain under  $\theta$ -solvent conditions, i.e., when  $B_2$  becomes zero. For instance, for a chain with  $N_b = 34$ ,  $\ell = 4$ , and  $\epsilon_{bb} = 0.3$ , the second virial coefficient  $B_2 = 0$  for  $\epsilon_{st}^\theta \approx 3.2$ . Note that even though the backbone monomers are under good solvent conditions (since  $\epsilon_{bb} = 0.3 < \epsilon_\theta = 0.45$ ), the chain as a whole is under

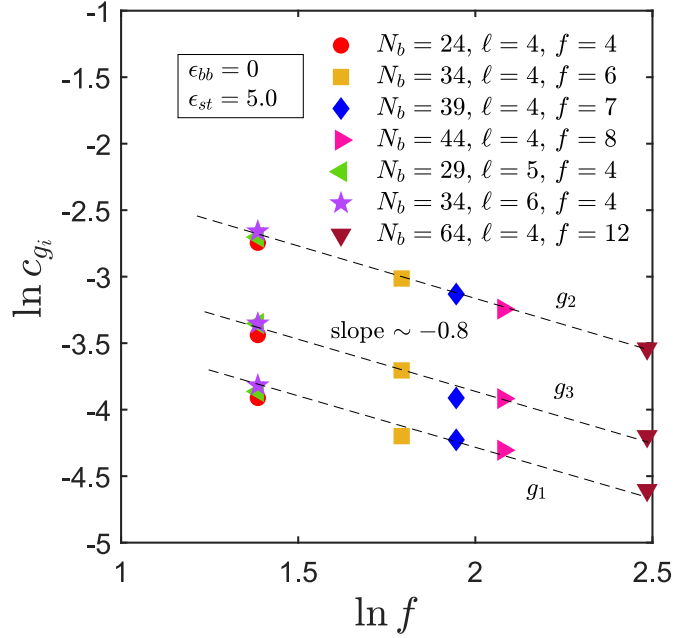


Figure 4.22: Gelation concentration,  $c_{g_i}$ , as a function of the number of stickers in a chain (see Eq. (4.15)), for the three different signatures of gelation in Regime II. The sticker strength and backbone solvent quality are kept constant at  $\epsilon_{st} = 5.0$  and  $\epsilon_{bb} = 0$ , respectively. Each symbol shape represents a system with a particular chain length  $N_b$ , spacer length  $\ell$  and number of stickers per chain  $f$  and the dashed lines are the scaling predictions for each of the gelation signatures.

$\theta$ -solvent conditions due to the affinity of the stickers for one another. It is clear then that a sticky polymer chain with  $N_b = 34$ ,  $\ell = 4$ ,  $\epsilon_{bb} = 0.45$  and  $\epsilon_{st} = 5$ , will be under poor solvent conditions (i.e., the second virial coefficient  $B_2 < 0$ ), since, firstly the backbone monomers are under  $\theta$ -solvent conditions, and secondly, the sticker strength,  $\epsilon_{st} = 5$ , is greater than  $\epsilon_{st}^\theta \approx 3.2$ , determined for the case  $\epsilon_{bb} = 0.3$ . We can anticipate that a solution of such sticky polymers will phase separate with increasing concentration, and indeed this seems to be the case as discussed below.

We have previously shown that simulation results validate the predictions of scaling theory for sticky polymers, as displayed in Figs. 4.4 for a range of concentrations. The plot of the ratio  $[p_2/(1 - p^2)]$  is reproduced in Fig. 4.23 (a), but this time at higher concentrations than shown previously. It is very clear that for sufficiently high concentrations, simulation data departs from the linear line representing the prediction of scaling theory, for both the approaches pursued here to simulate backbone monomers under  $\theta$ -solvent conditions.

It seems likely that the breakdown of scaling theory coincides with the occurrence of phase separation, as indicated in the snapshots from simulations displayed in Figs. 4.23 (b) and (c).

These figures represent snapshots of a system with  $N_b = 24$ ,  $\ell = 4$ , and  $\epsilon_{st} = 5.0$ , under  $\theta$ -solvent conditions for backbone monomers, at two different concentrations,  $c/c^* = 0.3$  and  $c/c^* = 1.0$ . The purple coloured beads belong to chains that are all a part of the same cluster. The grey coloured beads belong to chains that are not part of the cluster represented by the purple beads. At the relatively low concentration of  $c/c^* = 0.3$ , Fig. 4.23 (b) appears to suggest that there exist only small sized clusters, containing only a few chains, that are fairly homogeneously dispersed in the simulation cell. With increasing concentration, more free chains combine with existing clusters, along with the combination of clusters themselves, to give rise to increased cluster sizes, with more constituent chains in each cluster. At sufficiently high concentrations, such as at  $c/c^* = 1.0$ , the snapshot displayed in Fig. 4.23 (c) suggests that most of the chains have clumped together to form a single large cluster. Note that since the simulation box has periodic images in the three coordinate directions, all the purple beads representing the single cluster are in fact in the neighbourhood of each of the corners of the box. The aggregation of chains in the cluster does not span the system homogeneously, suggesting that the solution has phase separated at some concentration,  $0.3 < c/c^* < 1.0$ , which is the range in which the scaling theory also breaks down.

The situation is very different for a sticky polymer system in which the chains have backbone monomers under very good solvent conditions. Under these circumstances, as indicated schematically in Fig. 3.9, the sticker strength  $\epsilon_{st}^\theta$  required for the sticky chain as a whole to be under  $\theta$ -solvent conditions keeps increasing as  $\epsilon_{bb} \rightarrow 0$ . The solvent quality for the sticky chain as a whole remains good in spite of the presence of stickers, and phase separation does not occur with increasing monomer concentration. As a consequence, it can be anticipated that unlike for chains with backbone monomers under  $\theta$ -solvent conditions, scaling predictions will remain valid even at high concentrations. This has already been commented upon in the context of Fig. 4.4 in section 4.5.1, where it was pointed out the scaling relations remained valid even after the system is well into the gel phase. These observations are confirmed in Figs. 4.24, where in subfigure (a) it can be seen that the ratio involving the inter-chain degree of association scales with monomer concentration according

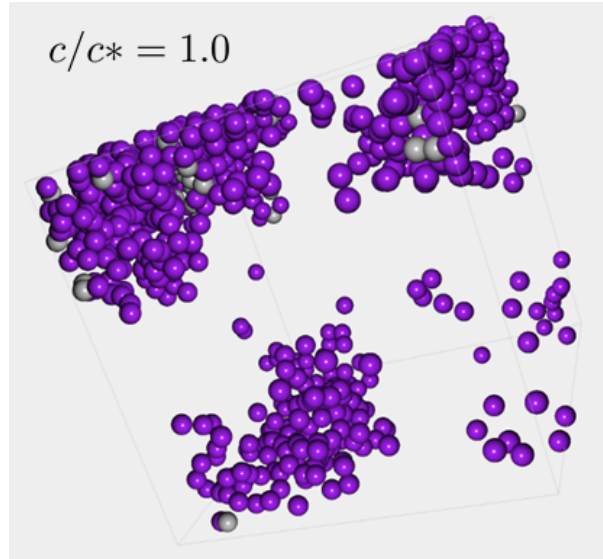
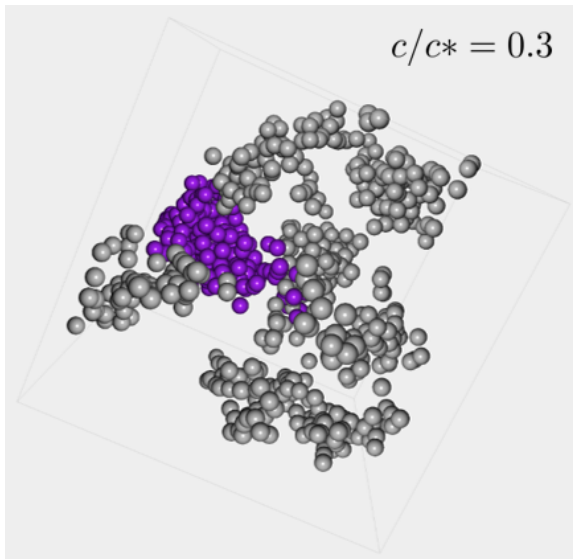
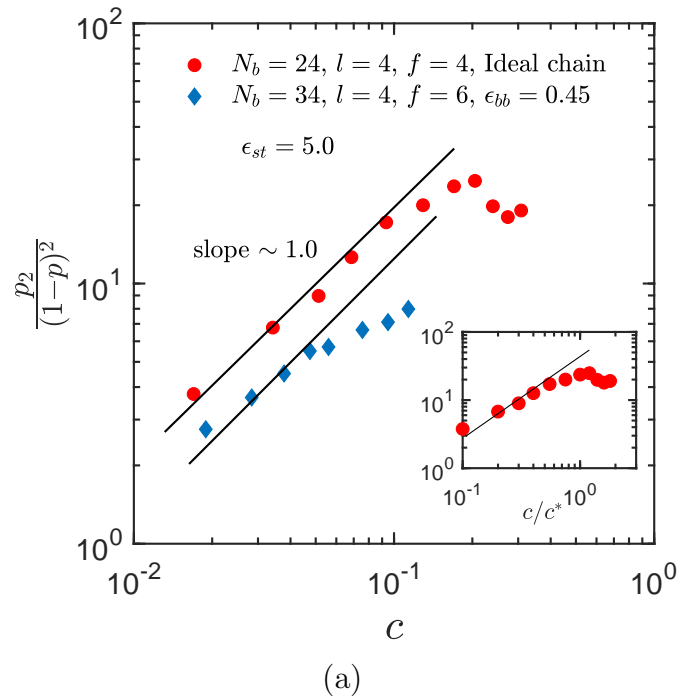


Figure 4.23: (a) Rescaled inter-chain degree of association as a function of monomer concentration, with backbone monomers under  $\theta$ -solvent conditions. For  $N_b = 24$ ,  $\theta$ -solvent conditions for the backbone are obtained by simulating ghost chains, while for  $N_b = 34$ ,  $\theta$ -solvent conditions for the backbone are obtained by using the SDK potential with  $\epsilon_{bb} = \epsilon_\theta = 0.45$ . Inset is a plot of the ratio versus  $c/c^*$ , for the case  $N_b = 24$ . The solid lines are drawn with slopes equal to the prediction by scaling theory, while symbols represent simulation data. (b) and (c) Snapshots from the simulations for the system with  $N_b = 24$  in sub-figure (a), at concentrations  $c/c^* = 0.3$ , and  $c/c^* = 1.0$ , respectively. The purple coloured beads belong to chains that are all a part of a single cluster, while the colour grey is used to represent beads in chains that do not belong to this cluster.

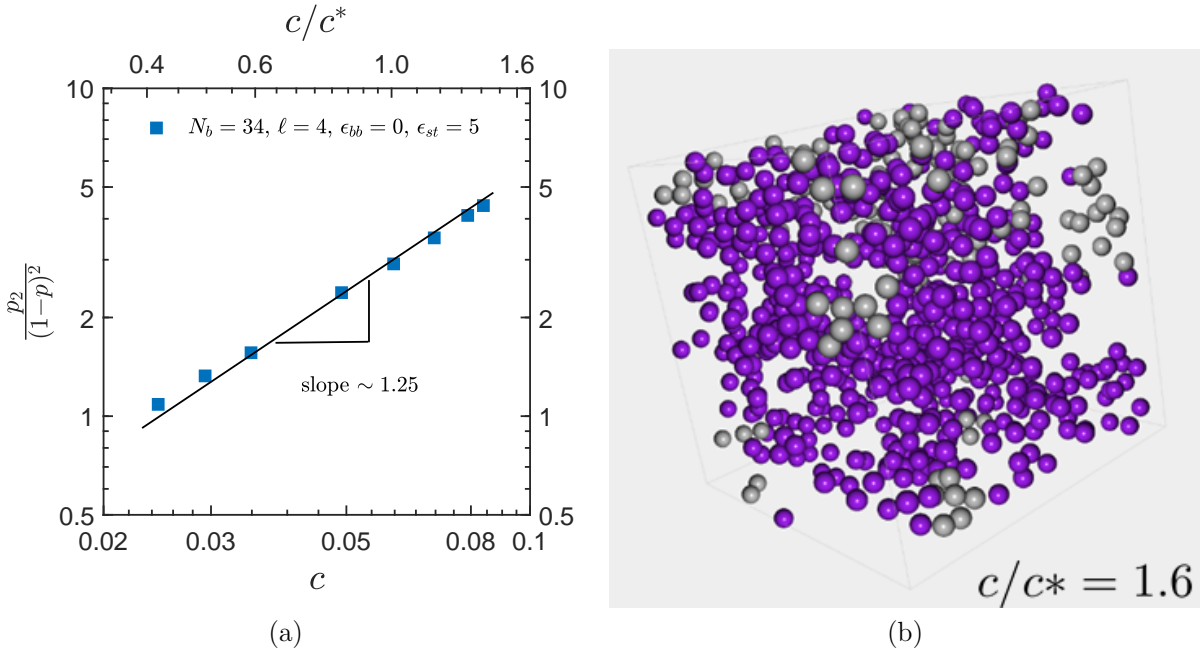


Figure 4.24: (a) Rescaled inter-chain degree of association as a function of monomer concentration, with backbone monomers under good solvent conditions corresponding to scaling regime II. The solid line is drawn with slope equal to the prediction by scaling theory, while symbols represent simulation data. (b) Snapshot from the simulations for systems with  $N_b = 34$ ,  $\ell = 4$ ,  $\epsilon_{bb} = 0$ , and  $\epsilon_{st} = 5.0$ , at concentration  $c/c^* = 1.6$ . Beads coloured purple are from chains that are all a part of the same system spanning cluster, while the grey coloured beads belong to chains that are not part of this cluster.

to the prediction of scaling theory even at the highest concentrations examined here, while subfigure (b) indicates that at the scaled concentration  $c/c^* = 1.6$ , there exists a system spanning cluster, and that the chains are distributed homogeneously across the system, with no sign of phase separation.

## 4.9 Summary and conclusions

A multi-particle Brownian dynamics simulation algorithm, with hydrodynamic interactions incorporated, which was formerly developed to describe semidilute polymer solutions (Jain et al., 2012), has been extended to describe associative polymer solutions. Pairwise interactions between monomers that are on the chain backbone and between the stickers themselves, have been described with the SDK potential (Soddemann et al., 2001)(Santra et al., 2019), which has advantages compared to other excluded volume potentials.

The main static properties that have been evaluated here are the intra-chain and inter-chain degrees of conversion  $p_1$  and  $p_2$ , respectively, and their dependence on system parameters such as the length of the chain,  $N_b$ , the number of stickers on a chain  $f$ , the distance between two stickers,  $\ell$ , the solvent quality parameter,  $\hat{\tau}$ , and the monomer concentration,  $c$ .

Comparisons have been carried out with the predictions of a lattice-based mean-field theory (Dobrynin, 2004) for ratios involving  $p_1$ ,  $p_2$ , and the total fraction of associated stickers  $p$ . The scaling theory identifies different regimes of behaviour depending on the quality of the solvent for the backbone monomers, the monomer concentration, and the density of stickers on a chain. The use of the SDK potential allows a careful choice of parameter values such that simulations can be used to explore each of the different scaling regimes. The cluster computation algorithm of Sevick et al. (Sevick et al., 1988) enables the calculation of the degrees of conversion, and the distribution of chain cluster sizes, along with their spatial extent.

The scaling theory of Dobrynin (Dobrynin, 2004) identifies two broad categories of behaviour based on whether the backbone monomers are under  $\theta$  or good solvent conditions. The latter category is further divided into three regimes depending on the relative magnitude of the spacer segment,  $\ell$ , the number of monomers in a thermal blob,  $g_T$ , and the number of monomers in a correlation blob,  $g_c$ . In Regime I,  $\ell < g_T < g_c$ , while in Regime II,  $g_T < \ell < g_c$ , and in Regime III,  $g_T < g_c < \ell$ .

Simulation results are shown to validate the predictions of Dobrynin's mean-field theory (Dobrynin, 2004) across a wide range of parameter values in all the scaling regimes, except for a slight deviation in the scaling of the intra-chain association fraction in Regime I, and data is shown to collapse onto master plots when plotted in terms of suitable quantities. An important conclusion of this study is that the value of the des Cloizeaux exponent (des Cloizeaux, 1980)(Duplantier, 1989)(Hsu et al., 2004) proposed by Dobrynin (Dobrynin, 2004),  $\theta_2 = 1/3$ , is accurate since it enables a collapse of the simulation data for all the scaling relations considered here.

The characterisation of gelation in these systems has also been examined. Three different signatures of gelation are identified: (i) the concentration  $c_{g_1}$  at which an incipient

system-spanning network occurs, (ii) the concentration threshold  $c_{g_2}$  at which the probability distribution of chain sizes becomes bimodal, and (iii) the monomer concentration  $c_{g_3}$  at which there is a maximum in the free-chain concentration. Each of these three different sol-gel transition signatures is found to occur at a different concentration. The identification of the concentration at the sol-gel transition enables a verification of the modified Flory-Stockmayer expression (Flory, 1953)(Stockmayer, 1944)(Dobrynin, 2004), which relates the degree of inter-chain conversion,  $p_2$ , to the degree of intra-chain conversion,  $p_1$ , and the number of stickers on a chain,  $f$ .

The only aspect of the phase behaviour of associative polymer solutions examined here is the gelation line, which separates the sol and gel phases. In this case as well, attention is restricted to the situation where the solvent quality and sticker strength are constant, and the sticky chain is in scaling Regime II. This simplification leads to an expression for the dependence of the concentrations at gelation,  $c_{g_i}$ ;  $i = 1, 2, 3$ , on the number of stickers on a chain. Simulation results confirm the prediction of scaling theory when the modified Flory-Stockmayer expression is used for  $p_2$ . This is an experimentally testable prediction of scaling theory and simulations which can facilitate the validation of both the des Cloizeaux exponent and the Flory-Stockmayer expression.

Finally, it is shown that phase separation occurs with increasing concentration for systems in which the backbone monomers are under  $\theta$ -solvent conditions. Curiously, the predictions of scaling theory are found to break down in the same range of concentrations in which phase separation is observed. On the other hand, for backbone monomer in good solvent conditions, there is no phase separation for the concentrations examined here, and scaling theory remains valid in both the sol and gel phases.

The success of the framework for the description of associative polymer solutions developed here in describing the predictions of static properties by scaling theory gives confidence that it can also be used to describe the equilibrium dynamics and the rheological behaviour of these solutions. In the following chapter we will investigate the dynamics and linear viscoelasticity of associative polymer solutions based on the framework developed in this chapter.

# Chapter 5

## Dynamic signatures of gelation in associative polymer solutions

### 5.1 Introduction

The unique rheological properties in solutions of associative polymers are contributed by the formation of reversible gels and the dynamics of sticker association. In Chapter 4 we have thoroughly investigated the static properties related to the scaling of intra-chain and inter-chain associations and different static signatures of gelation based on percolation transition, maxima in the free-chain concentration and onset of bimodality in the chain cluster size distribution. However, the relationship of these static signatures with the viscoelasticity and dynamic signatures of gelation is currently unknown. In this chapter we present different methods to characterise the dynamic signatures of gelation and correlate them with the static measures. We discuss the distinctions in the characteristics of gelation based on elasticity of the network and compare the scaling of the zero-shear rate viscosity and relaxation time in the post gel regime with the predictions of mean-field theory proposed by Semenov and Rubinstein (Rubinstein and Semenov, 1998)(Rubinstein and Semenov, 2001).

Associative polymers consist of stickers that can form intra-chain and inter-chain associations by the formation of reversible bonds. The onset of gelation in these systems is generally triggered by increase in monomer concentration, change in solution temperature, duration of reaction or increase in the strength of association, which we collectively define here as

the *triggering variable*. Gelation in polymeric solutions is typically characterised by carrying out small amplitude oscillatory shear flow experiments/simulations and calculating the viscoelastic response in terms of various properties such storage modulus ( $G'$ ), loss modulus ( $G''$ ) and loss tangent ( $\tan \delta$ , defined as the ratio of  $G''$  to  $G'$ ) (Winter, 2016)(Bromberg, 1998)(Thomas et al., 2009)(Wilson and Baljon, 2017)(Brassinne et al., 2017)(Suman and Joshi, 2020)(Ozaki et al., 2017). Generally, the storage and loss moduli as a function of the frequency of oscillation,  $\omega$ , for an unentangled homopolymer solution are well described by a Maxwell model with a single relaxation time, where there exists a terminal flow regime in the limit of low frequency. However, multi-sticker associative polymer solutions may exhibit broad power law relaxation spectra (Mewis et al., 2001)(Holten-Andersen et al., 2014)(Wagner and McKinley, 2017) with no readily discernible characteristic relaxation time scale, such that  $G' \sim G'' \sim \omega^n$  for a wide range of frequency (Winter, 2016)(Suman and Joshi, 2020). The onset of gelation for such systems is identified by plotting the loss tangent ( $\tan \delta$ ) as a function of *triggering variable* for a range of frequency, and then identifying the threshold value of the triggering variable for which  $\tan \delta$  becomes independent of frequency (Winter, 2016)(Suman and Joshi, 2020). The scale-free fractal microstructure of the transient network for multi-sticker systems is believed to lead to scale-free power law relaxation behaviour in time. However, this has not been systematically investigated and actual reason for such behaviour in multi-sticker polymer solutions is currently unknown. In associative polymer solutions, formation of a percolating network does not always guarantee the existence of an elastically active gel. Polymer chain length, monomer concentration, density of sticky groups along the polymer backbone are the parameters that determine the possibility of formation of an elastically active network (Brassinne et al., 2017)(Ozaki et al., 2017). It is interesting to note that depending on the elasticity of the network formed after gelation, the dynamic moduli ( $G'$  and  $G''$ ) may show power law scaling with no characteristic relaxation or a typical curve with a discernible relaxation time along with the terminal flow regime (Brassinne et al., 2017)(Ozaki et al., 2017)(Bromberg, 1998). For instance,  $G'$  and  $G''$  follow power-law scaling for elastically active networks, whereas, gels formed by association of relatively shorter chains do not exhibit a strong elastic response and their dynamic moduli show a terminal flow behaviour at low frequencies (Brassinne et al., 2017). Apart from the dynamic

moduli there are other alternative methods for the characterization of gelation in associative polymer solutions based on the scaling of zero-shear rate viscosity ( $\eta_p^0$ ) and terminal relaxation time ( $\tau$ ) with the triggering variable such as concentration or temperature (Bromberg, 1998)(Suman and Joshi, 2020)(Rubinstein and Semenov, 1998). For instance, the divergence of the zero-shear rate viscosity and terminal relaxation time at the onset of sol-gel transition are prominent dynamic signatures of gelation for strong elastically active gels (Suman and Joshi, 2020). However, for weak, thermo-reversible, transient gels, instead of divergence, both zero-shear rate viscosity and terminal relaxation time exhibit a sequence of power-law scaling in the post gel regime (Rubinstein and Semenov, 1998)(Rubinstein and Semenov, 2001)(Bromberg, 1998).

In this chapter, using Brownian dynamics, we have simulated systems of associative polymer solutions at finite concentration in the dilute and semi-dilute regimes at equilibrium and under shear flow to identify and characterise the dynamic signatures of gelation. As mentioned in Chapter 4, hydrodynamic interaction (HI) has a profound influence on the dynamics and viscoelasticity of polymer solutions. This implies that for associative polymer solutions both the short time sticker dynamics and the relaxation dynamics of the network as a whole are affected by hydrodynamic interaction. Thus, all the simulation results discussed in this chapter are carried out with HI. The scaling of dynamic properties such as  $G'$  &  $G''$ , zero-shear rate viscosity and relaxation times are investigated here to characterise gelation. Typically, the dynamic moduli ( $G'$  &  $G''$ ) and zero-shear rate viscosity are evaluated from non-equilibrium simulations or experiments involving simple and oscillatory shear flows. While these non-equilibrium setups are the only choice in experiments, in a numerical study the above mentioned dynamic properties can be easily calculated from equilibrium simulations. Most of these properties are computed here from stress auto-correlation and end-to-end vector auto-correlation functions which are obtained from equilibrium simulations. Here we have just provided a hint of the methodology that has been followed, while a further detail on the methods of evaluating dynamic properties from auto-correlation functions is given in subsequent sections. This chapter is organised as follows. The key governing equations for the simulations and computation of different dynamic properties are discussed in Section 5.2. In this section we compare the methods to calculate dynamic properties such

dynamic moduli and zero-shear rate viscosity from equilibrium and non-equilibrium simulations. The key results on dynamic properties such as zero-shear rate viscosity, dynamic moduli and relaxation time are presented in Section 5.3. In subsection 5.3.5, we discuss different measures of characteristic relaxation time based on stress auto-correlation, end-to-end vector auto-correlation function and zero-shear rate viscosity and compared the scaling of these properties with the predictions of scaling theory. The time scale associated with the sticker dynamics is also considered here in subsection 5.3.5. Finally, a summary of the key conclusions is presented in Section 5.4.

## 5.2 Governing equations

### 5.2.1 Model for associative polymer solutions

A bead-spring chain model, as described in Chapter 2, is implemented to simulate solutions of associative polymers using Brownian dynamics simulation algorithm. Multi-sticker polymer chains are modelled with sticker functionality,  $\varphi = 1$ , similar to that discussed in Chapter 2 and Chapter 4. For all the simulation results reported in this chapter, we use a value of the hydrodynamic interaction parameter  $h^* = 0.2$ .

### 5.2.2 Dynamic properties

The dynamic properties such as relaxation modulus, zero-shear rate viscosity, dynamic moduli ( $G'$  &  $G''$ ), investigated in this chapter, can be defined in terms of the components of stress-tensor (Bird et al., 1987b) for the polymer solutions. In the absence of external forces, the stress tensor ( $\boldsymbol{\sigma}^*$ ) (non-dimensionalized by  $n_p k_B T$ , where  $n_p$  is the number of polymer chains per unit volume), for a multi-chain system, can be shown to be (Stoltz, 2006)

$$\boldsymbol{\sigma}^* = \frac{\boldsymbol{\sigma}}{n_p k_B T} = \frac{1}{N_c} \left[ \sum_{\mu=1}^N \sum_{\nu=1}^N \langle \mathbf{r}_{\mu\nu} \mathbf{F}_{\mu\nu}^{\text{SDK}} \rangle + \sum_{\nu=1}^{N_c} \sum_{\nu=1}^{N_b-1} \langle \mathbf{Q}_{\nu} \mathbf{F}^c(\mathbf{Q}_{\nu}) \rangle \right] \quad (5.1)$$

Here,  $N_c$  is the total number of chains and  $N = N_c \times N_b$  is the total number of beads in the system. In the above equation, the first summation represents all the excluded volume and

associative interactions between backbone monomers and sticker monomers, where  $\mathbf{r}_{\mu\nu} = \mathbf{r}_\mu - \mathbf{r}_\nu$  is the vector between bead  $\mu$  and  $\nu$  and  $\mathbf{F}_{\mu\nu}^{\text{SDK}}$  is the force acting between the beads due to SDK potential. The second term represents the contribution from the spring force,  $\mathbf{F}^c(\mathbf{Q}_\nu)$ , due to the connector vector  $\mathbf{Q}_\nu = \mathbf{r}_{\nu+1} - \mathbf{r}_\nu$  between two adjacent beads along the backbone of a polymer chain.

Once the stress tensor is computed, we can easily estimate various dynamic properties and material functions for the polymer solutions. Here, we focus on the calculation of dynamic and linear viscoelastic properties in terms of relaxation modulus, shear viscosity and dynamic moduli. While these properties are typically computed from non-equilibrium simulations or experiments, there are sophisticated techniques for their calculation based on equilibrium simulations (Bird et al., 1987b)(Lee and Kremer, 2009)(Mours and Winter, 2012)(Wittmer et al., 2015b). We discuss some of these techniques in the subsequent sections.

### Relaxation modulus

The relaxation modulus,  $G(t)$ , is related to the stress auto-correlation function,  $C(t)$ , by the following equations,

$$G_{ij}(t) = G_{\text{eq}} + C_{ij}(t) \quad (5.2)$$

$$C_{ij}(t) = \frac{V}{k_B T} \langle \sigma_{ij}(0) \sigma_{ij}(t) \rangle \quad (5.3)$$

where  $G_{ij}(t)$  and  $C_{ij}(t)$  are the  $ij^{\text{th}}$  component of the relaxation modulus and stress auto-correlation function, respectively, and  $V$  is the total volume. The stress-autocorrelation function,  $C(t)$ , can be easily computed from equilibrium simulations using Eq. (5.3).  $G_{\text{eq}}$  is the equilibrium modulus which takes a non-zero value for systems having an infinite relaxation time (Wittmer et al., 2015b)(Wittmer et al., 2015a). For systems where  $G_{\text{eq}}$  is not zero, the general protocol is to estimate the equilibrium modulus by doing actual step strain experiments or simulations and allowing the system to relax. However, in the limit of  $G_{\text{eq}} = 0$ , the relaxation modulus is equal to the stress auto-correlation function. In such a case the relaxation modulus is exactly calculated from stress auto-correlation function. Additionally, the stress auto-correlation function may also be used for the determination of relaxation time scale, as explained in detail in Section 5.3.5. Since, at equilibrium the

stress-tensor,  $\boldsymbol{\sigma}$ , is isotropic, the relaxation modulus and stress auto-correlation function can be expressed as

$$G(t) = \frac{1}{3}(G_{xy}(t) + G_{xz}(t) + G_{yz}(t)) \quad (5.4)$$

$$C(t) = \frac{1}{3}(C_{xy}(t) + C_{xz}(t) + C_{yz}(t)) \quad (5.5)$$

Finally, we define a non-dimensionalized relaxation modulus and stress auto-correlation function given by

$$G^*(t) = \frac{G(t)}{n_p k_B T} \quad (5.6)$$

$$C^*(t) = \frac{C(t)}{n_p k_B T} \quad (5.7)$$

### Zero-shear rate viscosity

An important viscometric function to understand the dynamics and viscoelasticity of polymer solutions is the polymeric component of shear viscosity,  $\eta_p$ , calculated from shear flow experiments or simulations. For a planar shear flow, the velocity gradient tensor,  $\boldsymbol{\kappa} = (\nabla \mathbf{v})^T$ , presented in Eq. (2.1), is defined as,

$$\boldsymbol{\kappa} = \begin{bmatrix} 0 & \dot{\gamma} & 0 \\ 0 & 0 & 0 \\ 0 & 0 & 0 \end{bmatrix} \quad (5.8)$$

Here  $\dot{\gamma}$  is a constant shear rate. For such a system, the shear viscosity,  $\eta_p$ , is computed as

$$\eta_p = -\frac{\sigma_{xy}}{\dot{\gamma}} \quad (5.9)$$

While the study of shear viscosity at moderately high shear rates are important in non-linear rheology, for linear viscoelasticity the focus is on polymeric component of the zero-shear rate viscosity, defined as  $\eta_p^0 = \lim_{\dot{\gamma} \rightarrow 0} \eta_p$ , which is typically estimated by measuring the shear viscosity of the polymer solution subjected to multiple small values of shear rate, followed

by extrapolation to the zero-shear rate limit. Alternatively, for  $G_{\text{eq}} = 0$ ,  $\eta_p^0$  can be calculated from equilibrium simulations, by an application of the Green-Kubo relation (Fixman, 1981)(Pan et al., 2014a)(Lee and Kremer, 2009) to the stress auto-correlation function

$$\eta_p^{0*} = \frac{\eta_p^0}{n_p k_B T \lambda_H} = \int_0^\infty C^*(t) dt \quad (5.10)$$

In the above equation  $\eta_p^{0*}$  is the zero-shear rate viscosity non-dimensionalized by  $n_p k_B T \lambda_H$ , where  $n_p$  is the number of polymer chains per unit volume and  $\lambda_H = \zeta/4H$  is the typical time unit for Brownian dynamics simulations.

### Dynamic moduli ( $G'$ & $G''$ )

The elastic and viscous response of a viscoelastic fluid is generally characterised by the storage ( $G'$ ) and the loss ( $G''$ ) moduli, which are together referred to as the dynamic moduli. These properties are typically calculated from oscillatory shear flow (OSF) experiments or simulations. In numerical simulations an OSF is implemented by subjecting the simulation box to an oscillatory shear strain ( $\gamma(t)$ ), using Lees-Edwards boundary conditions (Lees and Edwards, 1972)(Jain, 2013)(Jain et al., 2015)(Myung et al., 2015), such that

$$\gamma(t) = \gamma_0 \sin(\omega t) \quad (5.11)$$

$$\dot{\gamma}(t) = \gamma_0 \omega \cos(\omega t) \quad (5.12)$$

where  $\gamma_0$  is the strain amplitude and  $\omega$  is the frequency of oscillation. The response to this oscillatory strain input produces an oscillatory stress component  $\sigma_{xy}(t)$ , from which  $G'$  and  $G''$  are extracted as follows

$$\begin{aligned} \sigma_{xy}(t) &= \sigma_0 \sin(\omega t + \delta) \\ &= \sigma_0 \cos(\delta) \sin(\omega t) + \sigma_0 \sin(\delta) \cos(\omega t) \end{aligned} \quad (5.13)$$

$$G'(\omega) = -\frac{\sigma_0 \cos(\delta)}{\gamma_0}, \quad G''(\omega) = -\frac{\sigma_0 \sin(\delta)}{\gamma_0} \quad (5.14)$$

Here  $\sigma_0$  is the amplitude of the stress response,  $\delta$  is the phase difference. It is important to note that  $\delta = 0$  for a Newtonian liquid, whereas,  $\delta = 90^\circ$  for a purely elastic solid. Since  $G'$  and  $G''$  determine the shear stress that is linearly dependent on the strain, these material functions are also linear viscoelastic properties. In the limit of very small strain amplitude ( $\gamma_0 \ll 1$ ),  $G'$  and  $G''$  can be estimated by Fourier transformation of the stress autocorrelation function,  $C(t)$ , (Mours and Winter, 2012)(Wittmer et al., 2015b) as described below,

$$G'(\omega) - G_{eq} = \int_0^\infty d(\omega t) C(t) \sin(\omega t) \quad (5.15)$$

$$G''(\omega) = \int_0^\infty d(\omega t) C(t) \cos(\omega t) \quad (5.16)$$

Finally, the dynamic moduli may be scaled by  $n_p k_B T$  to define the dimensionless storage modulus ( $G'^*$ ) and loss modulus ( $G''^*$ ).

For associative polymer solutions which undergo sol-gel transition with increase in monomer concentration, the characterization of the dynamic signatures of gelation depends on the behaviour of these linear viscoelastic properties as a function of monomer concentration. In the following section we present the results obtained from our simulations for different dynamic and viscoelastic properties and compare them with the scaling predictions of the mean-field theory proposed by Semenov and Rubinstein (Rubinstein and Semenov, 1998)(Rubinstein and Semenov, 2001).

### 5.3 Results and discussions

In Section 4.7 of Chapter 4 a detailed discussion on the characterization of different static signatures of gelation based on percolation transition ( $g_1$ ), onset of bimodality in the chain cluster size distribution ( $g_2$ ) and maxima in the free chain concentration ( $g_3$ ) was presented. The key findings from this study are that each of these different signatures occur at different values of scaled concentration,  $c/c^*$ , and these concentrations are independent of the chain length ( $N_b$ ) for a given spacer length ( $\ell$ ), backbone monomer interaction strength ( $\epsilon_{bb}$ ) and

sticker strength ( $\epsilon_{st}$ ). In the present chapter, we find the dynamic signatures of gelation in associative polymer solutions from the scaling of zero-shear rate viscosity and terminal relaxation time, and correlate them with the static measures.

The simulations carried out to study the dynamic properties consist of multi-sticker associative polymer solutions at finite concentrations with number of beads,  $N_b = 24$ , spacer length,  $\ell = 4$  and  $f = 4$  stickers per chain with an athermal solvent quality for the backbone,  $\epsilon_{bb} = 0$ , and a sticker strength of  $\epsilon_{st} = 5.0$ . For this specific system the three static signatures of gelation are observed at  $c_{g_1}/c^* \approx 0.3$ ,  $c_{g_2}/c^* \approx 1.0$  and  $c_{g_3}/c^* \approx 0.5$ , where the subscripts  $g_1$ ,  $g_2$  and  $g_3$  denote gelation signature at percolation transition, onset of bimodality and free chain maxima, respectively. Most of the simulations reported here are at equilibrium except for a few non-equilibrium shear flow simulations which are carried out to establish validity of the Green-Kubo relation. A typical simulation consists of a pre-equilibration run of about 3 to 4 Rouse relaxation times for a system of chains with only backbone monomers and no stickers, followed by the introduction of stickers and an equilibration run of about 5 Rouse relaxation times. Finally, sampling is carried out over a production run of about 5 to 20 Rouse relaxation times. During the production run, dynamic properties are calculated as a function of time from each independent trajectory. Ensemble averages and error of mean estimates of different dynamic properties are then computed over a collection of 500 to 1000 such independent trajectories. All simulations with HI (with  $h^* = 0.2$ ) have been carried out with a non-dimensional time-step  $\Delta t = 0.005$ .

### 5.3.1 Scaling of the chain cluster size distribution

Before examining the relaxation time scales and viscoelastic properties of associative polymer solutions at gelation transition, it is important to understand the structural changes that the associating network undergoes during this process. It has been shown in Section 4.7, that with increase in polymer concentration the chain cluster size increases, which results in the bimodality of the chain cluster size distribution and formation of much denser system spanning networks. Additionally, at the gel point the material structure becomes self-similar with no characteristic length scale and the cluster size distribution shows a power law scaling,  $P(m) \sim m^{-\tau_F}$ , where  $P(m)$  is the probability of finding a cluster of size  $m$  and the exponent

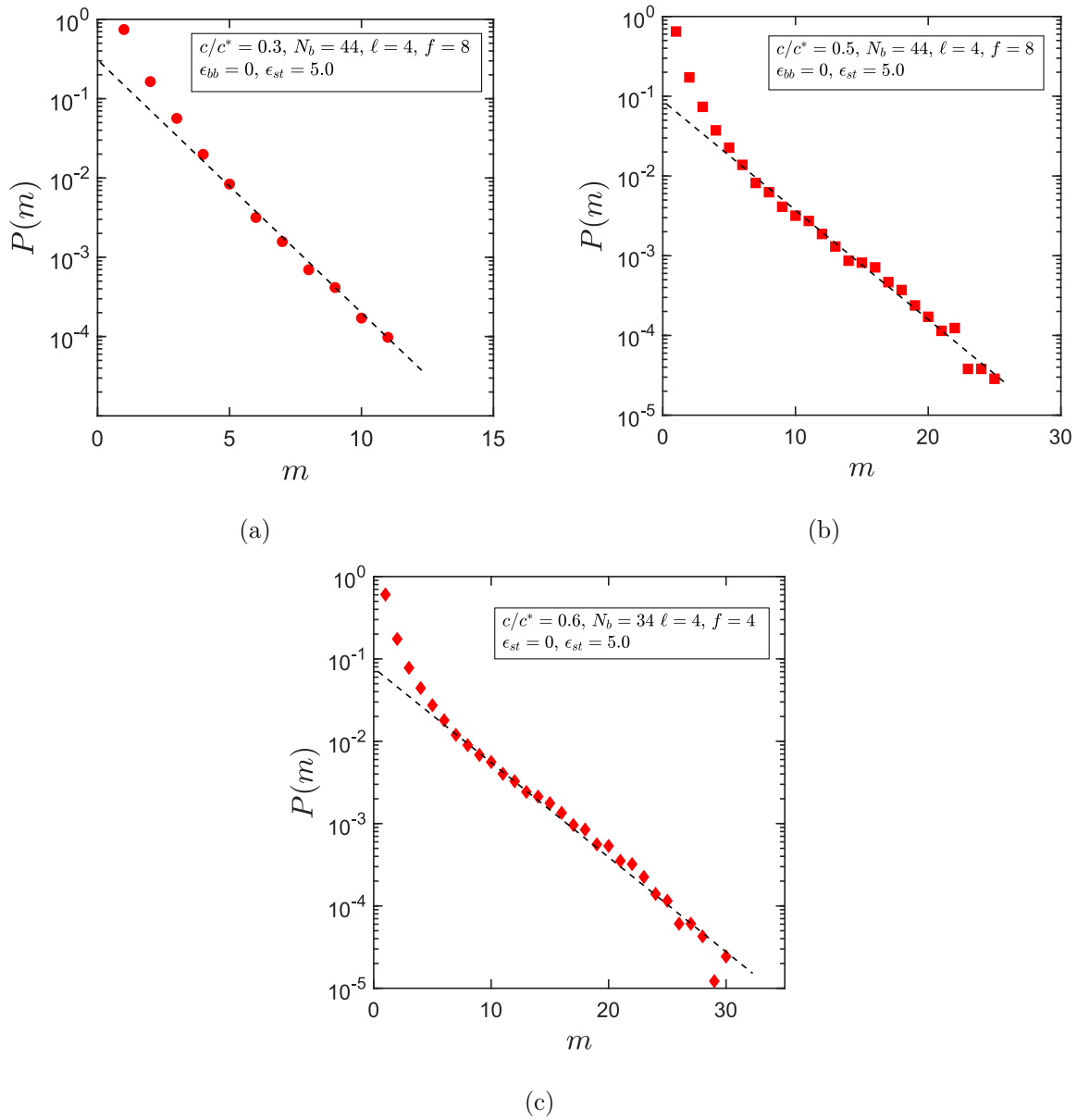


Figure 5.1: Chain cluster size distribution in semi-log scale for systems of associative polymers with spacer length  $\ell = 4$ ,  $\epsilon_{bb} = 0$  and  $\epsilon_{st} = 5.0$  at (a)  $c/c^* = 0.3$ ,  $N_b = 44$ , (b)  $c/c^* = 0.5$ ,  $N_b = 44$  and (c)  $c/c^* = 0.6$ ,  $N_b = 34$ . The solid red symbols are simulation data and the exponential decay of the cluster size distribution is shown by the dashed black lines.

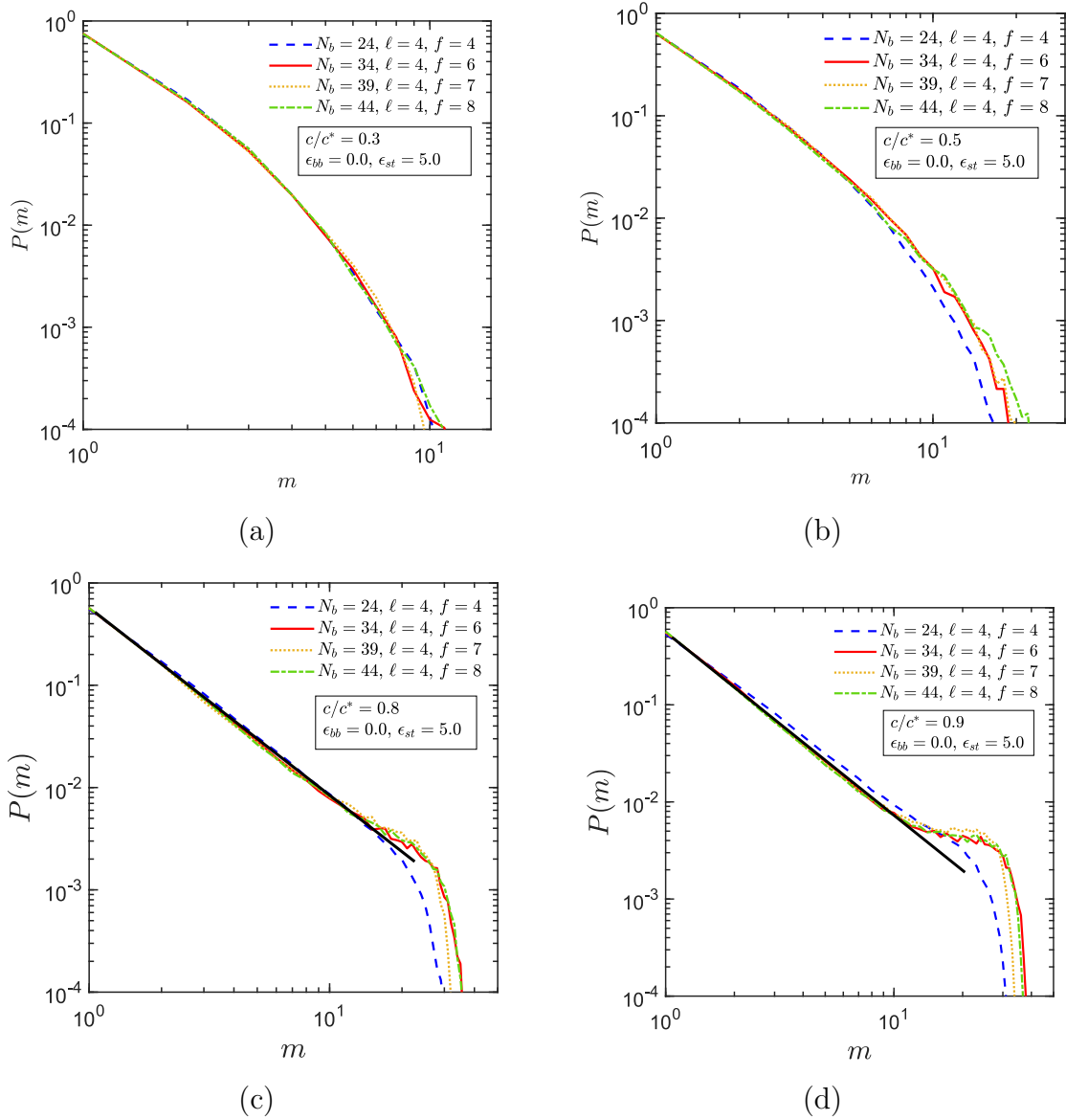


Figure 5.2: Chain cluster size distribution in log-log scale for systems of associative polymers with spacer length  $\ell = 4$ ,  $\epsilon_{bb} = 0$  and  $\epsilon_{st} = 5.0$  at different values of  $c/c^* = \{0.3, 0.5, 0.8, 0.9\}$  and different chain lengths,  $N_b$ . The power-law behaviour of the cluster size distribution is shown by the solid black lines in (c) and (d).

$\tau_F$  is often called the Fisher exponent (Stauffer et al., 2007)(Ozaki et al., 2017). Here, we have investigated the chain cluster size distribution,  $P(m)$ , of associative polymer solutions at different scaled concentrations,  $c/c^*$ , and different chain lengths,  $N_b$ , with spacer length,  $\ell = 4$ , backbone interaction strength,  $\epsilon_{bb} = 0$  and sticker association strength,  $\epsilon_{st} = 5.0$ . At low concentrations, such as  $c/c^* = 0.3, 0.5, 0.6$ , the probability of finding large cluster decreases exponentially as displayed in Figs. 5.1, whereas, at about  $c/c^* = 0.8$  and above the cluster size distributions, shown in Figs. 5.2 (c) and (d), indicate a power law scaling for a significantly wide range of values of cluster size,  $m$ . It is also noted that  $P(m)$  becomes independent of chain length with increase in  $N_b$ . The shouldering of the chain cluster size distribution observed at higher value of  $c/c^*(= 0.9)$  is because of the onset of bimodality in the distribution. From this analysis we interpret that the onset of gelation transition, based on the power-law scaling of the cluster size distribution, happens at about  $c/c^* \approx 0.8$ , which lies in between the  $c_{g3}/c^*$  and  $c_{g2}/c^*$ . This is another static signature of gelation which along other static signatures guide us to explore the range of concentration at which dynamic signatures are to be observed.

### 5.3.2 Stress auto-correlation function

In order to calculate the relaxation modulus, zero-shear rate viscosity or dynamic moduli from equilibrium simulations, it is first required to compute the non-dimensional stress-auto correlation function,  $C^*(t)$ . The stress auto-correlation function is evaluated for a range of scaled monomer concentration,  $c/c^*$ , in the dilute and semi-dilute regimes with chain length  $N_b = 24$ , spacer length,  $\ell = 4$ ,  $\epsilon_{bb} = 0$  and  $\epsilon_{st} = 5.0$ , as shown in Fig. 5.3. The decay in the stress auto-correlation function, obtained from simulations, is generally fitted with a sum of exponentials (Pan et al., 2014a), as given below, and all the subsequent calculations are carried out using the fit

$$C^*(t) = \sum_{i=1}^n a_i \exp(b_i t) \quad (5.17)$$

Here,  $a_i$  and  $b_i$  are the fitting parameters and  $n$  is the number of exponentials used to fit the auto-correlation function. All the stress auto-correlation functions evaluated here are typically fitted with 6 to 7 exponentials. From this fit, we can estimate the longest relax-

ation time by the relation,  $\tau_{max} = -\max\{1/b_i\}$ . Several other methods to estimate the longest relaxation time and their scaling with monomer concentration are discussed further in Section 5.3.5. In the following sections we present the linear viscoelastic properties, such as zero-shear rate viscosity and dynamic moduli, obtained from the stress auto-correlation function and their scaling with concentration to characterize the dynamic signatures of gelation.

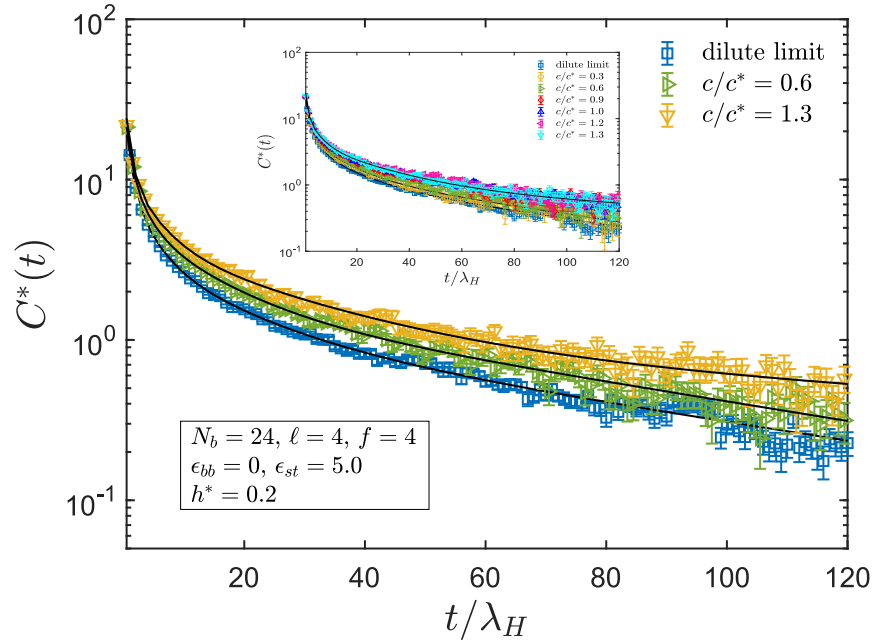


Figure 5.3: Non-dimensionalized stress auto-correlation function,  $C^*(t)$ , for systems of associative polymers with  $N_b = 24$ ,  $\ell = 4$ ,  $f = 4$ ,  $\epsilon_{bb} = 0$  and  $\epsilon_{st} = 5.0$  at different values of scaled monomer concentration,  $c/c^*$ , in the dilute and semi-dilute regimes. The solid black lines are fit to the simulation data using a sum of exponentials. The inset shows the entire range of  $c/c^*$  covered in the study.

### 5.3.3 Zero-shear rate viscosity

Once the stress auto-correlation function,  $C^*(t)$ , is evaluated, the relaxation modulus,  $G^*(t)$ , can be directly equated to  $C^*(t)$  subject to  $G_{eq} = 0$  (see Eq. (5.2)), which, as discussed shortly, is shown to be the case for the systems of polymer solutions studied here. Under such a condition, the zero-shear rate viscosity,  $\eta_p^{0*}$ , can be estimated by using the Green-Kubo relation defined in Eq. (5.10). However, a more direct method of estimating  $\eta_p^{0*}$  is

by performing shear flow simulations under very low shear rates and then extrapolating the value of the shear viscosity to the limit of zero-shear rate. Fig. 5.4 presents the non-dimensional shear viscosity,  $\eta_p^*$ , as a function of dimensionless shear rate,  $\dot{\gamma} \lambda_H$  (in a range of very small values of shear rate), at different  $c/c^*$ , where the extrapolated values of  $\eta_p^*$  in the limit of  $\dot{\gamma} \lambda_H \rightarrow 0$  are in good agreement with the zero-shear rate viscosity computed from Eq. (5.10), which are represented by the filled symbols. By considering these few representative concentrations for the systems of associative polymer solutions, we have illustrated that both the methods produce the same zero-shear rate viscosity, which implies that the equilibrium modulus,  $G_{\text{eq}}$ , is essentially 0.

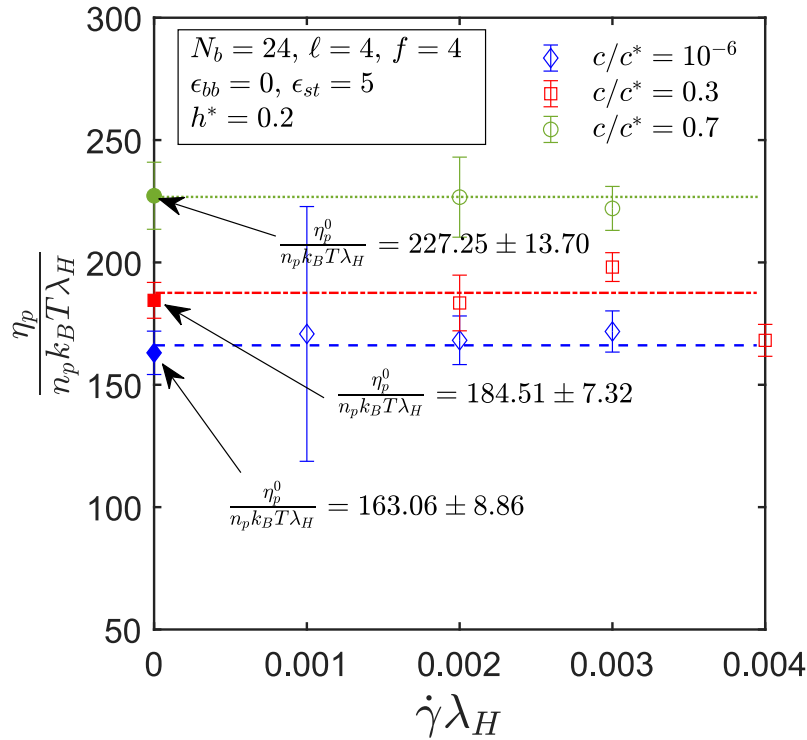


Figure 5.4: Polymeric component of the non-dimensionalized shear viscosity,  $\eta_p^* = \frac{\eta_p}{n_p k_B T \lambda_H}$ , as a function of non-dimensional shear rate ( $\dot{\gamma} \lambda_H$ ) for different values of monomer concentration,  $c/c^*$ . The open symbols are the values of  $\eta_p^*$  calculated from shear flow simulations and filled symbols are the values of zero-shear rate viscosity,  $\eta_p^{0*}$ , evaluated from Eq. (5.10).

Using the Green-Kubo relation to estimate the zero-shear rate viscosity,  $\eta_p^{0*}$ , we now investigate the scaling of  $\eta_p^{0*}$  with concentration,  $c/c^*$ . In Fig. 5.5, the ratio of zero-shear rate viscosity at finite concentration,  $\eta_p^{0*}$ , to its value in the dilute limit,  $\eta_{p0}^{0*}$ , is plotted against

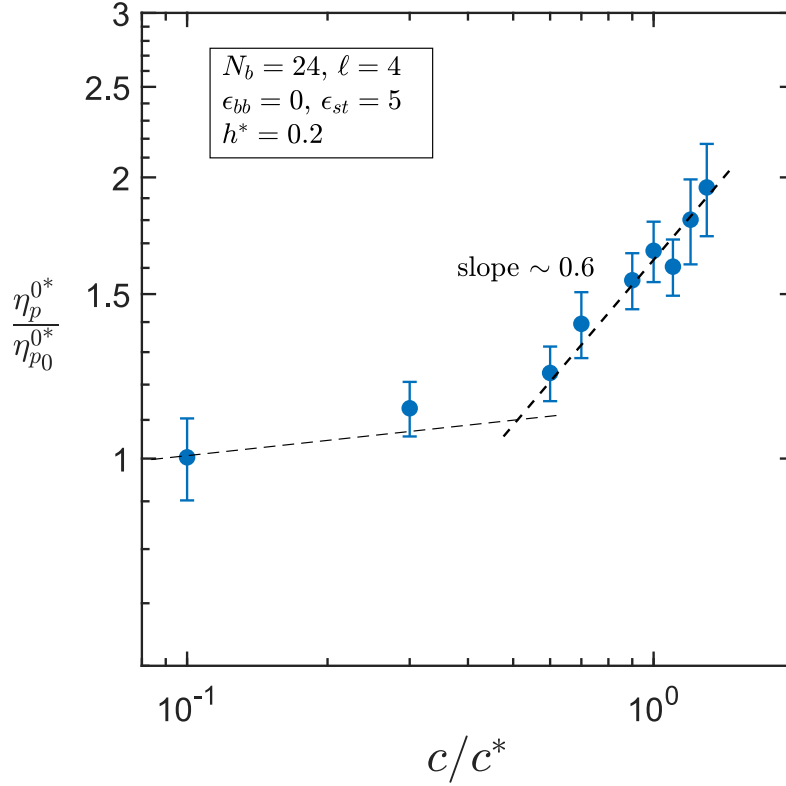


Figure 5.5: Scaling of the ratio of zero-shear rate viscosity at finite concentration,  $\eta_p^{0*}$ , to its value in the dilute limit,  $\eta_{p0}^{0*}$ , with the scaled concentration,  $c/c^*$ , for solutions of associative polymers with  $N_b = 24$ ,  $\ell = 4$ ,  $f = 4$ ,  $\epsilon_{bb} = 0$  and  $\epsilon_{st} = 5.0$ . The symbols from simulations and the dashed lines with slope 0.6 is obtained from least square fit.

the scaled monomer concentration,  $c/c^*$ , for associative polymer solutions with chain length,  $N_b = 24$ , spacer length  $\ell = 4$ , number of stickers per chain  $f = 4$ ,  $\epsilon_{bb} = 0$  and  $\epsilon_{st} = 5.0$ . The scaling of the normalised zero-shear rate viscosity,  $\eta_p^{0*}/\eta_{p0}^{0*}$ , with scaled concentration indicates a cross-over at  $c/c^* \approx 0.5$ , beyond which the scaling exponent takes an asymptotic value of 0.6. Interestingly, the maxima in the free chain concentration for this system, which occurs at  $c/c^* = 0.5$ , coincides with the cross-over concentration of the viscosity scaling. In the mean-field theory developed by Rubinstein and Semenov (Rubinstein and Semenov, 1998) for associative polymer solutions, the zero-shear rate viscosity ( $\eta_p^0$ ) in the post gel regime, close to the gel-point, is shown to scale with the relative distance,  $\Delta$ , from the gelation concentration ( $c_g$ ), where  $\Delta = (c - c_g)/c_g$ , as

$$\eta_p^0 \sim \Delta^{1/(3\nu-1)} \quad (5.18)$$

where,  $\nu = 0.6$  is the Flory exponent, which implies that the exponent  $1/(3\nu - 1) = 1.25$ . Defining  $\Delta = (c - c_g)/c_g$  and considering  $c_g/c^* = 0.5$ , we find  $\eta_p^0$  to scale with a slope of 1.25 in the post-gel regime, as shown in Fig. 5.6. Note that the zero-shear rate viscosity plotted vs  $\Delta$  in Fig. 5.6 is not scaled with the number density of polymer chain,  $n_p$  (which is related to monomer concentration  $c$ ), in order to bring out the concentration dependence explicitly. This is one of the dynamic signatures of gelation which is also in agreement with the prediction by the mean-field theory (Rubinstein and Semenov, 1998) and as observed by Bromberg (Bromberg, 1998) in experiments with thermo-reversible hydrogels.

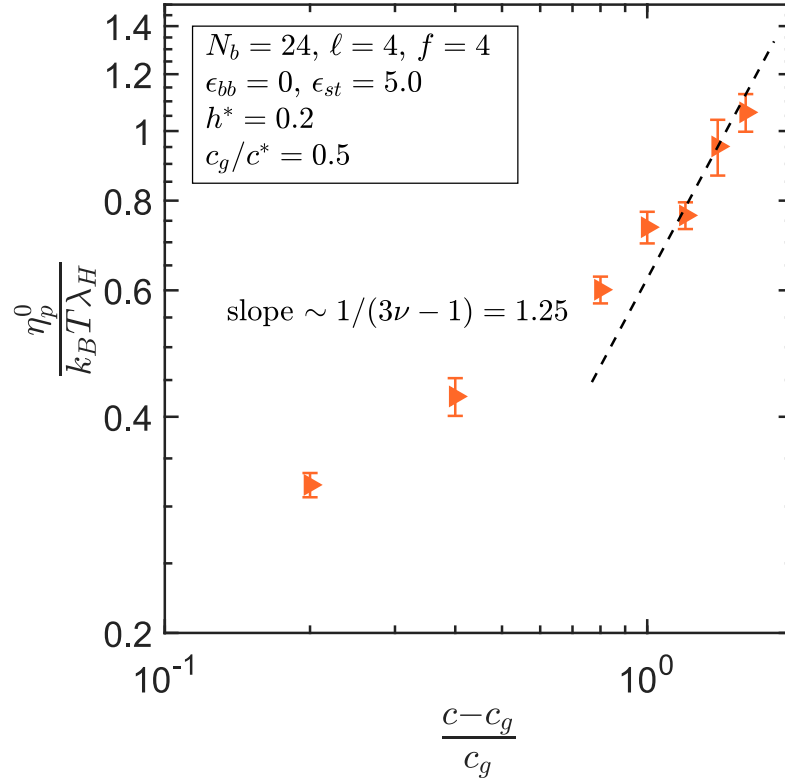


Figure 5.6: Scaling of the zero-shear rate viscosity with the relative distance from the gelation concentration ( $c_g$ ) in the post gel regime. Here the gelation concentration is at  $c_g/c^* = 0.5$ . The symbols are the simulation data and the dashed line is drawn with the slope predicted by the mean-field theory.

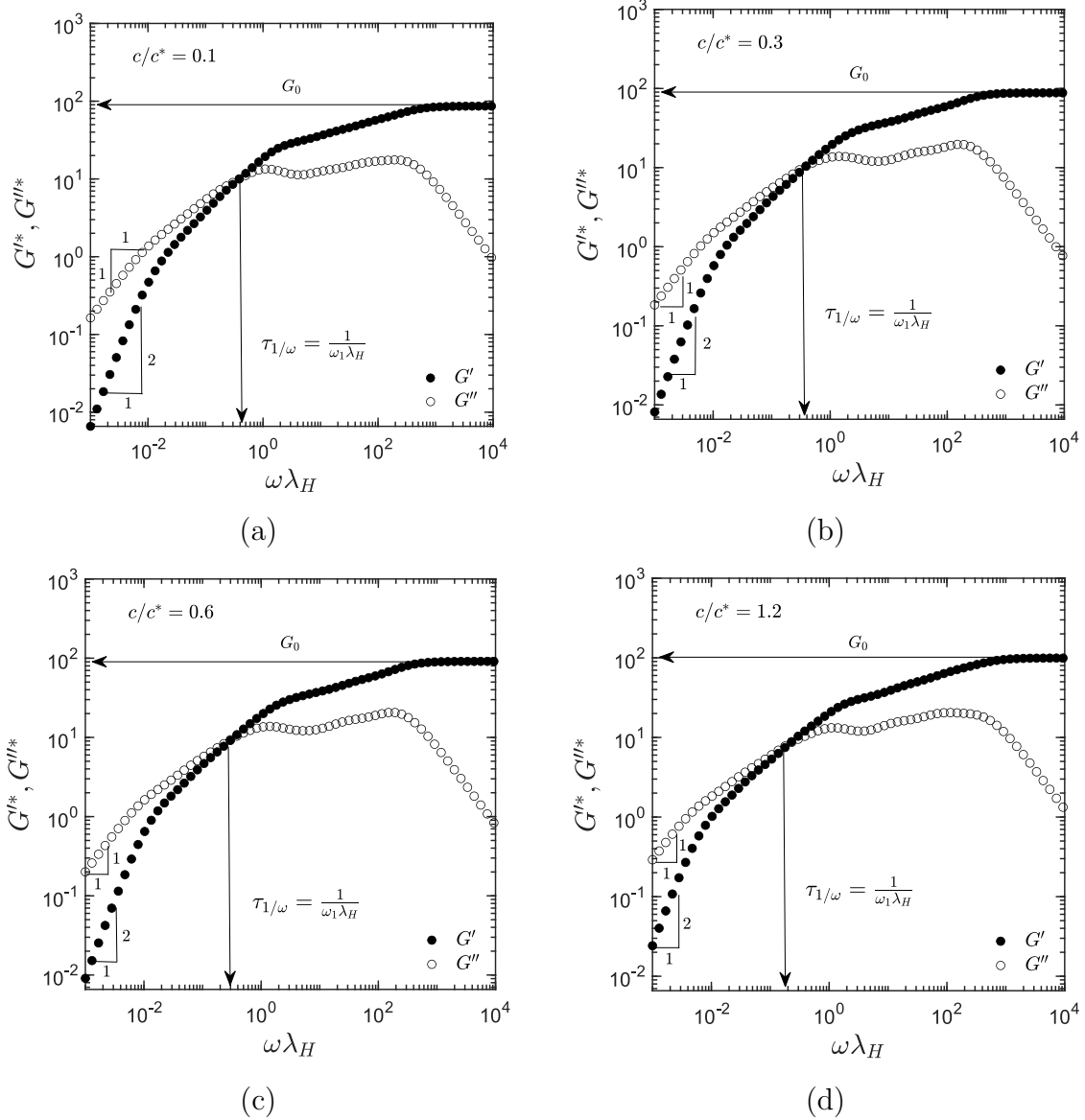


Figure 5.7: Non-dimensional storage ( $G'^*$ ) and loss ( $G''^*$ ) moduli of associative polymer solutions as a function of dimensionless frequency,  $\omega \lambda_H$ , for different values of  $c/c^*$  with chain length  $N_b = 24$ , spacer length  $\ell = 4$ , number stickers per chain  $f = 4$ , backbone monomer interaction strength  $\epsilon_{bb} = 0$  and sticker strength  $\epsilon_{st} = 5.0$ . The filled and open circles in the plots are  $G'$  and  $G''$ , respectively. The inverse of the frequency corresponding to the point of intersection of  $G'$  and  $G''$  curves represents the characteristic relaxation time  $\tau_{1/\omega} = 1/(\omega_1 \lambda_H)$ .  $G_0$  indicates the elastic modulus. The slopes of  $G'^*$  and  $G''^*$  in the terminal flow regime are 2 and 1, respectively, as indicated in the figures.

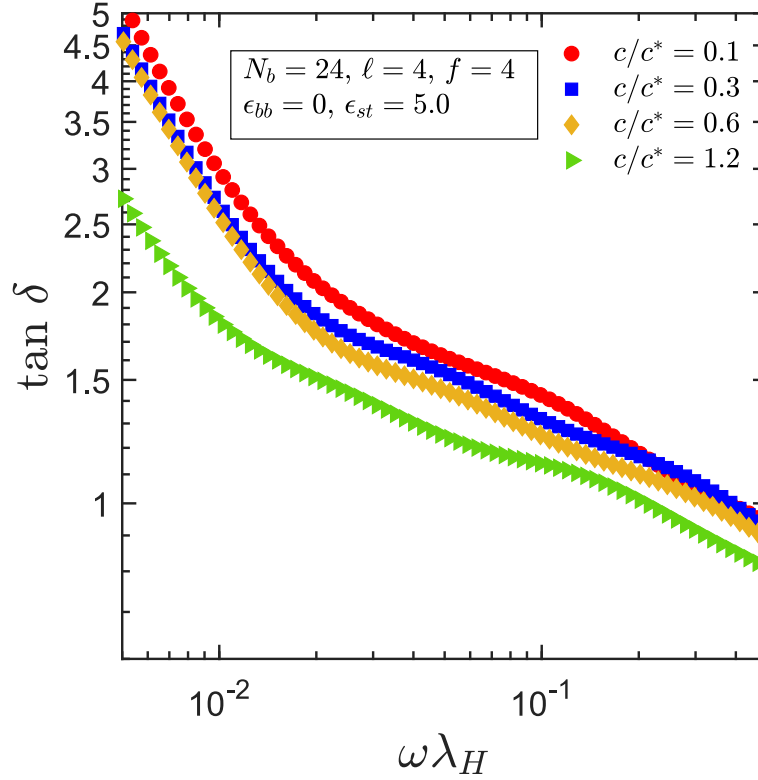


Figure 5.8: Variation of the loss tangent,  $\tan \delta$ , with the dimensionless frequency,  $\omega \lambda_H$ , at different values of  $c/c^*$  for associative polymer solutions with  $N_b = 24$ ,  $\ell = 4$ ,  $f = 4$ ,  $\epsilon_{bb} = 0$  and  $\epsilon_{st} = 5.0$ .

### 5.3.4 Storage ( $G'$ ) and loss ( $G''$ ) moduli

Gelation in associative polymer solutions is typically characterized by the frequency dependence of two linear viscoelastic properties, storage,  $G'(\omega)$ , and loss,  $G''(\omega)$ , moduli (also known as dynamic moduli), measured from small amplitude oscillatory shear flow (SAOS). As mentioned in Section 5.2.2, the dynamic moduli can also be calculated from equilibrium data by Fourier transformation of the stress auto-correlation function, given by Eq. (5.15) and Eq. (5.16). This has been illustrated in Appendix D for Rouse chains in a dilute solution, where the dynamic moduli computed from the stress auto-correlation is compared with that from SAOS and the analytical solution. For the associative polymer solutions, considered in the present study, we compute  $G'$  and  $G''$  from the stress auto-correlation function for a range of concentration,  $c/c^*$ , and investigate their frequency dependencies in the pre and post-gel regimes. Figs. 5.7 display the non-dimensional storage ( $G'^*$ ) and loss ( $G''^*$ ) moduli as a function of frequency for different concentrations,  $c/c^*$ , with chain length  $N_b = 24$ ,

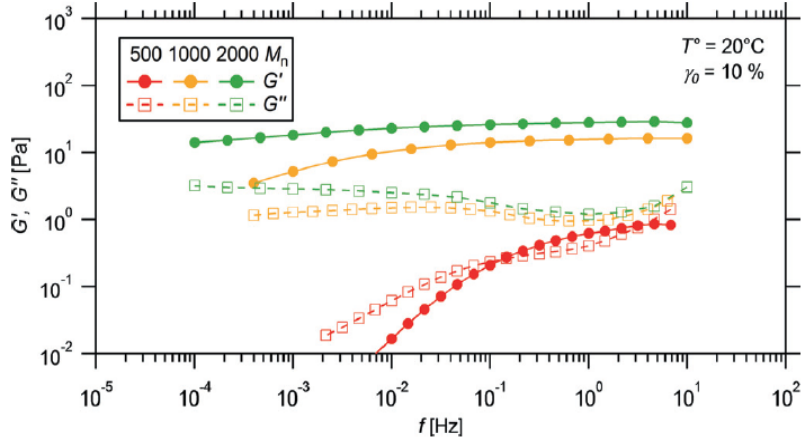


Figure 5.9: Effect of chain lengths on storage ( $G'$ ) and loss ( $G''$ ) moduli of ligand-decorated ultra-high molecular weight copolymers. This figure is reproduced from the article published by Brassine et al., *Journal of Rheology*, 61(6), 1123–1134 (2017).

spacer length  $\ell = 4$ , backbone monomer interaction strength  $\epsilon_{bb} = 0$  and sticker strength  $\epsilon_{st} = 5.0$ . The inverse of the frequency corresponding to the point of intersection of  $G'^*$  and  $G''^*$  is defined as a characteristic relaxation time of the polymer solutions,  $\tau_{1/\omega} = 1/(\omega_1 \lambda_H)$ , where  $\omega_1$  is the intersection frequency. For each concentration,  $c/c^*$ , the storage modulus,  $G'^*$ , in the limit of high frequency, saturates to a value  $G_0$ , which is identified as the elastic modulus. In addition, the variation of loss tangent, defined as  $\tan \delta = G''/G'$ , with frequency,  $\omega \lambda_H$ , is presented for different concentrations in Fig. 5.8. For all the concentrations, shown in Figs. 5.7, there exists a unique point of interaction between  $G'^*$  and  $G''^*$ , along with a terminal flow regime in the limit of low frequencies, where  $G' \sim \omega^2$  and  $G'' \sim \omega$  (Bird et al., 1987b)(Brassinne et al., 2017). Considering  $c_g/c^* = 0.5$  as the gel-point, these observations imply the existence of a finite terminal relaxation time for systems of associative polymer solutions in both the pre-gel and post-gel regimes. These results diverge from the typical power-law behaviour of  $G'(\omega)$  and  $G''(\omega)$ , with no discernible relaxation time scale, observed for physically or chemically associated polymer solutions with elastically active networks. Besides, the loss tangent,  $\tan \delta$ , becomes independent of frequency at the gelation concentration for a typical gel-forming polymer solution, which is not observed for the present systems, as  $\tan \delta$  decreases with frequency at all the values of  $c/c^*$ , as shown in Fig. 5.8. However, the nature of the dynamic moduli observed for the present systems is

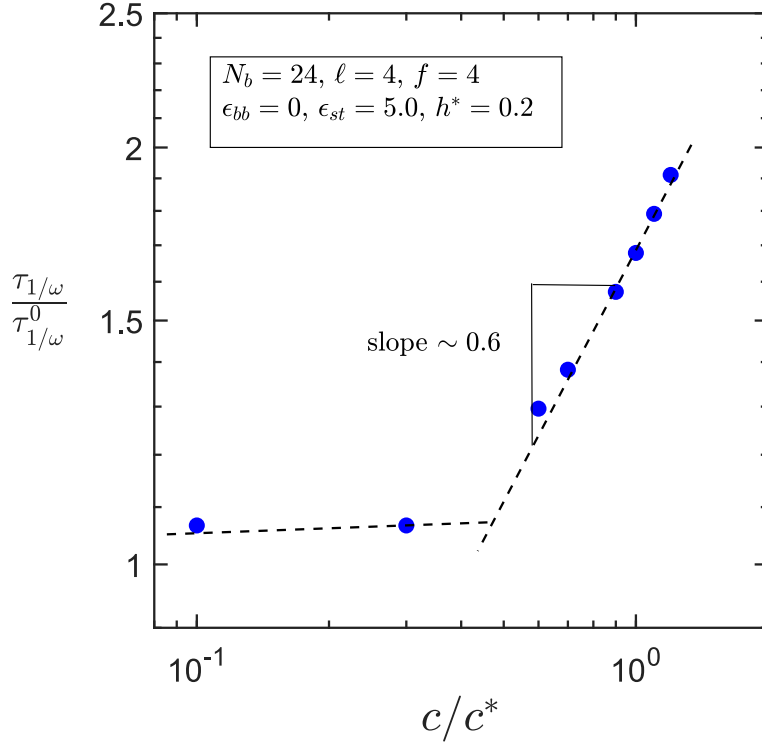


Figure 5.10: Scaling of the ratio of characteristic relaxation time,  $\tau_{1/\omega}$ , to its value in the dilute limit,  $\tau_{1/\omega}^0$ , with the scaled concentration,  $c/c^*$ , for solutions of associative polymers with  $N_b = 24$ ,  $\ell = 4$ ,  $f = 4$ ,  $\epsilon_{bb} = 0$  and  $\epsilon_{st} = 5.0$ . The symbols from simulations and the dashed lines with slope 0.6 is the best fit to the data.

qualitatively similar to that observed in experiments on supramolecular hydrogels with short chain lengths (Brassinne et al., 2017), displayed by red symbols in Figure 5.9. Associative polymer solutions with short chains have more dangling ends resulting in formation of gels that are elastically weak. Additionally, short associative polymer chains can diffuse faster in space following a bond dissociation event, causing relaxation of the network as a whole. Thus the results presented in Figs. 5.7 for relatively short chain length,  $N_b = 24$ , are likely to show a finite relaxation time scale and a terminal flow regime. In the subsequent section we show that the configurational relaxation time scale of the network formed by these short chains are comparable to the sticker-sticker bond lifetime, as a consequence of which the system always has a finite relaxation time.

Notably, the characteristic relaxation time,  $\tau_{1/\omega}$ , normalised with the relaxation time  $\tau_{1/\omega}^0$  in the dilute limit, plotted as a function of scaled monomer concentration,  $c/c^*$ , shown in

Fig. 5.10, exhibits a change in the scaling exponent at a value of  $c/c^* \approx 0.5$ , which is also the concentration ( $c_{g3}/c^*$ ) at which maxima in the free chain concentration and a crossover in the zero-shear rate viscosity scaling is observed. Surprisingly, the asymptotic value of the exponent following the crossover is 0.6, which is the same as that for the crossover in the scaling of zero-shear rate viscosity. Additionally, in Fig. 5.11 (a) we show a crossover in the scaling of the elastic modulus,  $G_0/k_B T$ , with monomer concentration, at  $c/c^* \approx 0.5$ . For the elastic modulus the scaling exponent is found to change from 1 to 1.2, following the crossover. According to the prediction of mean-field theory for associative polymer solutions proposed by Rubinstein and Semenov (Rubinstein and Semenov, 1998), the elastic modulus ( $G_0$ ) in the post-gel regime, close to the gel-point, scales with the relative distance from the gelation concentration,  $c_g$ , following the relation  $G_0 \sim \Delta^{3\mu}$ , where  $\Delta = (c - c_g)/c_g$  and exponent  $\mu = 0.85$  (i.e.  $3\mu = 2.55$ ). However, our simulations (see Fig. 5.11 (b)) show a much weaker dependence of  $G_0$  on  $\Delta$ , where the asymptotic value of the exponent in the post-gel regime, near the gel-point  $c_g/c^* = 0.5$ , is 0.64. This difference in the scaling of  $G_0$  between the simulations and theory may be a consequence of formation of weak, elastically inactive gels, where the increase in concentration in the post gel regime does not cause a sharp increase in the elastic modulus.

### 5.3.5 Calculation of relaxation time

Relaxation in associative polymer solutions occurs over different time scales. Starting from the bond lifetime of sticker-sticker association, relaxation of individual chains within a cluster to the relaxation of a network as a whole, there exists a spectrum of relaxation processes. In this section we compute the longest (or terminal) relaxation time of associative polymer solutions from different dynamic measurements, such as stress auto-correlation function, zero-shear rate viscosity, dynamic moduli and end-to-end vector auto-correlation function, and investigate their scaling with concentration in the pre and post-gel regimes. We also calculate the mean bond lifetime of the associated stickers and compare the time scale of association with that of the characteristic large scale relaxation of the polymer solutions.

In simulations, the terminal relaxation time of polymer solutions is typically evaluated by fitting the tail of the decay of stress auto-correlation or end-to-end vector auto-correlation

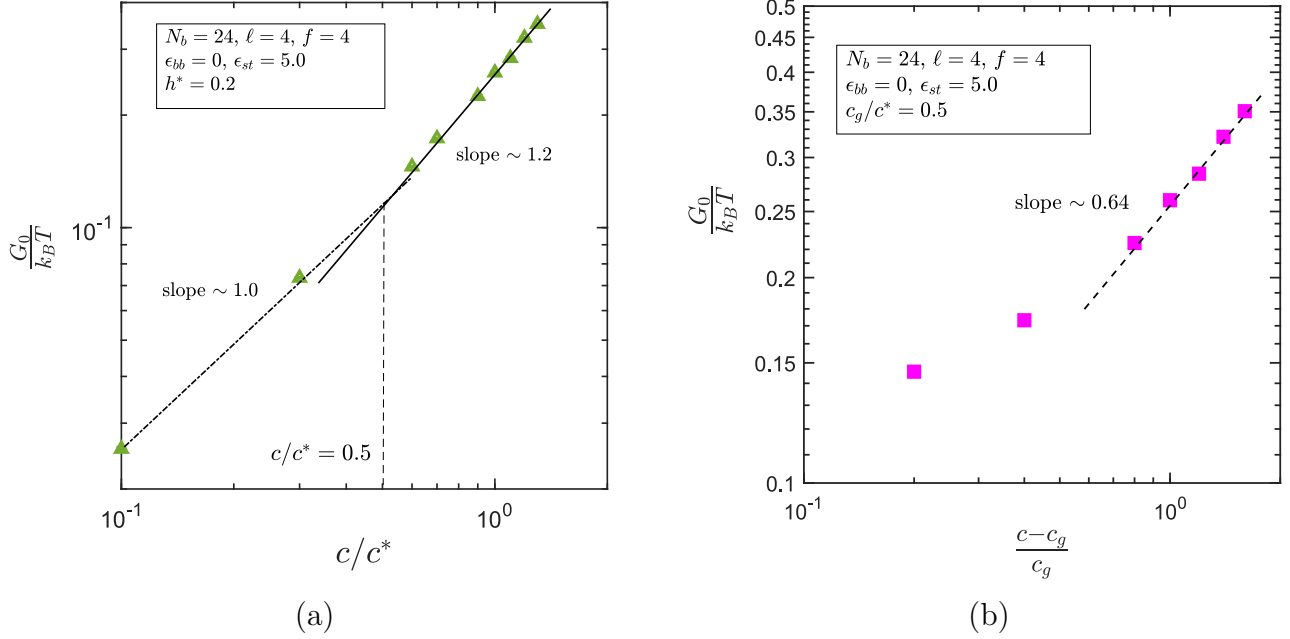


Figure 5.11: (a) Scaled elastic modulus,  $G_0/k_B T$ , versus concentration,  $c/c^*$ , for the solutions of associative polymers with  $N_b = 24$ ,  $\ell = 4$ ,  $f = 4$ ,  $\epsilon_{bb} = 0$ ,  $\epsilon_{st} = 5.0$ . (b) Elastic modulus,  $G_0/k_B T$ , as a function of the relative distance from the gelation concentration  $\Delta = (c - c_g)/c_g$ , near the gel-point in the post gel regime, where the gelation concentration is considered to be  $c_g/c^* = 0.5$ . Symbols are the simulation data and the solid and broken lines indicate the corresponding scaling exponents.

functions (Huang et al., 2010)(Pan et al., 2014a)(Nafar Sefiddashti et al., 2015). As mentioned in Section 5.3.2, the longest relaxation time can be extracted from the fit to the stress auto-correlation function by identifying the largest time constant,  $\tau_{max} = -\max\{1/b_i\}$ . Alternatively, a longest relaxation time scale can also be estimated by fitting a single exponential to the decay of end-to-end unit vector auto-correlation function of the polymer chains, defined as follows

$$u(t) = \frac{1}{N_c} \sum_{i=1}^{N_c} \langle \hat{\mathbf{R}}_e^i(0) \cdot \hat{\mathbf{R}}_e^i(t) \rangle \quad (5.19)$$

where,  $\hat{\mathbf{R}}_e^i$  is the end-to-end unit vector of the  $i^{\text{th}}$  chain and  $N_c$  is the number of chains in the system. Fig. 5.12 (a) presents the end-to-end unit vector auto-correlation function of associative polymer solutions at different concentrations, where last the 30 to 40 percent of the decay is fitted with an exponential of the form,  $\hat{u}(t) = A \exp(-t/\tau)$ , where  $\tau$  gives the estimate for the longest relaxation time. It becomes clear from Fig. 5.12 (a) that with

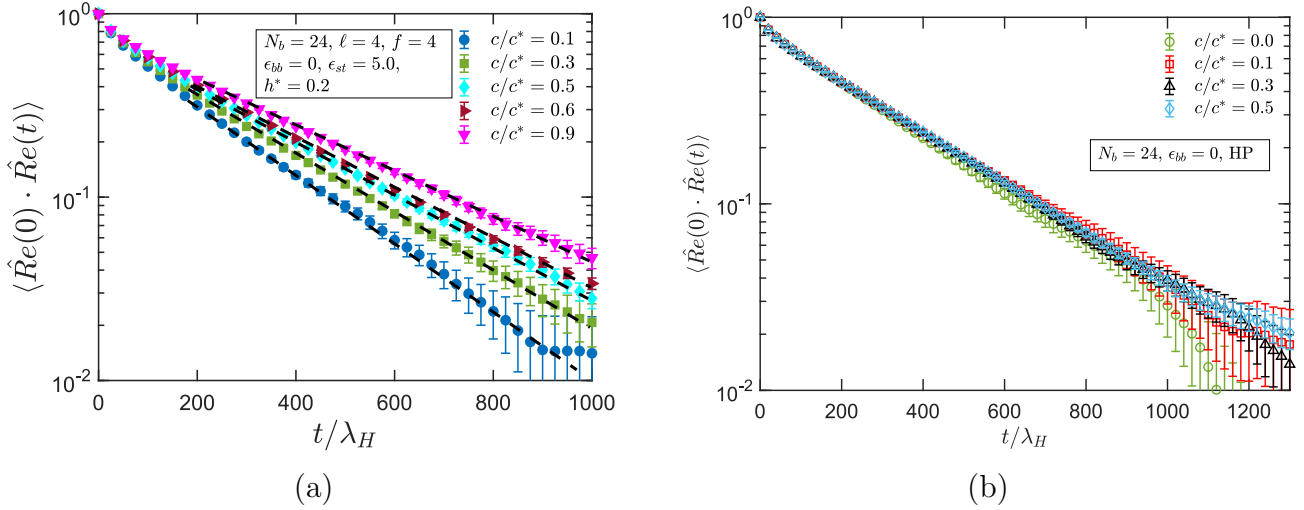


Figure 5.12: End-to-end unit vector auto-correlation function at different monomer concentrations,  $c/c^*$ , for (a) associative polymer solutions with  $N_b = 24$ ,  $\ell = 4$ ,  $f = 4$ ,  $\epsilon_{bb} = 0$  and  $\epsilon_{st} = 5.0$  and (b) homopolymer solutions in athermal solvent ( $\epsilon_{bb} = 0$ ) with chain length  $N_b = 24$ . Symbols represents the simulation data and dashed lines are the exponential fit at different concentrations.

increase in concentration the rate of decay of the auto-correlation function for associative polymers becomes progressively slower, whereas, in case of homopolymer solutions, shown in Fig. 5.12 (b), the decay of the end-to-end unit vector auto-correlation function has a very weak dependence on concentration,  $c/c^*$ .

Another alternative to estimate a large scale relaxation time ( $\lambda_\eta$ ) is based on the polymeric contribution of the zero-shear rate viscosity ( $\eta_p^0$ ), which is given by the following expression (Öttinger, 1996)

$$\lambda_\eta = \frac{M \eta_p^0}{c N_A k_B T} \quad (5.20)$$

where  $M$  is the molecular weight of the polymers,  $c$  is the monomer concentration. It noteworthy that normalising  $\lambda_\eta$  at a finite concentration with its value in the dilute limit,  $\lambda_\eta^0$ , gives the ratio  $\lambda_\eta/\lambda_\eta^0$ , which is equivalent to the ratio  $\eta_p^{0*}/\eta_{p0}^{0*}$ , used for the scaling of the zero-shear rate viscosity. Thus, the scaling of  $\lambda_\eta/\lambda_\eta^0$  and  $\eta_p^{0*}/\eta_{p0}^{0*}$  with concentration are identical. A characteristic large scale relaxation time is also obtained from the frequency corresponding to the point of intersection of the storage ( $G'$ ) and loss ( $G''$ ) moduli, as previously discussed in Section 5.3.4.

The scaling of the large scale terminal relaxation time ( $\tau$ ) with concentration is often used

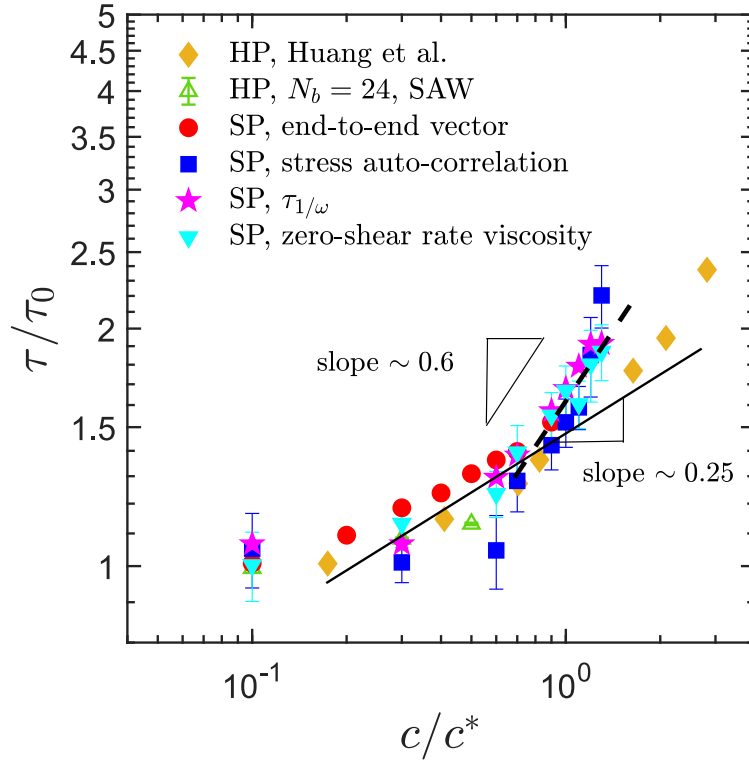


Figure 5.13: Ratio of the relaxation time,  $\tau$ , at finite concentration to its value in the dilute limit,  $\tau_0$ , as a function of scaled concentration,  $c/c^*$ , for solutions of homopolymers (HP) and associative (or sticky) polymers (SP). The associative polymers considered here are with  $N_b = 24$ ,  $\ell = 4$ ,  $f = 4$ ,  $\epsilon_{bb} = 0$  and  $\epsilon_{st} = 5.0$ . The homopolymer solutions, simulated using Brownian dynamics, are in athermal solvent with chain length  $N_b = 24$ . The yellow diamonds are data from the work by Huang et al. (Huang et al., 2010). The solid and dashed lines indicate the scaling exponents for homopolymer and associative polymer solutions, respectively.

to characterize the dynamic signatures of gelation in associative polymer solutions (Suman and Joshi, 2020)(Rubinstein and Semenov, 1998). For strong, elastically active networks the terminal relaxation time diverges at the gelation transition, whereas, the scaling of the relaxation time for elastically weak gels formed by associative polymer solutions consisting of short chains is explored here. As discussed above, the large scale relaxation time for associative polymers is estimated from four different dynamic properties based on end-to-end unit vector auto-correlation, stress auto-correlation, intersection of  $G'$  and  $G''$  and zero-shear rate viscosity. In Fig. 5.13, the ratios of the relaxation time ( $\tau$ ) at a finite concentration to its value in the dilute limit ( $\tau_0$ ), calculated from each of the four methods, are plotted as a function of scaled concentration,  $c/c^*$ . The scaling of the ratio  $\tau/\tau_0$  with  $c/c^*$  for

associative polymer solutions is compared with that of homopolymer solutions, where the terminal relaxation time for homopolymers are estimated from end-to-end unit vector auto-correlation function. Note that for homopolymers we have performed only few simulations in the dilute regime, and data has been acquired from the work by Huang et al. (Huang et al., 2010) (yellow diamonds in Fig. 5.13), for the purpose of comparing with associative polymers. By appropriately normalising the relaxation times, calculated from different methods, an universal curve is generated for the ratio  $\tau/\tau_0$ . Fig. 5.13 also indicates a cross-over in the scaling of  $\tau/\tau_0$  at around  $c/c^* \approx 0.5$ , following which the exponent becomes approximately equal to 0.6. Unsurprisingly, the cross-over concentration and the value of the exponent following the cross-over are identical to that observed for the scaling of the zero-shear rate viscosity (see Fig. 5.5) and  $\tau_{1/\omega}/\tau_{1/\omega}^0$  (see Fig. 5.10), since all these properties are related to the relaxation time. As compared to associative polymer solutions, the normalised relaxation time for the homopolymers goes through a broad cross-over with a scaling exponent of  $(2 - 3\nu)/(3\nu - 1) = 0.25$ , where the Flory exponent  $\nu = 0.6$ , which is a well known scaling law for relaxation time in the semi-dilute unentangled regime (de Gennes, 1979)(Huang et al., 2010). At higher values of  $c/c^*$ , the deviation of the simulation data for the homopolymers from 0.25 slope is probably due to the cross-over from the semi-dilute unentangled to the entangled regime. It is interesting to note that the onset of divergence between the scaling of homopolymer and associative polymer solutions begins at a concentration value of around,  $c/c^* = 0.5$ , which corresponds to the gelation concentration defined based on the maxima in free chain concentration.

Based on a mean-field theory, Rubinstein and Semenov (Rubinstein and Semenov, 1998)(Rubinstein and Semenov, 2001) have proposed the sticky Rouse model, which predicts the scaling of the relaxation time,  $\tau_{\text{relax}}$ , in unentangled solutions of associative polymers well above the gel point. According to the prediction

$$\tau_{\text{relax}} \approx \tau_{\text{bond}} (f p_2)^2 \quad (5.21)$$

where,  $\tau_{\text{bond}}$  is the bond lifetime of associated stickers,  $f$  is the number of stickers per chain and  $p_2$  is the fraction of inter-chain associated stickers. From its definition, the product

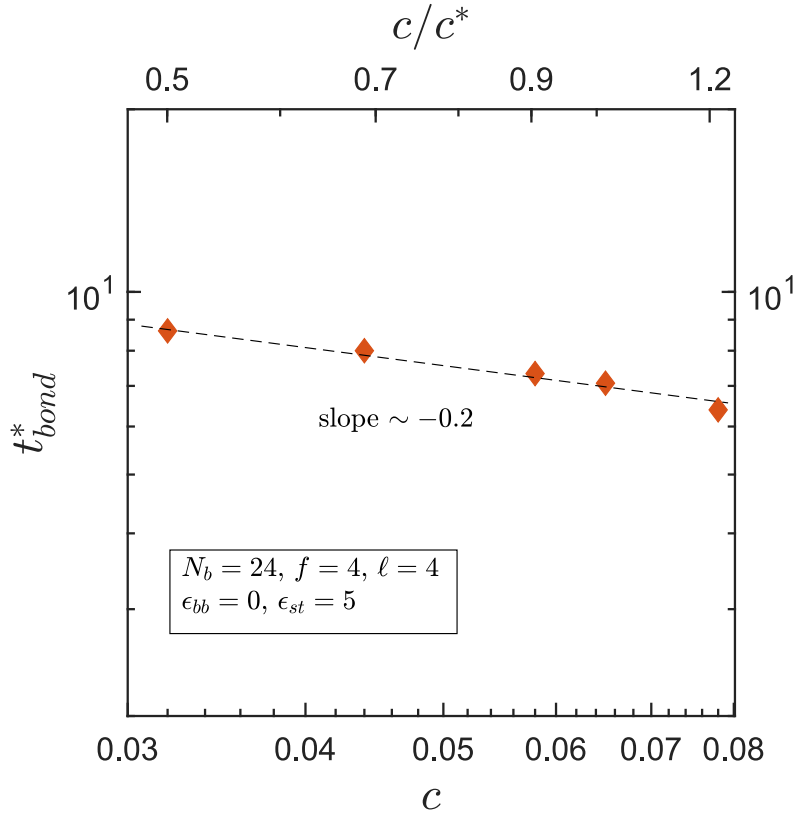


Figure 5.14: Dimensionless mean bond lifetime,  $t_{\text{bond}}^*$  as a function of concentration,  $c/c^*$ , for associative polymer solutions with  $N_b = 24$ ,  $\ell = 4$ ,  $f = 4$ ,  $\epsilon_{bb} = 0$  and  $\epsilon_{st} = 5.0$ . The symbols are from simulations and the dashed line is best fit to the data.

$f p_2$  is essentially the total fraction of inter-chain associated stickers in a chain. In order to verify this prediction for our model, we first calculate the average bond lifetime of associated stickers by considering all possible associating pairs for the systems of associative polymer solutions at different concentrations. According to the mean-field theory (Rubinstein and Semenov, 1998)(Rubinstein and Semenov, 2001),  $\tau_{\text{bond}}$  is effectively a function of only the sticker strength,  $\epsilon_{st}$ , however, from the Brownian dynamics simulations we find that at a constant value of sticker strength,  $\epsilon_{st} = 5.0$ , the bond lifetime also has a weak concentration dependence, as displayed in Fig. 5.14. It is important to note that the values of bond lifetime shown in Fig. 5.14 are of the same order as that of the large scale relaxation time computed from the point of intersection of storage and loss moduli (shown in Figs. 5.7). It is therefore reasonable to argue that, for the associative polymer solutions studied here, the relaxation time due to bond dissociation is comparable to the large scale relaxation time,

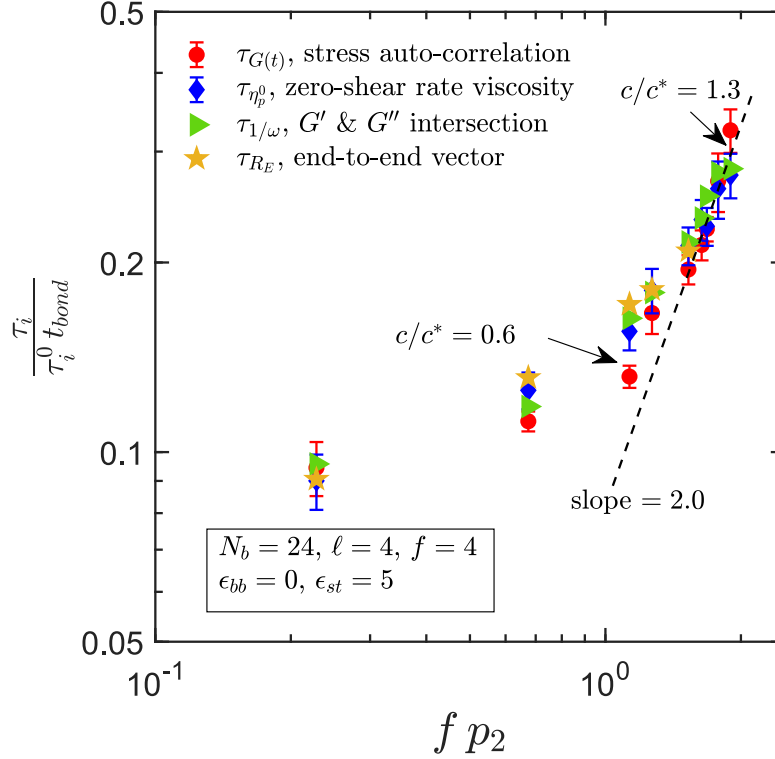


Figure 5.15: The ratio  $\tau_i/(\tau_i^0 t_{\text{bond}})$  as function of the fraction of inter-chain associated stickers,  $f p_2$ , at different values of monomer concentration in the pre and post-gel regimes. Here,  $\tau_i$ 's are the large scale relaxation time estimated from various methods (index  $i$  represents the different methods) as indicated in the figure and  $\tau_i^0$ 's are the corresponding values of relaxation time in the dilute limit. Each symbol corresponds to a specific method of estimating  $\tau$  and the dashed line is prediction of the mean-field theory.

which ultimately leads to a finite relaxation time scale for the polymer solutions. Using the scaling relation for  $t_{\text{bond}}$  with concentration,  $c/c^*$ , the ratio  $\tau_i/(\tau_i^0 t_{\text{bond}})$  is plotted as a function of  $f p_2$  at different values of monomer concentration in the pre and post-gel regimes, as shown in Fig. 5.15. Here,  $\tau_i$ 's are the large scale relaxation time estimated from various methods as discussed earlier in the section and  $\tau_i^0$ 's are the corresponding values of relaxation time in the dilute limit. From Fig. 5.15, it is clear that the ratio  $\tau_i/(\tau_i^0 t_{\text{bond}})$  is independent of the methods used to evaluate the relaxation time. Moreover, the scaling of the ratio  $\tau_i/(\tau_i^0 t_{\text{bond}})$  with  $f p_2$  goes through a cross-over and follows an asymptotic exponent of 2 for a range of concentration well above the gel-point ( $c_g/c^* = 0.5$ ), which is in agreement with the prediction of the sticky Rouse model, given in Eq. (5.21).

### 5.3.6 Chain-cluster lifetime

As has been discussed in Section 4.7, an increase in monomer concentration results in the formation of large clusters of chains. However, these clusters undergo continuous formation and disintegration due to the reversibility of the physical association between the stickers. The lifetime of a cluster is typically defined as the timespan within which the cluster breaks into equal halves (Rubinstein and Semenov, 1998). At a constant association strength, the lifetime of a particular cluster is essentially dependent on its size (i.e. number of constituent chains in the cluster) (Rubinstein and Semenov, 1998)(Ozaki et al., 2017). For instance, a big cluster consisting of many chains, has more breakable linkages, resulting in its shorter lifetime as compared to smaller clusters with fewer chains. Here, we investigate chain-cluster lifetime,  $t_c^{\text{life}}$ , as a function of cluster size,  $m$ , at different monomer concentrations,  $c/c^*$ , for associative polymer solutions with  $N_b = 24$ ,  $\ell = 4$ ,  $f = 4$ ,  $\epsilon_{bb} = 0$  and  $\epsilon_{st} = 5.0$ . The cluster lifetime is estimated by calculating the average time required for a cluster with  $m$  chains to lose half of its constituent chains from the time of formation of the cluster.

As shown in Fig. 5.16, with an increase in cluster size,  $m$ , the average lifetime of the cluster decreases, which is in qualitative agreement with the prediction of mean-field theory (Rubinstein and Semenov, 1998). It is also interesting to note that for relatively large clusters, with  $m \geq 10$ , the average lifetime increases with an increase in concentration,  $c/c^*$ . It should be recalled that the probability of formation of large cluster increases as concentration is increased, which is illustrated by the onset of bimodality in the cluster size distribution in Section 4.7. Additionally, with the increase in concentration there is an increase in the density of the network, due to the presence of more chains per unit volume. These factors cause the larger clusters to persist for longer, and the cluster lifetime is seen to increase with an increase in  $c/c^*$ , as observed in Fig. 5.16.

## 5.4 Conclusions

Dynamic signatures of gelation in associative polymer solutions have been investigated using Brownian dynamics simulations. Dynamic and linear viscoelastic properties like zero-shear rate viscosity, storage ( $G'$ ) and loss ( $G''$ ) moduli, relaxation modulus, large scale relaxation

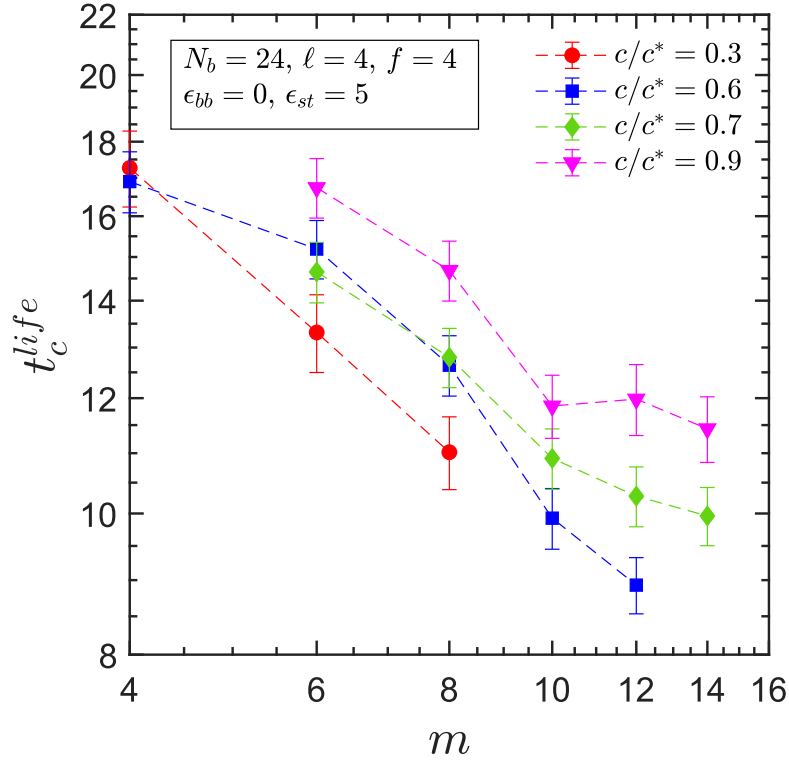


Figure 5.16: Chain cluster lifetime,  $t_c^{\text{life}}$ , as a function of cluster size,  $m$ , at different values of concentration,  $c/c^*$ , for associative polymer solutions with  $N_b = 24$ ,  $\ell = 4$ ,  $f = 4$ ,  $\epsilon_{bb} = 0$  and  $\epsilon_{st} = 5.0$ .

time and bond life lifetime are used to characterise the viscoelasticity of the associative polymer solutions in the pre and post-gel regimes. In this chapter we have shown that the concentration corresponding to the gelation transition, indicated by the dynamic measurements coincides with the maxima in free chain concentration, which is one of the static measures of gelation. Results obtained for the scaling of the zero-shear rate viscosity and terminal relaxation time are compared with the scaling prediction of the mean-field theory for associative polymers.

Viscoelastic properties, such as relaxation modulus, zero-shear rate viscosity and dynamic moduli have largely been computed from equilibrium simulations. The zero-shear rate viscosity obtained from shear flow simulations is found to agree with that obtained from equilibrium simulations using Green-Kubo relation, thus establishing the equivalence between the two methods. We have also shown that for the short chains used here, the equilibrium modulus ( $G_{\text{eq}}$ ) is essentially zero, which makes it possible to estimate  $G'$  and  $G''$

from Fourier transformation of stress auto-correlation function.

The cross-over in the scaling of zero-shear rate viscosity with concentration,  $c/c^*$ , is found to coincide with the value of  $c/c^*$  corresponding to the maxima in free chain concentration. From our simulations, the scaling of zero-shear rate viscosity with the relative distance from the gelation concentration, in the post-gel regime, is found to be in agreement with the prediction of the mean-field theory by Rubinstein and Semenov (Rubinstein and Semenov, 1998).

Dynamic moduli,  $G'$  &  $G''$ , of associative polymer solutions are studied as a function of frequency. The nature of the curves for  $G'$  &  $G''$  diverges from the typical power-law behaviour of gel forming polymer solutions. The dynamic moduli for the systems investigated here indicate formation of elastically weak gels which possess a finite relaxation time and a terminal flow regime. These features have also been observed experimentally in associative polymer solutions with short chains.

Different dynamic properties have been used to extract a large scale relaxation time for the associative polymer solutions. The normalized relaxation time as a function of concentration follows an universal curve, independent of the methods used to estimate the relaxation time. The scaling of the relaxation time with  $c/c^*$  also shows a cross-over at the concentration corresponding to the maxima in freechain concentration. A key finding of this study is that the relaxation time as a function of the fraction of inter-chain associated stickers per chain follows the scaling prediction by the sticky Rouse model (Rubinstein and Semenov, 1998)(Rubinstein and Semenov, 2001), in the post gel regime.

Finally, we have compared different relaxation time scales corresponding to the bond lifetime and large scale relaxation time of the polymer solutions. We show both these time scales are comparable, which results into a finite large scale relaxation time for the systems. The chain cluster lifetime is also investigated for these systems and their variation with cluster size is in qualitative agreement with the theory.

It is expected that the use of longer chains would result in formation of elastically active networks, and qualitatively different viscoelastic behaviour. We anticipate that the results presented in this chapter on the dynamics of associative polymer solutions would pave the way for a greater understanding of the rheology and viscoelasticity of thermo-reversible,

physically cross-linked polymer solutions.

In the following chapter we will discuss the static and dynamic properties polymeric rings, which are topologically different from the linear associative polymers. The focus of this chapter will be on the universal behaviour of dilute ring polymer solutions.

# Chapter 6

## Universality in polymeric rings at equilibrium

### 6.1 Introduction

The topological structure of a polymer chain plays a major role in determining the static and dynamic properties of a polymer solution. In case of linear chains, studied in the previous chapters, the relaxation behaviours of the terminal ends of a polymer chain are found to affect the dynamics of the polymer solutions. However, ring polymers are a special class of polymers which do not have any ends. This has resulted the ring polymer solutions to show unique dynamic and viscoelastic properties which are not observed in linear polymers. One such instance is the transition between tumbling and tank-treading motion of a polymeric ring under shear flow (Chen et al., 2013)(Wang et al., 2019). Such a transition leads to interesting rheological behaviour the are not observed in linear homopolymer solutions. However, in order to understand the viscoelasticity of ring polymer solutions it is first important to understand their equilibrium behaviour. In this chapter we present a comparative study on the mean size and stretch of linear homopolymers and ring polymers at equilibrium and established the universality of the static and dynamic properties of rings as a function of solvent quality in the single chain limit. The sections included in this chapter are as follows. In Section 6.2 we discuss the modelling and simulation methodology for ring polymers. Evaluation of universal ratios involving the static properties such radius of gyration ( $R_g$ ) and

mean-stretch along  $x$ -axis ( $\langle X \rangle$ ) is described in Section 6.3. In Section 6.4 we present the methods for computing diffusivity ( $D$ ) and hydrodynamic radius ( $R_H$ ). Different universal ratios involving hydrodynamic radius is also discussed in this section. Finally, the key conclusions are summarised in the Section 6.5.

## 6.2 Modelling and simulations

The polymeric ring is modelled as a sequence of bead-spring chain similar to linear polymers with the exception that here the chain ends are connected with a spring. Brownian dynamics (BD) simulation algorithm has been implemented with excluded volume (EV) and hydrodynamic interactions (HI). The bead positions in the BD simulations are updated by the Itô stochastic differential equation, defined by Eq. 2.1.

We use the regularized Rotne-Prager-Yamakawa (RPY) tensor to compute hydrodynamic interactions (HI). The bonded interaction between the adjacent beads is modelled by using a FENE spring force law with  $b = 50.0$ . Contrary to the SDK potential used in our previous study on associative polymer solutions, the excluded volume (EV) interaction is modelled here by using a narrow Gaussian potential given by,

$$E(\mathbf{r}_{\nu\mu}) = \left( \frac{z^*}{d^{*3}} \right) k_B T \exp \left\{ -\frac{1}{2} \frac{\mathbf{r}_{\nu\mu}^2}{d^{*2}} \right\} \quad (6.1)$$

Here,  $\mathbf{r}_{\nu\mu} = (\mathbf{r}_\nu - \mathbf{r}_\mu)$ ,  $d^*$  is a non-dimensional parameter that measures the range of interactions. The simulations are carried out over a range of solvent qualities by varying the parameter,  $z^*$ , which is the non-dimensional strength of excluded volume interactions. The solvent quality is essentially a function of the temperature and chain length which is defined as  $z = z^* \sqrt{N_b}$  in the context of narrow Gaussian potential. In the limit of  $z = 0$ , the solvent quality represents a  $\theta$ -condition, whereas  $z \rightarrow \infty$  produces an athermal solvent quality. An implicit predictor-corrector algorithm, similar to that suggested by Öttinger (Öttinger, 1996) and implemented in their study by Prabhakar et al. (Prabhakar and Prakash, 2004), is used here to solve the Itô stochastic differential equation.

A typical simulation for a single chain ring polymer consists of about 5 to 10 Rouse relax-

ation time in the equilibration step followed by 5 Rouse relaxation time for the production run. While computing dynamic properties such as long-time diffusivity, the production run may consist of several 1000 non-dimensional time units. All the simulations are carried out with a non-dimensional time step of  $\Delta t = 0.001$  and the output data are collected at an interval of 0.5 non-dimensional time units. The static equilibrium properties are computed as a block ensemble average over several trajectories. First, time average for different properties are calculated for each independent trajectory, followed by calculation of ensemble average over such independent time averages. However, the dynamic properties are simply calculated based on ensemble average over several independent trajectories. Typically, 1000 to 2000 independent trajectories are used to calculate different static and dynamic properties.

### 6.3 Universal ratios for static properties

Universal scaling of equilibrium static properties such as the mean squared radius of gyration and mean stretch of a single chain under different solvent qualities are well known for linear polymers (Kumar and Prakash, 2003)(Zhu et al., 2016). However, for ring polymers the universality of such static properties is not well established. It is fundamentally important to investigate the behaviour of these static properties in order to develop better models to simulate ring polymer solutions which could then be used to explain various experimental observations.

Fig. 6.1 (a) shows the scaling of radius of gyration as a function of chain length ( $N_b$ ) in the limit of  $\theta$  solvent ( $z = 0$ ) for both linear and ring chains. It is observed that both linear and ring polymers follow random walk statistics in the  $\theta$ -solvent limit. Furthermore, it may be seen from Fig. 6.1 (b) that the mean-squared radius of gyration of a single-ring is half that of a linear chain under theta-solvent conditions, in agreement with the theoretical prediction Kramers (1946)Zimm and Stockmayer (1949)Yamakawa (1971).

To investigate the effect of solvent quality on the mean stretch,  $\langle X \rangle$ , and radius of gyration,  $R_g$ , we have systematically increased the solvent quality parameter,  $z$ , and calculated the ratio  $\langle X \rangle / 2R_g$  for rings and linear chains along with the ratio of relative stretch,  $X_R / X_L$ , as a function of  $z$  ( $X_R$  and  $X_L$  are the respective mean stretch of a ring and linear chain

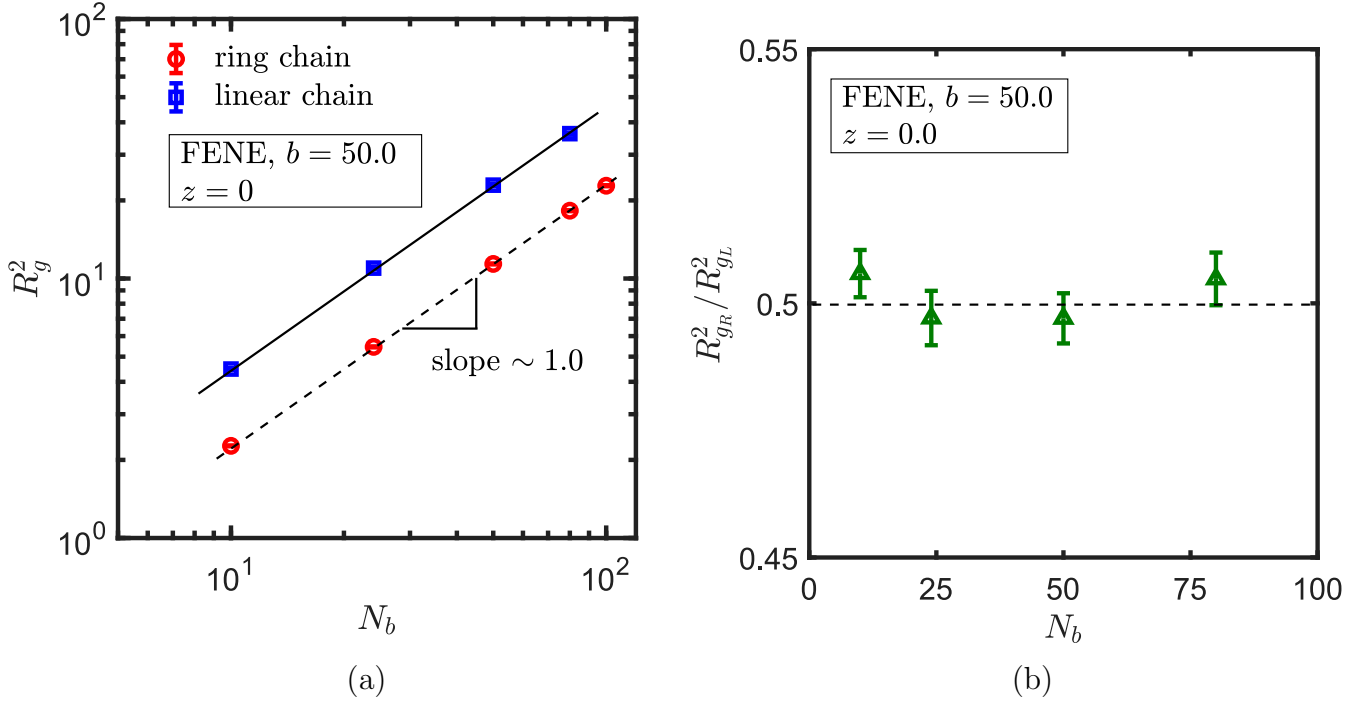


Figure 6.1: (a) Mean square radius of gyration,  $R_g^2$ , as function of chain length,  $N_b$ , for ring and linear polymers. (b) The variation of the ratio of  $R_g^2$  for ring and linear chains with chain length.

along  $x$ -axis). Since the solvent quality,  $z$ , is dependent on chain length ( $N_b$ ), the value of the parameter  $z^*$  for different chain lengths is adjusted such that  $z$  is kept constant for a particular solvent quality in the crossover regime. The quantity  $\langle X \rangle / 2R_g$  and  $X_R / X_L$  are evaluated in the limit of infinite chain length by progressively increasing  $N_b$  and extrapolating the values of these properties at  $N_b \rightarrow \infty$  as demonstrated in Fig. 6.2 for systems under  $\theta$ -solvent condition ( $z = 0$ ).

At this point it should be noted that since  $z = z^* \sqrt{N_b}$ , the asymptotic limit of  $z \rightarrow \infty$  can be reached by carrying out simulations at a fixed value of  $z^*$  for various chain lengths and extrapolating the measured property to  $N_b \rightarrow \infty$ . An example of this method is demonstrated in Fig. 6.3 for the ratio  $\langle X \rangle / 2R_g$  for rings. In Fig. 6.4 (a), we show that for both ring and linear chains the ratio  $\langle X \rangle / 2R_g$  is found to decrease with increase in solvent quality in the crossover regime and asymptotically tends to a constant value as  $z \rightarrow \infty$ . It can also be noted that  $\langle X \rangle / 2R_g$  for ring is larger than linear chain at any value of  $z$ . Previously, it has been predicted by Sunthar and Prakash Sunthar and Prakash (2005) that under  $\theta$ -solvent

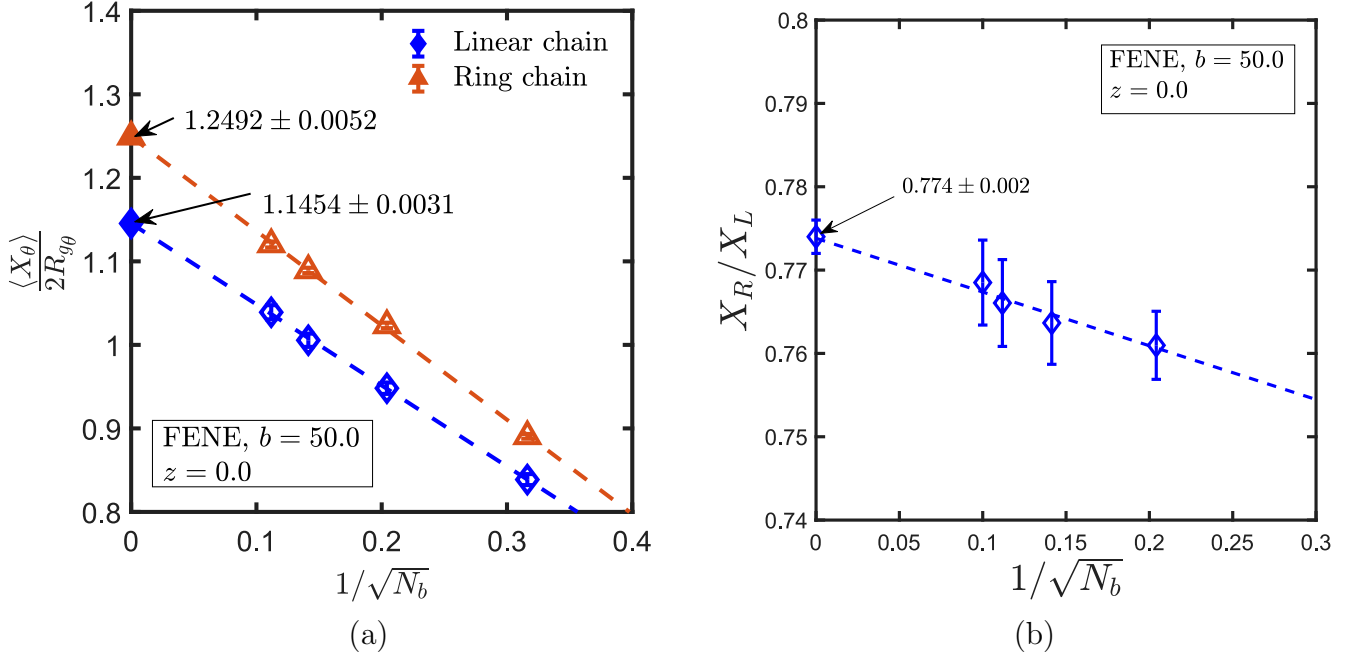


Figure 6.2: (a) The ratio  $\langle X \rangle / 2R_g$  as a function of  $1/\sqrt{N_b}$  for linear and ring chains in the limit of  $\theta$ -solvent quality. (b) The ratio of the mean stretch of a ring and linear chain,  $X_R/X_L$ , as a function of  $1/\sqrt{N_b}$  at the  $\theta$ -solvent condition. The extrapolated values in the limit of  $N_b \rightarrow \infty$  is shown in the figure. The symbols are simulation data and the broken lines are linear fits to the data.

condition at equilibrium  $\langle X \rangle / 2R_g \approx 1.132$  for linear polymers in the long chain limit. Zhu et al. Zhu et al. (2016) performed simulations based on Kremer-Grest bead-spring model for different topological polymers and found the values of the ratio  $\langle X \rangle / 2R_g$  equal to 1.13 and 1.255 for linear chains and rings, respectively. Both these values for the ratio  $\langle X \rangle / 2R_g$  are in close agreement with the present simulation results, which are  $1.145 \pm 0.003$  and  $1.249 \pm 0.005$  for linear and ring polymers, respectively. We find that the values of this ratio for linear and ring chains in the asymptotic limit of  $z \rightarrow \infty$  are  $1.06 \pm 0.01$  and  $1.126 \pm 0.003$ , respectively, which are also in good agreement with the prediction of Zhu et al. Zhu et al. (2016). The ratio  $X_R/X_L$ , on the other hand is independent of solvent quality,  $z$ , and assumes a constant value of approximately 0.8, as displayed in Fig. 6.4 (b). This value is identical to that obtained from the simulations by Zhu et al. Zhu et al. (2016) within numerical accuracy. Interestingly, at a given solvent quality a ring chain is less stretched compared to a linear chain having the same number of monomers or molecular weight.

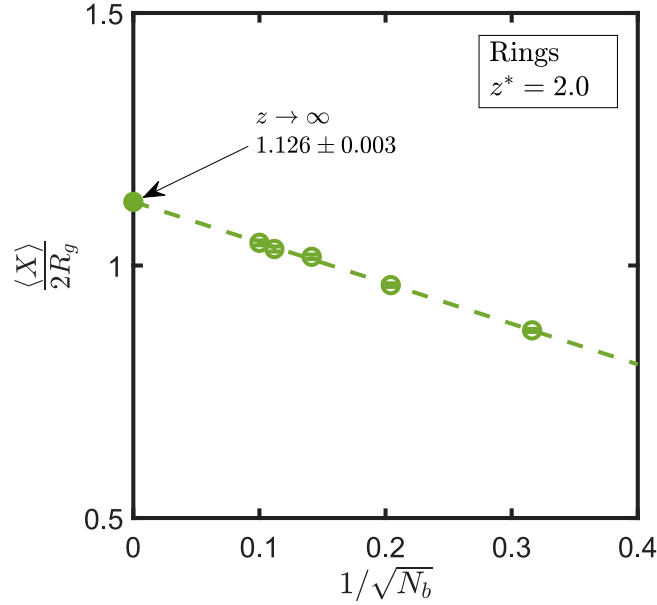


Figure 6.3: Ratio  $\langle X \rangle / 2R_g$  for rings as a function of  $N_b$  at a fixed value of  $z^*$ . The extrapolated value in the limit of  $z \rightarrow \infty$  is indicated in the figure.

## 6.4 Universal ratios involving hydrodynamic radius

In this section we discuss the methodology to compute the hydrodynamic radius,  $R_H$  (a dynamic property), of rings and calculate different universal ratios involving  $R_H$ . This along the mean-stretch (discussed in the Section. 6.3) are two important properties for a polymer solutions as they are more conveniently measured than  $R_g$  in experiments. This has motivated us to compute the ratio of mean span to  $R_H$  as a function of solvent quality for rings and compare them with that of linear chains. For completeness we have also studied the ratio  $R_H$  to  $R_g$  as a function of solvent quality.

The hydrodynamic radius is inversely proportional to the diffusivity ( $D^*$ ) of a polymer chain and can be related by the following equation

$$D^* = \frac{k_B T}{6\pi\eta} \frac{1}{R_H^*}$$

where  $k_B$  denotes the Boltzmann constant and  $\eta$  is the solvent viscosity. Note that all the dimensional variables are denoted with an asterisk as a superscript. The diffusivity,  $D^*$ , is computationally determined from the mean-squared displacement of the center of mass of a

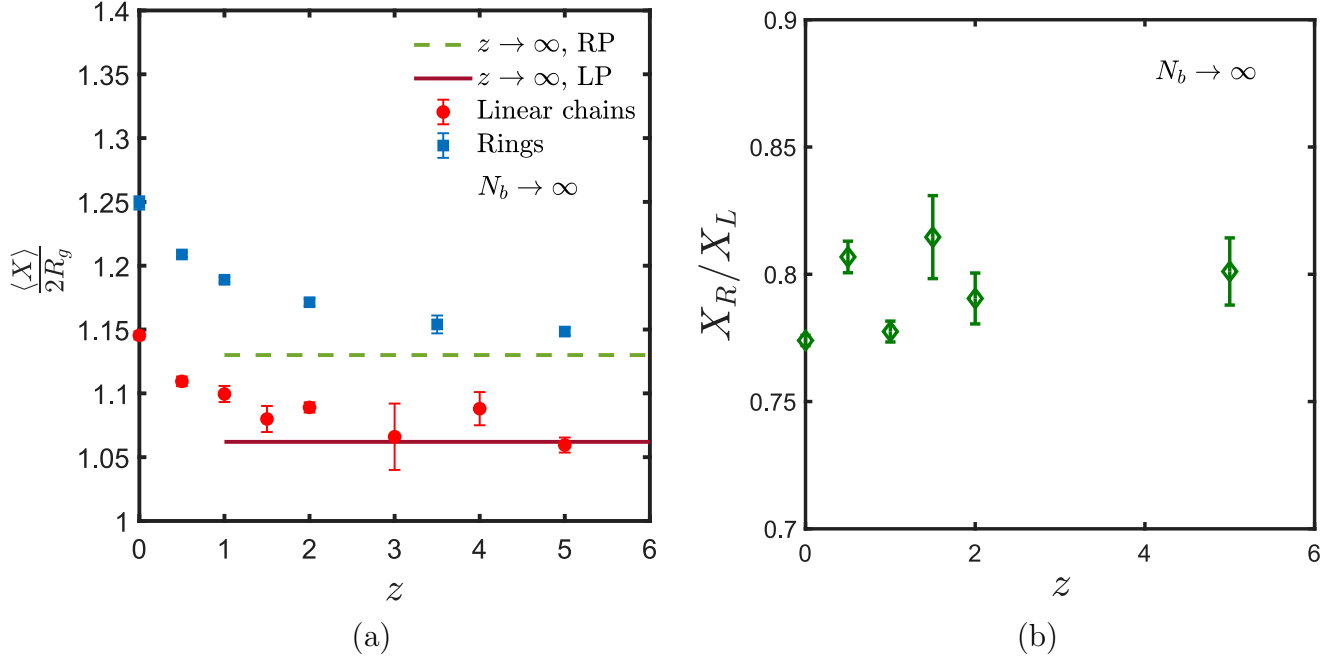


Figure 6.4: (a) The ratio  $\langle X \rangle / 2R_g$  as a function of  $z$  for linear and ring chains in the long chain limit. The solid and the dashed lines represents the value of  $\langle X \rangle / 2R_g$  in limit of  $z \rightarrow \infty$  for linear and ring polymers, respectively. (b) The ratio of the mean stretch of a ring and linear chain,  $X_R / X_L$ , as a function of  $z$  in the long chain limit.

polymer chain, given by

$$\langle \Delta r_{\text{cm}}^{*2} \rangle = 6 D^* t^* \quad (6.2)$$

where  $\Delta r_{\text{cm}}^*$  is the displacement of the center of mass and  $t^*$  denotes time. However, calculation of  $D^*$  from mean-squared displacement needs simulation of long trajectories and is more error prone. An alternative method involves using Fixman's formula and Kirkwood expression to estimate the long-time diffusivity. Fixman's formula is given as  $D^* = D_K^* - D_1^*$ , where  $D_K^*$  is the short time diffusivity calculated from Kirkwood expression and  $D_1^*$  represents the intermolecular dynamic correlation. The expression for  $D_K^*$  is written as follows

$$D_K^* = \frac{D_0^*}{N_b} + \frac{k_B T}{6\pi\eta} \frac{1}{R_1^*} \quad (6.3)$$

Here,  $D_0^* = k_B T / \zeta$  is the diffusivity of a single bead where  $\zeta = 6\pi\eta a$  is the friction coefficient

of a bead of radius  $a$ .  $R_1^*$  is the static inverse radius defined as

$$\frac{1}{R_1^*} = \frac{1}{N_b^2} \sum_{\substack{\mu, \nu=1 \\ \mu \neq \nu}}^{N_b} \left\langle \frac{1}{r_{\mu\nu}^*} \right\rangle \quad (6.4)$$

By appropriate non-dimensionalisation the dimensionless dynamic correlation function,  $D_1$ , is defined in terms of  $A_i = \frac{1}{4} \sum_{\mu} D_{\mu\nu ij} F_{\nu j}$  as

$$D_1 = \frac{1}{3N_b^2} \int_0^{\infty} dt \langle A_i(0) A_i(t) \rangle \quad (6.5)$$

here  $D_{\mu\nu ij}$  is the  $ij^{th}$  component of the diffusion tensor for bead pair  $\mu\nu$  and  $F_{\nu j}$  defines the force acting on bead  $\nu$  in  $j$  direction. In BD simulations the hydrodynamic interactions (HI) among different chain segments in a polymer solution, required to evaluate the dynamic correlation, is incorporated by using a hydrodynamic interaction parameter  $h^* = a/(\sqrt{\pi k_B T/H})$ , where  $a/(\sqrt{k_B T/H})$  is the non-dimensional bead radius. By using  $l_H = \sqrt{k_B T/H}$  and  $\lambda_H = \zeta/4H$  for non-dimensionalisation of the length and time scales we can derive the following dimensionless equation correlating the diffusivity and hydrodynamic radius.

$$D = \frac{h^* \sqrt{\pi}}{4R_H} \quad (6.6)$$

In the above expression  $D$  is non-dimensionalised with respect to  $\ell_H^2/\lambda_H$ . Previously it has been shown that the diffusivity computed for linear chains from the mean-squared displacement and Fixman's formula are consistent with each other Liu and Dünweg (2003). Fig. 6.5 confirms that the diffusivity for rings calculated by both the methods are also consistent in both  $\theta$  and good solvent limits. It also shows that, similar to linear polymers, the diffusivity of rings scales with chain length,  $N_b$ , as  $N_b^{-0.5}$  in  $\theta$  solvent and  $N_b^{-0.6}$  in a good solvent. This result is also in agreement with the diffusivity scaling observed in the experiments on circular DNA (Robertson et al., 2006).

With this necessary background to compute  $R_H$  from diffusivity, the variation of the universal ratio,  $U_{RD} = R_g/R_H$ , as a function of the solvent quality  $z$  is examined next. It is

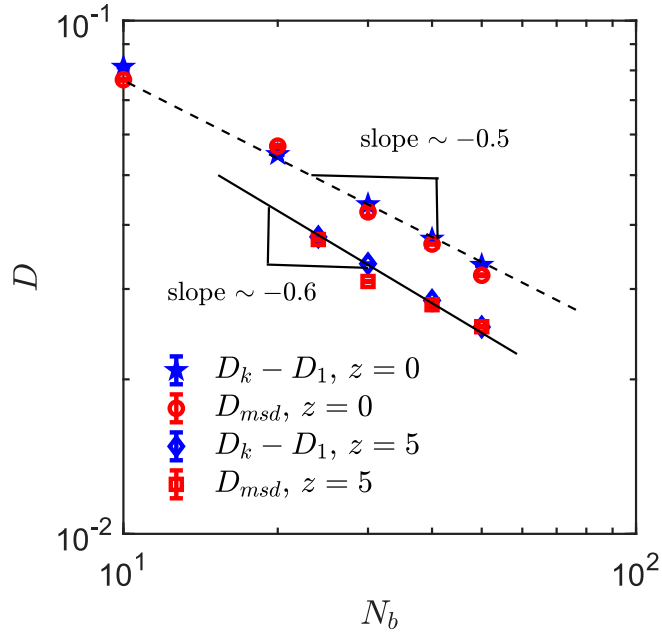


Figure 6.5: Scaling of diffusivity,  $D$ , with chain length,  $N_b$ , at  $z = 0$  ( $\theta$  solvent),  $h^* = 0.2$  and  $z = 5$  (good solvent),  $h^* = 0.24$  for rings. Here  $D$  is computed by the two methods discussed in the text. The dashed and solid lines indicate the scaling exponent for the two solvent qualities.

well established (Kröger et al., 2000)(Sunthar and Prakash, 2006) that for a specific value of the solvent quality parameter,  $z$ , the ratio  $U_{RD}$  is independent of the strength of HI ( $h^*$ ) in the non-draining limit,  $h \rightarrow \infty$ , where  $h = h^* \sqrt{N}$ . While Sunthar and Prakash Sunthar and Prakash (2006) have shown that universality holds true for linear chains, here we establish validity of this argument for rings. Normally, in simulations with the FENE spring force law,  $h_f^*$  (function of FENE  $b$  parameter) is kept constant instead of  $h^*$  in order to keep the contour length (corresponding to a specific number of Kuhn segments) unchanged with increase in number of beads ( $N_b$ ) Sunthar and Prakash (2005). However, since the present study considers infinite number of Kuhn segments (corresponding to infinite chain length), it is fair to keep  $h^*$  constant for simulations at different values of  $N_b$ . In Fig. 6.6 we present  $U_{RD}$  as a function of chain length for two different values of  $h^*$  at  $z = 0$ . In the extrapolated limit of  $N_b \rightarrow \infty$ , curves for both values of  $h^*$  converge to a common value,  $1.225 \pm 0.006$ . This determines the universal value of the ratio for rings, independent of the parameter  $h^*$ , at  $z = 0$ . For linear polymers the value of this ratio is found to be  $1.40 \pm 0.01$ , similar to previous predictions by Sunthar and Prakash Sunthar and Prakash (2005) and Kröger et

al. Kroger et al. (2000). Uehara et al. Uehara and Deguchi (2016) estimated the value of the ratio  $U_{\text{RD}}$  to be  $1.253 \pm 0.013$  for rings, which is significantly higher than our prediction. However, it should be noted that they have computed  $R_H$  from the Kirkwood expression without Fixman's correction, and such a treatment is valid only for the estimation of the short time diffusivity.

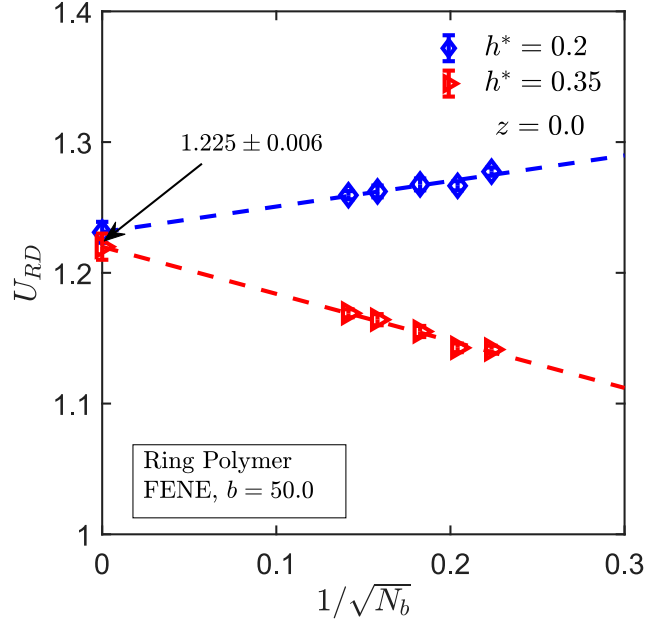


Figure 6.6: The ratio  $U_{\text{RD}}$  as a function of  $1/\sqrt{N_b}$  for rings in the limit of  $\theta$ -solvent quality,  $z = 0$ . The extrapolated value in the limit of  $N_b \rightarrow \infty$  is shown in the figure. The symbols are simulation data and the broken lines are linear fit to the data.

The difference in the values of the ratio  $U_{\text{RD}}$  for different  $h^*$  in the short chain limit is attributed to the leading order correction in the estimate of  $U_{\text{RD}}$ , which scales with chain length as follows Kroger et al. (2000)

$$U_{\text{RD}}(h^*, N_b) = \tilde{U}_{\text{RD}}^\infty + \frac{c_{\text{RD}}}{\sqrt{N_b}} \left( \frac{1}{h_{\text{RD}}^*} - \frac{1}{h^*} \right) + \mathcal{O}(1/N_b) \quad (6.7)$$

where  $\tilde{U}_{\text{RD}}^\infty$  is the value of the ratio in the limit of infinite chain length,  $c_{\text{RD}}$  and  $h_{\text{RD}}^*$  are constants. From Eq. (6.7) it is clear that one could find a fixed point by solving the above equation for  $c_{\text{RD}}$  and  $h_{\text{RD}}^*$  at which the leading order correction term drops and the ratio quickly converges to its universal value. For rings we found the fixed point at  $h^* \approx 0.24$ .

Following the above method the ratio  $U_{\text{RD}}$  is computed for a range of values of  $z$  with  $h^* = 0.24$  (at fixed point). In Fig.6.7 we show the variation of  $U_{\text{RD}}$  as a function of  $z$  for rings and linear chains. It is worth noting that the universal ratio,  $U_{\text{RD}}$ , for linear chains is computed from the formula  $U_{\text{RD}} = \alpha_g U_{\text{RD}}^0 \alpha_H^{-1}$ , where  $\alpha_g$  and  $\alpha_H$  are the swelling ratios of gyration radius and hydrodynamic radius, respectively. These swelling ratios are given by the following functional form,

$$f(z) = (1 + az + bz^2 + cz^3)^{m/2} \quad (6.8)$$

where  $f(z)$  represents the specific swelling ratio ( $\alpha_g$  or  $\alpha_H$ ) and  $a$ ,  $b$ ,  $c$  and  $m$  are fitting parameters the values of which are given in Table 6.1.

const	$\alpha_g$	$\alpha_H$
$a$	9.5286	9.528
$b$	19.48	19.48
$c$	14.92	14.92
$m$	0.133913	0.0995

Table 6.1: Coefficients and constants for the expression of the swelling ratio given in Eq. (6.8).

From Fig. 6.7 it is apparent that for rings  $U_{\text{RD}}$  asymptotically converges to a value equal to 1.345 in the limit of  $z \rightarrow \infty$ . Besides, the ratio  $U_{\text{RD}}$  grows more rapidly with  $z$  in case of linear chains as compared to rings.

Another quantity of interest is the ratio of mean stretch,  $\langle X \rangle$ , to hydrodynamic radius,  $R_H$ . Following a similar method of extrapolation to infinite chain length, the universal values of the ratio  $\langle X \rangle / R_H$  are computed for a range of solvent quality parameter,  $z$ . As seen from Fig. 6.8,  $\langle X \rangle / R_H$  for linear chains has an increasing trend with  $z$ , whereas for rings the ratio is practically independent of solvent quality. This is an important finding which suggests that for rings the swelling in mean stretch and hydrodynamic radius is identical. This fact is further demonstrated in the swelling curve discussed later. Contrary to linear polymers, the absence of any terminal ends in ring architecture makes  $\langle X \rangle$  and  $R_H$  to swell by equal proportion. However, this also implies that in experiments it is not possible to determine solvent quality of a solution of rings from the ratio  $\langle X \rangle / R_H$ .

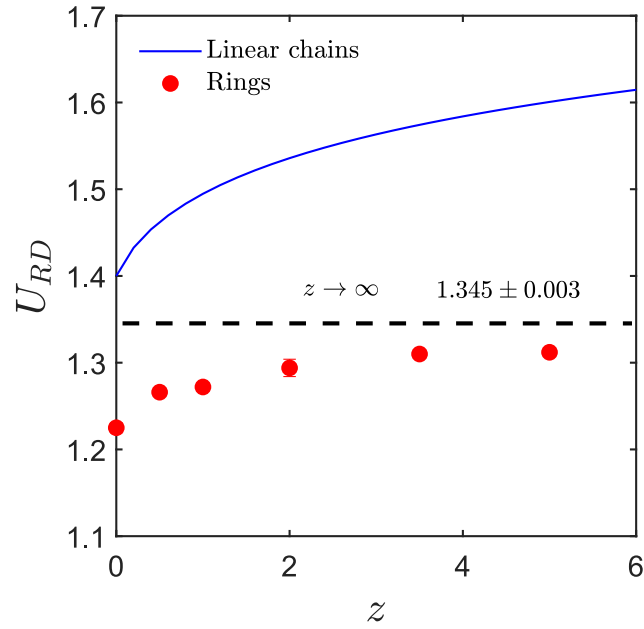


Figure 6.7: The ratio  $U_{RD}$  as a function of  $z$  for rings and linear chains in the long chain limit. The dashed lines represents the value of the ratio in the limit of  $z \rightarrow \infty$  for ring polymers.

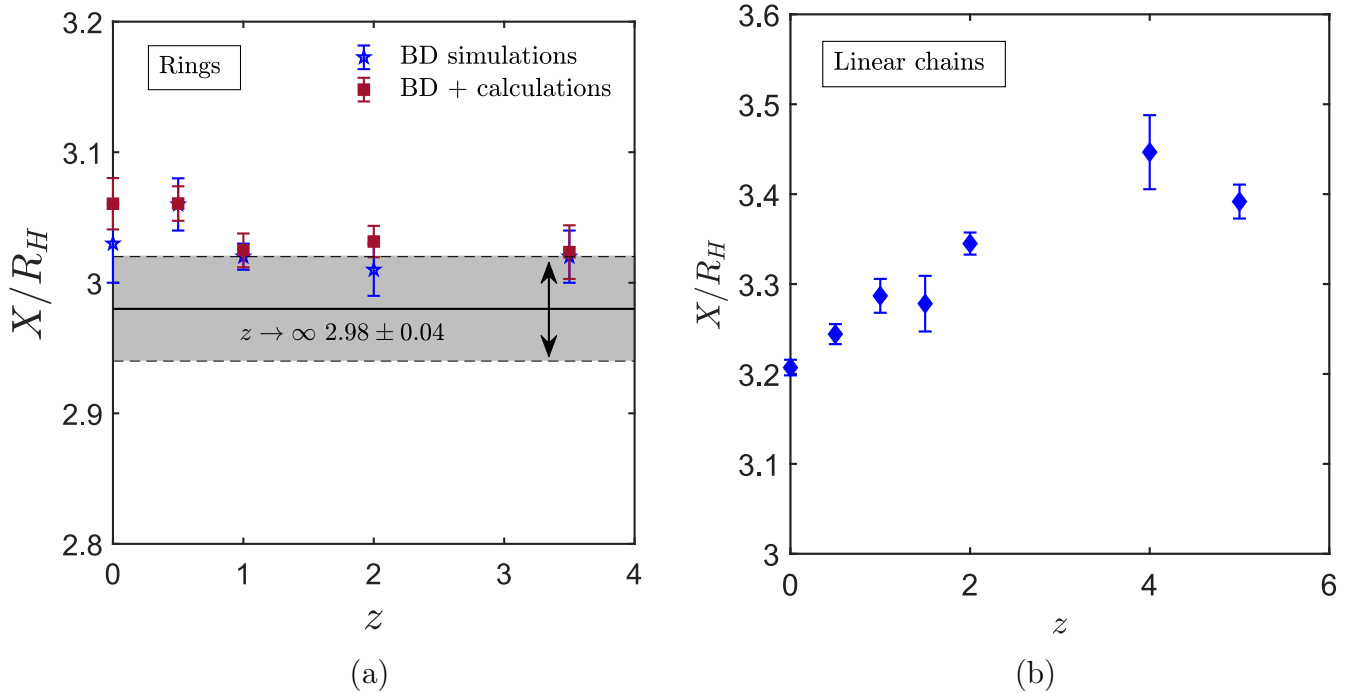


Figure 6.8: The ratio  $\langle X \rangle / R_H$  as a function of  $z$  for (a) rings and (b) linear chains in the long chain limit. The solid line (bounded by dashed lines) represents the value of the ratio in limit of  $z \rightarrow \infty$  for ring polymers.

An alternative method to determine the solvent quality for a given system of polymer solution is from the swelling curve for the gyration radius ( $\alpha_g = R_g/R_g^\theta$ ) or hydrodynamic radius ( $\alpha_H = R_H/R_H^\theta$ ). Fig. 6.9 displays the swelling ratio  $\alpha_g$ ,  $\alpha_H$  and  $\alpha_X$  (for mean stretch) as a function of  $z$  for rings and linear chains. The solid and dashed lines represent the curves obtained by fitting the functional form described in Eq. (6.8) for different swelling ratios. The values of the fitting parameters are given in Table 6.2. For linear polymers there is a clear distinction among the three swelling ratios whereas for rings the swelling of mean stretch,  $\alpha_X$ , and hydrodynamic radius,  $\alpha_H$ , are identical because of the reason discussed earlier. However,  $R_g$  and  $R_H$  swell differently for rings. It should be noted that in order to determine the swelling ratio, one has to estimate the value of  $R_H^\theta$  or  $R_g^\theta$  at the  $\theta$  condition. This could be easily determined by investigating the ratio of gyration radius or hydrodynamic radius of rings (R) to that of linear chains (L). At the  $\theta$  condition both these ratios assume an unique value, which are  $R_g^R/R_g^L = 1/\sqrt{2}$  for the gyration radius and  $R_H^R/R_H^L = 0.81$  for the hydrodynamic radius. Here the ratio  $R_H^R/R_H^L$  at the  $\theta$ -solvent condition is determined by using the formula  $(R_H^R/R_H^L)_\theta = U_{RD_R}^{-1}(R_g^R/R_g^L)_\theta U_{RD_L}$ . Using these universal values and information from the swelling curve it is straight forward to determine the solvent quality for a given polymeric solution of rings or linear chains.

	Linear			Rings		
const	$\alpha_g$	$\alpha_H$	$\alpha_X$	$\alpha_g$	$\alpha_H$	$\alpha_X$
<i>a</i>	9.5286	9.528	10.1358	10.7936	7.5364	7.5364
<i>b</i>	19.48	19.48	11.3791	20.3279	17.45	17.45
<i>c</i>	14.92	14.92	15.0749	2.8128	2.6393	2.6393
<i>m</i>	0.133913	0.0995	0.1159	0.166	0.1464	0.1464

Table 6.2: Coefficients and constants for the expression of the swelling ratio given in Eq. (6.8) for Linear chains and rings.

In addition to the individual swelling behaviour for rings and linear chains, we have also investigated the dependence of the ring to linear ratio for  $R_g$  and  $R_H$  as a function of solvent quality,  $z$ . The ratio of mean stretch as a function of  $z$  for ring to linear chain has already been addressed. Fig. 6.10 shows that the ratio for the gyration radius becomes fairly independent of solvent quality for  $z > 0$ , whereas, the ratio for the hydrodynamic radius displays a significant dependence on the solvent quality. This also suggests that the swelling

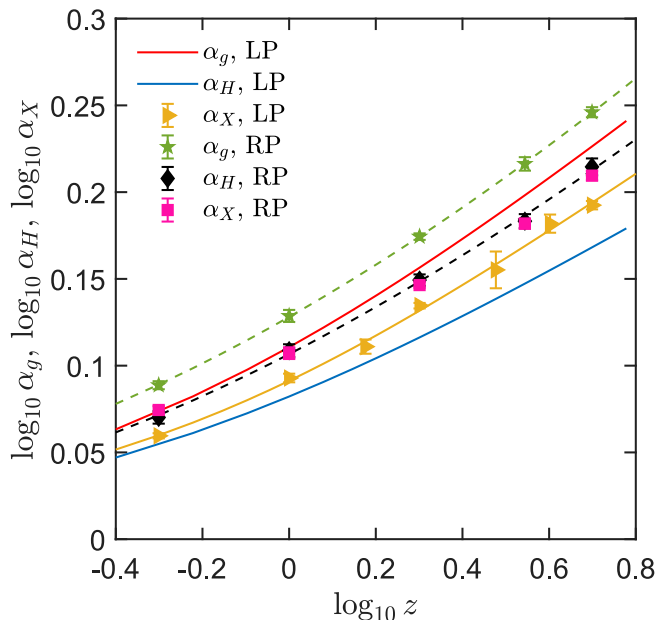


Figure 6.9: Swelling ratio  $\alpha_g$ ,  $\alpha_H$  and  $\alpha_X$  plotted as a function of solvent quality,  $z$ , for linear (LP) and ring (RP) polymers.

ratio of the dynamic radius scales differently for rings and linear polymers.

## 6.5 Conclusions

Using Brownian dynamics simulations we have computed different static and dynamic properties of dilute ring polymer solutions at equilibrium. The universal values of the ratios involving radius of gyration and mean-stretch are calculated as a function of solvent quality,  $z$ , in the limit of infinite chain length and compared with that of linear chains.

Two different methods based on mean-squared displacement and Fixman's formula are used to evaluate the diffusivity and hydrodynamic radius of ring polymers. Interestingly, the results obtained from both the methods are in very good agreement with each other. This suggests the applicability of Fixman's formula to compute the long time diffusion coefficient for polymeric rings. We have also pointed out the importance of Fixman's correction in the evaluation of long-time diffusivity which has not been addressed before for ring polymers.

Universal ratios  $U_{RD}$  and  $X/R_H$  involving hydrodynamic radius,  $R_H$ , are evaluated as a function of solvent quality,  $z$  and compared with the respective values for linear polymers. In

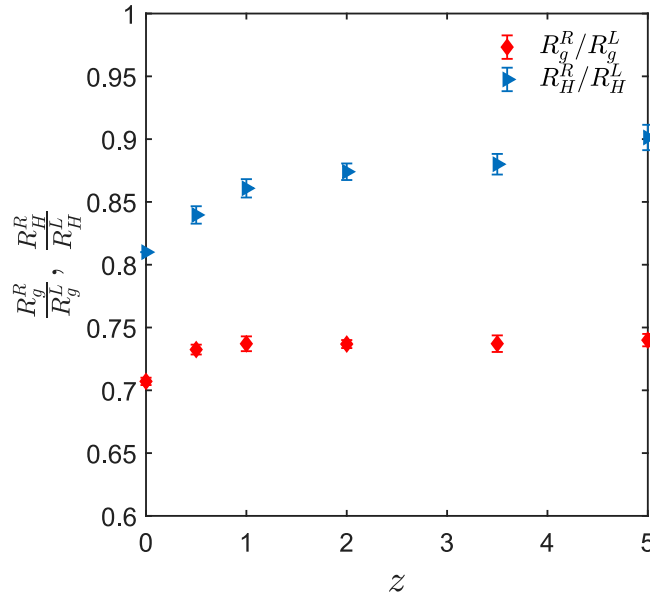


Figure 6.10: Ratio of gyration radius and hydrodynamic radius for ring to linear chain plotted as a function of solvent quality,  $z$ .

this regard we have found a fixed point value for the hydrodynamic interaction parameter,  $h^*$ , which leads to quick convergence of the ratio  $U_{RD}$  to its universal limit.

In this work we have suggested an alternative method to determine the solvent quality of ring polymer solutions from the universal curve for the swelling ratios. The values of the universal ratios and the swelling curve can be used to accurately estimate the solvent quality for an experimental system of ring polymers which can then be used to model ring polymer chains in simulations.

This is a preliminary work to understand the static and dynamic behaviour of a dilute solution of ring polymers. Although, the results discussed here are from equilibrium simulations, they are, however, the basis to investigate the interesting rheological and viscoelastic properties of ring polymer solutions, such as tumbling and tank-treading dynamics in a shear flow.

# Chapter 7

## Summary and future work

Static and dynamic properties of associative polymer solutions in the dilute and semi-dilute regimes have been investigated in this thesis using Brownian dynamics (BD) simulations. A modified Soddemann-Dünweg-Kremer (SDK) potential (Soddemann et al., 2001)(Santra et al., 2019) is implemented to model the association between the stickers in associative polymers. This is one of the first comprehensive studies, where the microscopic topology is systematically correlated with the macroscopic viscoelasticity of associative polymer solutions. The entire study is based on the framework of a mean-field theory proposed by Rubinstein and Semenov (Semenov and Rubinstein, 1998)(Rubinstein and Semenov, 1998)(Rubinstein and Semenov, 2001) and later developed further by Dobrynin (Dobrynin, 2004). The results obtained from the simulations are compared with the scaling predictions of the mean-field theory (Dobrynin, 2004)(Semenov and Rubinstein, 1998)(Rubinstein and Semenov, 1998)(Rubinstein and Semenov, 2001), and are found to largely agree with the theoretical predictions. One of the key features of associative polymer solutions is the formation of reversible physical gels at fairly low concentrations. In this thesis the static and dynamic signatures of gelation are characterized using different definitions of sol-gel transition. Hydrodynamic interaction (HI) is implemented using an optimised Ewald-summation algorithm which scales with the number of particles as  $N^{1.5}$  (Jain et al., 2012). However, with this method the speed of the simulations gets considerably slower with an increase in system size. We are therefore limited by the computational technique to the study of associative polymers of short chain lengths. The dynamics of longer chains may be explored by using

fast BD algorithms such as the one developed by Fiore et al. (Fiore et al., 2017). Moreover, the study carried out in this thesis has helped to understand many of the underlying physical phenomena which leads to the unique viscoelastic responses of associative polymer solutions. This will also allow us to look at the dynamics of associative polymer solutions with long chains, and see the effect of chain length on the rheology and gelation signatures.

This thesis also discusses a problem related to the understanding of the static and dynamic properties of dilute ring polymer solutions, where the universal behaviour of different equilibrium static and dynamic properties of polymeric rings is studied as a function of solvent quality. The work carried out in this project forms the foundation to investigate the more interesting linear and non-linear viscoelasticity of single polymeric rings in solution. It is required to develop an accurate model for polymer solutions in order to compare the simulation predictions with actual experimental systems. We hope that the method proposed here for the estimation of the solvent quality and size of polymeric rings will help in better modelling of ring polymer solutions.

# Appendix A

## The cut-off radius for the SDK potential

As it is mentioned in Chapter 2 and 3, in the original study by Soddemann et al. (Soddemann et al., 2001) the cut-off radius of the SDK potential,  $r_c$ , was chosen to be  $1.5\sigma$  in order to include only the first neighboring shell of interactions, determined from the first minimum of the pair correlation function. In this section, we first show that in the context of the Brownian dynamics simulations carried out in this work, the choice of  $r_c = 1.5\sigma$  leads to the prediction of unphysical asymptotic scaling behaviour in the poor solvent limit. We then discuss how an appropriate value of the cut-off radius can be estimated. The material discussed in this section is taken from the supplementary information of the study carried out by Santra et al. (Santra et al., 2019) on swelling of sticky polymers. For the sake of completeness and clarity, we repeat some of the equations that have already been displayed in the main text.

The potential proposed by Soddemann-Dünweg-Kremer (SDK) (Soddemann et al., 2001)

has the form,

$$U_{\text{SDK}} = \begin{cases} 4 \left[ \left( \frac{\sigma}{r} \right)^{12} - \left( \frac{\sigma}{r} \right)^6 + \frac{1}{4} \right] - \epsilon; & r \leq 2^{1/6}\sigma \\ \frac{1}{2}\epsilon \left[ \cos \left( \alpha \left( \frac{r}{\sigma} \right)^2 + \beta \right) - 1 \right]; & 2^{1/6}\sigma \leq r \leq r_c \\ 0; & r \geq r_c \end{cases} \quad (\text{A.1})$$

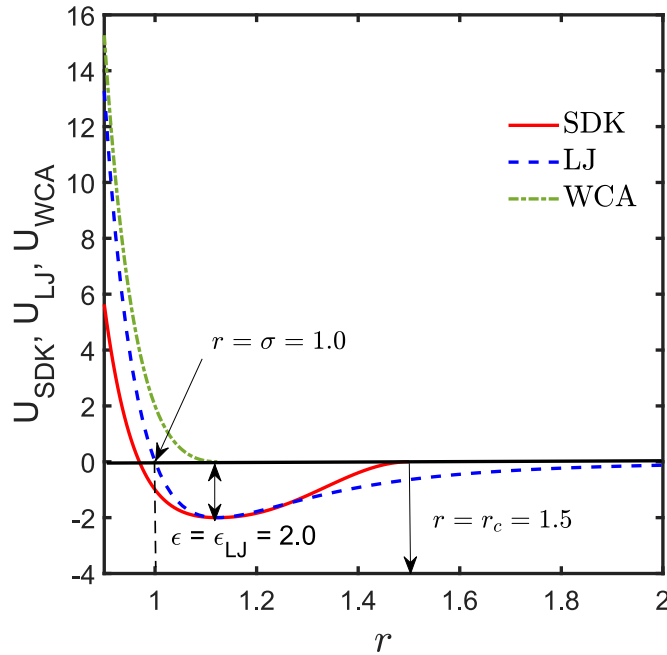


Figure A.1: (Color online) Comparison between the SDK potential ( $U_{\text{SDK}}$ ) and the conventional LJ ( $U_{\text{LJ}}$ ) and WCA ( $U_{\text{WCA}}$ ) potentials as a function of the radial distance,  $r$ , for well depths  $\epsilon = \epsilon_{\text{LJ}} = 2.0$ ,  $\sigma = 1$ , and  $r_c = 1.5$  (see text for corresponding values of  $\alpha$  and  $\beta$ ).

A comparison is drawn in Fig. A.1 between the SDK potential and the conventional Lennard-Jones (LJ) and Weeks-Chandler-Andersen (WCA) potentials, the expressions of which are given in Eq. (A.2) and Eq. (A.3), respectively.

$$U_{\text{LJ}} = 4\epsilon_{\text{LJ}} \left[ \left( \frac{\sigma}{r} \right)^{12} - \left( \frac{\sigma}{r} \right)^6 \right] \quad (\text{A.2})$$

$$U_{\text{WCA}} = \begin{cases} 4\epsilon_{\text{LJ}} \left[ \left(\frac{\sigma}{r}\right)^{12} - \left(\frac{\sigma}{r}\right)^6 + \frac{1}{4} \right]; & r \leq 2^{1/6}\sigma \\ 0; & r > 2^{1/6}\sigma \end{cases} \quad (\text{A.3})$$

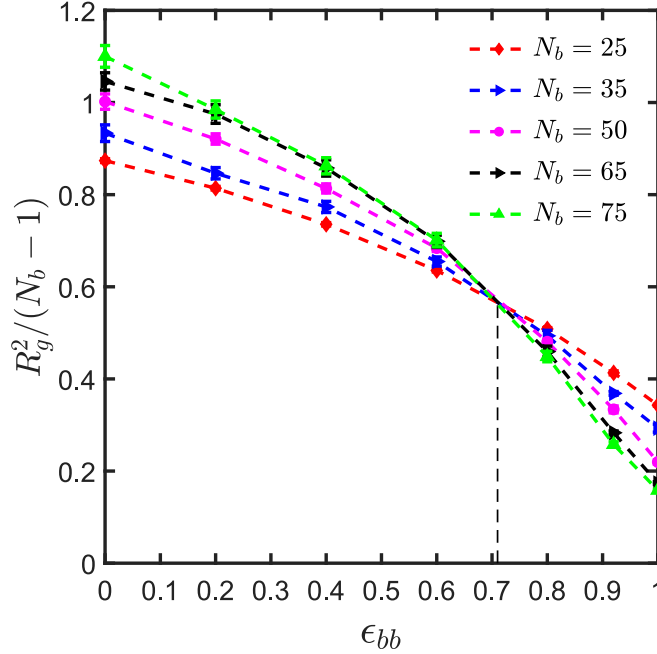


Figure A.2: (Color online) The ratio  $R_g^2/(N_b - 1)$  as a function of the well depth of the SDK potential,  $\epsilon_{bb}$ , used to estimate the  $\theta$ -point for the cutoff radius  $r_c = 1.5\sigma$ . The symbols represent simulation data and the dotted lines are drawn to guide the eye. The  $\theta$ -point is estimated as the intersection of all the curves and leads to  $\epsilon_{bb} = 0.72$ .

In the above equations,  $\sigma$  is the non-dimensional distance at which the LJ potential becomes zero, and its value is taken to be 1 in the present study. The quantities  $\epsilon$  and  $\epsilon_{\text{LJ}}$  are the attractive well depths of the SDK and LJ potentials, respectively. As shown in Fig. A.1, unlike the LJ potential, which has a long attractive tail, the short ranged attractive tail of the SDK potential smoothly approaches zero at a finite distance  $r_c$ . The choice  $\epsilon = 0$  in the SDK potential is equivalent to  $\epsilon_{\text{LJ}} = 1.0$  in the purely repulsive WCA potential.

The constants  $\alpha$  and  $\beta$  (as discussed in Chapter 2) are determined by applying the two boundary conditions, namely,  $U_{\text{SDK}} = 0$  at  $r = r_c$ , and  $U_{\text{SDK}} = -\epsilon$  at  $r = 2^{1/6}\sigma$ . Based on these two boundary conditions,  $\alpha$  and  $\beta$  are calculated by solving the following set of

equations,

$$2^{1/3}\alpha + \beta = \pi \quad (\text{A.4})$$

$$\left(\frac{r_c}{\sigma}\right)^2 \alpha + \beta = 2\pi \quad (\text{A.5})$$

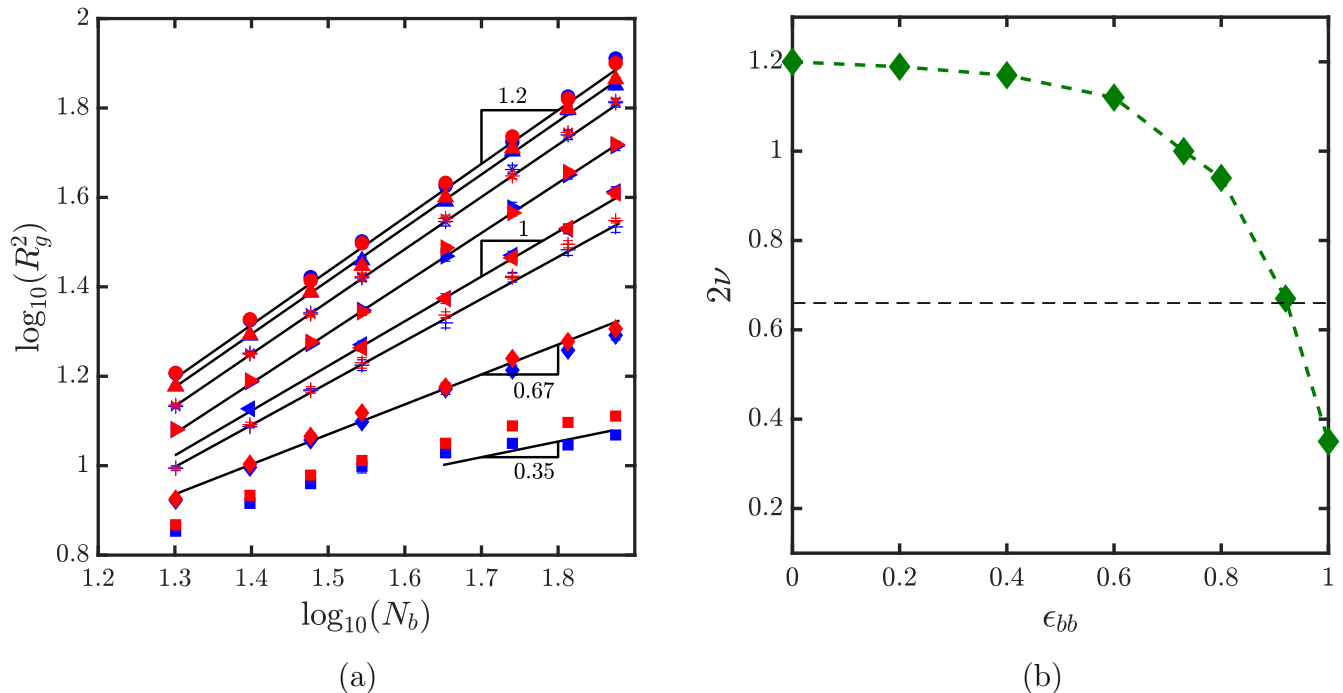


Figure A.3: (Color online) (a) The mean-squared radius of gyration as a function of the number of beads in a chain. The blue-coloured symbols are for different values of well-depth,  $\epsilon_{bb}$ , in the absence of hydrodynamic interactions.  $\bullet$   $\epsilon_{bb} = 0$ ,  $\blacktriangle$   $\epsilon_{bb} = 0.2$ ,  $*$   $\epsilon_{bb} = 0.4$ ,  $\blacktriangleright$   $\epsilon_{bb} = 0.6$ ,  $\blacktriangleleft$   $\epsilon_{bb} = 0.72$ ,  $+$   $\epsilon_{bb} = 0.8$ ,  $\blacklozenge$   $\epsilon_{bb} = 0.92$  and  $\blacksquare$   $\epsilon_{bb} = 1$ . The same symbols are used with a red colour for simulations with hydrodynamic interactions. The straight lines are of slope  $2\nu$  at different values of  $\epsilon_{bb}$ . (b) Effective exponent  $2\nu$  versus the well-depth,  $\epsilon_{bb}$ , for cutoff radius  $r_c = 1.5\sigma$ .

In Section 3.3 of the main text it is shown how the value of  $\epsilon_{bb}$  at the  $\theta$ -point can be estimated by plotting the ratio  $R_g^2/(N_b - 1)$  versus  $\epsilon_{bb}$  for different chain lengths,  $N_b$ , and finding the point of intersection at which curves for different values of  $N_b$  intersect (Steinhauser, 2005)(Huissmann et al., 2009). With the cut-off radius set to  $r_c = 1.5\sigma$ , the  $\theta$ -point for a homopolymer chain with beads connected by FENE springs having a maximum stretchable length of  $Q_0^2 = 50.0$ , is found to be  $\epsilon_{bb} = 0.72$  as shown in Fig. A.2. This is in contrast to the value of  $\epsilon_{bb} = 0.45$  obtained for  $r_c = 1.82\sigma$ , as was demonstrated in Section 3.3. The

reasons for the unsuitability of using  $r_c = 1.5\sigma$  are discussed below.

With increasing values of  $\epsilon_{bb}$  beyond  $\epsilon_{bb} = 0.72$ , the chain begins to collapse due to decreasing solvent quality. In the limit of a poor solvent, linear polymer chains obey the scaling law  $R_g \sim (N_b - 1)^{1/3}$ , indicating that the chains are space filling. Fig. A.3 (a) studies the chain length dependence of  $R_g^2$  for various well depths  $\epsilon_{bb}$ . For  $\epsilon_{bb} = 0$  (the athermal limit) and  $\epsilon_{bb} = 0.72$  (the  $\theta$ -point), the expected power law exponents of 1.2 and 1.0, respectively, are observed. For intermediate values in the crossover regime,  $0 < \epsilon_{bb} < 0.72$ , one expects, strictly speaking, a curve beginning with slope 1 at small values of  $N_b$ , and gradually increasing to 1.2 for asymptotically long chains. However, for the fairly short chains studied here, this curvature is very hard to observe; instead the data can be well described in terms of an effective exponent, whose variation with  $\epsilon_{bb}$  is shown in Fig. A.3 (b). An analogous crossover from a slope of 1.0 to  $(2/3)$  is expected as the well depth is increased beyond the  $\theta$  value of 0.72, with the effective exponent remaining at  $(2/3)$  for sufficiently large  $\epsilon_{bb}$ . However, as can be seen from Figs. A.3 (a) and (b), the “asymptotic” slope at  $\epsilon_{bb} = 1$  seems to be only 0.35, which is obviously unphysical, if interpreted as an asymptotic scaling law. We can only speculate here about the reasons for this behaviour — since we were able to “cure” the problem without a detailed investigation, we did not attempt to analyse it in depth. However, a few observations may be made.

Firstly, Fig. A.3 (a) shows clearly that the data at  $\epsilon_{bb} = 1$  are hampered by equilibration problems. This becomes obvious via the comparison of data accumulated with and without hydrodynamic interactions, which, as static averages, must be identical if strict thermal equilibrium and sufficient sampling is achieved. Secondly, it has already been pointed out in Soddemann et al. (Soddemann et al., 2001) that the SDK potential with  $r_c = 1.5\sigma$  has a propensity to induce crystallisation, i.e., highly ordered structures. It is then quite conceivable that the growth of a highly collapsed globule with chain length occurs essentially in a layer-by-layer fashion, which would then give rise to a fairly abrupt increase of  $R_g^2$  as soon as a new layer begins to be populated. The small slope of 0.35 that we observe in Fig. A.3 (a) may then perhaps be part of a quasi-plateau that corresponds to oscillations that are added on top of the leading  $N^{2/3}$  behaviour.

Prompted by our experience with using a simple Lennard-Jones potential in analogous

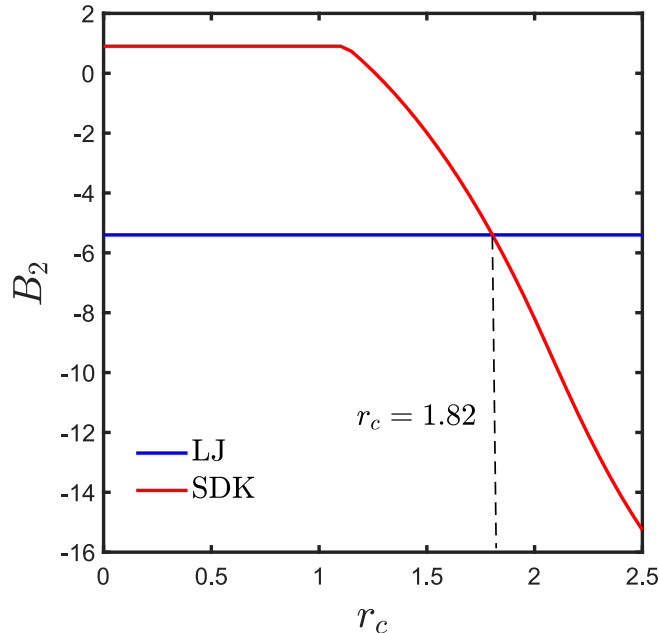


Figure A.4: (Color online) The second virial coefficient  $B_2$  of the SDK potential, compared with the corresponding value for the LJ potential, as a function of the cutoff radius,  $r_c$ , for well-depths  $\epsilon_{bb} = \epsilon_{LJ} = 1.0$ , and  $\sigma = 1$ .

studies of collapsing polymer chains (Pham et al., 2010), which did not exhibit this problem, we attempted to solve it by modifying the SDK potential such that it would mimic more closely the attributes of the Lennard-Jones potential. In practice, we adjusted the range of the SDK potential  $r_c$  by requiring that, for  $\epsilon_{LJ} = \epsilon_{bb} = 1$  and  $\sigma = 1$ , both potentials give rise to the same value of the second virial coefficient given by the integral (Rubinstein and Colby, 2003)

$$B_2 = \int_0^{\infty} 2\pi r^2 (1 - \exp[-U(r)/k_B T]) dr. \quad (\text{A.6})$$

Matching this value with the corresponding LJ value results in  $r_c = 1.82 \sigma$  (see Fig. A.4), for which  $\alpha = 1.5306333121$  and  $\beta = 1.213115524$ . In view of the remarks made earlier, it is well conceivable that such a smoother potential will exhibit less pronounced oscillations or perhaps none at all.

As seen in Fig. A.5 (a), the effective exponent shows a gradual decrease from 1.2 at  $\epsilon_{bb} = 0$  to 0.67 at  $\epsilon_{bb} = 0.55$ , and it remains constant at 0.67 well beyond  $\epsilon_{bb} = 0.55$ , as shown in Fig. A.5 (b). The values of the mean-squared radius of gyration,  $R_g^2$ , are reproduced with

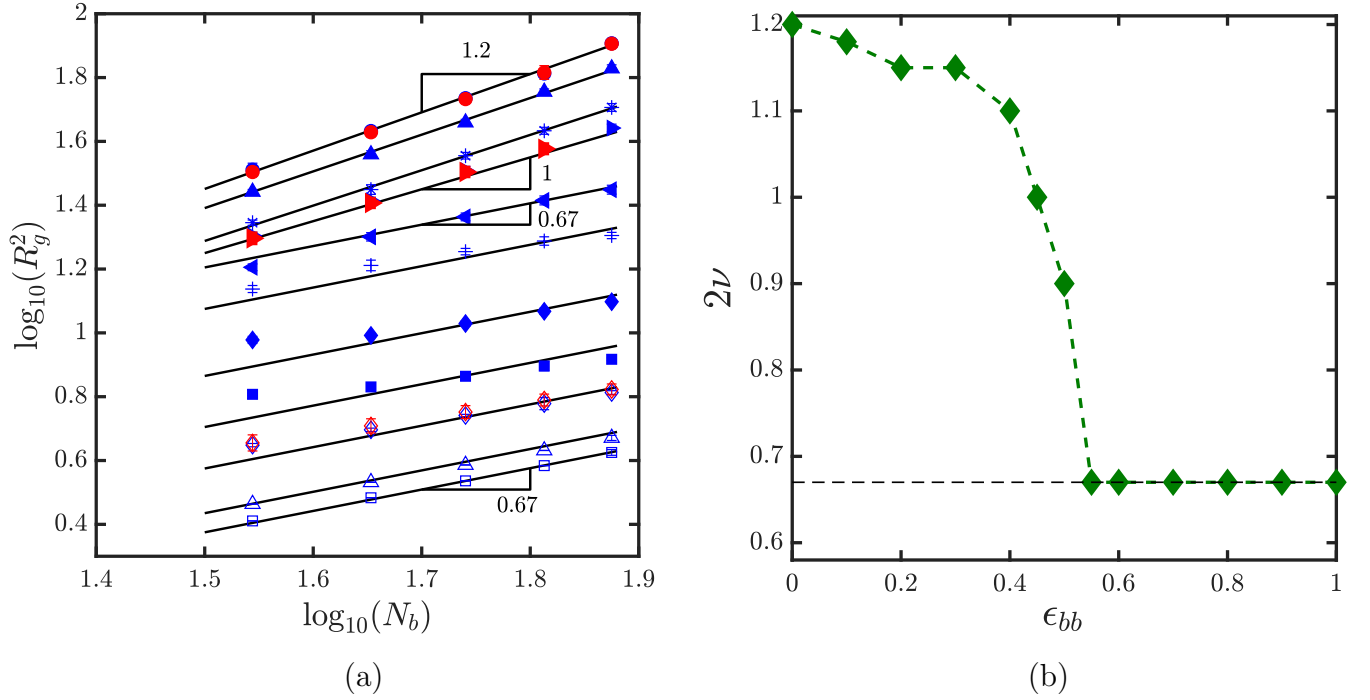


Figure A.5: (Color online) (a) The mean-squared radius gyration versus number of beads in a chain. The blue-coloured symbols are for different values of well-depth,  $\epsilon_{bb}$ , in the absence of hydrodynamic interactions.  $\bullet$   $\epsilon_{bb} = 0$ ,  $\blacktriangle$   $\epsilon_{bb} = 0.2$ ,  $*$   $\epsilon_{bb} = 0.4$ ,  $\blacktriangleright$   $\epsilon_{bb} = 0.45$ ,  $\blacktriangleleft$   $\epsilon_{bb} = 0.55$ ,  $+$   $\epsilon_{bb} = 0.6$ ,  $\blacklozenge$   $\epsilon_{bb} = 0.7$  and  $\blacksquare$   $\epsilon_{bb} = 0.8$ ,  $\diamond$   $\epsilon_{bb} = 1$ ,  $\triangle$   $\epsilon_{bb} = 2$  and  $\square$   $\epsilon_{bb} = 3$ . The same symbols are used with a red colour for simulations with hydrodynamic interactions. The straight lines are of slope  $2\nu$  at different values of  $\epsilon_{bb}$ . (b) Exponent  $2\nu$  versus the well-depth,  $\epsilon_{bb}$ , at cutoff radius  $r_c = 1.82\sigma$ .

HI for  $\epsilon_{bb} = 0, 0.45$  and  $1.0$ , for different chain lengths and found to be consistent with the results without HI (as seen in Fig. A.5 (a)). All the results reported in the current work with the SDK potential are consequently for  $r_c = 1.82\sigma$ .

# Appendix B

## Equivalence of sticking rules

The rules implemented in the current algorithm for deciding when a pair of stickers associate with each other have been described in Section 2.5. In particular, in cases where three or more stickers are within the cut-off radius, the sticking pairs are selected based on the order of labelling of the stickers. This rule is denoted here as scheme 1. An alternative scheme could be to pick the sticking pairs at random when three or more stickers are within the interaction range (denoted here as scheme 2). We anticipate that since a large ensemble of chains are distributed randomly in a simulation box, bead labels of neighbouring beads are essentially random, and since the probability of three or higher body interactions for stickers is very low, the two schemes should effectively produce the same results. This is illustrated in Figs. B.1 where the radius of gyration, and the intra-chain and inter-chain association fractions are plotted against time after reaching the stationary state. It can be seen that for each of the static properties, the results of both the schemes agree within error-bars, with the values fluctuating about the equilibrium averages.

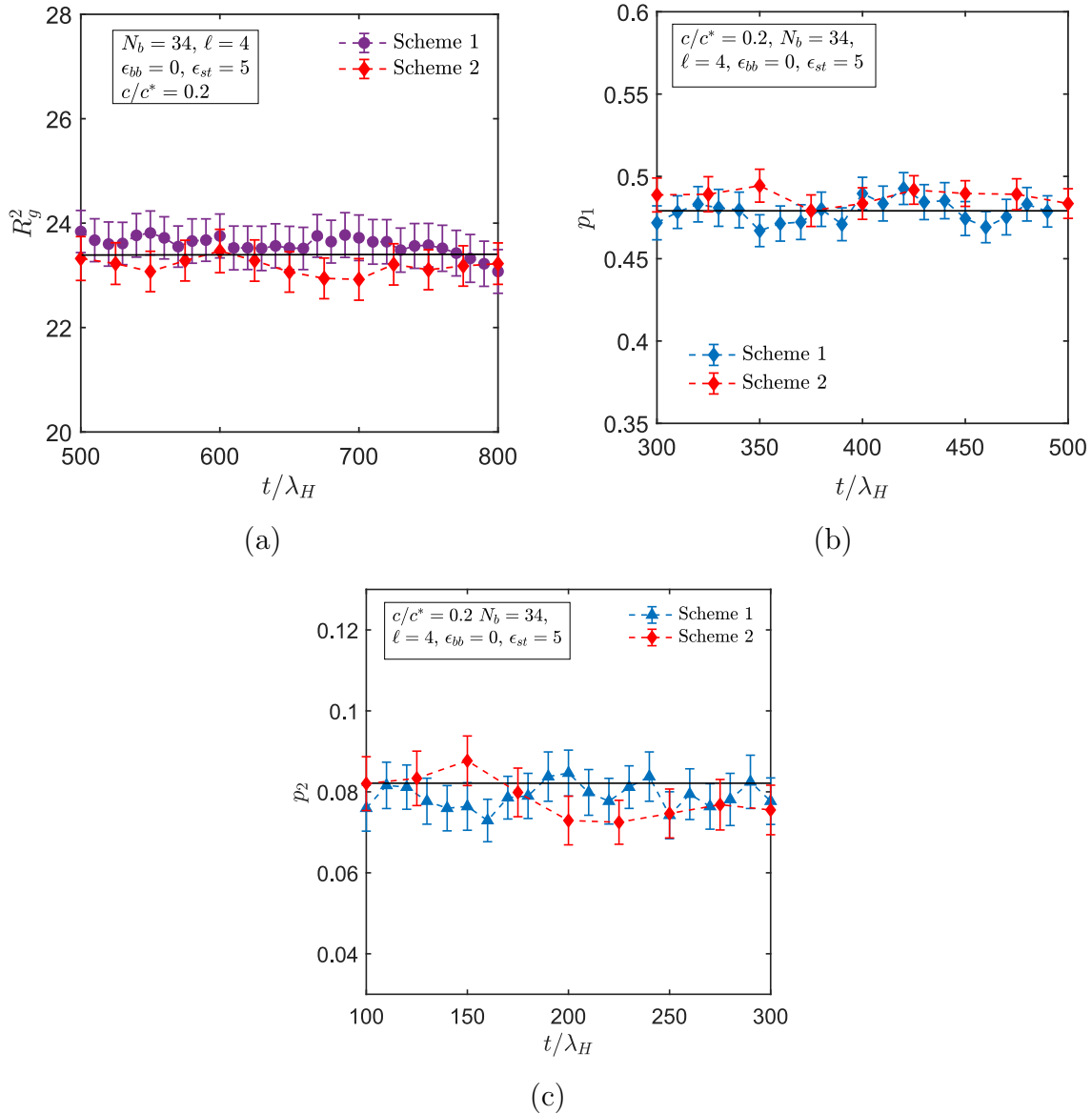


Figure B.1: Comparison of the equilibrium values of (a) radius of gyration,  $R_g^2$ , (b) intra-chain association fraction,  $p_1$ , and (c) inter-chain association fraction,  $p_2$ , predicted by the two different sticking rules, scheme 1 and scheme 2. Simulations are carried out with chain length  $N_b = 34$ , spacer length  $\ell = 4$ , sticker strength  $\epsilon_{st} = 5$ , and concentration  $c/c^* = 0.2$ , for the backbone monomers under athermal solvent conditions, i.e.,  $\epsilon_{bb} = 0$ . The symbols are from simulations and the solid lines are equilibrium averaged values of the static properties.

# Appendix C

## Scaling relations in associative polymer solutions from lattice-based mean-field theory

The scaling relations for associative polymer solutions, derived by Dobrynin (Dobrynin, 2004), based on a lattice-based mean-field theory involves minimisation of the free energy of the system, obtained from the partition function,  $Z$ , as discussed below. In an associative polymer solution the partition function can be decomposed into three components, namely,  $Z_{\text{mix}}$ ,  $Z_{\text{bond}}$  and  $Z_{\text{int}}$  as follows,

$$Z = Z_{\text{mix}}Z_{\text{bond}}Z_{\text{int}} \quad (\text{C.1})$$

Here,  $Z_{\text{mix}}$  is the term involving different arrangements of the solvent molecules,  $N_s$ , and polymers,  $N_p$ , in  $n$  lattice sites.  $Z_{\text{bond}}$  is the contribution from the sticker-sticker binding interaction and  $Z_{\text{int}}$  describes the interactions between the solvent molecules and polymers. Although, in BD simulations lattice geometry is not applicable but it still gives a useful framework to analyse the results obtained from the simulations.  $Z_{\text{mix}}$  and  $Z_{\text{int}}$  together constitute the polymeric contribution to the free energy,  $F_{\text{pol}}$ , without the sticker associations. In a system with  $\phi$  as the probability of occupancy of lattice sites (equivalent to the monomer concentration,  $c$ ) and  $\tau_s$  as the effective solution temperature,  $F_{\text{pol}}$  is given by the following

expression (Dobrynin, 2004),

$$\frac{F_{\text{pol}}}{nk_B T} \approx \frac{\phi}{N_b} \ln \frac{\phi}{eN_b} + C_2 \tau_s^{3/4} \phi^{9/4} \quad (\text{C.2})$$

here,  $N_b$  is the degree of polymerisation,  $k_B$  is the Boltzmann constant and  $T$  is the temperature. The above equation is valid in the good solvent condition where  $\tau_s > N_b^{-1/2}$ . With the inclusion of stickers, there will be additional contributions to the free energy from the intra-chain and inter-chain associations of the stickers. In the following sections we briefly discuss the probability of intra-chain and inter-chain associations under various conditions, as derived by Dobrynin (Dobrynin, 2004), which is used to calculate their contributions to the free energy.

## C.1 Intra-chain association scaling

Before discussing the intra-chain scaling in different regimes for associative polymer solutions it is required to consider the following two arguments for finding the probability for a given monomer to encounter any other monomer on the same chain.

*Argument 1:*

The overlap volume fraction for  $N_b$  monomers in a volume  $R^3$  pervaded by a chain is given by (Rubinstein and Colby, 2003)

$$\phi^* = \frac{N_b b^3}{R^3} = \frac{N_b b^3}{b^3 N_b^{3\nu}} = N_b^{1-3\nu} \quad (\text{C.3})$$

where  $b$  is the monomer size and  $\nu$  is the Flory exponent. In this case the probability of one monomer encountering another monomer (any of the  $N_b$ ) is simply  $\phi^*$ . The total number of monomer-monomer contacts is then given as,

$$N_b \phi^* \sim N_b \times N_b^{1-3\nu} \sim N_b^{2-3\nu} \quad (\text{C.4})$$

In a  $\theta$ -solvent the total number of contacts reduces to  $N_b^{1/2}$ .

*Argument 2:*

The second argument is based on the probability of loop formation between two ends of a chain segment. The end-to-end vector of a Gaussian chain has a probability distribution,

$$P(N_b, \mathbf{r}) = \left( \frac{3}{2\pi N_b b^2} \right)^{3/2} \exp \left( -\frac{3\mathbf{r}^2}{2N_b b^2} \right) \quad (\text{C.5})$$

so the probability of the two ends forming a loop is found by setting  $\mathbf{r} = \mathbf{0}$ , so that

$$P_{\text{loop}} = \left( \frac{3}{2\pi N_b b^2} \right)^{3/2} \sim N_b^{-3/2} \quad (\text{C.6})$$

For a segment of chain with  $\ell$  monomer ( $\ell$  is the spacer length),  $P(\ell) \sim \ell^{-3/2}$ . These two arguments have been used in different contexts in the scaling theory to derive the expressions for the intra-chain and inter-chain association fractions (Dobrynin, 2004).

**Regime I:**  $\ell < g_T < g_c$

In this regime there are many associating groups in a thermal blob and within the thermal blob the chain still obeys Gaussian statistics. So the probability of intra-chain association scaling in this case is given by  $P(\ell) \sim \ell^{-3/2}$  as discussed above.

**Regime II:**  $g_T < \ell < g_c$

In this case there are many thermal blobs between two associating groups. Here, the calculation of the probability that two associating groups come in contact involves several steps. Firstly, in good solvent, des Cloizeaux has derived a formula for the probability of contact,  $P_{\text{good}}$ , between two segments of a chain separated by  $m$  monomers which is given as (des Cloizeaux, 1980)(Dobrynin, 2004)

$$P_{\text{good}} \sim \left( \frac{\delta}{r(m)} \right)^{3+\theta_2} \quad (\text{C.7})$$

where,  $\delta$  is the actual spatial distance between the monomers, and  $r(m)$  is the mean square end-to-end distance between two segments separated by  $m$  monomers. The value of the exponent  $\theta_2$  is obtained by des Cloizeaux using perturbation expansion.

Since thermal blobs within a correlation blob are undergoing self-avoiding walk (SAW) statistics, then for a fixed temperature,

$$r(\ell) = \xi_T \left( \frac{\ell}{g_T} \right)^\nu \sim \ell^\nu \quad (\text{C.8})$$

For two thermal blobs, containing the associating groups, to come in contact,  $\delta = \xi_T$  and  $r(m) = r(\ell)$ . So the probability of contact between two such thermal blobs is

$$P_T \sim \left( \frac{g_T}{\ell} \right)^{(3+\theta_2)\nu} \quad (\text{C.9})$$

Now the probability that two associating groups in these overlapping thermal blobs come in contact can be calculated by assuming that there are approximately  $g_T$  monomers between them, so the probability is  $g_T^{-3/2}$  (from Eq. C.6). Therefore the total probability of intra-chain pairing in Regime II is given by

$$P(\ell) = \left( \frac{g_T}{\ell} \right)^{\nu(3+\theta_2)} g_T^{-3/2} \quad (\text{C.10})$$

**Regime III:**  $g_T < g_c < \ell$

In Regime III there are many correlation blobs between two associating groups. In this case the association between two groups involves a three step process which is discussed as follows. (i) Two correlation blobs containing the associating groups have to come in contact, (ii) the two thermal blobs within the correlation blobs containing the associating groups have to come together, (iii) the two associating groups inside the overlapping thermal blobs have to find each other. Total probability is a combination of the probabilities for each of these steps.

In the first step, since correlation blobs execute random walk (RW) statistics, and there are  $(\ell/g_c)$  correlation blobs between stickers, the probability of two correlation blobs forming a loop is proportional to  $(\ell/g_c)^{-3/2}$  from argument 2. Once two correlation blobs are in contact the two thermal blobs, containing the stickers, within the correlation blobs have to come together. As the thermal blobs execute SAW statistics and there are  $(g_c/g_T)$  thermal blobs in a correlation blob, the probability that two thermal blobs inside a correlation blob

will form a loop is proportional to  $(g_T/g_c)^{\nu(3+\theta_2)}$ . Finally, the two associating groups inside a thermal blob can form a loop with probability  $g_T^{-3/2}$ . Combining all these, the total probability of intra-chain pairing in Regime III is

$$P(\ell) = \left(\frac{g_c}{\ell}\right)^{3/2} \left(\frac{g_T}{g_c}\right)^{\nu(3+\theta_2)} g_T^{-3/2} \quad (\text{C.11})$$

## C.2 Inter-chain association scaling

Similar to the intra-chain associations, the probability of inter-chain associations can also be found using simple arguments. Assuming a system of space filling correlation blobs in a lattice geometry with coordination number  $z$ , there are  $z$  correlation blobs surrounding any one correlation blob. Two of these contain the segment of the same chain, so there are  $(z-2)$  correlation blobs from other chains. In order to form an inter-chain association with the stickers within the concerned correlation blob, the second associating group must belong any of the surrounding  $(z-2)$  correlation blobs. Similar to the intra-chain associations there are several regimes for the inter-chain association scaling as discussed below.

**Regime I:**  $\ell < g_T < g_c$

In this case there is more than one sticker in a thermal blob and for any two associating groups to stick, two thermal blobs have to come close to each other. Since the thermal blobs follow SAW statistics, this happens with a probability proportional to  $(g_T/g_c)^{\nu(3+\theta_2)}$ , as there are  $(g_c/g_T)$  thermal blobs in a correlation blob. Now, for an inter-chain association the second associating group should come from a thermal blob within the surrounding  $(z-2)$  correlation blobs. Since there are  $(z-2)(g_c/g_T)$  such thermal blobs, the probability should be multiplied by this factor. Within a thermal blob there are  $(g_T/\ell)$  stickers and the probability of contact between any two of those stickers is proportional to the volume fraction of the stickers inside a thermal blob, which is given as

$$\frac{(g_T/\ell)}{\xi_T^3} = \frac{(g_T/\ell)}{b^3 g_T^{3/2}} \sim \ell^{-1} g_T^{-1/2} \quad (\text{C.12})$$

The total probability of inter-chain pairing in this regime is then obtained by combining all these factors,

$$\begin{aligned}
 P_{\text{inter}} &= \left(\frac{g_T}{g_c}\right)^{\nu(3+\theta_2)} \left(\frac{g_c}{g_T}\right) (z-2) \frac{1}{\ell g_T^{1/2}} \\
 &= (z-2) \left(\frac{g_c}{\ell}\right) \left(\frac{g_T}{g_c}\right)^{\nu(3+\theta_2)} g_T^{-3/2}
 \end{aligned} \tag{C.13}$$

**Regime II:**  $g_T < \ell < g_c$

Here there are many thermal blobs between associating groups, and many associating groups within a correlation blob. Since each correlation blob has  $(g_c/\ell)$  stickers, so there are altogether  $(z-2)(g_c/\ell)$  associating groups surrounding any particular correlation blob. The probability of contact between two thermal blob is again  $(g_T/g_c)^{\nu(3+\theta_2)}$  as in the case above. Now since there is one associating group in a thermal blob, the probability of stickers to come together within a thermal blob is  $g_T^{-3/2}$ , according to *argument 2*. Putting all these together, the total probability of inter-chain association in this regime is obtained as,

$$P_{\text{inter}} = (z-2) \left(\frac{g_c}{\ell}\right) \left(\frac{g_T}{g_c}\right)^{\nu(3+\theta_2)} g_T^{-3/2} \tag{C.14}$$

**Regime III:**  $g_T < g_c < \ell$

In this case there are many correlation blobs between two stickers. For two stickers to come in close contact in this regime, the following steps have to be followed. (i) Two correlation blobs (containing a sticker each) have to come in contact. (ii) Within the correlation blob two thermal blobs containing the stickers have to come together. (iii) Two associating groups inside the overlapping thermal blobs have to find each other.

It should be noted that in this regime a correlation blob can have at most one sticker. So the total volume fraction of the correlation blobs containing stickers is

$$\frac{\frac{N_b}{\ell} N_c \xi_c^3}{\frac{N_b}{g_c} N_c \xi_c^3} = \frac{g_c}{\ell}$$

where  $N_b/\ell$  is the number of stickers per chain (or number of correlation blobs per chain which contain a sticker),  $N_c$  is the number of chains,  $N_b/g_c$  is the number of correlation blobs per chain and  $\xi_c$  is the size of a correlation blob. The probability of contact between two correlation blobs, containing a sticker each, is simply given by  $(z - 2)(g_c/\ell)$ . Now, the probability of contact between two thermal blobs in a correlation blob is  $(g_T/g_c)^{\nu(3+\theta_2)}$ , considering that thermal blobs follow self avoiding walk (SAW) statistics within a correlation blob. Finally, the probability that two stickers within a thermal blob comes together is given by  $g_T^{-3/2}$ . Combining all these, the total probability of inter-chain association is

$$P_{\text{inter}} \approx (z - 2) \frac{g_c}{\ell} \left( \frac{g_T}{g_c} \right)^{\nu(3+\theta_2)} g_T^{-\frac{3}{2}}$$

This expression for  $P_{\text{inter}}$  in Regime III is exactly the same as that derived for the other two regimes.

### C.3 Free energy of associative polymers in dilute solutions

The probability of intra-chain and inter-chain associations can be used to find the partition function,  $Z_{\text{bond}}$ , for the sticker-sticker binding interaction. By combining the free energy calculated from the partition function,  $Z_{\text{bond}}$ , with the free energy for polymeric contribution,  $F_{\text{pol}}$ , Dobrynin found the total free energy of the system in a good solvent, which is given by (Dobrynin, 2004)

$$\frac{F_{\text{tot}}}{nk_B T} \approx \frac{\phi}{N} \ln \frac{\phi}{eN} + C_2 \tau^{3/4} \phi^{9/4} + \frac{\phi}{\ell} \left( \frac{p}{2} + \ln(1 - p) \right) \quad (\text{C.15})$$

here,  $p = p_1 + p_2$ , where  $p_1$  and  $p_2$  are degrees of intra-chain and inter-chain conversions of the stickers. By minimising the total free energy of the system,  $F_{\text{tot}}$ , with respect to  $p_1$  and  $p_2$  one can obtain the scaling relations for the intra-chain and inter-chain associations shown in Table 4.1

# Appendix D

## Storage ( $G'$ ) and loss ( $G''$ ) moduli for a dilute solution of Rouse chains

In Chapter 5, we have discussed two different methods of computing the storage and loss moduli based on oscillatory shear flow (OSF) and equilibrium simulations. In the study carried out in Chapter 5, we use Fourier transformation of the stress auto-correlation function, calculated from equilibrium simulations, to evaluate  $G'$  and  $G''$  for associative polymer solutions. Alternatively,  $G'$  and  $G''$  can be directly estimated from the output response of small amplitude oscillatory shear flow (SAOS) experiments or simulations. Here, we calculate dynamic moduli using these two methods and compare the results with the analytical solution for Rouse chains. For Rouse model of polymer solutions, consisting of bead-spring chains with  $(N_b - 1)$  Hookean springs per chain, the analytical expression for the constitutive equation is well known. For such a model there is a spectrum of relaxation times,  $\lambda_j$ , given by (Bird et al., 1987a)

$$\lambda_j = \frac{\zeta/2H}{4 \sin^2(j\pi/2N_b)} \quad (\text{D.1})$$

where  $\zeta$  is the friction coefficient and  $H$  is spring constant. For a dilute solution of Rouse chains subjected to small amplitude oscillatory shear flow, the polymeric contribution of the complex modulus can be decomposed into the following real and imaginary parts,

$$G' = n_p k_B T \sum_{j=1}^{N_b-1} \frac{\lambda_j^2 \omega^2}{1 + (\lambda_j \omega)^2} \quad (\text{D.2})$$

$$G'' = n_p k_B T \sum_{j=1}^{N_b-1} \frac{\lambda_j \omega}{1 + (\lambda_j \omega)^2} \quad (\text{D.3})$$

Here,  $\omega$  is the frequency of oscillation and  $n_p$  is the number density of chains. Fig. D.1 shows very good agreement among different methods used to compute  $G'$  and  $G''$  for a dilute solution of Rouse chains. Both equilibrium and SAOS (with amplitude,  $\gamma_0 = 0.2$ ) simulations produce the same results which is also in agreement with the analytical expressions. This study establishes the validity of the method used in Chapter 5 to calculate  $G'$  and  $G''$  from stress-auto correlation function.

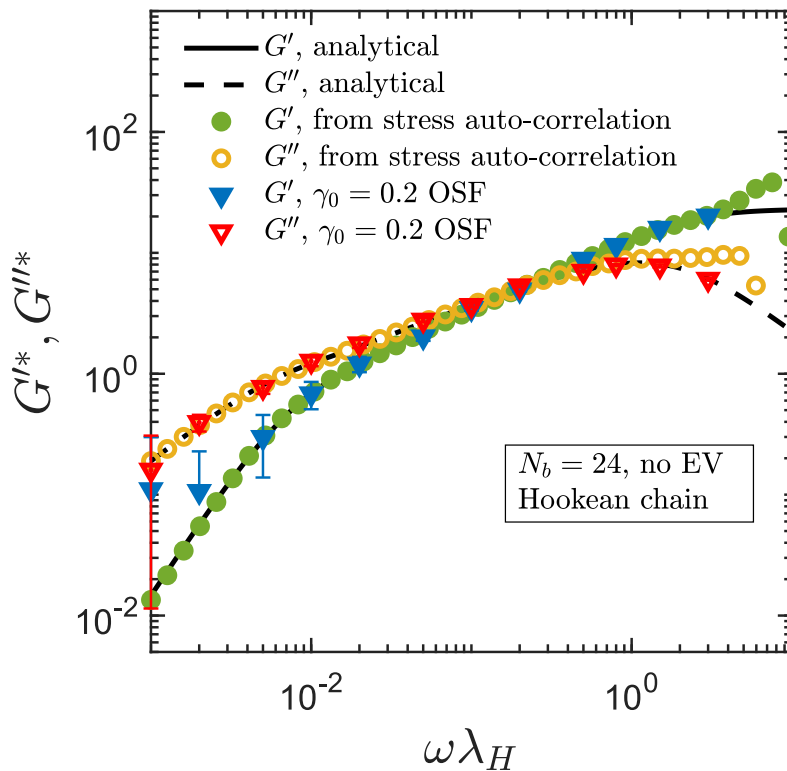


Figure D.1: Non-dimensionalized dynamic moduli ( $G'^*$  &  $G''^*$ ) as a function of dimensionless frequency,  $\omega \lambda_H$ , for a dilute solution of Rouse chains with chain length,  $N_b = 24$ . The filled (for  $G'$ ) and open (for  $G''$ ) symbols are from BD simulations at equilibrium and under oscillatory shear flow (OSF), where  $\gamma_0$  is the amplitude of oscillation. The solid and broken lines are analytical solutions for  $G'$  and  $G''$ , respectively, for Rouse chains in a dilute solution.

# Appendix E

## Scaling of computational cost with chain size

The majority of the results reported in this work have been carried out on the supercomputer *Gadi*, which is Australia's peak research supercomputer based at the National Computational Infrastructure in Canberra. *Gadi*, ranked 24 on the TOP500 list, is a 3,200 node supercomputer (with 155,000 CPU cores and 567 Terabytes of memory) comprising the latest generation Intel Cascade Lake and Nvidia V100 processors, with over 9 petaflops of peak performance. The technical specifications of the processors are: Primergy CX2570 M5, Thinksystem SD650, Xeon Platinum 8274/8268, Nvidia Tesla V100 SXM2, Mellanox HDR Infiniband cluster manufactured by FUJITSU. The computational cost estimates for simulating chains of various lengths  $N_b$ , spacer lengths  $\ell$ , and concentrations  $c/c^*$  on this machine have been given in Table E.1.

	$N_b$	Spacer length ( $\ell$ )	$c/c^*$	CPU time for 10 Rouse times (DD:HH:MM)
Regime II	34	6	2.0	00 : 03 : 07
	154	30	2.0	12 : 00 : 00
	254	50	2.0	54 : 07 : 00
Regime III	64	12	6.5	01 : 19 : 00
	79	15	6.5	03 : 09 : 00
	154	30	6.5	25 : 00 : 00
	254	50	6.5	112 : 00 : 00

Table E.1: Estimates of CPU wall time required on the supercomputer *Gadi* to simulate a single data point on systems with different chain lengths and concentrations in Regimes II and III.

## Appendix F

### Tabulated values of simulation results for $R_g$ , $p_1$ and $p_2$ as a function of the parameters $\{N_b, \ell, f, \epsilon_{bb}, \epsilon_{st}, c, c/c^*\}$

The data presented in Chapter 4 for the dependence of  $R_g$ ,  $p_1$  and  $p_2$  on the various parameters  $\{N_b, \ell, f, \epsilon_{bb}, \epsilon_{st}, c, c/c^*\}$ , in the form of figures, is given here in tabular form, so that they are readily available for comparison with any model predictions that may be made in the future.

Table F.1: List of values for the radius of gyration ( $R_g$ ), and the intra-chain ( $p_1$ ) and inter-chain ( $p_2$ ) degrees of conversion as a function of concentration for different sets of parameters used in this work.

$(N_b, \ell, f)$	$\epsilon_{bb}$	$\epsilon_{st}$	$c/c^*$	$c$	$R_g$	$p_1$	$p_2$
(24, 4, 4)	No EV	No EV	0.0	0.0	$3.23 \pm 0.00$	–	–
	No EV	5.0	0.1	0.017	$2.59 \pm 0.01$	$0.548 \pm 0.004$	$0.213 \pm 0.004$
	No EV	5.0	0.2	0.034	$2.64 \pm 0.01$	$0.448 \pm 0.003$	$0.330 \pm 0.004$
	No EV	5.0	0.3	0.051	$2.67 \pm 0.01$	$0.401 \pm 0.004$	$0.390 \pm 0.005$
	No EV	5.0	0.4	0.069	$2.72 \pm 0.01$	$0.345 \pm 0.004$	$0.464 \pm 0.006$
	No EV	5.0	0.55	0.093	$2.79 \pm 0.01$	$0.295 \pm 0.004$	$0.530 \pm 0.005$
	No EV	5.0	0.75	0.129	$2.91 \pm 0.01$	$0.255 \pm 0.004$	$0.576 \pm 0.005$
	No EV	5.0	1.0	0.170	$3.00 \pm 0.01$	$0.222 \pm 0.003$	$0.617 \pm 0.003$
	No EV	5.0	1.2	0.205	$3.08 \pm 0.01$	$0.206 \pm 0.002$	$0.634 \pm 0.002$
	No EV	5.0	1.4	0.240	$3.18 \pm 0.01$	$0.181 \pm 0.002$	$0.639 \pm 0.002$
(34, 6, 4)	No EV	5.0	1.6	0.274	$3.22 \pm 0.02$	$0.163 \pm 0.002$	$0.648 \pm 0.002$
	No EV	No EV	0.0	0.0	$3.87 \pm 0.00$	–	–
	No EV	2.5	0.12	0.017	$3.68 \pm 0.05$	$0.338 \pm 0.005$	$0.074 \pm 0.006$
	No EV	2.5	0.2	0.030	$3.65 \pm 0.05$	$0.308 \pm 0.005$	$0.134 \pm 0.006$
	No EV	2.5	0.3	0.042	$3.64 \pm 0.03$	$0.287 \pm 0.005$	$0.193 \pm 0.006$
	No EV	2.5	0.5	0.068	$3.73 \pm 0.02$	$0.249 \pm 0.005$	$0.263 \pm 0.005$

*Continued on next page*

Table F.1 – Continued from previous page

$(N_b, \ell, f)$	$\epsilon_{tb}$	$\epsilon_{st}$	$c/c^*$	$c$	$R_g$	$p_1$	$p_2$
(34, 6, 4)	No EV	2.5	0.6	0.085	$3.77 \pm 0.02$	$0.225 \pm 0.005$	$0.314 \pm 0.004$
	No EV	No EV	0.0	0.0	$3.87 \pm 0.00$	–	–
	No EV	5.0	0.12	0.017	$2.74 \pm 0.04$	$0.643 \pm 0.004$	$0.121 \pm 0.007$
	No EV	5.0	0.3	0.042	$2.98 \pm 0.04$	$0.505 \pm 0.004$	$0.283 \pm 0.006$
(34, 4, 6)	No EV	5.0	0.5	0.068	$3.06 \pm 0.03$	$0.445 \pm 0.004$	$0.360 \pm 0.005$
	0.45	0.45	0.0	0.0	$4.42 \pm 0.01$	–	–
	0.45	5.0	0.2	0.019	$3.76 \pm 0.02$	$0.468 \pm 0.004$	$0.238 \pm 0.005$
	0.45	5.0	0.3	0.028	$3.86 \pm 0.02$	$0.416 \pm 0.003$	$0.298 \pm 0.003$
(34, 4, 6)	0.45	5.0	0.4	0.038	$3.95 \pm 0.02$	$0.367 \pm 0.002$	$0.353 \pm 0.003$
	0.45	5.0	0.5	0.047	$4.01 \pm 0.02$	$0.334 \pm 0.003$	$0.397 \pm 0.004$
	0.45	5.0	0.6	0.056	$4.09 \pm 0.02$	$0.319 \pm 0.002$	$0.412 \pm 0.003$
	0.45	5.0	0.8	0.076	$4.25 \pm 0.02$	$0.275 \pm 0.003$	$0.461 \pm 0.003$
(29, 4, 5)	0.45	5.0	1.0	0.095	$4.29 \pm 0.02$	$0.257 \pm 0.002$	$0.482 \pm 0.002$
	0.45	5.0	1.2	0.113	$4.40 \pm 0.02$	$0.228 \pm 0.002$	$0.517 \pm 0.002$
	0.45	0.45	0.0	0.0	$4.07 \pm 0.02$	–	–
	0.45	5.0	0.2	0.020	$3.54 \pm 0.02$	$0.447 \pm 0.004$	$0.250 \pm 0.005$
(29, 4, 5)	0.45	5.0	0.3	0.032	$3.63 \pm 0.02$	$0.376 \pm 0.004$	$0.336 \pm 0.005$
	0.45	5.0	0.4	0.043	$3.72 \pm 0.01$	$0.346 \pm 0.004$	$0.370 \pm 0.004$
	0.45	5.0	0.5	0.052	$3.80 \pm 0.02$	$0.304 \pm 0.003$	$0.421 \pm 0.003$

Continued on next page

Table F.1 – Continued from previous page

$(N_b, \ell, f)$	$\epsilon_{tb}$	$\epsilon_{st}$	$c/c^*$	$c$	$R_g$	$p_1$	$p_2$
(29, 4, 5)	0.45	5.0	0.6	0.063	$3.89 \pm 0.02$	$0.281 \pm 0.003$	$0.445 \pm 0.003$
	0.45	5.0	0.8	0.083	$3.98 \pm 0.02$	$0.242 \pm 0.003$	$0.490 \pm 0.003$
(34, 6, 4)	0.45	0.45	0.0	0.0	$4.42 \pm 0.01$	–	–
	0.45	2.5	0.1	0.010	$4.25 \pm 0.06$	$0.210 \pm 0.005$	$0.042 \pm 0.005$
	0.45	2.5	0.2	0.019	$4.28 \pm 0.05$	$0.204 \pm 0.005$	$0.095 \pm 0.005$
	0.45	2.5	0.3	0.029	$4.28 \pm 0.03$	$0.186 \pm 0.004$	$0.135 \pm 0.005$
	0.45	2.5	0.48	0.045	$4.34 \pm 0.04$	$0.168 \pm 0.004$	$0.185 \pm 0.004$
	0.45	2.5	0.6	0.054	$4.37 \pm 0.03$	$0.155 \pm 0.003$	$0.221 \pm 0.004$
(29, 4, 5)	0.3	0.3	0.0	0.0	$4.41 \pm 0.02$	–	–
	0.3	2.5	1.0	0.082	$4.32 \pm 0.02$	$0.185 \pm 0.001$	$0.272 \pm 0.002$
	0.3	2.5	1.2	0.095	$4.33 \pm 0.01$	$0.176 \pm 0.001$	$0.306 \pm 0.001$
	0.3	2.5	1.4	0.112	$4.33 \pm 0.01$	$0.166 \pm 0.001$	$0.339 \pm 0.001$
	0.3	2.5	1.8	0.144	$4.34 \pm 0.01$	$0.146 \pm 0.001$	$0.406 \pm 0.001$
Regime I	0.3	2.5	2.0	0.161	$4.31 \pm 0.01$	$0.140 \pm 0.001$	$0.431 \pm 0.001$
	0.3	2.5	2.2	0.178	$4.33 \pm 0.01$	$0.133 \pm 0.001$	$0.459 \pm 0.001$
	0.3	2.5	2.4	0.193	$4.31 \pm 0.01$	$0.128 \pm 0.001$	$0.478 \pm 0.001$
	0.3	0.3	0.0	0.0	$4.79 \pm 0.04$	–	–
(34, 4, 6)	0.3	2.5	0.8	0.059	$4.65 \pm 0.02$	$0.219 \pm 0.002$	$0.203 \pm 0.002$
	0.3	2.5	1.0	0.074	$4.67 \pm 0.02$	$0.205 \pm 0.002$	$0.245 \pm 0.002$

Continued on next page

Table F.1 – Continued from previous page

$(N_b, \ell, f)$	$\epsilon_{tb}$	$\epsilon_{st}$	$c/c^*$	$c$	$R_g$	$p_1$	$p_2$
(34, 4, 6) Regime I	0.3	2.5	1.2	0.088	$4.72 \pm 0.02$	$0.190 \pm 0.002$	$0.287 \pm 0.002$
	0.3	2.5	1.4	0.103	$4.73 \pm 0.02$	$0.178 \pm 0.001$	$0.321 \pm 0.001$
	0.3	2.5	1.6	0.118	$4.71 \pm 0.02$	$0.173 \pm 0.001$	$0.349 \pm 0.001$
(34, 6, 4) Regime I	0.3	0.3	0.0	0.0	$4.79 \pm 0.04$	–	–
	0.3	2.0	0.8	0.059	$4.78 \pm 0.02$	$0.100 \pm 0.002$	$0.140 \pm 0.002$
	0.3	2.0	1.0	0.074	$4.76 \pm 0.02$	$0.097 \pm 0.001$	$0.173 \pm 0.002$
(34, 6, 4) Regime I	0.3	2.0	1.2	0.088	$4.72 \pm 0.02$	$0.096 \pm 0.001$	$0.204 \pm 0.001$
	0.3	2.0	1.4	0.103	$4.76 \pm 0.02$	$0.092 \pm 0.001$	$0.236 \pm 0.001$
	0.3	2.0	1.6	0.118	$4.74 \pm 0.02$	$0.088 \pm 0.001$	$0.266 \pm 0.001$
(34, 6, 4) Regime I	0.35	0.35	0.0	0.0	$4.72 \pm 0.02$	–	–
	0.35	2.5	1.1	0.085	$4.67 \pm 0.01$	$0.120 \pm 0.001$	$0.250 \pm 0.001$
	0.35	2.5	1.3	0.100	$4.67 \pm 0.01$	$0.115 \pm 0.001$	$0.284 \pm 0.001$
	0.35	2.5	1.5	0.0115	$4.70 \pm 0.02$	$0.107 \pm 0.001$	$0.315 \pm 0.001$
	0.35	2.5	1.7	0.131	$4.68 \pm 0.01$	$0.103 \pm 0.001$	$0.342 \pm 0.001$
(24, 4, 4) Regime II	0.0	0.0	0.0	0.0	$4.47 \pm 0.05$	–	–
	0.0	5.0	0.1	0.007	$3.97 \pm 0.02$	$0.487 \pm 0.002$	$0.057 \pm 0.002$
	0.0	5.0	0.2	0.013	$4.01 \pm 0.01$	$0.437 \pm 0.002$	$0.118 \pm 0.002$
	0.0	5.0	0.3	0.020	$4.04 \pm 0.01$	$0.401 \pm 0.002$	$0.168 \pm 0.002$
	0.0	5.0	0.4	0.026	$4.09 \pm 0.01$	$0.372 \pm 0.002$	$0.207 \pm 0.002$

Continued on next page

Table F.1 – Continued from previous page

$(N_b, \ell, f)$	$\epsilon_{bb}$	$\epsilon_{st}$	$c/c^*$	$c$	$R_g$	$p_1$	$p_2$
(24, 4, 4) Regime II	0.0	5.0	0.5	0.032	4.14 ± 0.01	0.342 ± 0.002	0.247 ± 0.002
	0.0	5.0	0.6	0.039	4.15 ± 0.01	0.316 ± 0.001	0.283 ± 0.001
	0.0	5.0	0.8	0.052	4.20 ± 0.01	0.267 ± 0.002	0.356 ± 0.002
	0.0	5.0	1.0	0.064	4.24 ± 0.01	0.233 ± 0.002	0.409 ± 0.002
	0.0	5.0	1.14	0.073	4.21 ± 0.01	0.219 ± 0.002	0.436 ± 0.002
	0.0	5.0	1.28	0.083	4.25 ± 0.01	0.195 ± 0.002	0.473 ± 0.002
	0.0	5.0	1.6	0.102	4.26 ± 0.01	0.163 ± 0.001	0.525 ± 0.002
	0.0	0.0	0.0	0.0	5.48 ± 0.02	–	–
	0.0	5.0	0.2	0.010	4.81 ± 0.02	0.487 ± 0.002	0.079 ± 0.003
	0.0	5.0	0.35	0.018	4.87 ± 0.02	0.438 ± 0.002	0.141 ± 0.003
(34, 4, 6) Regime II	0.0	5.0	0.5	0.025	4.95 ± 0.02	0.404 ± 0.002	0.189 ± 0.003
	0.0	5.0	0.6	0.030	4.99 ± 0.01	0.385 ± 0.002	0.214 ± 0.002
	0.0	5.0	0.8	0.040	5.01 ± 0.1	0.344 ± 0.002	0.273 ± 0.002
	0.0	5.0	0.9	0.044	5.07 ± 0.02	0.321 ± 0.002	0.301 ± 0.002
	0.0	5.0	1.0	0.049	5.11 ± 0.02	0.305 ± 0.002	0.325 ± 0.002
	0.0	5.0	1.2	0.060	5.12 ± 0.02	0.278 ± 0.001	0.367 ± 0.002
	0.0	5.0	1.4	0.070	5.15 ± 0.02	0.249 ± 0.002	0.410 ± 0.002
	0.0	5.0	1.6	0.079	5.17 ± 0.02	0.226 ± 0.002	0.445 ± 0.002

Continued on next page

Table F.1 – Continued from previous page

$(N_b, \ell, f)$	$\epsilon_{bb}$	$\epsilon_{st}$	$c/c^*$	$c$	$R_g$	$p_1$	$p_2$
	0.0	5.0	1.7	0.084	$5.14 \pm 0.02$	$0.217 \pm 0.002$	$0.459 \pm 0.002$
	0.0	0.0	0.0	0.0	$5.98 \pm 0.04$	–	–
	0.0	5.0	0.2	0.009	$5.16 \pm 0.02$	$0.492 \pm 0.002$	$0.080 \pm 0.003$
	0.0	5.0	0.3	0.014	$5.24 \pm 0.02$	$0.474 \pm 0.002$	$0.104 \pm 0.002$
	0.0	5.0	0.4	0.017	$5.26 \pm 0.02$	$0.448 \pm 0.002$	$0.137 \pm 0.002$
(39, 4, 7)	0.0	5.0	0.5	0.022	$5.30 \pm 0.02$	$0.426 \pm 0.002$	$0.165 \pm 0.002$
Regime II	0.0	5.0	0.7	0.031	$5.38 \pm 0.02$	$0.384 \pm 0.002$	$0.222 \pm 0.002$
	0.0	5.0	0.9	0.039	$5.45 \pm 0.02$	$0.351 \pm 0.002$	$0.267 \pm 0.002$
	0.0	5.0	1.0	0.044	$5.46 \pm 0.02$	$0.334 \pm 0.002$	$0.290 \pm 0.002$
	0.0	5.0	1.1	0.048	$5.48 \pm 0.02$	$0.320 \pm 0.002$	$0.312 \pm 0.002$
	0.0	5.0	1.2	0.053	$5.52 \pm 0.02$	$0.303 \pm 0.002$	$0.336 \pm 0.002$
	0.0	0.0	0.0	0.0	$6.45 \pm 0.03$	–	–
	0.0	5.0	0.2	0.008	$5.49 \pm 0.03$	$0.513 \pm 0.002$	$0.058 \pm 0.003$
	0.0	5.0	0.3	0.012	$5.53 \pm 0.02$	$0.483 \pm 0.002$	$0.097 \pm 0.003$
(44, 4, 8)	0.0	5.0	0.5	0.020	$5.61 \pm 0.02$	$0.447 \pm 0.002$	$0.146 \pm 0.002$
Regime II	0.0	5.0	0.7	0.028	$5.72 \pm 0.02$	$0.408 \pm 0.002$	$0.196 \pm 0.002$
	0.0	5.0	0.9	0.035	$5.78 \pm 0.02$	$0.375 \pm 0.002$	$0.242 \pm 0.002$
	0.0	5.0	1.0	0.039	$5.86 \pm 0.02$	$0.358 \pm 0.002$	$0.264 \pm 0.002$
	0.0	5.0	1.2	0.047	$5.90 \pm 0.02$	$0.330 \pm 0.002$	$0.303 \pm 0.002$

*Continued on next page*

Table F.1 – Continued from previous page

$(N_b, \ell, f)$	$\epsilon_{tb}$	$\epsilon_{st}$	$c/c^*$	$c$	$R_g$	$p_1$	$p_2$
(44, 4, 8)	0.0	5.0	1.4	0.055	$5.93 \pm 0.02$	$0.304 \pm 0.002$	$0.340 \pm 0.002$
Regime II	0.0	5.0	1.6	0.063	$5.99 \pm 0.02$	$0.277 \pm 0.001$	$0.378 \pm 0.001$
	0.0	0.0	0.0	0.0	$5.48 \pm 0.02$	–	–
	0.0	5.0	0.2	0.010	$5.08 \pm 0.02$	$0.334 \pm 0.002$	$0.079 \pm 0.002$
	0.0	5.0	0.4	0.020	$5.12 \pm 0.02$	$0.292 \pm 0.002$	$0.156 \pm 0.003$
	0.0	5.0	0.6	0.029	$5.15 \pm 0.01$	$0.259 \pm 0.002$	$0.221 \pm 0.003$
(34, 6, 4)	0.0	5.0	0.8	0.039	$5.17 \pm 0.02$	$0.234 \pm 0.002$	$0.271 \pm 0.002$
Regime II	0.0	5.0	1.0	0.049	$5.18 \pm 0.01$	$0.215 \pm 0.002$	$0.323 \pm 0.002$
	0.0	5.0	1.4	0.069	$5.17 \pm 0.02$	$0.172 \pm 0.002$	$0.415 \pm 0.002$
	0.0	5.0	1.5	0.075	$5.19 \pm 0.02$	$0.163 \pm 0.002$	$0.434 \pm 0.002$
	0.0	5.0	1.6	0.079	$5.20 \pm 0.02$	$0.156 \pm 0.002$	$0.449 \pm 0.002$
	0.0	5.0	1.7	0.084	$5.16 \pm 0.02$	$0.149 \pm 0.002$	$0.467 \pm 0.002$
	0.0	0.0	0.0	0.0	$5.01 \pm 0.02$	–	–
	0.0	5.0	0.35	0.019	$4.61 \pm 0.02$	$0.348 \pm 0.002$	$0.151 \pm 0.002$
(29, 5, 4)	0.0	5.0	0.4	0.022	$4.62 \pm 0.02$	$0.328 \pm 0.002$	$0.186 \pm 0.003$
Regime II	0.0	5.0	0.6	0.033	$4.67 \pm 0.01$	$0.292 \pm 0.002$	$0.247 \pm 0.002$
	0.0	5.0	0.8	0.044	$4.70 \pm 0.01$	$0.254 \pm 0.002$	$0.311 \pm 0.002$
	0.0	5.0	0.9	0.049	$4.71 \pm 0.01$	$0.240 \pm 0.002$	$0.336 \pm 0.002$
	0.0	5.0	1.0	0.055	$4.72 \pm 0.01$	$0.222 \pm 0.002$	$0.367 \pm 0.002$

*Continued on next page*

Table F.1 – Continued from previous page

$(N_b, \ell, f)$	$\epsilon_{bb}$	$\epsilon_{st}$	$c/c^*$	$c$	$R_g$	$p_1$	$p_2$
(29, 5, 4)	0.0	5.0	1.2	0.067	$4.74 \pm 0.01$	$0.199 \pm 0.001$	$0.413 \pm 0.002$
Regime II	0.0	5.0	1.4	0.078	$4.72 \pm 0.01$	$0.182 \pm 0.001$	$0.451 \pm 0.002$
	0.0	0.0	0.0	0.0	$5.48 \pm 0.02$	–	–
	0.0	4.0	0.6	0.029	$5.22 \pm 0.01$	$0.187 \pm 0.001$	$0.143 \pm 0.001$
(34, 6, 4)	0.0	4.0	0.8	0.039	$5.23 \pm 0.01$	$0.173 \pm 0.001$	$0.192 \pm 0.001$
Regime II	0.0	4.0	0.9	0.044	$5.23 \pm 0.01$	$0.168 \pm 0.001$	$0.214 \pm 0.001$
	0.0	4.0	1.0	0.049	$5.22 \pm 0.01$	$0.163 \pm 0.001$	$0.235 \pm 0.001$
	0.0	4.0	1.1	0.054	$5.21 \pm 0.01$	$0.158 \pm 0.001$	$0.256 \pm 0.001$
	0.0	0.0	0.0	0.0	$8.03 \pm 0.05$	–	–
	0.0	5.0	0.33	0.01	$7.78 \pm 0.07$	$0.141 \pm 0.006$	$0.051 \pm 0.004$
	0.0	5.0	0.5	0.015	$7.78 \pm 0.06$	$0.130 \pm 0.005$	$0.079 \pm 0.004$
	0.0	5.0	0.7	0.021	$7.76 \pm 0.05$	$0.129 \pm 0.003$	$0.114 \pm 0.003$
(64, 12, 4)	0.0	5.0	1.0	0.030	$7.59 \pm 0.04$	$0.124 \pm 0.004$	$0.160 \pm 0.003$
Regime II	0.0	5.0	1.5	0.045	$7.59 \pm 0.03$	$0.107 \pm 0.003$	$0.249 \pm 0.003$
Regime III	0.0	5.0	2.0	0.060	$7.51 \pm 0.03$	$0.098 \pm 0.002$	$0.318 \pm 0.003$
	0.0	5.0	3.0	0.090	$7.33 \pm 0.03$	$0.084 \pm 0.002$	$0.425 \pm 0.002$
	0.0	5.0	4.0	0.119	$7.21 \pm 0.03$	$0.072 \pm 0.002$	$0.500 \pm 0.002$
	0.0	5.0	4.8	0.141	$7.08 \pm 0.02$	$0.069 \pm 0.001$	$0.538 \pm 0.001$
	0.0	5.0	5.0	0.148	$7.04 \pm 0.02$	$0.068 \pm 0.001$	$0.549 \pm 0.001$

*Continued on next page*

Table F.1 – Continued from previous page

$(N_b, \ell, f)$	$\epsilon_{tb}$	$\epsilon_{st}$	$c/c^*$	$c$	$R_g$	$p_1$	$p_2$
	0.0	5.0	5.5	0.162	$7.00 \pm 0.02$	$0.065 \pm 0.001$	$0.567 \pm 0.001$
	0.0	5.0	6.0	0.177	$6.96 \pm 0.02$	$0.059 \pm 0.001$	$0.589 \pm 0.001$
	0.0	0.0	0.0	0.0	$9.11 \pm 0.06$	–	–
(79, 15, 4)	0.0	5.0	5.0	0.123	$7.96 \pm 0.03$	$0.061 \pm 0.001$	$0.484 \pm 0.002$
Regime III	0.0	5.0	5.5	0.137	$7.91 \pm 0.03$	$0.058 \pm 0.001$	$0.510 \pm 0.001$
	0.0	5.0	6.0	0.149	$7.86 \pm 0.02$	$0.056 \pm 0.001$	$0.532 \pm 0.001$
	0.0	5.0	6.5	0.162	$7.82 \pm 0.03$	$0.054 \pm 0.001$	$0.550 \pm 0.001$
	0.35	0.35	0.0	0.0	$4.72 \pm 0.02$	–	–
	0.35	3.6	0.2	0.016	$4.49 \pm 0.02$	$0.266 \pm 0.003$	$0.107 \pm 0.003$
	0.35	3.6	0.3	0.024	$4.52 \pm 0.02$	$0.249 \pm 0.002$	$0.146 \pm 0.003$
	0.35	3.6	0.5	0.039	$4.59 \pm 0.02$	$0.217 \pm 0.003$	$0.211 \pm 0.003$
	0.35	3.6	0.7	0.054	$4.62 \pm 0.02$	$0.199 \pm 0.002$	$0.259 \pm 0.003$
(34, 6, 4)	0.35	3.6	0.9	0.070	$4.62 \pm 0.01$	$0.178 \pm 0.002$	$0.310 \pm 0.002$
Sticky $\theta$ chain	0.35	3.6	1.1	0.085	$4.63 \pm 0.1$	$0.162 \pm 0.002$	$0.351 \pm 0.002$
	0.35	3.6	1.3	0.100	$4.67 \pm 0.01$	$0.148 \pm 0.001$	$0.386 \pm 0.001$
	0.35	3.6	1.5	0.116	$4.70 \pm 0.01$	$0.135 \pm 0.001$	$0.419 \pm 0.001$
	0.35	3.6	2.5	0.193	$4.69 \pm 0.01$	$0.098 \pm 0.001$	$0.532 \pm 0.001$
	0.35	3.6	3.5	0.268	$4.66 \pm 0.01$	$0.080 \pm 0.001$	$0.596 \pm 0.001$
	0.35	3.6	4.0	0.308	$4.64 \pm 0.02$	$0.075 \pm 0.001$	$0.620 \pm 0.001$

Continued on next page

Table F.1 – Continued from previous page

$(N_b, \ell, f)$	$\epsilon_{bb}$	$\epsilon_{st}$	$c/c^*$	$c$	$R_g$	$p_1$	$p_2$
	0.35	3.6	4.5	0.348	$4.63 \pm 0.02$	$0.069 \pm 0.001$	$0.640 \pm 0.001$
	0.35	3.6	5.0	0.387	$4.63 \pm 0.01$	$0.066 \pm 0.001$	$0.656 \pm 0.001$
	0.35	3.6	5.5	0.425	$4.59 \pm 0.01$	$0.064 \pm 0.001$	$0.670 \pm 0.001$

# Bibliography

- P. Ahlrichs and B. Dünweg. Simulation of a single polymer chain in solution by combining Lattice Boltzmann and molecular dynamics. *J. Chem. Phys.*, 111(17):8225–8239, 1999.
- P. Ahlrichs, R. Everaers, and B. Dünweg. Screening of hydrodynamic interactions in semidilute polymer solutions: A computer simulation study. *Phys. Rev. E*, 64:040501, 2001.
- A. Jain, B. Dünweg, and J. R. Prakash. Dynamic crossover scaling in polymer solutions. *Phys. Rev. Lett.*, 109:088302, 2012.
- C. Aust, M. Kröger, and S. Hess. Structure and dynamics of dilute polymer solutions under shear flow via nonequilibrium molecular dynamics. *Macromolecules*, 32(17):5660–5672, 1999.
- A. R. C. Baljon, D. Flynn, and D. Krawczun. Numerical study of the gel transition in reversible associating polymers. *J. Chem. Phys.*, 126, 2007.
- M. Bercea, C. Ioan, S. Ioan, B. C. Simionescu, and C. I. Simionescu. Ultrahigh molecular weight polymers in dilute solutions. *Prog. Polym. Sci.*, 24:379–424, 1999.
- R. B. Bird, C. F. Curtiss, and R. C. A. and O. Hassager. Dynamics of polymeric liquids. 2, 1987a.
- R. B. Bird, C. F. Curtiss, and R. C. A. and O. Hassager. Dynamics of polymeric liquids. 1, 1987b.
- L. Böni, P. Fischer, L. Böcker, S. Kuster, and P. A. Rühs. Hagfish slime and mucin flow properties and their implications for defense. *Sci. Rep.*, 6, 30371, 2016.

- 
- J. Brassinne, A. Cadix, J. Wilson, and E. van Ruymbeke. Dissociating sticker dynamics from chain relaxation in supramolecular polymer networks—the importance of free partner! *Journal of Rheology*, 61(6):1123–1134, 2017.
- L. Bromberg. Scaling of rheological properties of hydrogels from associating polymers. *Macromolecules*, 31(18):6148–6156, 1998.
- M. J. Cass, D. M. Heyes, R.-L. Blanchard, and R. J. English. Simulations and experiments of self-associating telechelic polymer solutions. *J. Phys.: Condens. Matter*, 20(33):335103, Aug. 2008.
- J. Castillo-Tejas, O. Castrejon-Gonzalez, S. Carro, V. Gonzalez-Coronel, J. F. J. Alverado, and O. Manero. Associative polymers. part iii: Shear rheology from molecular dynamics. *Colloids and Surfaces A: Physicochemical and Engineering Aspects*, 491:37–49, 2016.
- C. Chassenieux, T. Nicolai, and L. Benyahia. Rheology of associative polymer solutions. *Current Opinion in Colloid and Interfacial Science*, 16:18–26, 2011.
- W. Chen, J. Chen, and L. An. Tumbling and tank-treading dynamics of individual ring polymers in shear flow. *Soft Matter*, 9:4312–4318, 2013.
- K. Christensen and N. R. Moloney. *Complexity and Criticality*. Imperial College Press, London, 2005.
- M. Daoud, J. P. Cotton, B. Farnoux, G. Jannink, G. Sarma, H. Benoit, C. Duplessix, C. Picot, and P. G. de Gennes. Solutions of flexible polymers. neutron experiments and interpretation. *Macromolecules*, 8(6):804–818, 1975.
- J. Dautenhahn and C. K. Hall. Monte carlo simulation of off-lattice polymer chains: Effective pair potentials in dilute solution. *Macromolecules*, 27:5399–5412, 1994.
- R. L. A. David, M. Wei, and J. A. Kornfield. Effects of pairwise, donor-acceptor functional groups on polymer solubility, solution viscosity and mist control. *Polymer*, 50:6323–6330, 2009a.

- 
- R. L. A. David, M. Wei, D. Liu, B. F. Bathel, J. P. Plog, A. Ratner, and J. A. Kornfield. Effects of pairwise, self-associating functional side groups on polymer solubility, solution viscosity, and mist control. *Macromolecules*, 42:1380–1391, 2009b.
- P. G. de Gennes. *Scaling Concepts in Polymer Physics*. Cornell University Press, Ithaca, 1979.
- J. des Cloizeaux. Short range correlation between elements of a long polymer in a good solvent. *J. Phys. France*, 41:223–238, 1980.
- J. des Cloizeaux and G. Jannink. *Polymers in Solution, Their Modeling and Structure*. Oxford Science Publishers: New York, 1990.
- A. V. Dobrynin. Phase diagram of solutions of associative polymers. *Macromolecules*, 37:3881–3893, 2004.
- M. Doi and S. F. Edwards. The theory of polymer dynamics. *Clarendon Press*, 1986.
- B. Dünweg and A. J. C. Ladd. Lattice Boltzmann simulations of soft matter systems. *Adv. Poly. Sci.*, 221:89–166, 2009.
- B. Duplantier. Statistical mechanics of polymer networks of any topology. *J. Stat. Phys.*, 54:581–680, 1989.
- D. J. Earl and M. W. Deem. Parallel tempering: Theory, applications, and new perspectives. *Phys. Chem. Chem. Phys.*, 7(23):3910–3916, 2005.
- I. M. El-Sherbiny and M. H. Yacoub. Hydrogel scaffolds for tissue engineering: Progress and challenges. *Global Cardiology Science and Practice*, 2013(3):316–342, 2013.
- D. L. Ermak and J. A. McCammon. Brownian dynamics with hydrodynamic interactions. *J. Chem. Phys.*, 69:1352–1360, 1978.
- I. Erukhimovich, M. V. Thamm, and A. V. Ermoshkin. Theory of the sol-gel transition in thermoreversible gels with due regard for the fundamental role of mesoscopic cyclization effects. 1. thermodynamic and structural characteristics of the gel phase. *Macromolecules*, 34(16):5653–5674, 2001.

- 
- A. M. Fiore, F. B. Usabiaga, A. Donev, and J. W. Swan. Rapid sampling of stochastic displacements in brownian dynamics simulations. *The Journal of Chemical Physics*, 146:124116, 2017.
- M. Fixman. Inclusion of hydrodynamic interaction in polymer dynamical simulations. *Macromolecules*, 14(6):1710–1717, 1981.
- M. Fixman. Implicit algorithm for brownian dynamics of polymers. *Macromolecules*, 19:1195–1204, 1986.
- P. J. Flory. Molecular size distribution in three dimensional polymers. i. gelation. *Journal of American Chemical Society*, 63 (11):3083–3090, 1941.
- P. J. Flory. *Principles of Polymer Chemistry*. Cornell University Press, Ithaca, 1953.
- K. F. Freed. *Renormalization Group Theory of Macromolecules*. Wiley: New York, 1987.
- D. Frenkel and B. Smit. Understanding molecular simulation, from algorithm to applications. *Academic Press*, 1996.
- T. Furuya and T. Koga. Molecular simulation of structure formation and rheological properties of mixtures of telechelic and monofunctional associating polymer. *J. Polym. Sci., Part B: Polym. Phys.*, 56:1251–1264, 2018.
- J. E. Glass, D. N. Schulz, and C. F. Zukoski. Polymers as rheology modifiers. *ACS Symposium Series*, 462:2–17, 1991.
- G. Gompper, T. Ihle, D. M. Kroll, and R. G. Winkler. *Multi-Particle Collision Dynamics: A Particle-Based Mesoscale Simulation Approach to the Hydrodynamics of Complex Fluids*, pages 1–87. Springer Berlin Heidelberg, 2009.
- A. Y. Grosberg and A. R. Khokhlov. *Statistical physics of macromolecules*. AIP Press, New York, 1994.
- X. Guo, A. A. Abdala, B. L. May, S. F. Lincoln, S. A. Khan, and R. K. Prudhomme. Novel associative polymer networks based on cyclodextrin inclusion compounds. *Macromolecules*, 38:3037–3040, 2005.

- 
- R. C. Hayward and W. W. Graessley. Excluded volume effects in polymer solutions. 1. Dilute solution properties of linear chains in good and theta solvents. *Macromolecules*, 32(10):3502–3509, 1999.
- J. G. Hernández Cifre, T. M. A. O. M. Barenbrug, J. D. Schieber, and B. H. A. A. van den Brule. Brownian dynamics simulation of reversible polymer networks under shear using a non-interacting dumbbell model. *J. Non-Newtonian Fluid Mech.*, 113(2-3):73–96, Aug. 2003.
- J. G. Hernández Cifre, R. Pamies, A. L. Kjøniksen, K. D. Knudsen, B. Nyström, and J. García de la Torre. Brownian dynamics simulation of reversible polymer networks using a non-interacting bead-and-spring chain model. *J. Non-Newtonian Fluid Mech.*, 146(1-3):3–10, Oct. 2007.
- N. Holten-Andersen, A. Jaishankar, M. J. Harrington, D. E. Fullenkamp, G. DiMarco, L. He, G. H. McKinley, P. B. Messersmith, and K. Y. C. Lee. Metal-coordination: using one of nature’s tricks to control soft material mechanics. *J. Mater. Chem. B*, 2:2467–2472, 2014.
- R. S. Hoy and G. H. Fredrickson. Thermoreversible associating polymer networks. i. interplay of thermodynamics, chemical kinetics, and polymer physics. *J. Chem. Phys.*, 131:224902, 2009.
- H.-P. Hsu, W. Nadler, and P. Grassberger. Scaling of star polymers with 1-80 arms. *Macromolecules*, 37(12):4658–4663, 2004.
- C. C. Huang, R. G. Winkler, G. Sutmann, and G. Gompper. Semidilute polymer solutions at equilibrium and under shear flow. *Macromolecules*, 43(23):10107–10116, 2010.
- S. Huissmann, R. Blaak, and C. N. Likos. Star polymers in solvents of varying quality. *Macromolecules*, 42(7):2806–2816, 2009.
- M. Ishida and F. Tanaka. Theoretical study of postgel regime in thermoreversible gelation. *Macromolecules*, 30:3900–3909, 1997.

- 
- A. Jain. *Unravelling the dynamics of semidilute polymer solutions using Brownian dynamics (Ph.D. thesis)*. Monash University, 2013.
- A. Jain, P. Sunthar, B. Dünweg, and J. R. Prakash. Optimization of a brownian-dynamics algorithm for semidilute polymer solutions. *Physical Review E*, 85:066703, 2012.
- A. Jain, C. Sasmal, R. Hartkamp, B. D. Todd, and J. R. Prakash. Brownian dynamics simulations of planar mixed flows of polymer solutions at finite concentrations. *Chem. Eng. Sci.*, 121:245–257, 2015.
- A. Jaishankar, M. Wee, L. Matia-Merino, K. K. T. Goh, and G. H. McKinley. The cation-controlled and hydrogen bond-mediated shear-thickening behaviour of a tree-fern isolated polysaccharide. *Carbohydrate Polymers*, 2015.
- R. M. Jendrejack, M. D. Graham, and J. J. de Pablo. Hydrodynamic interactions in long chain polymers: Application of the Chebyshev polynomial approximation in stochastic simulations. *J. Chem. Phys.*, 113(7):2894–2900, 2000.
- C. Jeppesen and K. Kremer. Single-chain collapse as a first-order transition: model for PEO in water. *Europhys. Lett.*, 34(8):563–568, June 1996.
- T. Kairn, P. J. Davis, M. L. Matin, and I. K. Snook. Concentration dependence of viscometric properties of model short chain polymer solutions. *Polymer*, 45(7):2453–2464, Mar. 2004.
- R. Kapral. Multiparticle collision dynamics: Simulation of complex systems on mesoscales. *Advances in Chemical Physics*, pages 89–146, 2008.
- S. Kirchhof, A. M. Goepferich, and F. P. Brandl. Hydrogels in ophthalmic applications. *Euro. J. Pharmaceutics and Biopharmaceutics*, 95:227–238, 2015.
- V. Krakoviack, J. P. Hansen, and A. A. Louis. Influence of solvent quality on effective pair potentials between polymers in solution. *Phys. Rev. E*, 67:041801, 2003.
- H. A. Kramers. The behavior of macromolecules in inhomogeneous flow. *J. Chem. Phys.*, 14:415, 1946.

- 
- M. Kröger. Simple models for complex nonequilibrium fluids. *Physics Reports*, 390(6):453–551, 2004.
- M. Kroger, A. Alba-Perez, M. Laso, and H. C. Öttinger. Variance reduced brownian simulation of a bead-spring chain under steady shear flow considering hydrodynamic interaction effects. *J. Chem. Phys.*, 113:11, 2000.
- K. S. Kumar and J. R. Prakash. Equilibrium swelling and universal ratios in dilute polymer solutions: Exact brownian dynamics simulations for a delta function excluded volume potential. *Macromolecules*, 36:7842–7856, 2003.
- S. K. Kumar and J. F. Douglas. Gelation in physically associating polymer solutions. *Phys. Rev. Lett.*, 87(18):188301, 2001.
- S. K. Kumar and A. Z. Panagiotopoulos. Thermodynamics of reversibly associating polymer solutions. *Phys. Rev. Lett.*, 82(25):5060–5063, 1999.
- R. G. Larson. The rheology of dilute solutions of flexible polymers: Progress and problems. *J. Rheol.*, 49(1):1–70, 2005.
- W. B. Lee and K. Kremer. Entangled polymer melts: Relation between plateau modulus and stress autocorrelation function. *Macromolecules*, 42(16):6270–6276, 2009.
- A. W. Lees and S. F. Edwards. The computer study of transport processes under extreme conditions. *Journal of Physics C: Solid State Physics*, 5(15):1921–1928, aug 1972.
- L. Li and Y. Aoki. Rheological images of poly (vinyl chloride) Gels. 1. The dependence of sol-gel transition on concentration. *Macromolecules*, 30:7835–7841, 1997.
- L. Li, H. Uchida, Y. Aoki, and M. L. Yao. Rheological Images of Poly(vinyl chloride) Gels. 2. Divergence of Viscosity and the Scaling Law before the Sol–Gel Transition. *Macromolecules*, 30(25):7842–7848, Dec. 1997.
- B. Liu and B. Dünweg. Translational diffusion of polymer chains with excluded volume and hydrodynamic interactions by brownian dynamics simulation. *J. Chem. Phys.*, 118:17, 2003.

- 
- J. Mewis, B. Kaffashi, J. Vermant, and R. J. Butera. Determining relaxation modes in flowing associative polymers using superposition flows. *Macromolecules*, 34(5):1376–1383, 2001.
- D. Michieletto, E. Orlandini, and D. Marenduzzo. Polymer model with Epigenetic Recoloring Reveals a Pathway for the *de novo* Establishment and 3D Organization of Chromatin Domains. *Phys. Rev. X*, 6:041047, 2016.
- Y. Miyaki and H. Fujita. Excluded-volume effects in dilute polymer solutions. 11. tests of the two-parameter theory for radius of gyration and intrinsic viscosity. *Macromolecules*, 14:742–746, 1981.
- M. Mours and H. Winter. Mechanical spectroscopy of polymers. *Experimental Methods in Polymer Science: Modern Methods in Polymer Research and Technology*, pages 495–546, 01 2012.
- J. S. Myung, R. G. Winkler, and G. Gompper. Self-organised structures of attractive end-functionalized semiflexible polymer suspensions. *Macromolecules*, 47:4118–4125, 2014.
- J. S. Myung, R. G. Winkler, and G. Gompper. Self-organization in suspensions of end-functionalized semiflexible polymers under shear flow. *The Journal of Chemical Physics*, 143:243117, 2015.
- M. H. Nafar Sefiddashti, B. J. Edwards, and B. Khomami. Individual chain dynamics of a polyethylene melt undergoing steady shear flow. *Journal of Rheology*, 59(1):119–153, 2015.
- A. Narros, A. J. Moreno, and C. N. Likos. Effects of knots on ring polymers in solvents of varying quality. *Macromolecules*, 46:3654–3668, 2013.
- M. O’Leary, B. Hanson, and C. J. Smith. Viscosity and non-newtonian features of thickened fluids used for dysphagia therapy. *J. Food Sci.*, 75:E330–E338, 2010.
- A. K. Omar and Z.-G. Wang. Shear-induced heterogeneity in associating polymer gels: Role of network structure and dilatancy. *Phys. Rev. Lett.*, 119(11):117801, 2017.

- 
- H. C. Öttinger. *Stochastic Processes in Polymeric Fluids*. Springer-Verlag: Berlin, 1996.
- H. Ozaki and T. Koga. Theory of transient networks with a well-defined junction structure. *J. Chem. Phys.*, 152(18):184902, 2020.
- H. Ozaki, T. Narita, T. Koga, and T. Indei. Theoretical analysis of critical flowable physical gel cross-linked by metal ions and polyacrylamide-derivative associating polymers containing imidazole groups. *Polymers*, 9(256), 2017.
- S. Pan, D. Ahirwal, D. A. Nguyen, P. Sunthar, T. Sridhar, and J. R. Prakash. Viscosity radius of polymers in dilute solutions: Universal behaviour from DNA rheology and Brownian dynamics simulations. *Macromolecules*, 47(21):7548–7560, 2014a.
- S. Pan, D. A. Nguyen, P. Sunthar, T. Sridhar, and J. R. Prakash. Universal solvent quality crossover of the zero shear rate viscosity of semidilute DNA solutions. *J. Rheol.*, 58(2): 339–368, 2014b.
- G. W. Park and G. Ianniruberto. A new stochastic simulation for the rheology of telechelic associating polymers. *J. Rheol.*, 61(6):1293–1305, Nov. 2017.
- A. Pelissetto. Osmotic pressure and polymer size in semidilute polymer solutions under goodsolvent conditions. *J. Chem. Phys.*, 129:044901, 2008.
- D. Petera and M. Muthukumar. Brownian dynamics simulation of bead-rod chains under shear with hydrodynamic interaction. *J. Chem. Phys.*, 111(16):7614–7623, 1999.
- T. T. Pham, B. Dünweg, and J. R. Prakash. Collapse dynamics of copolymers in a poor solvent: Influence of hydrodynamic interactions and chain sequence. *Macromolecules*, 43: 10084–10095, 2010.
- R. Prabhakar and J. R. Prakash. Viscometric functions for Hookean dumbbells with excluded volume and hydrodynamic interactions. *J. Rheol.*, 46(5):1191–1220, 2002.
- R. Prabhakar and J. R. Prakash. Multiplicative separation of the influences of excluded volume, hydrodynamic interactions and finite extensibility on the rheological properties of dilute polymer solutions. *J. Non-Newtonian Fluid Mech.*, 116:163–182, 2004.

- 
- R. Prabhakar, J. R. Prakash, and T. Sridhar. A successive fine-graining scheme for predicting the rheological properties of dilute polymer solutions. *J. Rheol.*, 48:1251–1278, 2004.
- J. R. Prakash. Universal dynamics of dilute and semidilute solutions of flexible linear polymers. *Current Opinion in Colloid & Interface Science*, 43:63–79, 2019. ISSN 1359-0294.
- J. R. Prakash and H. C. Öttinger. Viscometric functions for a dilute solution of polymers in a good solvent. *Macromolecules*, 32:2028–2043, 1999.
- S. Redner. Distribution functions in the interior of polymer chains. *J. Phys. A: Math. Gen.*, 13:3525–3541, 1980.
- R. M. Robertson, S. Laib, and D. E. Smith. Diffusion of isolated dna molecules: Dependence on length and topology. 103(19):7310–7314, 2006.
- T. Rossow and S. Seiffert. Supramolecular Polymer Networks: Preparation, Properties, and Potential. In *Supramolecular Polymer Networks and Gels*, pages 1–46. Springer, Cham, Cham, 2015.
- M. Rubinstein and R. H. Colby. *Polymer Physics*. Oxford University Press, Oxford, 2003.
- M. Rubinstein and A. Dobrynin. Solutions of associative polymers. *Trends in Polymer Science*, 5:181–186, 06 1997.
- M. Rubinstein and A. N. Semenov. Thermoreversible gelation in solutions of associative polymers. 2. linear dynamics. *Macromolecules*, 31:1386–1397, 1998.
- M. Rubinstein and A. N. Semenov. Dynamics of entangled solutions of associative polymers. *Macromolecules*, 34:1058–1068, 2001.
- J. F. Ryder and J. M. Yeomans. Shear thinning in dilute polymer solutions. *The Journal of Chemical Physics*, 125(19):194906, 2006.
- A. Saadat and B. Khomami. Matrix-free Brownian dynamics simulation technique for semidilute polymeric solutions. *Phys. Rev. E*, 92:033307, 2015.

- 
- A. Santra, K. Kumari, R. Padinhateeri, B. Dünweg, and J. R. Prakash. Universality of the collapse transition of sticky polymers. *Soft Matter*, 15:7876–7887, 2019.
- L. Schäfer. *Excluded Volume Effects in Polymer Solutions*. Springer-Verlag: Berlin, 1999.
- V. F. Scolari and M. C. Lagomarsino. Combined collapse by bridging and self-adhesion in a prototypical polymer model inspired by the bacterial nucleoid. *Soft Matter*, 11:1677–1687, 2015.
- A. N. Semenov and M. Rubinstein. Thermoreversible gelation in solutions of associative polymers. 1. statics. *Macromolecules*, 31:1373–1385, 1998.
- E. M. Sevick, P. A. Monson, and J. M. Ottino. Monte carlo calculations of cluster statistics in continuum models of composite morphology. *J. Chem. Phys.*, 88:1198, 1988.
- E. S. G. Shaqfeh. The dynamics of single-molecule DNA in flows. *J. Non-Newtonian Fluid Mech.*, 130:1–28, 2005.
- C. E. Sing and A. Alexander-Katz. Equilibrium structure and dynamics of self-associating single polymers. *Macromolecules*, 44:6962–6971, 2011.
- T. Soddemann, B. Dünweg, and K. Kremer. A generic computer model for amphiphilic systems. *Eur. Phys. J.*, 6:409–419, 2001.
- J. Sprakel, E. Spruijt, J. van der Gucht, J. T. Padding, and W. J. Briels. Failure-mode transition in transient polymer networks with particle-based simulations. *Soft Matter*, 5(23):4748–4756, Nov. 2009.
- D. Stauffer and A. Aharony. *Introduction to Percolation Theory*. Taylor and Francis, London, 1992.
- D. Stauffer, A. Coniglio, and M. Adam. *Gelation and Critical Phenomena*, volume 44, pages 103–158. 08 2007.
- M. O. Steinhauser. A molecular dynamics study on universal properties of polymer chains in different solvent qualities. part i. a review of linear chain properties. *J. Chem. Phys.*, 122:094901, 2005.

- 
- W. H. Stockmayer. Theory of molecular size distribution and gel formation in branched-chain polymers. *J. Chem. Phys.*, 11:45–55, 1943.
- W. H. Stockmayer. Theory of molecular size distribution and gel formation in branched polymers ii. general cross linking. *J. Chem. Phys.*, 12:125–131, 1944.
- C. Stoltz. *Simulation of Dilute Polymer and Polyelectrolyte Solutions: Concentration Effects (Ph.D. thesis)*. The University of Wisconsin, 2006.
- C. Stoltz, J. de Pablo, and M. Graham. Concentration dependence of shear and extensional rheology of polymer solutions: Brownian dynamics simulations. *J. Rheol.*, 50:137–167, 2006.
- K. Suman and Y. M. Joshi. On the universality of the scaling relations during sol-gel transition. *Journal of Rheology*, 64(4):863–877, 2020.
- P. Sunthar and J. R. Prakash. Parameter-free prediction of dna conformations in elongational flow by successive fine graining. *Macromolecules*, 38:617–640, 2005.
- P. Sunthar and J. R. Prakash. Dynamic scaling in dilute polymer solutions: The importance of dynamic correlations. *Europhys. Lett.*, 75 (1):77–83, 2006.
- S. Suzuki, T. Uneyama, T. Inoue, and H. Watanabe. Nonlinear rheology of telechelic associative polymer networks: Shear thickening and thinning behavior of hydrophobically modified ethoxylated urethane (heur) in aqueous solution. *Macromolecules*, 45:888–898, 2012.
- F. Tanaka. Polymer-surfactant interaction in thermoreversible gels. *Macromolecules*, 31:384–393, 1998.
- F. Tanaka. *Polymer Physics: Applications to Molecular Association and Thermoreversible Gelation*. Cambridge University Press, Cambridge, 2011. ISBN 9781139500708.
- F. Tanaka and A. Matsuyama. Tricriticality in thermoreversible gels. *Phys. Rev. Lett.*, 62:2759–2762, 1989.

- 
- D. G. Thomas, R. J. DePuit, and B. Khomami. Dynamic simulations of individual macromolecules in oscillatory shear flow. *Journal of Rheology*, 53(2):275–291, 2009.
- B. D. Todd and P. J. Daivis. Homogeneous non-equilibrium molecular dynamics simulations of viscous flow: techniques and applications. *Mol. Simulation*, 33(3):189–229, Mar. 2007.
- A. Tripathi, K. C. Tam, and G. H. McKinley. Rheology and dynamics of associative polymers in shear and extension: Theory and experiments. *Macromolecules*, 39:1981–1999, 2006.
- C. Tsitsilianis. Responsive reversible hydrogels from associative “smart” macromolecules. *Soft Matter*, 6(11):2372–2388, May 2010.
- M. Q. Tu, M. Lee, R. M. Robertson-Anderson, and C. M. Schroeder. Direct observation of ring polymer dynamics in the flow-gradient plane of shear flow. *Macromolecules*, 53(21):9406–9419, 2020.
- E. Uehara and T. Deguchi. Statistical and hydrodynamic properties of topological polymers for various graphs showing enhanced short-range correlation. *J. Chem. Phys.*, 145:164905, 2016.
- B. H. A. A. van den Brule and P. J. Hoogerbrugge. Brownian Dynamics simulation of reversible polymeric networks. *J. Non-Newtonian Fluid Mech.*, 60(2-3):303–334, Nov. 1995.
- P. Vidakovic and F. Rondelez. Temperature dependence of the hydrodynamic radius of flexible coils in solutions. 3. experimental evidence for the crossover between Gaussian and excluded-volume single chain statistics. *Macromolecules*, 18:700–708, 1985.
- L. Voorhaar and R. Hoogenboom. Supramolecular polymer networks: hydrogels and bulk materials. *Chem. Soc. Rev.*, 45(14):4013–4031, July 2016.
- C. E. Wagner and G. H. McKinley. Age-dependent capillary thinning dynamics of physically-associated salivary mucin networks. *Journal of Rheology*, 61(6):1309–1326, 2017.

- Z. Wang, Q. Zhai, W. Chen, X. Wang, Y. Lu, and L. An. Mechanism of Nonmonotonic Increase in Polymer Size: Comparison between Linear and Ring Chains at High Shear Rates. *Macromolecules*, 52:8144–8154, 2019.
- H. R. Warner. Kinetic theory and rheology of dilute suspensions of finitely extendible dumbbells. *Industrial & Engineering Chemistry Fundamentals*, 11(3):379–387, 1972.
- J. Weeks, D. Chandler, and H. Andersen. *J. Chem. Phys.*, 54, 1971.
- M. A. Wilson and A. R. C. Baljon. Microstructural origins of nonlinear response in associating polymers under oscillatory shear. *Polymers*, 9(556), 2017.
- H. H. Winter. *Gel Point*, pages 1–15. American Cancer Society, 2016. ISBN 9780471440260.
- H. H. Winter and F. Chambon. Analysis of Linear Viscoelasticity of a Crosslinking Polymer at the Gel Point. *J. Rheol.*, 30(2):367–382, July 1986.
- I. M. Withers, A. V. Dobrynin, M. L. Berkowitz, and M. Rubinstein. Monte carlo simulation of homopolymer chains. i. second virial coefficient. *J. Chem. Phys.*, 118:4721–4732, 2003.
- T. A. Witten and J. J. Prentis. The interpenetration of two chain polymers in a good solvent. *J. Chem. Phys.*, 77(8):4247–4253, 1982.
- J. Wittmer, H. Xu, and J. Baschnagel. Shear-stress relaxation and ensemble transformation of shear-stress autocorrelation functions. *Physical Review E*, 91, 02 2015a.
- J. Wittmer, H. Xu, O. Benzerara, and J. Baschnagel. Fluctuation-dissipation relation between shear stress relaxation modulus and shear stress autocorrelation function revisited. *Molecular Physics*, 113(17-18):2881–2893, 2015b.
- H. Yamakawa. *Modern Theory of Polymer Solutions*. Harper and Row: New York, 1971.
- L. Zhu, X. Wang, J. Li, and Y. Wang. Radius of gyration, mean span, and geometric shrinking factors of bridged polycyclic ring polymers. *Macromol. Theory Simul.*, 25:482–496, 2016.

B. H. Zimm and W. H. Stockmayer. The dimensions of chain molecules containing branches and rings. *J. Chem. Phys.*, 17:1301, 1949.

W. Zylka. Gaussian approximation and Brownian dynamics simulations for Rouse chains with hydrodynamic interaction undergoing simple shear flow. *J. Chem. Phys.*, 94(6): 4628–4636, Mar. 1991.